# Numerical Modeling Studies of Wake Vortex Transport and Evolution Within the Planetary Boundary Layer

## NASA Grant NCC-1-188

## Final Report
### (1/7/1994 – 4/6/2000)

submitted to the
NASA Langley Research Center

by

**Yuh-Lang Lin**
**S. Pal Arya**
**Michael L. Kaplan**
**Jongil Han**

Department of Marine, Earth and Atmospheric Sciences
North Carolina State University
Raleigh, NC 27695-8208
Tel: (919) 515-1438
E-mail: yl_lin@ncsu.edu

May, 2000

# Table of Contents

Appendix A: Planetary Boundary Layer Simulation Using TASS

Appendix B: The Sensitivity of Large-Eddy Simulation to Local and Nonlocal Drag
          Coefficients at the Lower Boundary

Appendix C: Two Dimensional Wake Vortex Simulation in the Atmosphere:
          Preliminary Sensitivity Studies

Appendix D: Toward Three-Dimensional Modeling of a Wake Vortex Pair in the
          Turbulent Planetary Boundary Layer

Appendix E: Large Eddy Simulation of Aircraft Wake Vortices within Homogeneous
          Turbulence: Crow Instability

## 1. Objectives and Goals of the Research

The fundamental objective of this research is to study behavior of aircraft wake vortices within atmospheric boundary layer (ABL) in support of developing the system, Aircraft VOrtex Spacing System (AVOSS), under NASA's Terminal Area Productivity (TAP) program that will control aircraft spacing within the narrow approach corridors of airports. The purpose of the AVOSS system is to increase airport capacity by providing a safe reduction in separation of aircraft compared to the now-existing flight rules. In our first funding period (7 January 1994 – 6 April 1997), we have accomplished extensive model development and validation of ABL simulations. Using the validated model, in our second funding period (7 April 1997 – 6 April 2000) we have investigated the effects of ambient atmospheric turbulence on vortex decay and descent, Crow instability, and wake vortex interaction with the ground. Recognizing the crucial influence of ABL turbulence on wake vortex behavior, we have also developed a software generating vertical profiles of turbulent kinetic energy (TKE) or energy dissipation rate (EDR), which are, in turn, used as input data in the AVOSS prediction algorithms. The above mentioned works accomplished during the past funding period are briefly described in the following sections.

## 2. Validated Simulations of Atmospheric Boundary Layer and Wake Vortices

For numerical modeling studies of the ABL and wake vortices, we have used a three-dimensional, high-resolution, nonlinear, compressible, nonhydrostatic large-eddy simulation model, the Terminal Area Simulation System (TASS: Proctor 1987, 1996). TASS was originally developed at the NASA Langley Research Center for studying meso-$\gamma$ scale phenomena, such as microbursts and severe thunderstorms in the atmosphere. Thus, we have had to modify the model for study of the ABL and wake vortices.

### 2.1. Planetary Boundary Layer Simulation Using TASS

In this study, we have added ABL simulation capability to TASS and validated results with observed data. There are several options for the surface boundary conditions, one of which is a validated surface energy budget using the slab model. We have made comparisons with both the Wangara and Minnesota boundary layer experiments and have shown that results compare well with the observed data, especially considering the limitations in determining initial conditions. Details of the results are given in Appendix A.

### 2.2. The Sensitivity of Large-Eddy Simulation to Local and Nonlocal Drag Coefficients at the Lower Boundary

During model development and validation, we observed an unexpected sensitivity to the surface stress boundary condition. It was found that the homogeneity of the surface drag coefficient plays an important role in the large scale structure of turbulence in large-eddy simulation of the convective atmospheric boundary layer. In particular, when a ground surface temperature was specified, large horizontal anistropies occurred when the drag coefficient depended upon local velocities and heat fluxes. This was due to the formation of streamwise roll structures in the boundary layer. In reality, these structures have been found to form when shear

thermal plume structures. We have found that, in general, a global drag coefficient is preferable. Details of the results are given in Appendix B.

## 2.3. Two- and Three-Dimensional Wake Vortex Simulations Using TASS

It has been found that two-dimensional simulations are useful for investigating the effects of stratification and wind shear on wake vortex transport. However, the addition of two-dimensional background resolved-scale turbulence had only minor effects on vortex transport. Details of the two-dimensional simulation results are given in Appendix C.

A nested grid scheme and three-dimensional initial and boundary conditions have been demonstrated as seen in Appendix D. The nested grid scheme allows multiple one-way or two-way simulations using mass-conservative interpolation and averaging schemes along with radiative boundary conditions which lets unwanted wave energy pass out of the finer mesh domains. The three-dimensional wake vortex initial and boundary conditions enforce fully-developed wake vortices on the upstream boundary but permit the vortices within the domain to develop spatially and temporally.

## 3. Effects of Atmospheric Turbulence on Wake Vortices

Three-dimensional simulations using TASS-LES model have been performed with ambient resolved-scale turbulence. In these numerical experiments, we have examined the effects of atmospheric turbulence on Crow instability (Crow 1970), vortex decay and descent, vortex behavior in ground effect (IGE) and the convective boundary layer (CBL). Three-dimensional real case simulations with atmospheric turbulence are also included.

## 3.1. Effects of Atmospheric Turbulence on Wake Vortices in the Free Atmosphere

### 3.1.1. Large Eddy Simulation of Aircraft Wake Vortices within Homogeneous Turbulence: Crow Instability

The simulation results confirm that the most-amplified wavelength of the Crow instability and the lifetime of wake vortices are significantly influenced by ambient turbulence. The Crow instability becomes well developed in most atmospheric turbulence levels, but in strong turbulence the vortex pair deforms more irregularly due to turbulence advection. The most-amplified wavelength of the instability decreases with increasing dimensionless turbulence intensity ($\eta$), whereas it increases with increasing turbulence integral length scale. The vortex lifespan is controlled primarily by $\eta$ and decreases with increasing $\eta$, whereas the effect of integral scale of turbulence on vortex lifespan is of minor importance. The lifespan is estimated to be about 40 % larger than Crow and Bate's (Crow and Bate 1976) predicted value, but in agreement with Sarpkaya's recent modification (Sarpkaya 1998) to Crow and Bate's theory. This larger lifespan is also supported by data from water tank experiments and direct numerical simulations. There appears to be a possibility that the scatter in vortex lifespans due to ambient turbulence alone decreases with increasing Reynolds number, whereas larger scatter of lifespans in flight tests may result from other factors such as stratification, wind shear, and inhomogeneous ambient turbulence. Details of the results are given in Appendix E.

### 3.1.2. Numerical Study of Wake Vortex Decay and Descent in Homogeneous Atmospheric Turbulence

Numerical simulations are performed in order to isolate the effect of ambient turbulence on the wake vortex decay rate within a neutrally-stratified atmosphere. Simulations are conducted for a range of turbulence intensities, by injecting wake vortex pairs into an approximately homogeneous and isotropic turbulence field. Consistent with field observations, the decay rate of the vortex circulation increases clearly with increasing levels of ambient turbulence and decreases with increasing radial distance. Based on the results from the numerical simulations, simple decay models for the vortex pair are proposed as functions of nondimensional ambient turbulence intensity, nondimensional radial distance, and nondimensional time. Showing good agreement with the numerical results, a Gaussian type of vortex decay model is proposed for weak turbulence, while an exponential type of vortex decay model is more appropriate for strong turbulence. A relationship for the vortex descent based on above vortex decay model is also proposed. The proposed models are compared to Lidar vortex measurements. For strong atmospheric turbulence, the model predictions are in reasonable agreement with the observational data. For weak turbulence with stable stratification, the model, based on turbulence dissipation alone, largely underestimate the observed circulation decay with consistent overestimation of the observed vortex descent. However, this underestimation is significantly reduced when the stratification effect is added in the models. Some other possible reasons for the underestimation of vortex decay in weaker turbulence cases are also discussed. Details of the results are given in Appendix F.

### 3.2. Numerical Study of Wake Vortex Interaction with the Ground

Simulations with the three-dimensional LES and with environmental turbulence show strong decay of the vortex circulation, which agrees very well with the observations, whereas a two-dimensional simulation largely underestimates the observed rate of decay. For the three-dimensional cases, the circulation decay in the IGE simulations appears only weakly sensitive to ambient turbulence levels, while in the simulations free from the IGE (i.e., Appendix F) the decay rate of the vortex circulation increases clearly with increasing levels of ambient turbulence. The implication of IGE vortex prediction is that crude approximation of ambient turbulence level may be adequate for prediction of circulation decay. In addition, the LES results indicate that the lateral and vertical transport of wake vortices in ground effect is weakly influenced by ambient turbulence. On the other hand, our numerical simulations of wake vortices for IGE show that ambient turbulence may trigger a vortex to link with its image beneath the ground. This linking with the ground (which is observed in real cases) gives the appearance of a vortex tube that bends to become vertically oriented and that terminates at the ground. The linking time for IGE appears to be similar to the linking time for vortices in the free atmosphere as shown in Appendix E; i.e., a function of ambient turbulence intensity. Details of the IGE simulation results are given in Appendices G and H.

### 3.3. Large Eddy Simulation of Wake Vortices in the Convective Boundary Layer

This study presents the results of numerical simulations which were carried out for understanding how wake vortices behave in the CBL. Our results show that the vortices are largely deformed due to strong turbulent eddy motion while a sinusoidal Crow instability develops. Vortex rising is found to be caused by the updrafts (thermals) during daytime

convective conditions and increases with increasing nondimensional turbulence intensity $\eta$. In the downdraft region of the convective boundary layer, vortex sinking is found to be accelerated proportional to increasing $\eta$, with faster speed than that in an ideal line vortex pair in an inviscid fluid. Wake vortices are also shown to be laterally transported over a significant distance due to large turbulent eddy motion. On the other hand, the decay rate of the vortices in the convective boundary layer that increases with increasing $\eta$, is larger in the updraft region than in the downdraft region because of stronger turbulence in the updraft region. Details of the simulation results are given in Appendix I.

### *3.4. Real Case Numerical Simulations of Wake Vortices*

Numerical simulations using TASS-LES model have been conducted for two cases from the 1994-1995 Memphis fields measurements. The selected cases have an atmospheric environment of weak turbulence and stable stratification. The purpose for this study is to validate the use of TASS for simulating the decay and transport of wake vortices in a real atmosphere. Our results indicate that the TASS model predicts well the behavior of aircraft wake vortices. Good agreement is obtained between simulations and measurements for the wake vortex trajectories. Exceptional agreement with the measurements is obtained for vortex decay. The simulation results indicate that ambient turbulence, stratification and wind shear play important roles in the decay and transport of wake vortices. In especial, ambient turbulence significantly influences the vortex decay. Details of the simulation results are given in Appendix J.

### 4. An Estimation of Turbulent Kinetic Energy and Energy Dissipation Rate Based on Atmospheric Boundary Layer Similarity Theory

One of the key input elements for AVOSS prediction algorithms (Robins et al. 1998; Sarpkaya et al. 2000) for wake vortex transport and decay is the ABL turbulence of which the intensity can be represented by turbulent kinetic energy (TKE) or eddy energy dissipation rate (EDR). While the prediction algorithm requires the vertical profiles for the TKE and EDR at least up to the vortex generation height, the observational data for the TKE and EDR are available only at the heights of 5 and 40 $m$ above the ground. Algorithms are developed to extract atmospheric boundary layer profiles for turbulence kinetic energy (TKE) and energy dissipation rate (EDR), with data from a meteorological tower as input. The profiles are based on similarity theory and scalings for the atmospheric boundary layer. The calculated profiles of EDR and TKE are required to match the observed values at 5 and 40 m. The algorithms are coded for operational use and yield plausible profiles over the diurnal variation of the atmospheric boundary layer. Details of the software development and comparison of the theory with observation are given in Appendix K.

### 5. List of References

Crow, S. C., 1970: Stability Theory for a Pair of Trailing Vortices. *AIAA Journal*, Vol. 8, No. 12, pp. 2172-2179.

Crow, S. C. and E. R. Bate, 1976: Lifespan of Trailing Vortices on a Turbulent Atmosphere. *Journal of Aircraft*, Vol. 7, No. 7, pp. 476-482.

Proctor, F. H., 1987: The Terminal Area Simulations System. Volume 1: Theoretical Formulation. NASA Contractor Report 4046, DOT/FAA/PM-86/50, 1, 176 pp.

Proctor, F. H., 1996: Numerical Simulation of Wake Vortices Measured During the Idaho Fall and Memphis Field Programs. *14th AIAA Applied Aerodynamics Conference*, Proceedings, Part II, New Orleans, LA, AIAA Paper No. 96-2496, pp. 943-960.

Robins, R. E., D. P. Delisi, and G. C. Greene, 1998: Development and Validation of a Wake Vortex Prediction Algorithm. *36th Aerospace Sciences Meeting & Exhibit*, Reno, NV, AIAA-98-0665, 10 pp.

Sarpkaya, T., 1998: Decay of Wake Vortices of Large Aircraft. *AIAA Journal*, Vol. 36, No. 9, pp. 1671-1679.

Sarpkaya, T., R. E. Robins, and D. P. Delisi, 2000: Wake-Vortex Eddy-Dissipation Model Predictions Compared with Observations. *38th Aerospace Sciences Meeting & Exhibit*, Reno, NV, AIAA-2000-0625, 10 pp.

## 6. List of Publications

Schowalter, D. G., D. S. DeCroix, F. H. Proctor, Y.-L. Lin, S. P. Arya, and M. L. Kaplan, 1995: Turbulent Statistics in the Amospheric Boundary Layer: A Comparison of Large Eddy Simulation with Observations. *11th Symposium on Boundary Layers and Turbulence*, Charlotte, NC, March pp. 552-555.

Schowalter, D. G., D. S. DeCroix, Y.-L. Lin, S. P. Arya, and M. L. Kaplan, 1996: Planetary Boundary Layer Simulation Using TASS. NASA Contrator Report 198325, 34 pp.

Schowalter, D. G., D. S. DeCroix, Y.-L. Lin, S. P. Arya, and M. L. Kaplan, 1996: The Sensitivity of Large-Eddy Simulation to Local and Nonlocal Drag Coefficients at the Lower Boundary. NASA Contrator Report 198310, 36 pp.

Proctor, F. H., D. A. Hinton, J. Han, D. G. Schowalter, and Y.-L. Lin, 1997: Two-Dimensional Wake Vortex Simulations in the Atmosphere: Preliminary Sensitivity Studies. *35th Aerospace Sciences Meeting & Exhibit*, Reno, NV, AIAA-97-0056, 13 pp.

Schowalter, D. G., D. S. DeCroix, G. F. Switzer, Y.-L. Lin, and S. P. Arya, 1997: Toward Three-Dimensional Modeling of a Wake Vortex Pair in the Turbulent Planetary Boundary Layer. *35th Aerospace Sciences Meeting & Exhibit*, Reno, NV, AIAA-97-0058, 13 pp.

Han, J., Y.-L. Lin, D. G. Schowalter, S. P. Arya, and F. H. Proctor, 1997: Large-Eddy Simulation of Aircraft Wake Vortices: Atmospheric Turbulence Effects. *12th Symposium on Boundary Layers and Turbulence*, Vancouver, Canada, pp. 237-238.

Han, J., Y.-L. Lin,.S. P. Arya, and C. Kao, 1997: Large-Eddy Simulation of Aircraft Wake Vortices: Atmospheric Turbulence Effects. *NASA First Wake Vortex Dynamic Spacing Workshop Proceedings*, Hampton, VA, NASA CP-97-206235, pp. 131-144.

Han, J., Y.-L. Lin, S. P. Arya, S. Shen, and F. H. Proctor, 1999: Decay of Aircraft Wake Vortices in a Homogeneous Atmospheric Turbulence: A Large Eddy Simulation Study. *13th Symposium on Boundary Layers and Turbulence*, Dallas, TX, 2 pp.

Han, J., Y.-L. Lin, S. P. Arya, and F. H. Proctor, 1999: Large Eddy Simulation of Aircraft Wake Vortices in a Homogeneous Atmospheric Turbulence: Vortex Decay and Descent. *37th Aerospace Sciences Meeting & Exhibit*, Reno, NV, AIAA-99-0756, 21 pp.

Proctor, F. H. and J. Han, 1999: Numerical Study of Wake Vortex Interaction with the Ground Using the Terminal Area Simulation System. *37th Aerospace Sciences Meeting & Exhibit*, Reno, NV, AIAA-99-0754, 12 pp.

Shen, S., F. Ding, J. Han, Y.-L. Lin, S. P. Arya, and F. H. Proctor, 1999: Numerical Modeling Studies of Wake Vortices: Real Case Simulations. *37th Aerospace Sciences Meeting & Exhibit*, Reno, NV, AIAA-99-0755, 16 pp.

Han, J., S. Shen, S. P. Arya, and Y.-L. Lin, 1999: An Estimation of Turbulent Kinetic Energy and Energy Dissipation Rate Based on Atmospheric Boundary Layer Similarity Theory. *Submitted as a NASA Contract Report.*

Han, J., Y.-L. Lin, D. G. Schowalter, S. P. Arya, and F. H. Proctor, 2000: Large Eddy Simulation of Aircraft Wake Vortices Within Homogeneous Turbulence: Crow Instability. *AIAA J.* Vol. 38, No. 2, pp. 292-300.

Han, J., Y.-L. Lin, S. P. Arya, and F. H. Proctor, 2000: Numerical Study of Wake Vortex Decay and Descent in a Homogeneous Atmospheric Turbulence. *AIAA J.* Vol. 38, No. 4.

Lin, Y.-L., J. Han, J. Zhang, F. Ding, S. P. Arya, and F. H. Proctor, 2000: Large Eddy Simulation of Wake Vortices in the Convective Boundary Layer. *38th AIAA Aerospace Sciences Meeting & Exhibit*, Reno, NV, AIAA-2000-0753, 8 pp.

Proctor, F. H., D. W. Hamilton, and J. Han, 2000: Wake Vortex Transport and Decay in Ground Effect: Vortex Linking with the Ground. *38th AIAA Aerospace Sciences Meeting & Exhibit*, Reno, NV, AIAA-2000-0757, 14 pp.

## 7. List of Reports

Lin, Y.-L., S. P. Arya, M. L. Kaplan, and D. G. Schowalter, 1995: Numerical Modeling Studies of Wake Vortex Transport and Evolution Within the Planetary Boundary Layer. NASA FY95 Annual Report, Grant NCC-1-188.

Lin, Y.-L., S. P. Arya, D. G. Schowalter, and M. L. Kaplan, 1996: Numerical Modeling Studies of Wake Vortex Transport and Evolution Within the Planetary Boundary Layer. Research Proposal for Cooperative Agreement with NASA Langley Research Center.

Lin, Y.-L., S. P. Arya, M. L. Kaplan, and S. Shen, 1998: Numerical Modeling Studies of Wake Vortex Transport and Evolution Within the Planetary Boundary Layer. NASA FY97 Annual Report, Grant NCC-1-188.

Lin, Y.-L., S. P. Arya, M. L. Kaplan, and J. Han, 1999: Numerical Modeling Studies of Wake Vortex Transport and Evolution Within the Planetary Boundary Layer. NASA FY98 Annual Report, Grant NCC-1-188.

**Appendix A: Planetary Boundary Layer Simulation Using TASS**

NASA Contractor Report 198325
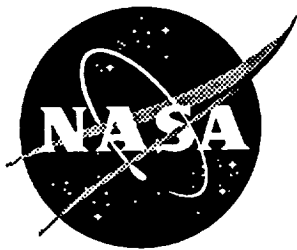
# Planetary Boundary Layer Simulation Using TASS

David G. Schowalter, David S. DeCroix, Yuh-Lang Lin, S. Pal Arya, and
Michael Kaplan
*North Carolina State University, Raleigh, North Carolina*

# Abstract

Boundary conditions to an existing large-eddy simulation model have been changed in order to simulate turbulence in the atmospheric boundary layer. Several options are now available, including the use of a surface energy balance. In addition, we compare convective boundary layer simulations with the Wangara and Minnesota field experiments as well as with other model results. We find excellent agreement of modelled mean profiles of wind and temperature with observations and good agreement for velocity variances. Neutral boundary layer simulation results are compared with theory and with previously used models. Agreement with theory is reasonable, while agreement with previous models is excellent.

# TABLE OF CONTENTS

# LIST OF TABLES

# LIST OF FIGURES

**Figure 9.** (a) Horizontal and (b) vertical velocity variances for the Minnesota Experiment, Run 5A1.

**Figure 10.** Vertical heat flux for Run 5A1 of the Minnesota Experiment.

**Figure 11.** Dimensionless wind shear profiles for a neutral boundary layer from (*a*) TASS and (*b*) Andren

et al. (1994).

**Figure 12.** Same as figure 11 but for $\Phi_c$.

# 1. Introduction

Over the past two years, this group has been working in support of the numerical modeling arm of the NASA Wake Vortex Program. It is believed that the turbulence in the planetary boundary layer will have a significant effect on the evolution of wake vortices. Therefore, a first step is the accurate simulation of this turbulence using Large-eddy simulation. Eventually, a nested grid capability will enable the insertion of a wake vortex pair into the boundary layer. Our goal has been to add proper boundary conditions and to validate the TASS (Terminal Area Simulation System) model for the planetary boundary layer simulation.

What follows in Section 2 is a description of the boundary condition changes to TASS and the associated theory. Section 3 discusses the validation results and Section 4 contains a discussion of neutral boundary layer runs. Section 5 is a summary and we have also included an appendix with instructions for using the boundary layer options with the model.

# 2. New boundary conditions in TASS

The horizontal velocity at the top of the computational domain may now be specified. This is accomplished with a three layer sponge technique much like what was done previously with potential temperature. This velocity may be a function of time.

The geostrophic wind may now be specified. It is not a function of time, but may be a function of height. This is equivalent to specification of the horizontal pressure gradient.

There is a choice of four possible heating (cooling) boundary conditions at the bottom of the computational domain:

1. Simple uniform heating specified as a function of time in which a rate term (in $W/m^2$) is added to the equation for potential temperature at the ground. This should not be used for large heating rates because strong temperature gradients will not be properly accounted for in the surface layer similarity scheme.

2. Specification of surface heat and moisture fluxes in kinematic units ( $°K·m/s$ and $m/s$). In this case, the rate terms are added to the equations for potential temperature and for water vapor at the ground. In addition, the Obukhov length is properly calculated using the value of the heat flux rather than using temperature gradients which may be under-resolved.

3. Specification of the air temperature and moisture close to the ground. Surface layer similarity is then used to calculate the proper heat and moisture fluxes. Again, the Obukhov length is calculated using the surface heat flux. This method was described in detail in our recent Annual Report (Lin *et al.* 1994).

4. Use of a surface energy budget for calculation of soil moisture, soil temperature, and the resulting heat and moisture fluxes to the atmosphere. We use the slab model introduced by Bhumralkar (1975) and Blackadar (1976).

The details and validation of method 4 have not been shown previously and will be given here. In addition, we will discuss validation results for the simulation of the Atmospheric Boundary Layer in general.

2

## 2.1 Surface Energy Budget: Theory

The surface energy budget is essentially equivalent to the one proposed by Bhumralkar (1975) and Blackadar (1976). This method was tested by Deardorff (1978) and shown to be both efficient and accurate. Although this addition was a central item on our original proposal, it was felt that the code should be as simple as possible. The first reason for this is that the option will be used rarely. The original plans for our research did not include either of the other surface boundary condition options, which are simpler *and* more accurate than a surface energy balance. To clarify, the purpose of the entire surface energy balance scheme is to calculate the surface heat and moisture fluxes. A large number of parameters describing soil characteristics goes into the scheme. Many of these are usually not known accurately if they are known at all. If, however, the surface heat and moisture flux are known with any degree of accuracy, it makes infinitely more sense to use those values than to try to predict them using parameters that are questionable. The same is true if the temperature and humidity are known at some level close to the ground. The second reason for keeping the scheme simple is to minimize the additional computational time during its use. For these reasons, a vegetation layer has not been included in the surface energy budget code.

The scheme models the soil as a thin slab whose temperature changes throughout the day above a substrate whose temperature remains constant. The rate equation for the temperature of the slab can then be written as

$$\frac{\partial T_s}{\partial t} = -c_1(Q_h + L_h E_g - Q_r)/(\rho_s c_s d_1) - c_2(T_s - T_m)/\tau_1$$

3

where $T_s$ is the slab temperature, $T_m$ is the temperature of the substrate, $c_s$ is the heat capacity of the soil, $\tau_1$ is the diurnal period, $\rho_s$ is the density of the soil, $d_1$ is the depth of the slab, $Q_h$ is the sensible heat flux to the atmosphere, $Q_r$ is the net radiative heat flux to the slab, $E_g$ is the rate of evaporation of soil moisture, and $L_s$ is the latent heat of evaporation. $c_1$ and $c_2$ are constants, set to $2\pi^{1/2}$ and $2\pi$ respectively. The last term represents the heat exchanged between the slab and the substrate. We may write

$$d_1 = \sqrt{\lambda_s \tau_1} \, ,$$

where $\lambda_s$ is the thermal conductivity of the soil.

The radiative heat flux may be written as

$$Q_r = K_s + I \downarrow - I \uparrow ,$$

where $K_s$ represents the solar radiation, $I\downarrow$ the incoming longwave radiation, and $I\uparrow$ the outgoing longwave radiation. The outward radiative flux is straightforwardly written as

$$I \uparrow = \varepsilon_g \sigma T_s^4 ,$$

$\varepsilon_g$ being the emmisivity of the ground and $\sigma$ being the Stefan-Boltzmann constant. The incoming longwave radiation is more complicated and must be parameterized. Like Deardorff, we use the approximation of Staley and Jurica (1972),

$$I \downarrow = \{\sigma_l + \sigma_m + \sigma_h + [1 - (\sigma_l + \sigma_m + \sigma_h)][0.67][1670q_a]^{0.08}\}\sigma T_a^4 ,$$

in which $q_a$ is the mean humidity at the first model level in the atmosphere and $\sigma_l$, $\sigma_m$, and

$\sigma_h$ are the cloud fractions for middle, low, and high clouds, respectively. Incoming solar

radiation is written as

$$K_s = (1370\frac{W}{m^2})T_K(1-\alpha)\sin\Psi$$

in which $\alpha$ represents the albedo of the ground, $T_k$ is the transmissivity of the atmosphere,

and $\Psi$ is the solar zenith angle. Following Stull (1988),

$$T_K = (0.6 + 0.2\sin\Psi)(1 - 0.4\sigma_h)(1 - 0.7\sigma_m)(1 - 0.4\sigma_l)$$

and

$$\sin\Psi = \sin\phi\sin\delta_s - \cos\phi\cos\delta_s \cos[(\frac{\pi t_{UTC}}{12}) - \lambda_E],$$

where $\delta_s$ is the solar declination angle, $\phi$ is the latitude in radians, $\lambda_e$ is the longitude in

radians, and $t_{utc}$ is the time at $0°$ longitude. We may write the solar declination angle as

$$\delta_s = \phi_r \cos[\frac{2\pi(d - d_r)}{365.25}],$$

5

where $d$ is the day number (out of 365) and $d_r$ (173) is the day of the summer solstice.

$Q_h$, the sensible heat flux is estimated as

$$Q_h = \rho c_p u_* \theta_*,$$

where

$$u_* = \frac{k\sqrt{u^2 + v^2}}{\ln(\frac{z}{z_0}) - \Psi_M(\frac{z}{L})},$$

and

$$\theta_* = \frac{k(\theta - \theta_0)}{\ln(\frac{z}{z_0}) - \Psi_H(\frac{z}{L})}.$$

In these equations, $z_0$ is the surface roughness length, $z$ the height above the ground, $u$ the mean eastward horizontal velocity, $v$ the mean northward horizontal velocity, $\theta$ the potential temperature, $\theta_0$ the potential temperature at $z_0$, and $L$ the Obukhov length. The functional forms used for $\Psi_M(z/L)$ and $\Psi_H(z/L)$ are given in Lin et al. (1994). The problem which then arises is to calculate $\theta_0$. We use the formula of Zilitinkevich (1970),

$$\theta_0 = \theta_s + \frac{0.74}{k}\theta_* [0.13(\frac{u_* z_0}{v})^{0.45}],$$

6

in which $v$ is the kinematic viscosity of air, $\theta_s$ is the potential temperature of the surface

(slab), and $u_*$ and $\theta_*$ from the previous time step are used.

Moisture flux, $E_g$, is calculated in the same manner. We let

$$E_g = \rho u_* q_*,$$

where

$$q_* = \frac{k(q - q_0)}{\ln(\frac{z}{z_0}) - \Psi_H(\frac{z}{L})},$$

$$q_0 = q_s + \frac{0.74}{k} q_* [0.13(\frac{u_* z_0}{v})^{0.45}],$$

and $q$ represents the moisture fraction (g/g) in the atmosphere.

We now come to the determination of the surface value of the moisture fraction. Following Deardorff (1978), a slab model is used for moisture as well as temperature. Thus, we let $w_g$ denote the soil moisture fraction in uppermost portion and $w2$ represent this value for the substrate. $q_s$, the surface atmospheric moisture fraction is given as

$$q_s = \alpha' q_{sat}(T_s, P_s) + (1 - \alpha')q_a \qquad q_s \leq q_{sat}(T_s, P_s)$$

$$\alpha' = \min(1, w_g / w_k),$$

7

where $w_k$ is the value of $w_g$ at which the atmosphere is saturated and $q_{sat}(T_s,P_s)$ is the atmospheric saturation mixing ratio at the surface. The rate equation for the slab soil moisture is

$$\frac{\partial w_g}{\partial t} = -C_1 \frac{(E_g - P)}{\rho_w d_1'} - C_2 \frac{(w_g - w_2)}{\tau_1} \qquad 0 \le w_g \le w_{max},$$

where , $\rho_w$ is the density of liquid water, $P$ is the horizontally meaned precipitation rate. $w_{max}$ is the maximum value of $w_g$ above which runoff occurs. We let $d_1'$ be 10 cm and $d_2'$ be 50 cm, typical values for most soils. We let $C_2$ be 0.9. $C_1$ depends upon soil moisture in the following way:

$$C_1 = 0.5 \qquad\qquad w_g / w_{max} \ge 0.75$$

$$C_1 = 14 - 22.5[(w_g / w_{max}) - 0.15] \qquad 0.15 \le w_g / w_{max} \le 0.75$$

$$C_1 = 14 \qquad\qquad w_g / w_{max} \le 0.15$$

The rate equation for $w_2$ is

$$\frac{\partial w_2}{\partial t} = \frac{-(E_g - P)}{\rho_w d_2'} \qquad 0 \le w_2 \le w_{max}$$

# 3. Validation

## 3.1 Surface energy budget validation

The energy budget scheme was tested as a self-standing entity (outside of TASS) with data from Day 1 in Lettau & Davidson (1957). This extensive field experiment was performed near O'Neill, Nebraska. The ground and radiative heat fluxes were measured directly and the latent and sensible heat fluxes could be estimated by assuming surface layer similarity and using the given vertical profiles of temperature and humidity. For the atmospheric wind speed as a function of time, we linearly interpolated between the values given in Lettau & Davidson, table 4.2 at a height of 6.4 m starting at 0035 local time. The atmospheric humidity (mixing ratio) was converted from the vapor pressure values given in their table 4.3.a. The linear interpolation was done in the same manner. Wind speed at the same height was taken from table 4.1.a and interpolated. Thus these values which are normally contained at the first grid level within TASS were taken from observed data for this validation.

The soil moisture variables were assigned in the following way. Moisture tension values given in table 2.3 of Lettau & Davidson were used in conjunction with soil temperatures in table 2.1.a and the graph (figure 2.3.3, p. 54) to estimate the mass ratio of water to soil. To calculate the volume ratio, we then use

$$w = \frac{\rho_s r_m}{\rho_w},$$

where $r_m$ is the mass ratio, $\rho_s$ is the density of the dry soil (shown in figure 2.2.3.2), and $\rho_w$ is the density of liquid water. We estimated values of soil moisture for 5 cm. depth (slab), and 40 cm. depth (substrate). The next difficulty is estimating $w_k$. The soil at O'Neill, Nebraska for the referenced study was described as a "sandy loam." In Sellers

(1965), we see that for dry clay soil, the volume ratio of solid to total is 0.417. For sand, the ratio is 0.585. Thus, one would estimate that for a sandy loam, the correct ratio might be roughly 0.5. For a sandy loam, Sellers lists the field capacity to be 0.43 times this ratio. The field capacity is the maximum amount of water that a soil can hold against gravity. Thus we have a volume of 0.22 for the field capacity. One would guess that the moisture fraction at which the *air* at the ground is saturated would be somewhat larger than the field capacity. Thus, we use $w_k$=0.30. A summary of all soil parameters is shown table 1 of this paper.

| | |
|---|---|
| $\alpha$ | 0.25 |
| $\lambda_s$ (m$^2$/s) | 0.5 X 10$^{-6}$ |
| $\rho_s c_s$ (j/m$^3$K) | 1.51 X 10$^{-6}$ |
| $\varepsilon$ | 0.90 |
| $w_2$ | 0.21 |
| $w_g$ | 0.16 |
| $w_k$ | 0.30 |

**Table 1.** Soil parameters used for energy budget validation case.

Heat flux and moisture flux for the observational data were calculated from the given profiles by assuming surface layer similarity. In figure 1, these are plotted against the calculated values. Notice that, for heat flux, the observed and calculated values are nearly identical until about 0700, local time. After this time, the agreement is fair. Figure 2 shows the time history of the other portions of the energy budget. All are in good agreement with observation with the exception of the latent heat flux. This is considerably larger in magnitude than the observations in the early morning and considerably smaller than observations in the afternoon. This discrepancy is what causes the mild disagreement with the sensible heat flux. Early in the morning, the larger latent heat flux results in a smaller sensible heat flux, and vice versa in the afternoon. This is due to the lack of a
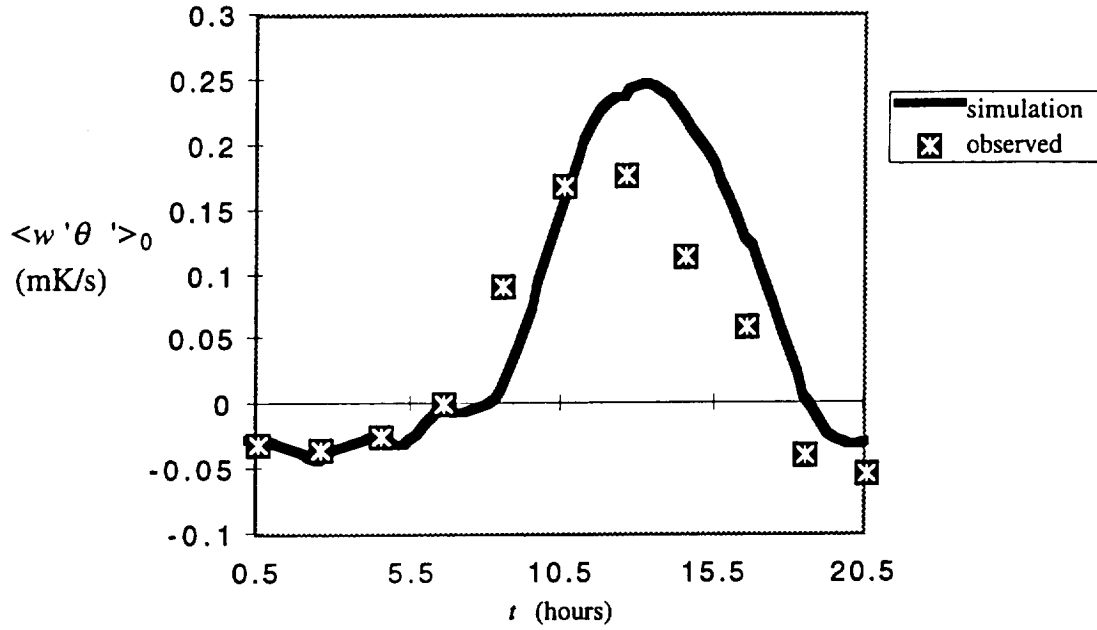
**Figure 1.** Sensible heat flux for the validation case compared with observed values. Observed values were calculated from observed profiles by assuming surface layer similarity.
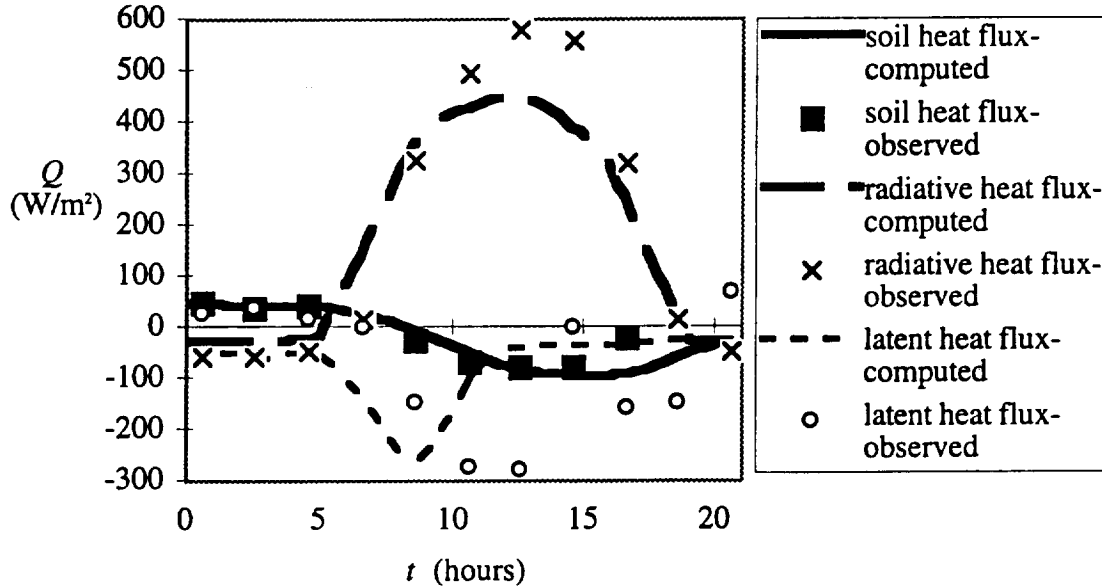


**Figure 2.** Radiative, latent, and soil heat flux for the validation case. Observed values were measured directly for the radiative heat fluxes, were numerically calculated in Lettau & Davidson for the soil heat flux from temperature profiles, and were deduced for the latent heat flux by assuming surface layer similarity.

11

vegetation parameterization in the model. Deardorff (1978) shows the same effect when comparing results with and without vegetation parameterization.

Thus, as mentioned in section 1, we have chosen an energy budget scheme which is simple and provides acceptably accurate results. If deemed necessary in the future, we may add parameterization for vegetation, which would increase the accuracy.

### 3.2 Wangara Validation

Validation of TASS with data from the Wangara Experiment (Clarke *et al.* 1971) has been discussed in some detail by Lin *et al.* (1994). The subgrid contribution to the velocity variances, however, were estimated incorrectly in that paper. Thus, we will show the most important results here. In this case, temperature and moisture at 2m were specified. These values were given in the data report. Resolution for the case shown is 40X40X40, with a horizontal grid resolution of 125 m. and a vertical resolution of 50 m. Figure 3 shows how well this boundary condition works for the potential temperature. Shown are the potential temperature profiles for 0900, 1200, and 1500 local time. The 0900 profile is from the observations and was used to initialize the model. Note that there is larger scatter in the observed data, because they represent single point measurements. The model output was averaged horizontally. The higher potential temperature near the surface for the 1500 observations probably indicates that the rawinsonde balloon was released within a thermal plume. The mean potential temperature within the mixed layer is constant, and the agreement at the top of the boundary layer is excellent, meaning the balloon has probably moved outside of the thermal by this time.

In figure 4, we compare the TASS results for mean winds with the observations and with Deardorff's (1974) results. Again, the scatter in the observed data is due to the single

point nature of the measurements. It is clear from the figure that TASS predicts the wind speeds extremely well.
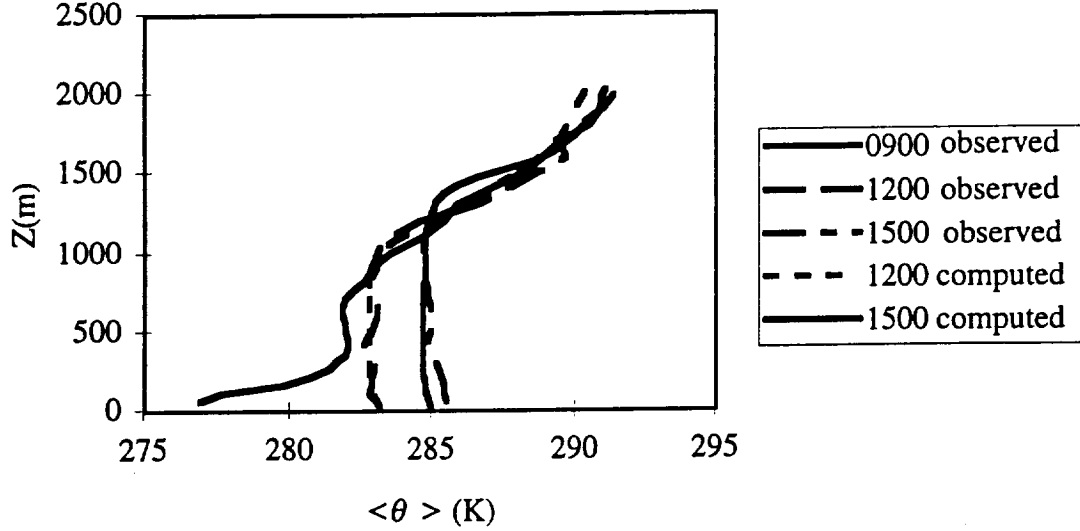


**Figure 3.** Observed and computed potential temperature profiles for the Wangara Experiment, Day 33. The 0900 profile was used to initialize the model.

Horizontal and vertical velocity variances are shown in figure 5. The variances are non-dimensionalized with $w*$, the velocity scale for a convective boundary layer $(w*=[g<w'\theta>_0 Z_i/<\theta>]^{1/3})$. Here, $Z_i$ is the mixed layer depth, $g$ is the gravitational acceleration, $<w'\theta>_0$ is the heat flux at the surface, and $<\theta>$ is the mean potential temperature within the mixed layer. Although no turbulence statistics were measured in the Wangara Experiment, typical dimensionless values for these variances within convective mixed layers are between 0.2 and 0.4, which agrees well with our results.

In addition, we have run one simulation of the Wangara case using the energy budget scheme. Table 2 shows the soil parameters used. Results for potential temperature are shown in figure 6. Notice that the temperature specification boundary condition

13

(previously shown) is much more accurate. The energy budget results, however, are just as accurate as the results of Pleim & Xiu (1995), who used a similar soil model with a one dimensional simulation of Wangara Day 33.

### 3.3 Minnesota Validation

Because the Wangara Experiment contained no data on turbulent intensities and fluxes, it was necessary to look elsewhere for validation of these quantities. We chose the Minnesota Experiment of 1973 ( Izumi & Caughey, 1976). One of the difficulties in this case is that the large scale pressure gradients are not known. For example, as previously mentioned, the geostrophic wind profile may be used by the model. These profiles, however, were not measured in the experiment. To account for this forcing, we obtained synoptic network rawinsonde data (available every twelve hours) on the day of the experiment we chose to simulate. We then performed an objective analysis to extract geostrophic winds as a function of height within our model domain. This is extremely important for predicting mean horizontal winds and for comparing momentum fluxes with observed values. As described in Lin *et al.* (1994), for a steady flow,

$$f(\langle u \rangle - u_g) = -\frac{\partial}{\partial z}\langle v' w' \rangle$$

$$f(\langle v \rangle - v_g) = \frac{\partial}{\partial z}\langle u' w' \rangle$$

where $f$ is the Coriolis parameter, $u$ is the eastward velocity, $v$ the northward velocity, $w$ the vertical velocity, $u_g$ and $v_g$ denote the geostrophic components, and $\langle \rangle$ denotes averaging. The twelve hour spaced geostrophic wind data was then interpolated in time to correspond to the middle of our run, remaining constant throughout the run. The

14

(a)



(b)
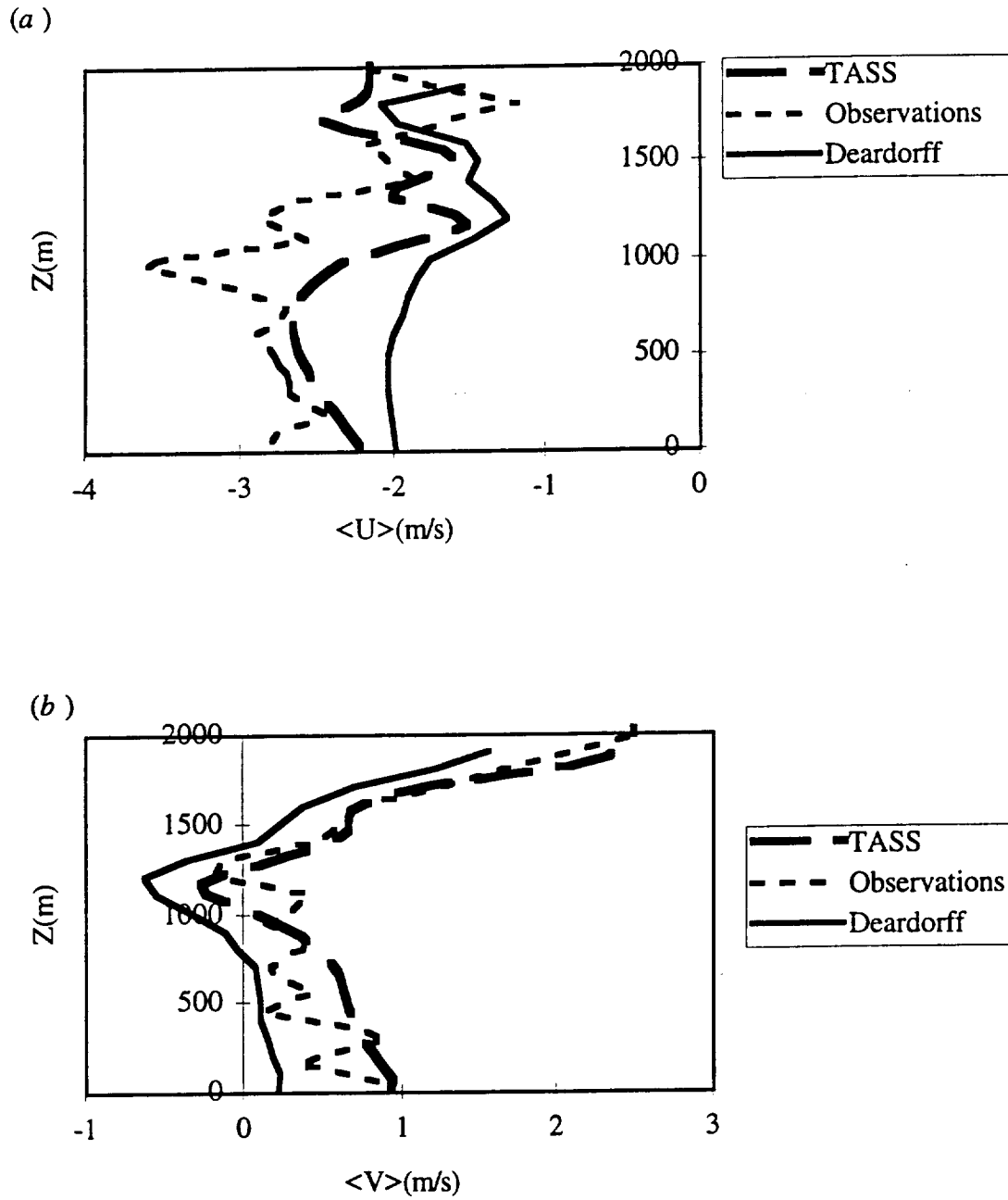


Figure 4. Comparison of mean horizontal velocity results from TASS with Deardorff
(1974) and with observed data. (a) Eastward wind component and (b) northward wind
component. Results shown are for 1200 local time, after three hours of simulation.
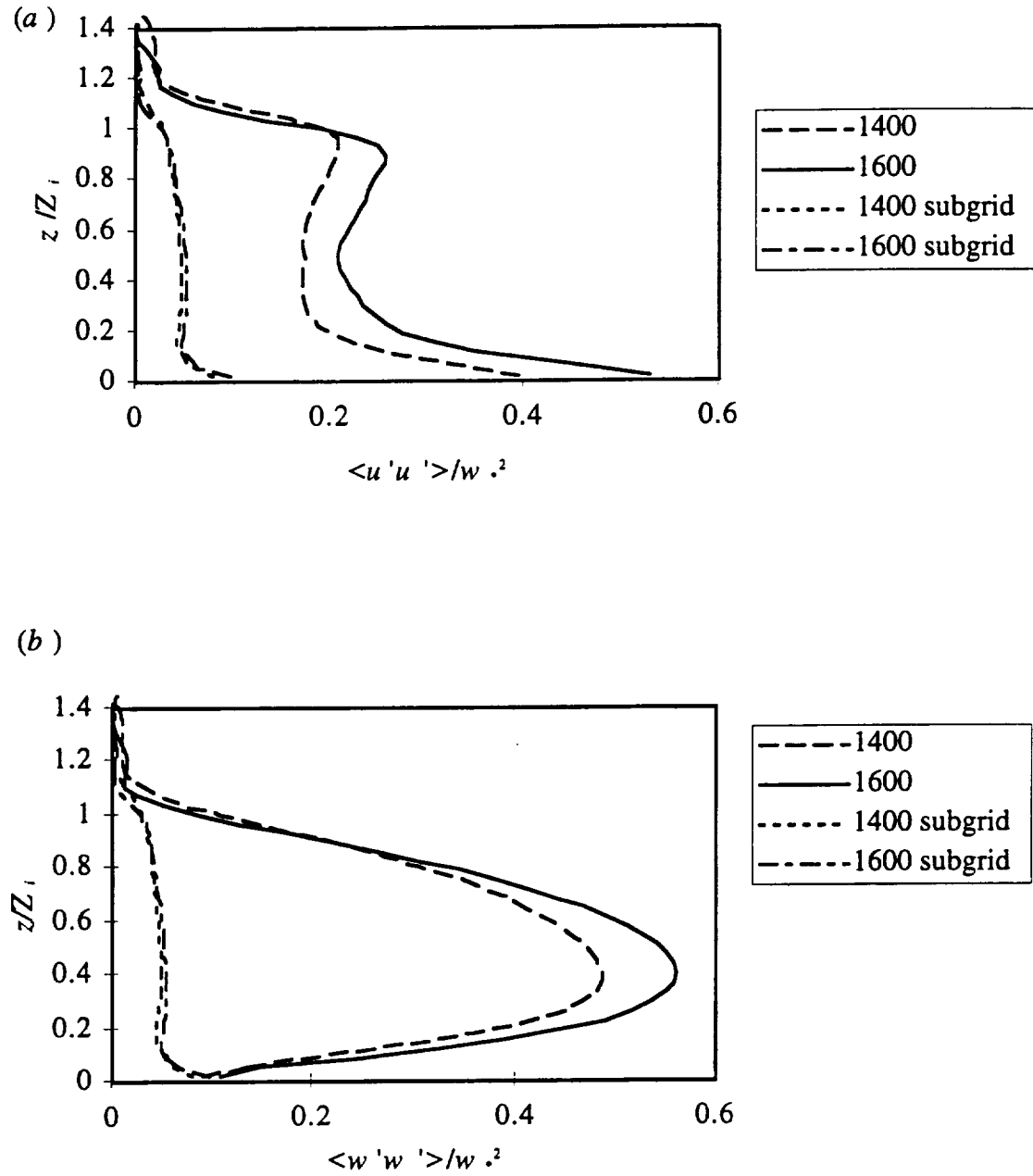
**Figure 5.** (a) Horizontal and (b) vertical velocity variances for the TASS simulation of the Wangara Experiment. Values were averaged horizontally over the domain as well as over one hour in time, centered on the local hour indicated. Subgrid contributions are estimates based on the magnitude of the local deformation tensor.

| | |
|---|---|
| $\alpha$ | 0.25 |
| $\lambda_s$ (m²/s) | 0.5 X 10⁻⁶ |
| $\rho_s c_s$ (J/m³K) | 2.1 X 10⁻⁶ |
| $\varepsilon$ | 0.85 |
| $w_2$ | 0.0245 |
| $w_g$ | 0.002 |
| $w_k$ | 0.2 |

**Table 2.** Soil parameters used for the Wangara case.
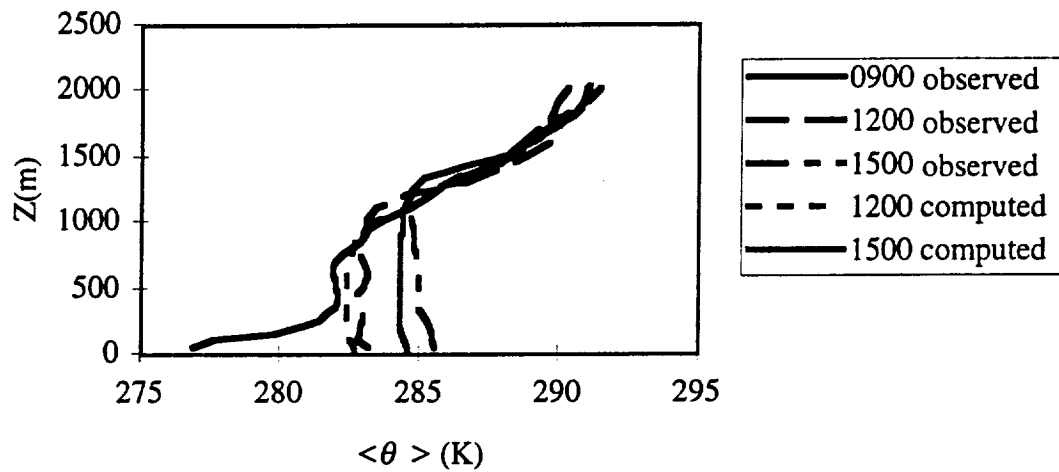


**Figure 6.** Observed and computed potential temperature profiles for Wangara Day 33 using the energy budget scheme in TASS. The observed 0900 profile was used to initialize the model.

model used a 70X70X50 grid, with 50 meter horizontal resolution, and 36 meter vertical resolution with periodic horizontal boundary conditions. Flux specification was used for the lower boundary heating condition.

The model was initialized with a 1259 local time sounding from the experimental site on September 15, 1973. Run 5A1, with which we are comparing, contains quantities

averaged from 1622 to 1737 local time. Thus the model is run for over three hours before the comparison. Model averaging was accomplished by averaging horizontally over the entire domain. These averages were taken every five minutes and, in turn, averaged over the 75 minutes of the experiment. The experimental mixed layer height, $Z_i$, was 1085 meters. The model, however, predicted a height of 1420 meters. This disparity is due primarily to an overestimate of the heat flux between 1259 and the observation period. Only the average surface heat flux during the observation period was given.

Figure 7 shows a comparison of observed and modeled average winds. The overall magnitude is in good agreement, but the observed winds show a large shear within the mixed layer. This is most probably due to a mesoscale effect which could not be captured by the geostrophic wind profiles deduced from the synoptic data. This brings us to figure 8, which shows the vertical momentum fluxes as a function of height. The flux of northward momentum, $<v'w'>$, is in excellent agreement with the observed values. The flux of eastward momentum, $<u'w'>$, is in fair agreement. The curve's shape is similar to the observed profile, but the magnitudes do not agree higher up in the mixed layer. Again, this is a mesoscale effect and the results are quite good considering the data available for our synoptic forcing.
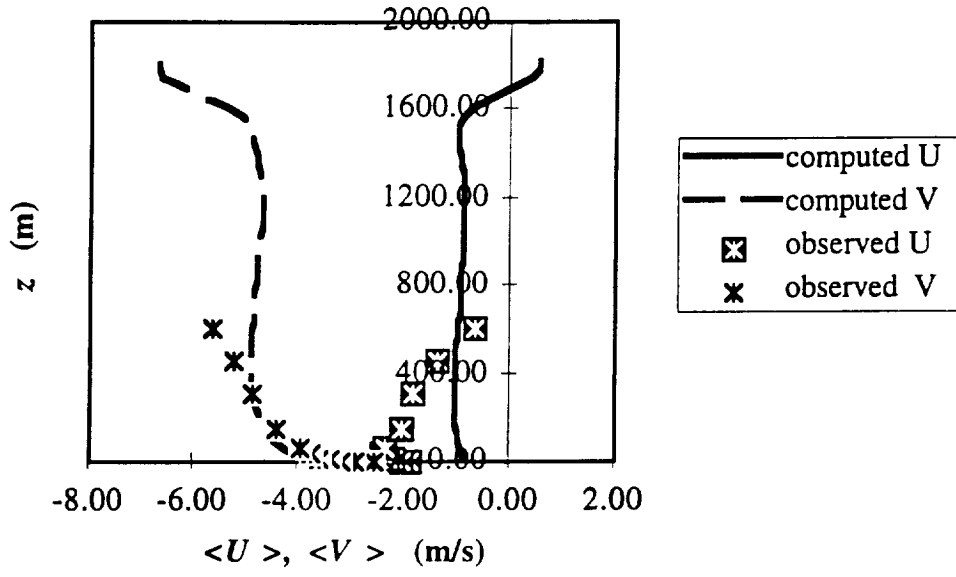
**Figure 7.** Comparison of computed mean winds with observed winds, Run 5A1 of the Minnesota experiment.
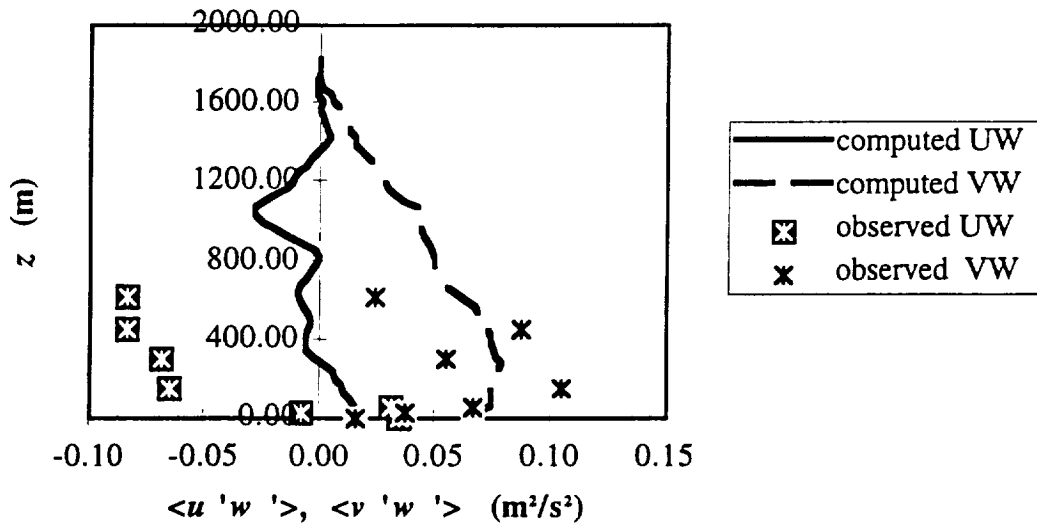


**Figure 8.** Same as figure 7, but for vertical momentum fluxes.

Figure 9 shows horizontal and vertical velocity variances. Both show good agreement, though there is less vertical mixing in the observed mixed layer than in the modeled mixed layer. This is consistent with the unusually high shear observed in figure 7. It is normally expected that the maximum of the vertical velocity variance should occur at between 1/3 and 1/2 of the inversion height, as shown by the model results. The maximum in the observations, however, is much lower. This same effect can be seen in the heat flux profiles of figure 10. Here, the model shows excellent agreement low in the boundary layer. The observed mixed layer, however, shows an unusually small amount of heat flux. The modeled profile is more what one would expect given the surface heat flux and the inversion height.

Thus, the Minnesota Simulation has shown TASS to be acceptable in predicting turbulent fluxes and variances within the convective atmospheric boundary layer. There seems, however, to have been some mesoscale forcing which caused lower mixing strengths than would be expected for a boundary layer with the given surface heat flux and depth. This effect could not be duplicated because the forcing was not resolved by the synoptic network used to obtain geostrophic wind profiles. In addition, some of the disagreement could be due to the lack of information of the surface heat flux *as a function of time*. Only an average was given for the experimental observation period. In the model, the surface heat flux time dependency was determined such that: (1) roughly the right amount of heat would be added from initialization to middle of the observation period to give the right values of potential temperature, (2) the average surface heat flux for the observation period would have the correct value, and (3) the time dependency would be consistent with diurnal variation. Other small time scale variations, however, could have had an effect.
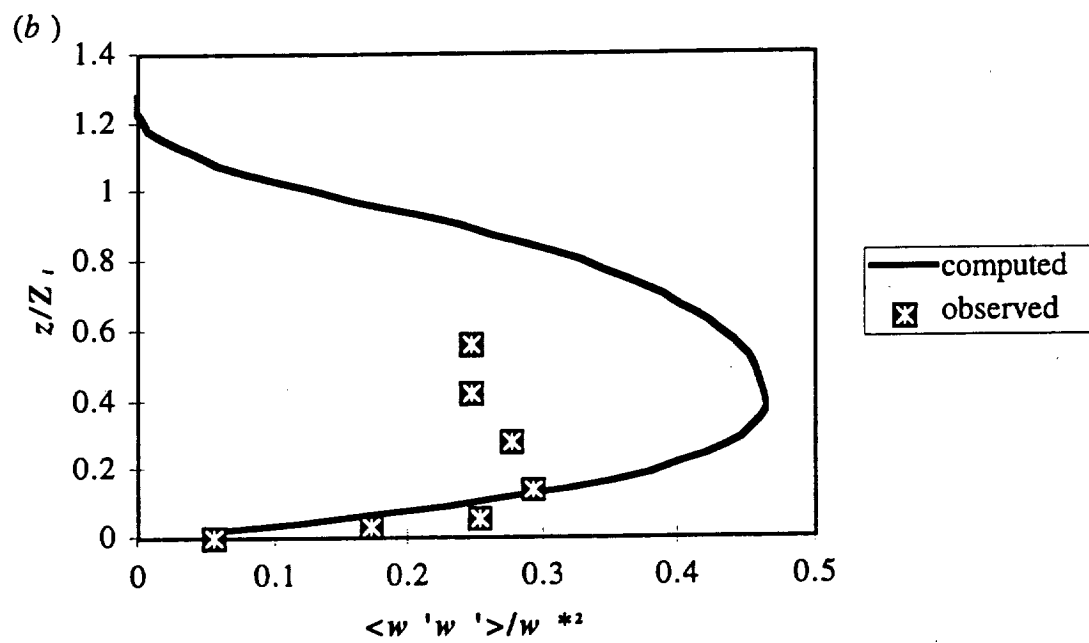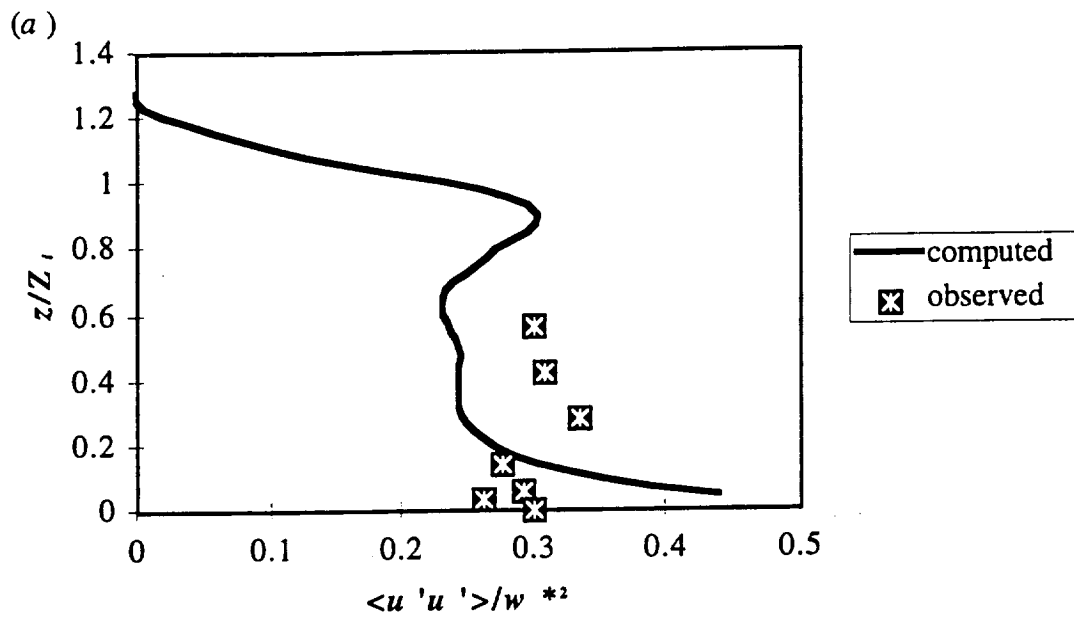
**Figure 9.** (a) Horizontal and (b) vertical velocity variances for the Minnesota
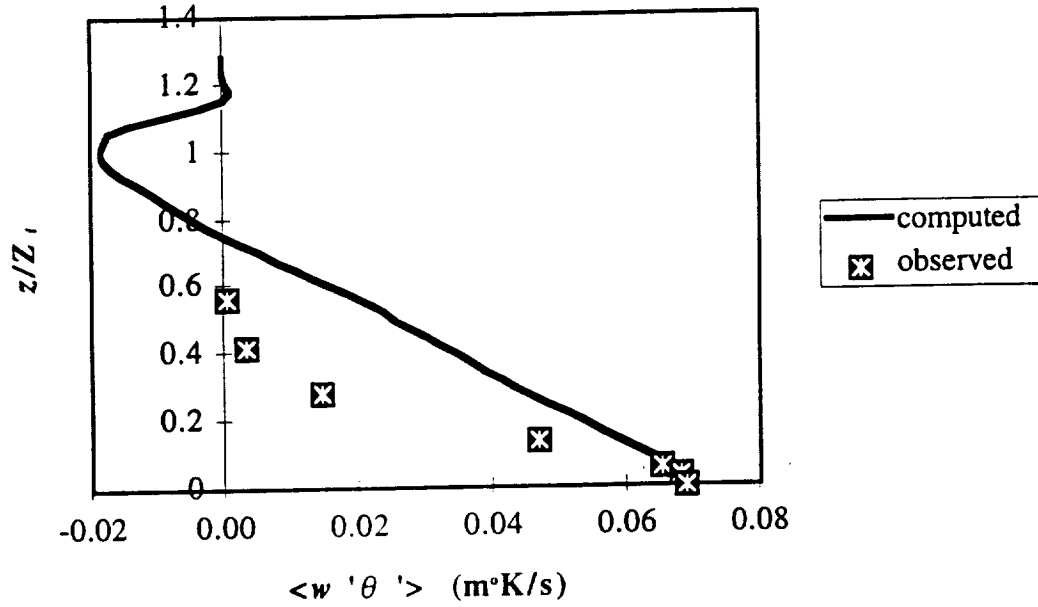
Experiment, Run 5A1.

**Figure 10.** Vertical heat flux for Run 5A1 of the Minnesota Experiment.

# 4. Neutral boundary layer

Although there are few high quality observational data sets of the overall structure of the neutral atmospheric boundary layer, we can compare with theory and empirical surface layer data (the surface layer is the lowest portion of the boundary layer). Given the postulate that stress is constant within the surface layer, it is found that the dimensionless wind shear, $\Phi_M$ is equal to one. This wind shear is expressed as

$$\Phi_M = \frac{kz}{u_*} \sqrt{\left(\frac{\partial\langle u \rangle}{\partial z}\right)^2 + \left(\frac{\partial\langle v \rangle}{\partial z}\right)^2}$$

where $u_*$ is the friction velocity, and $k$ is von Karmann's constant which has been empirically determined to be about 0.4. The friction velocity is expressed as

22

$$u_* = \tau_0 / \rho$$

where $\tau_0$ is the surface stress. In addition, the dimensionless scalar gradient, $\Phi_C$ should be one. This is expressed as

$$\Phi_c = \frac{kz}{c_*} \frac{\partial \langle c \rangle}{\partial z}$$

where $-u_* c_*$ is the surface flux of the scalar $c$. In order to compare to other computer codes, we have duplicated neutral simulations performed by Andren *et al.* (1994), who compared four computer codes.

Figure 11 shows profiles of $\Phi_M$ from *Andren et al.* and from TASS output. We see that, although there is excessive shear close to the ground, TASS shows approximately the same results as most of those in Andren *et al.* The best results for $\Phi_M$ are from Mason's code, which employed the backscatter method discussed in Mason and Thomson (1992). The thrust of this technique involves adding random velocities to the calculated velocities close to the ground at each time step. The rationale is that the turbulent eddies there are under-resolved and that this "backscatter" of energy from small scales to large scales will account for the lack of resolution. There are, however, a number of tunable constants in this process and we believe that, for simulating vortices especially, this type of method may lead to more problems than it solves.

Figure 12 shows a comparison of $\Phi_C$ between Andren *et al.* and TASS. Here, all values are quite close to one throughout the boundary layer.

*(a)*
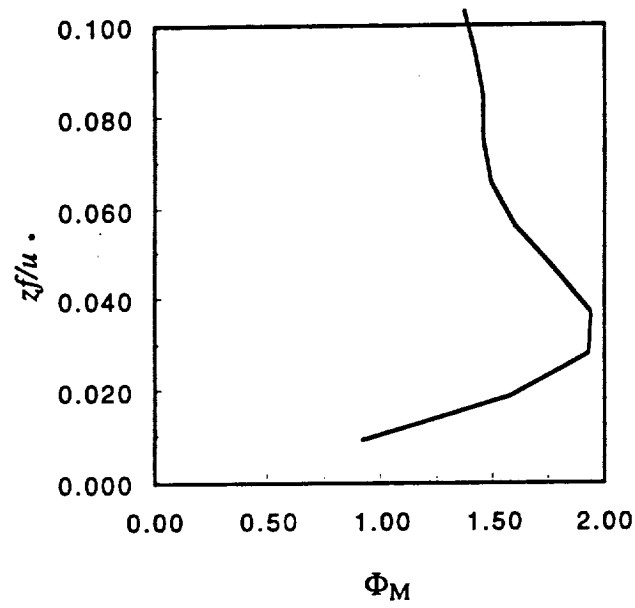


*(b)*
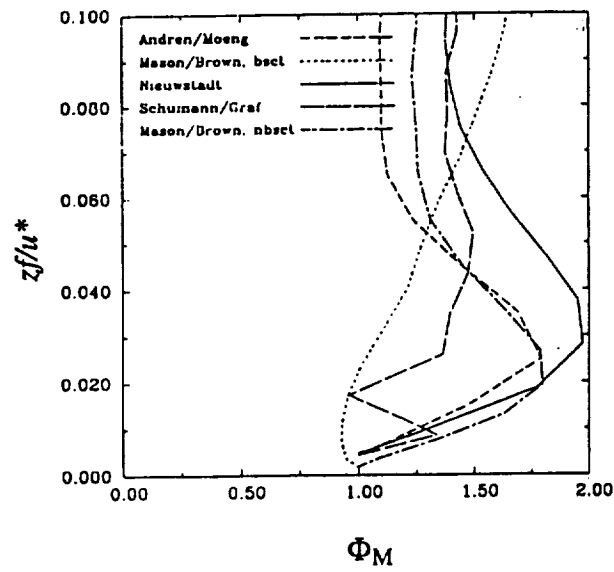


**Figure 11.** Dimensionless wind shear profiles for a neutral boundary layer from (*a*) TASS and (*b*) Andren *et al.* (1994).
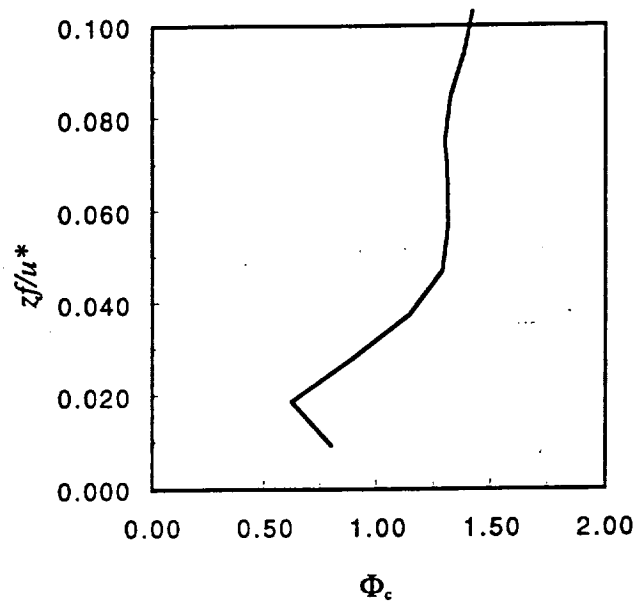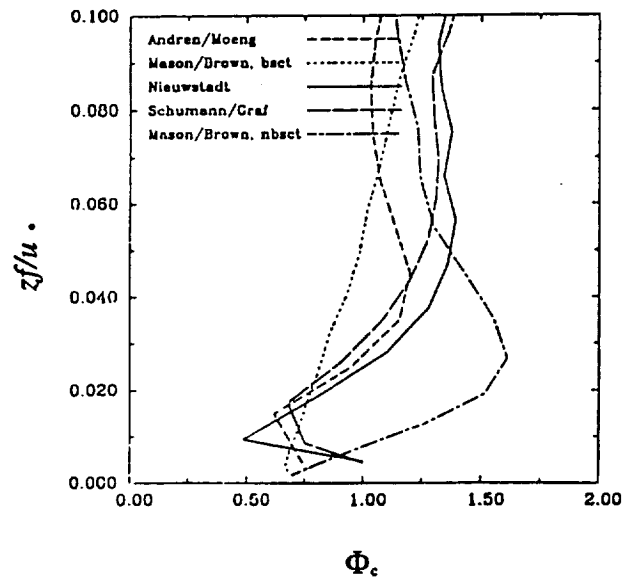
**Figure 12.** Same as figure 11 but for $\Phi_C$.

# 5. Summary

In summary, we have added planetary boundary layer simulation capability to TASS and validated results with observed data. There are several options for the surface boundary conditions, one of which is a validated surface energy budget using the slab model. We have made comparisons with both the Wangara and Minnesota boundary layer experiments and have shown that results compare well with the observed data, especially considering the limitations in determining initial conditions.

# References

Andren, A. Brown, A. R., Graf, J., Mason, P. J, Moeng, C.-H., Nieuwstadt, F.T.M., & Schumann, U. 1994. Large-eddy simulation of a neutrally stratified boundary layer: A comparison of four computer codes. *Q. J. R. Meteor. Soc.*, **120**, 1457-1484.

Bhumralkar, C. M. 1975. Numerical experiments on the computation of ground surface temperature in an atmospheric general circulation model. *J. Appl. Meteorol.* **14**, 1246-1258.

Blackadar, A. K. 1976. Modeling the nocturnal boundary layer, *Proceedings of the Third Symposium on Atmospheric Turbulence, Diffusion and Air Quality*, pp. 46-49, American Meteorological Society, Boston, MA.

Clarke, R. H., Dyer, A. J., Brook, R. R., Reid, D. G., & Troup, A. J. 1971. The Wangara Experiment: Boundary Layer Data. CSIRO Div. of Meteorol. Phys. Tech. Paper No. 19.

Deardorff, J. W. 1978. Efficient prediction of ground surface temperature and moisture, with inclusion of a layer of vegetation. *J. Geophys. Res.* **83** (C4), 1889-1903.

Izumi, Y. & Caughey, S. J. 1976. Minnesota 1973 Boundary Layer Data Report. Environmental Research Paper No. 547, AFGL, Bedford, MA.

Lettau, H. H. & Davidson, B. 1957. Exploring the Atmosphere's First Mile, vols. 1 and 2. Pergamon, New York.

Lin, Y.-L., Arya, S. P. Kaplan, M. L., & Schowalter, D. G. 1994. Numerical modeling studies of wake vortex transport and evolution within the planetary boundary layer. FY94 Annual Report. Grant #NCC-1-188.

Mason, P.J. & Thomson, D.J. 1992. Stochastic backscatter in large-eddy simulation of boundary layers. *J. Fluid Mech.*, **242**, 51-78.

Pleim, J. E. & Xiu, A. 1995. Development and testing of a surface flux and planetary boundary layer model for application in mesoscale models. *J. App. Met.* **34**, pp. 16-32.

Sellers, W. A. 1965. Physical Climatology. University of Chicago Press, Chicago, Illinois.

Staley, D. O. & Jurica, G. M. 1972. Effective atmospheric emissivity under clear skies. *J. Appl. Meteorol.* **11**, 349-356.

Stull, R. B. 1988. An Introduction to Boundary Layer Meteorology. Kluwer Academic Publishers, Dordrecht.

Zilitinkevich, S. S. 1970. Dynamics of the Atmospheric Boundary Layer, Hydrometeorological Publishing House, Leningrad.

# Appendix : Directions for using TASS PBL boundary conditions

To run TASS in the boundary layer mode, one additional input file is needed, fortran unit 7. If this file is not present, the model will run in the original mode In the boundary layer mode, unit 7 must be present for all restarts, and unit 7 must contain the following information.

1. Five logical variable values, format (5L4) each in the following order: UNHEAT, TSPEC, FLXSPEC, EBUDG, TKE. UNHEAT refers to uniform heating. If this variable is true, then a uniform heating is input at the first grid level. The Obukhov length is not explicitly calculated. TSPEC refers to temperature specification. When true, the heat and moisture fluxes are calculated by assuming surface layer similarity. The Obukhov length is explicitly calculated for stress determination. If FLXSPEC is true, then the heat and moisture fluxes are specified in kinematic units. Again, the Obukhov length is explicitly calculated. When EBUDG is true, the energy balance scheme is used to calculate the fluxes. Only one of the previous four variables may be true, otherwise an error message will appear and the run will be terminated. In addition, if any of the above variables are true, a random temperature perturbation is introduced into the first three layers of the domain to start up perturbations on a resolvable scale. When TKE is true, the amount of turbulent kinetic energy at each level in $z$ may be specified.

2. XITMAX, the number of data items for heating specification.

3. Heating data. Each line is free format, with the data in the following order:

if UNHEAT=.T.: time in minutes, heat rate in W/m$^2$, U(m/s) at top boundary, V(m/s) at top boundary.

if TSPEC=.T.: time in minutes, temperature (C) at $z_a$, humidity (g/g) at $z_a$, U(m/s) at top boundary, V(m/s) at top boundary.

if FLXSPEC=.T.: time in minutes, heat flux (K·m/s), moisture flux (m/s), U(m/s) at top boundary, V(m/s) at top boundary.

if EBUDG=.T.: time in minutes, middle cloud fraction, high cloud fraction, U(m/s) at top boundary, V(m/s) at top boundary.

4. If TSPEC=.T., then $z_a$ appears on the line below the heating data items.

5. Logical variable value for GFORCE (L4). If this is true, then the geostrophic wind is specified and the logical variable NOSTEADY should be set to true. If GFORCE is false, NOSTEADY may be either true or false.

6. If GFORCE is true, the next line must contain a logical value to be assigned to GWCONST (L4). If GWCONST is true, the geostrophic wind is constant with height and only one value of the eastward and northward components of the geostrophic winds need be specified.

7. If GFORCE is true, next comes a line delimited list of geostrophic wind values, with the eastward component first and the northward component second on each line.

There must be a line for each K value starting at K=2 and ending at K=KS. If GWCONST is true, then only one line is necessary.

8.  If TKE =.T., the next lines contain values of turbulent kinetic energy for each K level starting at K=2 and ending at K=KS-2.

9.  The logical value of the variable DFLUX. If true, dust is introduced from the ground throughout the simulation and the environmental values throughout the atmosphere are 0.

10. If DFLUX=.T., the real value of DUSTIN, the dust flux at the surface.

11. If EBUDG=.T., a line containing the values of UTC (the time at $0°$ longitude at the initialization time of the model), DAY (the day of the year, between 1 and 365), LNGT (the longitude), and TS (the surface temperature at initialization).

12. If EBUDG=.T., a line containing the values of ALB (ground albedo) , LAMS (thermal conductivity of the soil in $m^2/s$), TM (the substrate temperature in K), WKW ($w_k$ in $m^3/m^3$), WMAX ($w_{max}$ in $m^3/m^3$), W2 ($w_2$ at initialization in $m^3/m^3$), and WG ($w_g$ in $m^3/m^3$ at initialization).

13. If EBUDG=.T., line containing the values of CS ($\rho_s c_s$ in $[J \cdot kg]/[K \cdot m^3]$), EMISS (the ground emissivity), D1PRIME ($d_1{}'$ in m), and D2PRIME ($d_2{}'$ in m).

We now show two examples of unit 7 files.

EXAMPLE 1

In this example, KS is 13. The energy budget scheme is employed and a resolved scale turbulent kinetic energy is specified at each level, level 2 being the only non-zero value. The heating value items show no middle or high clouds. Eastward winds at the upper boundary vary from 0.5 m/s at the beginning of the simulation to -4.15 m/s at 999 minutes. Northward winds here vary from 1.10 m/s to 1.47 m/s in the same time period. There are 11 heating data items. There is geostrophic wind specification which is a function of height. There is not dust flux at the surface and the soil parameters and other parameters used for the energy budget scheme appear at the bottom.

```
.F. .F. .F. .T. .T.              # unheat, tspec, flxspec, ebudg,tke

 11                               # xitmax: number of data items for heating

  0.  0.0  0.0  0.5 1.10

 60.  0.0  0.0  0.07 1.96

120.  0.0  0.0   -1.19 2.60

180   0.0  0.0  -2.23 2.55

240.  0.0  0.0  -1.67 1.96        # time in minutes; middle cloud cover;

300.  0.0  0.0  -2.85 2.10        # high cloud cover; u at top boundary (m/s);

360.  0.0  0.0  -3.13 1.89        # v at top boundary (m/s)

420.  0.0  0.0  -3.83 2.07

480.  0.0  0.0  -3.74 1.79

540.  0.0  0.0  -4.15 1.47

999.  0.0  0.0  -4.15 1.47

.T.                               # gforce

.F.                               # gwconst

 -5.4275   0.0
```

32

-5.2825  0.0                         # geostrophic wind values (u,v) in m/s, K=2,13

-5.1375    0.0

-4.9925    0.0

-4.8475    0.0

-4.7025    0.0

-4.5575    0.0

-4.4125    0.0

-4.2675    0.0

-4.1225    0.0

-3.9775    0.0

-3.8325    0.0

0.365                                # tke values

0.0

0.0

0.0

0.0

0.0

0.0

0.0

0.0

0.0

.F.                                  # dflux

23.34   226.  -144.93     282.43     # utc, day, lngt,ts

0.25  0.5E-06  280.5  0.20  0.25  0.0245  0.002      # alb, lams, tm, wkw, wmax, w2, wg

2.1E+06   0.85  0.10  0.50           # cs, emiss, d1prime, d2prime


EXAMPLE 2




33

In this example, a neutral boundary layer is being studied. Thus the UNHEAT option is used with the heating rate set to 0. We specify a constant geostrophic wind of 10 m/s in the Eastward direction. We also introduce a dust flux of 0.001g/g·s at the lower boundary. Again, KS=13.

```
.T. .F. .F. .F. .T.          # unheat, tspec, flxspec, ebudg, tke

2                            # xitmax: number of data items for heating

0.  0.   10.0  0.0           # 0 heating rate, 10 m/s Eastward wind at top of

10000.  0.   10.0  0.0       # domain.

.T.                          # gforce

.T.                          # gwconst:  geos. wind is constant with ht.

10.0  0.0                    # geostrophic wind

0.365                        # tke values for each vertical level

0.295

0.245

0.205

0.175

0.145

0.120

0.100

0.085

0.070

.T.                          # dflux

0.001                        # dustin
```

# Appendix B: The Sensitivity of Large-Eddy Simulation to Local and Nonlocal Drag Coefficients at the Lower Boundary

NASA Contractor Report 198310
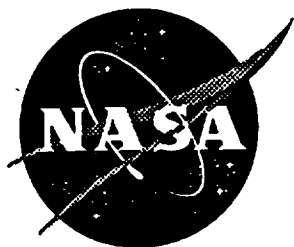
# The Sensitivity of Large-Eddy Simulation to Local and Nonlocal Drag Coefficients at the Lower Boundary

D. G. Schowalter, D. S. DeCroix, Y-L. Lin, S. P. Arya, and M. L. Kaplan
*North Carolina State University, Raleigh, North Carolina*

# Abstract

It was found that the homogeneity of the surface drag coefficient plays an important role in the large scale structure of turbulence in large-eddy simulation of the convective atmospheric boundary layer. Particularly when a ground surface temperature was specified, large horizontal anisotropies occurred when the drag coefficient depended upon local velocities and heat fluxes. This was due to the formation of streamwise roll structures in the boundary layer. In reality, these structures have been found to form when shear is approximately balanced by buoyancy. The present cases, however, were highly convective. The formation was caused by particularly low values of the drag coefficient at the entrance to thermal plume structures.

# Contents

iii

# List of Tables

iv

# List of Figures

# 1 Introduction

The work presented in this paper is part of a joint NASA FAA program to predict aircraft wake vortex behavior under various meteorological conditions within the planetary boundary layer. As described by Hinton (1995), the long term goal is to have safer, more efficient spacing requirements for landing aircraft. In the short term, we plan to simulate wake vortex interaction with atmospheric turbulence. As a first step, we have achieved validated large-eddy simulation of atmospheric boundary layer turbulence in convective conditions and have found some important results with regard to the implementation of the surface stress boundary condition. Some of the validation results are contained in Schowalter *et al.* (1995).

A number of recent publications have addressed the effects of nonhomogeneous surface heating in large-eddy simulation. Hechtel *et al.* (1990) have studied the effects of random variations in surface heat flux on large-eddy simulations of the convective boundary layer. They found no significant differences between the homogeneous and nonhomogeneous cases. Shen and Leclerc (1994), however, found that sinusoidal variations in surface heat flux had a significant effect on the turbulence statistics when the mean wind was weak. Shen and Leclerc (1995) further found that the most significant differences in variance structure occurred when the length scales of the sinusoidal variations were on the order of the boundary layer depth.

Large-eddy simulation involves explicit rendering of the large-scale turbulent eddies and a parameterization of the small scale eddies. Thus, the equations are filtered such that small scale motions cannot be resolved. Be-

cause the scales of motion close to the ground are particularly unresolved, calculating the stress there is especially problematic. Past researchers (Deardorff, 1973, 1974, Moeng, 1984, Mason, 1989, Schmidt and Schumann, 1989, among others) have used Monin-Obukhov similarity laws to calculate the stress at the surface. Usually, the local stress at the surface is related to the local velocity near the surface by

$$\tau_0 = -C_D \|\mathbf{u}\| \mathbf{u}, \tag{1}$$

where $\tau_0$ represents the local surface stress, $C_D$ the drag coefficient, $\mathbf{u}$ the local horizontal velocity vector, and $\|\mathbf{u}\|$ is the magnitude of that velocity. The drag coefficient is dependent upon the stability characteristics of the surface and is calculated using the similarity laws. Although the stress is proportional to the square of the *local* velocity, the drag coefficient may or may not be horizontally homogeneous.

Deardorff's (1973, 1974), Mason's (1989), and Schmidt and Schumann's (1989) drag coefficients depended upon local variables, but Moeng's (1984) was based upon horizontal averages of the variables. There is little explanation in any of these cases as to why the choice was made. Deardorff (1973) did explain, however, that Monin-Obukhov similarity laws were based upon long time or ensemble averages and that using them locally was not strictly correct.

In this paper, we compare both approaches and find significant differences in turbulent structure. The LES model and boundary conditions are described in section 2 while sensitivity tests of various domain sizes and resolutions and a discussion of those results are found in section 3. Concluding

remarks are made in section 4.

## 2  Model Description

We have used the TASS model (Proctor 1988; Proctor and Bowles 1992) for the simulations. The model was originally developed for the study of thunderstorms and microbursts, but only required a change in boundary conditions for the simulation of the planetary boundary layer. Not allowing precipitation in the present simulations, the equations solved were

$$
\begin{aligned}
\frac{\partial u_i}{\partial t} = & -\frac{H}{\rho_0}\frac{\partial p}{\partial x_i} + u_i\frac{\partial u_j}{\partial x_j} - \frac{\partial(u_i u_j)}{\partial x_j} \\
& + g(H-1)\delta_{i3} - 2\Omega_j(u_k - u_{g_k})\epsilon_{ijk} \\
& + \frac{1}{\rho_0}\frac{\partial \tau_{ij}}{\partial x_j}
\end{aligned}
\tag{2}
$$

$$
\frac{\partial p}{\partial t} = -\frac{C_p P}{C_v}\frac{\partial u_j}{\partial x_j} + \rho_0 g u_j \delta_{j3}
\tag{3}
$$

$$
\begin{aligned}
\frac{\partial \theta}{\partial t} = & -\frac{1}{\rho_0}\frac{\partial(\theta \rho_0 u_j)}{\partial x_j} + \frac{\theta}{\rho_0}\frac{\partial(\rho_0 u_j)}{\partial x_j} \\
& + \frac{1}{\rho_0}\frac{\partial S_j(\theta)}{\partial x_j}
\end{aligned}
\tag{4}
$$

$$
\begin{aligned}
\frac{\partial Q_v}{\partial t} = & -\frac{1}{\rho_0}\frac{\partial(Q_v \rho_0 u_j)}{\partial x_j} + \\
& \frac{Q_v}{\rho_0}\frac{\partial(\rho_0 u_j)}{\partial x_j} + \frac{1}{\rho_0}\frac{\partial S_j(Q_v)}{\partial x_j}.
\end{aligned}
\tag{5}
$$

Here, $u_i$ are the velocity components, $p$ the pressure deviation from the environment $P_0$, $\Omega_j$ the earth's rotation vector, $g$ the gravitational acceleration,

3

$C_p$ the specific heat at constant pressure, $C_v$ the specific heat at constant volume, $\rho_0$ the density of the environment, $u_{g_k}$ the geostrophic wind vector, $\tau_{ij}$ the subgrid turbulent stress tensor, $\theta$ the potential temperature, $Q_v$ the water vapor mixing ratio, and $S_j(Q)$ is the subgrid turbulent flux of the scalar $Q$. Additionally,

$$H = (\frac{\theta}{\theta_0} - \frac{pC_v}{P_0 C_p})[1 + 0.61(Q_v - Q_{v0})], \tag{6}$$

where $Q_{v0}$ is the water vapor mixing ratio of the environment.

A modified Smagorinsky first order closure was used in which the eddy viscosity depended upon stability:

$$\tau_{ij} = \rho_0 K_M D_{ij} = \rho_0 K_M (\frac{\partial u_i}{\partial x_j} +$$

$$\frac{\partial u_j}{\partial x_i} - \frac{2}{3}\frac{\partial u_k}{\partial x_k}\delta_{ij}) \tag{7}$$

$$S_j(\theta) = \rho_0 K_H \frac{\partial \theta}{\partial x_j} \tag{8}$$

$$K_M = (l)^2 \sqrt{\frac{1}{2} D_{ij} \cdot D_{ij}(1 - R_f)} \tag{9}$$

where

$$l = \qquad \alpha \Delta \qquad kz \geq \alpha \Delta \tag{10}$$

$$l = \frac{\alpha \Delta [1 + (\alpha \Delta / kz)^{n-1}]}{1 + (\alpha \Delta / kz)^n} \quad \alpha \Delta > kz > k\Delta z/2 \tag{11}$$

$$l = \qquad kz \qquad z \leq \Delta z/2 \tag{12}$$

$$\Delta = (2\Delta x 2\Delta y 2\Delta z)^{1/3} \tag{13}$$

and

$$K_H = 3K_M. \tag{14}$$

4

Here, $R_f$ denotes the local flux Richardson's number, $\alpha$ is an empirical constant, and $k$ is von Karman's constant. The purpose of Equation 11 is to match the mixing length to the appropriate value close to the ground where the flow is under-resolved. For the current runs, the matching parameter, $n$ was set to 2.5.

These equations were solved on an Arakawa C type mesh. Periodic boundary conditions have been used in the horizontal directions, while a sponge layer with three grid intervals has been added on the top of the physical domain. At the top boundary, there existed neither heat nor mass transfer.

The lower boundary employed a no-slip condition. We have used two methods of heat transfer from the ground to the atmosphere. In the first case, the air temperature at a specified level close to the ground has been given as a function of time. The heat flux was then calculated based upon the difference between the atmospheric temperature at the first grid level and the temperature close to the ground. This is useful for comparison to experimental observations in which heat flux was not directly measured, but careful temperature measurements were made. Appendix A gives the details of this calculation. The second method was the explicit specification of surface heat flux as a function of time.

Because the first grid point above the ground is assumed to be within the constant stress surface layer, the drag coefficient could be calculated through the use of Monin-Obukhov similarity laws. The result is

$$C_D = \{\frac{k}{\ln(z_a/z_0) - \Psi_M(z_a/L)}\}^2, \tag{15}$$

where $z_a$ is the height of the first grid level, $z_0$ is the roughness height, $\Psi_M$

is the stability function given by Paulson (1970), and $L$ is the Obukhov length. Specifics of the calculation of $\Psi_M$ may be found in the Appendix. The local velocity at height $z_a$ was then used in Equation (1) to calculate the local stress at the ground. For a horizontally varying drag coefficient, the Obukhov length may be calculated as

$$L = -\frac{\theta u_*^3}{g\overline{(w'\theta')_s}},$$ (16)

where

$$u_* = \frac{k u_a}{\ln(z_a/z_0) - \Psi_M(z_a/L)}.$$ (17)

Here, $u_a$ is the local velocity magnitude at $z_a$ and $\overline{(w'\theta')_s}$ is the local surface heat flux. For a global drag coefficient, we would have

$$L = -\frac{\langle\theta\rangle u_*^3}{g\langle\overline{(w'\theta')_s}\rangle},$$ (18)

and

$$u_* = \frac{k\langle u_a\rangle}{\ln(z_a/z_0) - \Psi_M(z_a/L)},$$ (19)

where $\langle\ \rangle$ denotes a horizontal average over the entire domain. Note that a value of $L$ is required in Equations (17) and (19). The value from the previous time step was used here.

For the homogeneous drag coefficient case, the model has been compared with observations of the Wangara Experiment, Day 33 [4]. Figure 1 ($a$) shows potential temperatures as a function of local time of day for simulation and observations. The simulation was started from the 0900 local sounding. Figure 1 ($b$) shows a comparison of mean wind profiles after three hours of simulation. In the latter case, results from Deardorff (1974) are also shown.

6

Notice that a 40 × 40 × 40 grid was used for this case with 125 m horizontal resolution and 50 m vertical resolution. The model reasonably reproduced the experimental results.

For testing of the boundary conditions, simplified initial and environmental conditions were contrived. All cases to be discussed in section 3 used a constant westerly geostrophic wind of 3.0 ms$^{-1}$. Winds were initialized at this geostrophic value. The sounding from 1200 local time on Day 33 of the Wangara experiment was used for the initial temperature profile. The inversion was located at approximately 1000 m. Random temperature perturbations with a maximum of $\pm$ 1 C were introduced within the lowest three layers of the grid at initialization to start convection. A total of seven different runs, listed in Table 1, were made with different specifications of surface temperature or heat flux, horizontal domain size, and vertical resolution.

# 3 Results and Discussion

## 3.1 70 × 70 × 36 Domain

Cases ALT, ALF, and AGF, discussed here, contained 70 points in both the $x$ (easterly) and $y$ (northerly) directions, while 36 points were used in the $z$ (vertical) direction. Each grid cell had a resolution of 50 m in all directions. This resulted in a domain size of 3500 m × 3500 m × 1800 m with the center of the first grid cell at 25 m above the ground. For case ALT (Local Temperature), the temperature at $z$=2 m was specified and increased in time at a rate of 0.72 C hr$^{-1}$. The surface heat flux thus depended upon the local

(a)

(b)
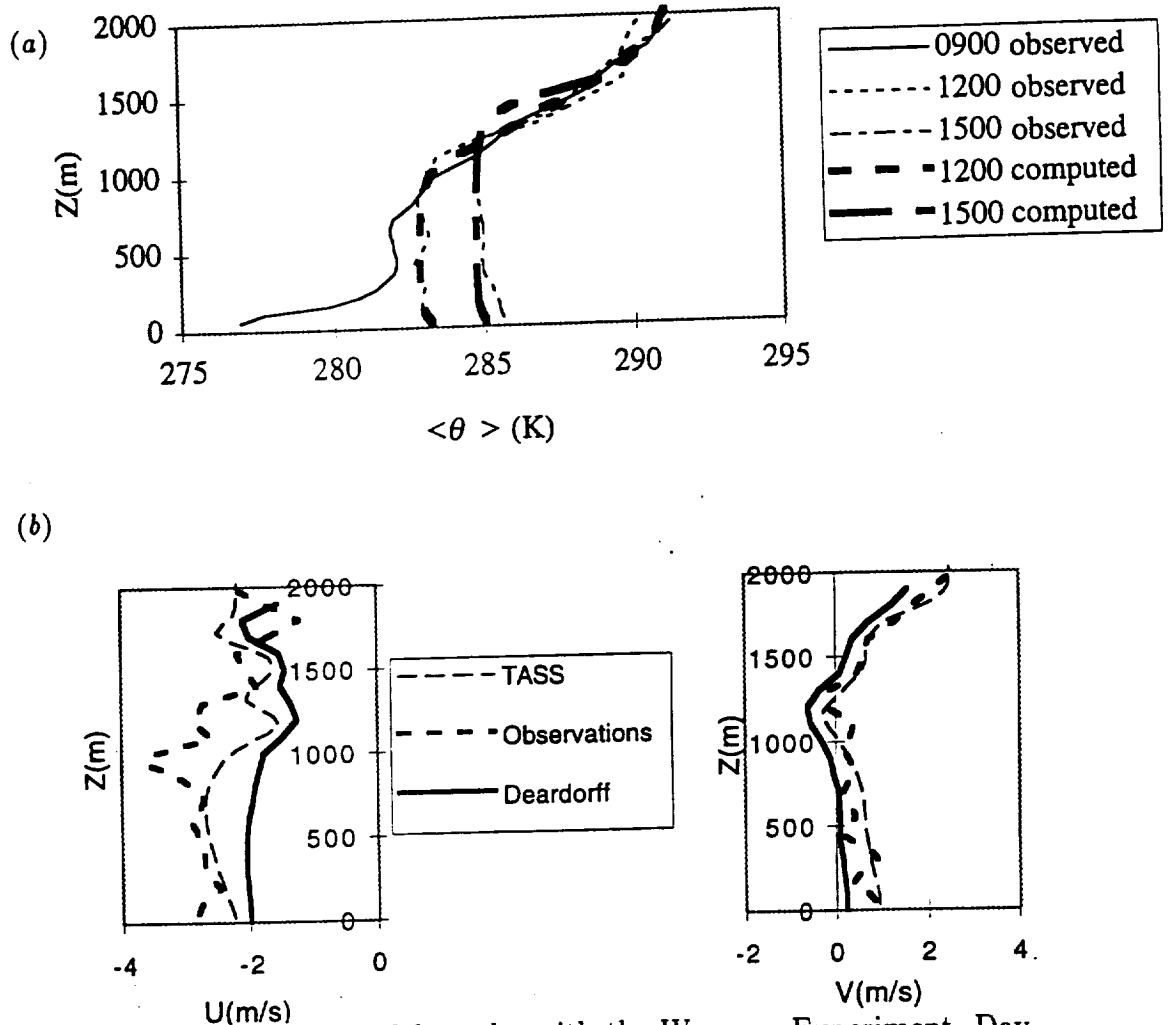
Figure 1: Comparison of model results with the Wangara Experiment, Day 33. (a) Potential temperature profiles at various local times of day. (b) Mean winds at 1200 local time, after three hours of simulation. Also shown are Deardorff's (1974) results.

| Abbreviation | Run Description |
| --- | --- |
| ALT | Local Drag Coefficient, Surface Temperature Specified |
| ALF | Local Drag Coefficient, Surface Heat Flux Specified |
| AGF | Global Drag Coefficient, Surface Heat Flux Specified |
| BLT | ALT with increased horizontal domain size |
| BGF | AGF with increased horizontal domain size |
| CLT | ALT with increased vertical resolution and moderate horizontal domain size |
| CGF | AGF with increased vertical resolution and moderate horizontal domain size |

Table 1: Abbreviations for experiments performed in this study.

temperature difference between $z=2$ m and $z=25$ m. The drag coefficient was then a function of horizontal position. Appendix A contains further details of this calculation. For case ALF (Local Flux), the horizontally averaged surface heat flux was extracted from the ALT run as a function of time and was specified uniformly at the surface. The drag coefficient, however, remained a function of horizontal position. For case AGF (Global Flux), the same value of surface heat flux was used, but the drag coefficient was horizontally homogeneous.

### 3.1.1  Variances

Figure 2 shows the velocity variance structure throughout the boundary layer for each case mentioned above. These variances were calculated by averaging horizontally over the entire domain every two minutes from 120 minutes to 180 minutes in simulation time. Then, these values were averaged in turn so that the result was an average over time and space. The resolved values of the correlations were added to an estimate of the subgrid contribution. This estimate was calculated by the method of Mason and Thomson (1992). In Figure 2($a$), it is noticeable that the horizontal velocity variance was significantly less when the heat flux was uniformly specified and the drag coefficient was nonhomogeneous (ALF). The vertical velocity variance, shown in Figure 2($b$), was nearly the same for each case. Figure 2($c$) reveals the most striking difference which is in the ratio between the two horizontal velocity variances. For case ALT, in which the surface temperature was specified and the drag coefficient was nonhomogeneous, there are large anisotropies at

10
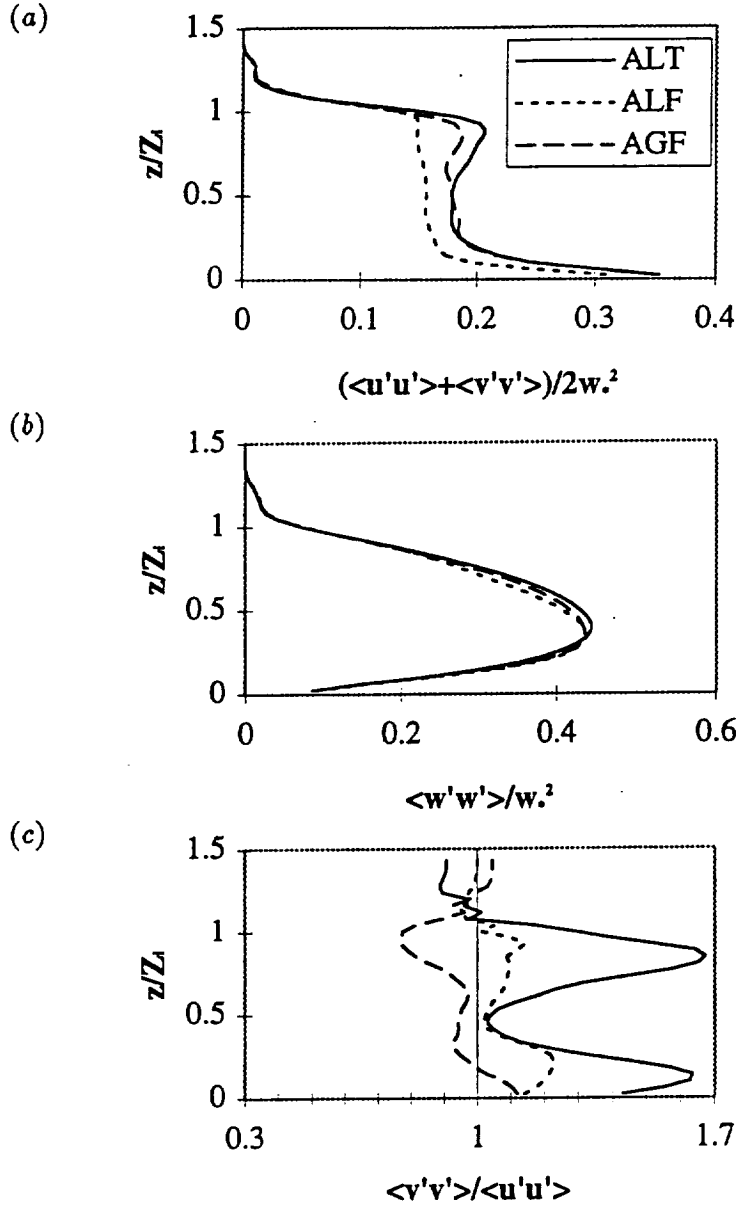
Figure 2: Comparison of cases ALT, ALF, and AGF. (a) horizontal velocity variance, (b) vertical velocity variance, and (c) horizontal anisotropy.
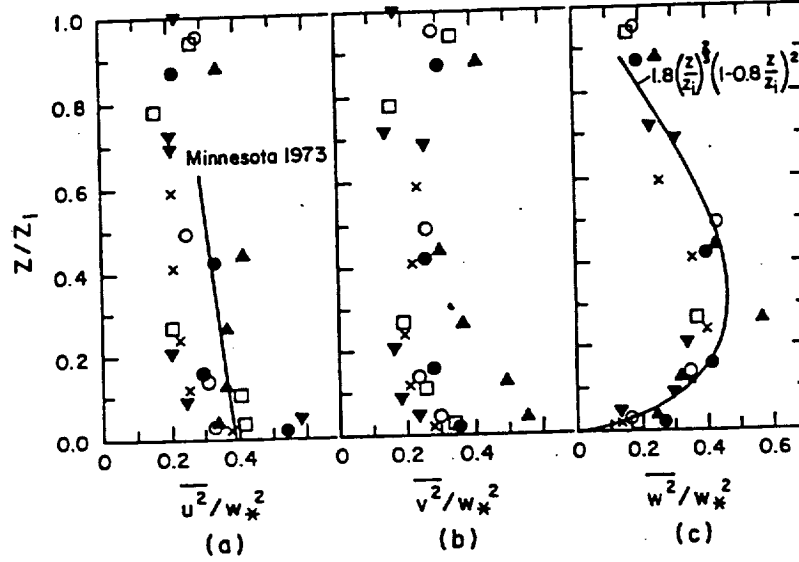
Figure 3: Velocity variances from the AMTEX experiment. Reproduced from Lenschow *et al.* (1980).

the bottom and at the top of the mixed layer. For case ALF, in which the drag coefficient was nonhomogeneous, but the surface heat flux was homogeneously specified, the anisotropy is qualitatively similar to case ALT, but the magnitudes are not as large. For case AGF, in which the drag coefficient was global and the surface heat flux was specified, the horizontal variances are generally equal except near the top of the mixed layer, where $\langle u'u' \rangle$ is larger than $\langle v'v' \rangle$. This latter case seems more reasonable, since the two components are expected to be the same in the mixed layer in convective conditions. It is also expected that $\langle u'u' \rangle$ would be somewhat larger in the entrainment region, since the shear production term is large there, the geostrophic wind being entirely westerly.

Simulated variances may be compared with those measured in the atmo-

| Symbol | Date | $Z_i/L$ |
|:------:|:----:|:-------:|
| □ | 2/15 | -17.9 |
| ▼ | 2/16 | -40.2 |
| ● | 2/18 | -26.2 |
| × | 2/22 | -32.4 |
| ○ | 2/24 | -61.8 |
| ▲ | 2/26 | -13.2 |

Table 2: Symbols for figure 3.

spheric boundary layer under convective conditions ( Lenschow *et al.* 1980)
This data was taken by aircraft during the AMTEX experiment. Table 2
shows the dates and dimensionless inversion heights for the cases shown in
the figure. We see that the simulated variances from Figure 2 are similar to
those in Figure 3, especially for cases ALT and AGF. In terms of anisotropy,
we see that $\langle v'v' \rangle$ is quite close to $\langle u'u' \rangle$ for each individual day, with the
exception of the data from February 26. In our simulations, horizontal vari-
ances are much smaller than vertical variances in the middle of the mixed
layer. The reverse is true in the surface layer, where shear-generated turbu-
lence dominates over convective turbulence.

### 3.1.2 Spectra

To investigate further the anisotropic behavior in the simulations, we have
calculated various one-dimensional velocity spectra. Let us define $S_{11}$ as
the power spectrum of $u$ along the $x$ direction. Similarly, we can define
$S_{22}$ as the power spectrum of $v$ along the $y$ direction. If the turbulence
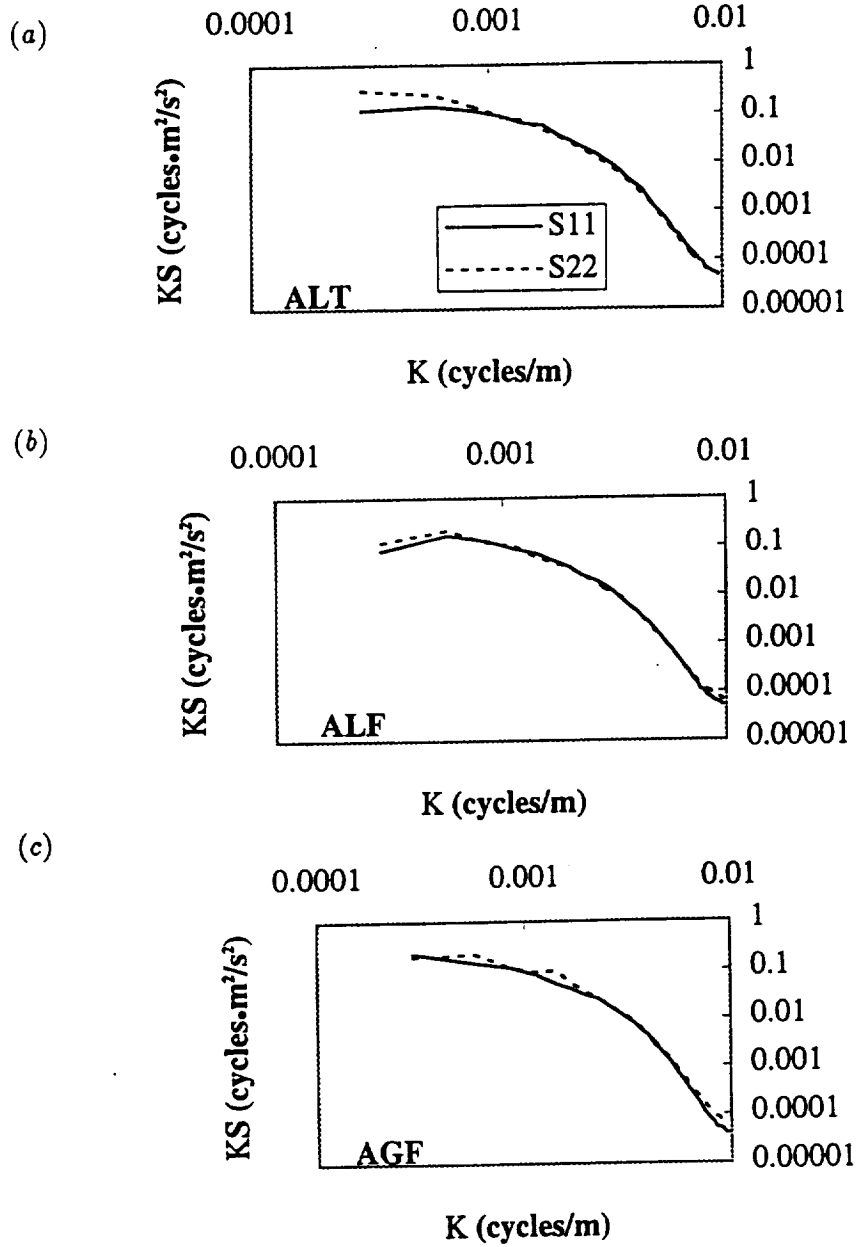
Figure 4: Longitudinal spectra at $z/Z_i = 0.12$ for ($a$) case ALT (local drag coefficient, surface temperature specified), ($b$) case ALF (local drag coefficient, surface flux uniformly specified), and ($c$) case AGF (global drag coefficient, surface flux uniformly specified).

in the mixed layer were horizontally isotropic, these two spectra would be identical. Figure 4 shows these spectra for the three cases discussed. Spectra were calculated for each longitudinal grid line at the specified height, then averaged in the other horizontal direction. That is, $S_{11}$ was averaged in the $y$ direction and $S_{22}$ was averaged in the $x$ direction. The spectra were also averaged in time in the same manner as the variances. We can determine the scales of the anisotropy by observing the wavenumbers for which $S_{11}$ and $S_{22}$ are different. For case ALT, the anisotropy near the surface occurs at the smallest wavenumbers, at length scales roughly the size of the domain. In fact, the spectral peak for $S_{22}$ occurs at the domain size wavenumber. For case ALF, in which the surface flux was uniform, but the the drag coefficient nonhomogeneous, the anisotropy also occurs at the highest wavenumbers. It is worth noting, however, that a spectral peak above the domain size wavenumber does exist. Although Figure 2(c) shows some mild anisotropy near the surface for case AGF, Figure 4 (c) reveals that this is distributed throughout the wavenumber range.

Figure 5 shows the same spectral results near the top of the mixed layer. The curves for cases ALT and ALF are qualitatively similar at this height, but the spectra for case AGF show that the $u$ variance is *larger* than the $v$ variance at this height and at low wavenumbers. As previously stated, this is most likely due to shear production at the inversion. Thus, the evidence from the variances and the spectra point to a large scale anomaly in the cross-stream velocity deviation from the mean, both near the surface and near the inversion for local evaluation of the drag coefficient.

(a)



(b)



(a)
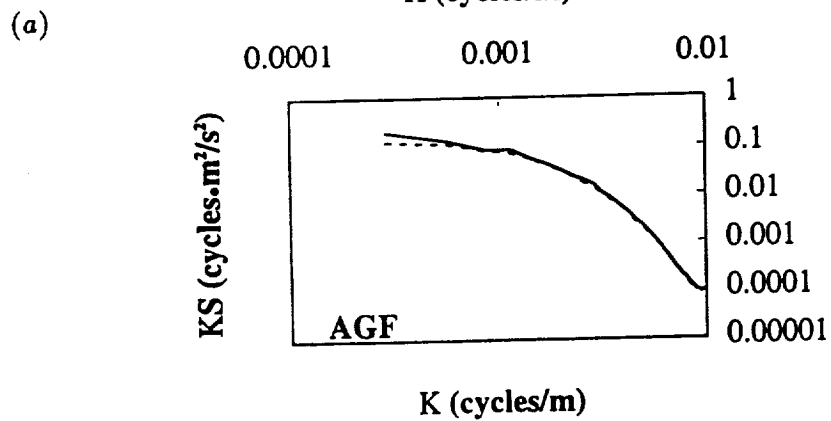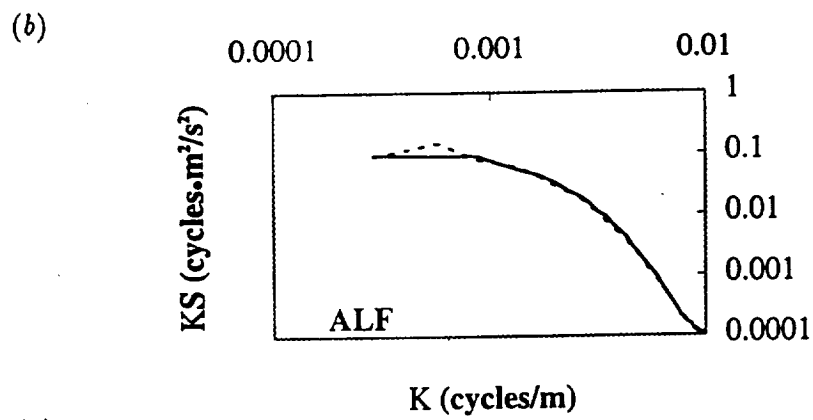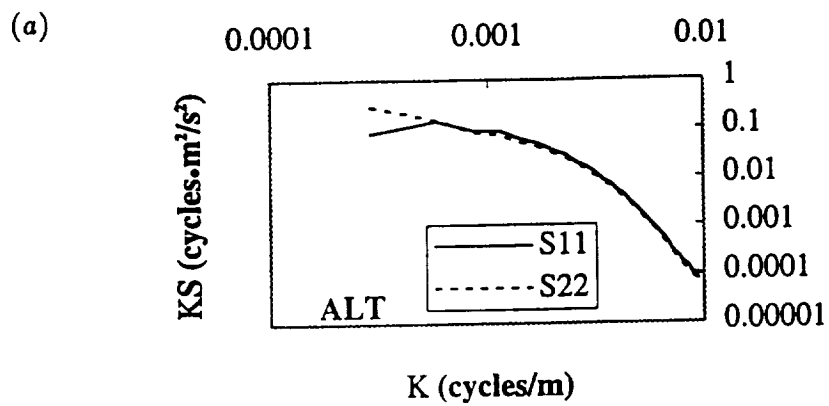


Figure 5: Same as figure 4 but for $z/Z_i = 0.86$.

16
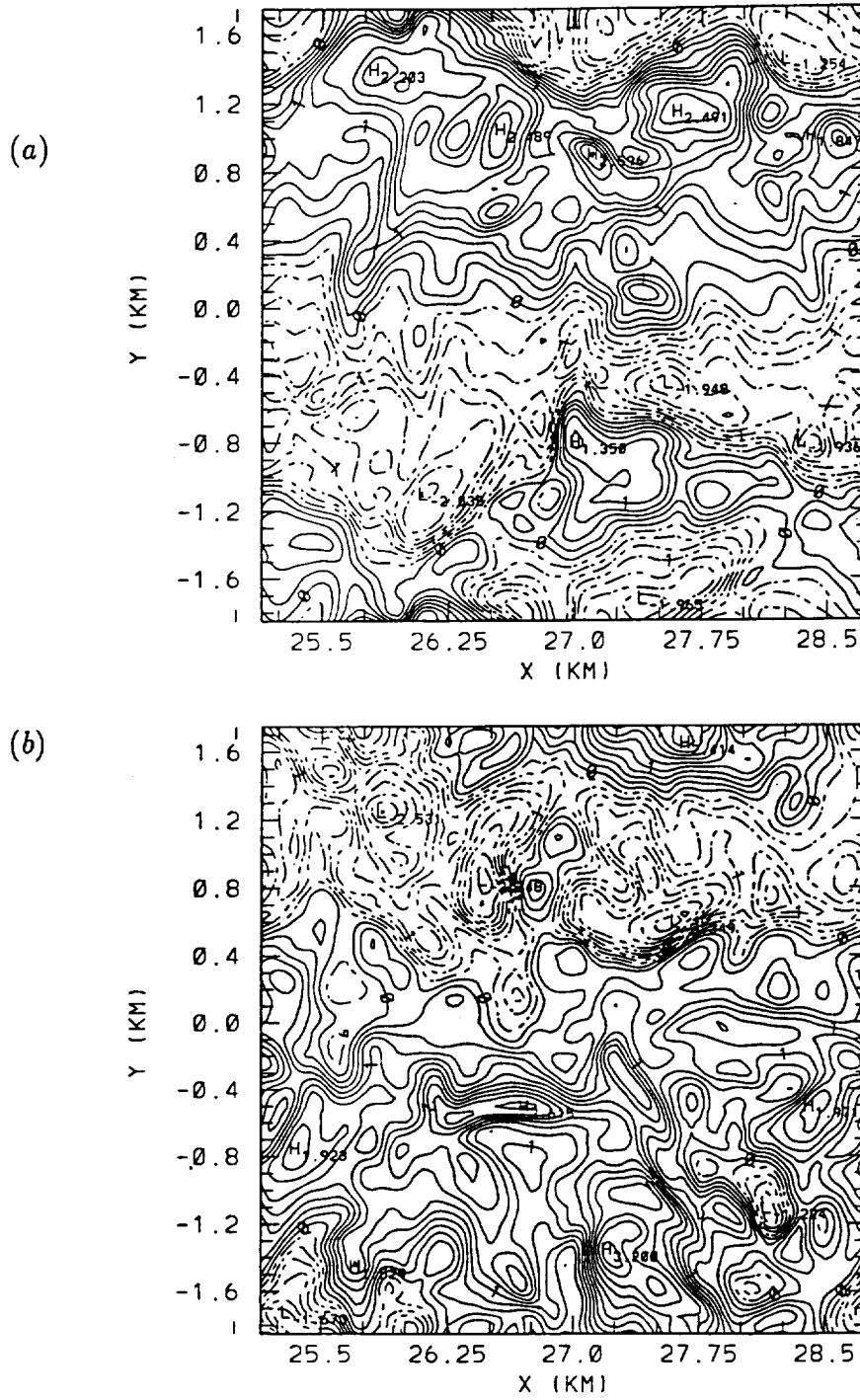
Figure 6: Contour plots of cross-stream velocity for case ALT after 150 minutes of simulation time. (a) $z/Z_i = 0.12$ (from -2.0 ms$^{-1}$ to 2.5 ms$^{-1}$ by 0.25) (b) $z/Z_i = 0.86$ (from -2.5 ms$^{-1}$ to 3.0 ms$^{-1}$ by 0.25). Negative contours are dashed.

17
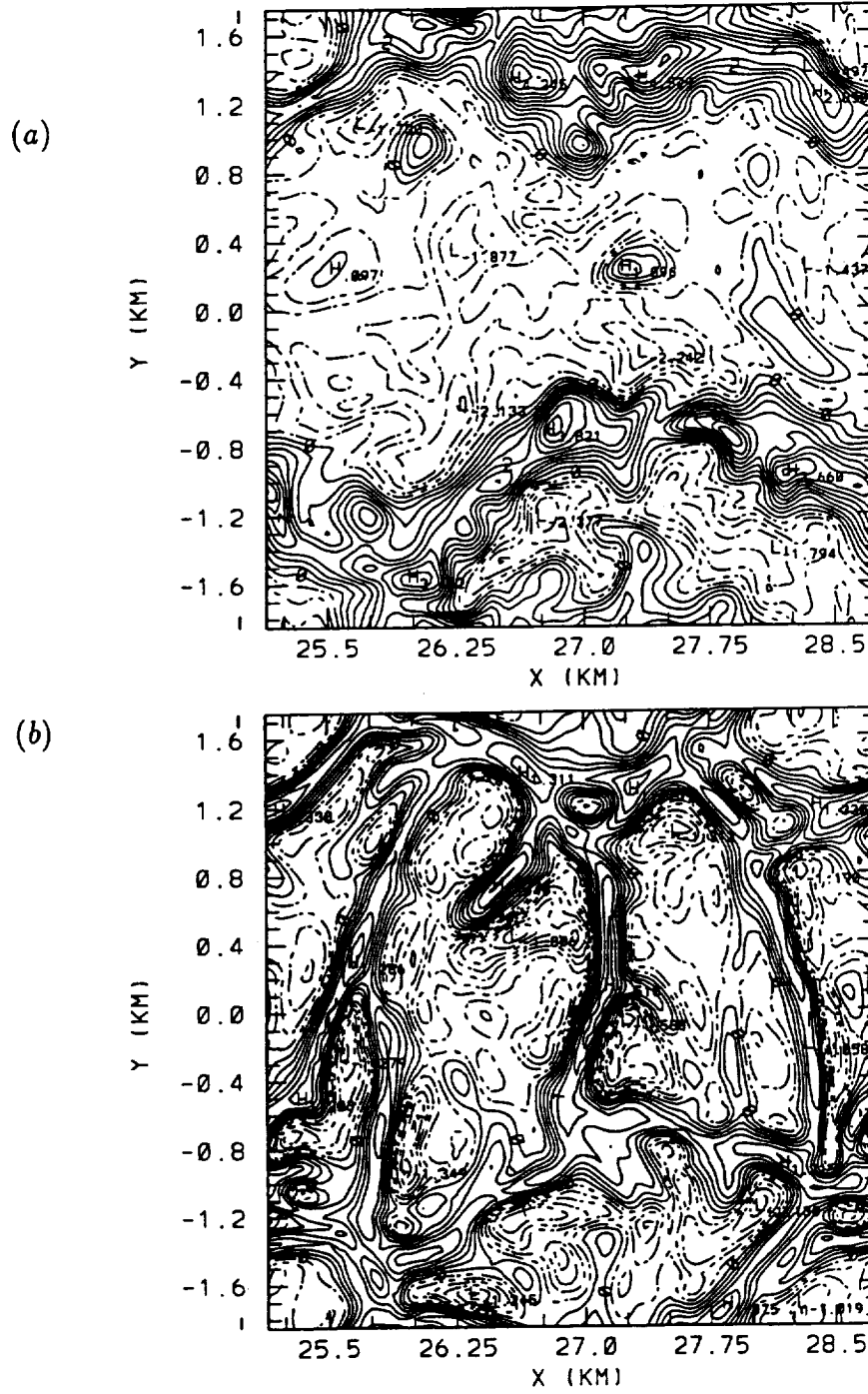
Figure 7: Contour plots of vertical velocity after 150 minutes of simulation time for case ALT. (a) $z/Z_i = 0.47$ (from -2.0 ms$^{-1}$ to 4.4 ms$^{-1}$ by 0.4) (b) $z/Z_i = 0.04$ (from -1.8 ms$^{-1}$ to 1.4 ms$^{-1}$ by 0.2). Again, negative contours are dashed.

18
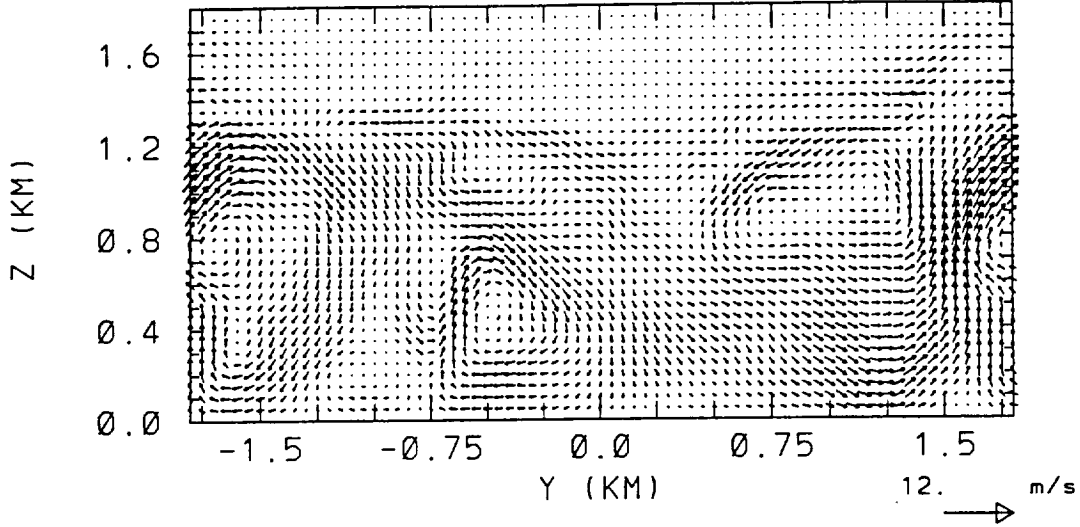
Figure 8: Velocity vectors at $x = 27.75$km for case ALT after 150 minutes of simulation time.

### 3.1.3 Instantaneous Velocity Contours

Contour plots of cross-stream velocity near the surface and at the inversion for case ALT in Figure 6 complete the picture of this anomaly. The cross-stream velocity contours show streaks aligned roughly in the stream-wise direction, whose wavelength is the domain size. That is, in Figure 6(a), the cross-stream velocity is predominantly positive between $y = 0.4$ km and $y = 1.6$ km while it is predominantly negative elsewhere. In Figure 6(b), at the top of the mixed layer, the behavior is opposite in that the cross-stream velocity is predominantly negative between $y = 0.4$ km and $y = 1.6$ km and positive elsewhere. The vertical velocity also shows some streaky behavior. In Figure 7(a), we observe an updraft structure extending across the entire

19

domain in the $x$ direction at $y \simeq 1.6$ km (the domain is horizontally periodic). Thus we seem to have streamwise roll vortices in which the dominant thermal structure is aligned with the mean wind. Near the ground, there is a strong positive cross-stream flow to the south of this structure and a strong negative cross-stream flow to the north. At the top of the mixed layer, this is reversed as the flow recirculates. This is also illustrated in Figure 8, a vector plot for a plane perpendicular to the mean flow direction. Here, again, we observe the dominant thermal structure at $y \simeq 1.6$ km with strong northerly and southerly flows feeding the plume from the bottom and exiting at the top of the mixed layer. This would account for the large anisotropies at these vertical levels. Although there is certainly some random behavior in these plots, they are only snapshots. The one hour averages of variance and spectra show the persistence of this behavior.

As a comparison, horizontal cross-sections of vertical velocity for case AGF, in which the drag coefficient was globally calculated, are shown in Figure 9. Here, we observe no clear streamwise structure. In addition, at $z/Z_i = 0.04$, we observe a spoke pattern in which the thermal structures consist of arms emanating from central nodes. There are well-defined nodes at $(x,y)$ points (28.75,0.2), (26.25, -1.0), (27.0,1.2),and (27.75, -0.10). It is interesting to note that this spoke pattern of Rayleigh-Bénard type convection also observed by Schmidt and Schumann does not occur at $z/Z_i = 0.47$. Perhaps there is only a small part of the boundary layer in which this type of convection should be expected. This topic deserves further study and is beyond the scope of the present paper.
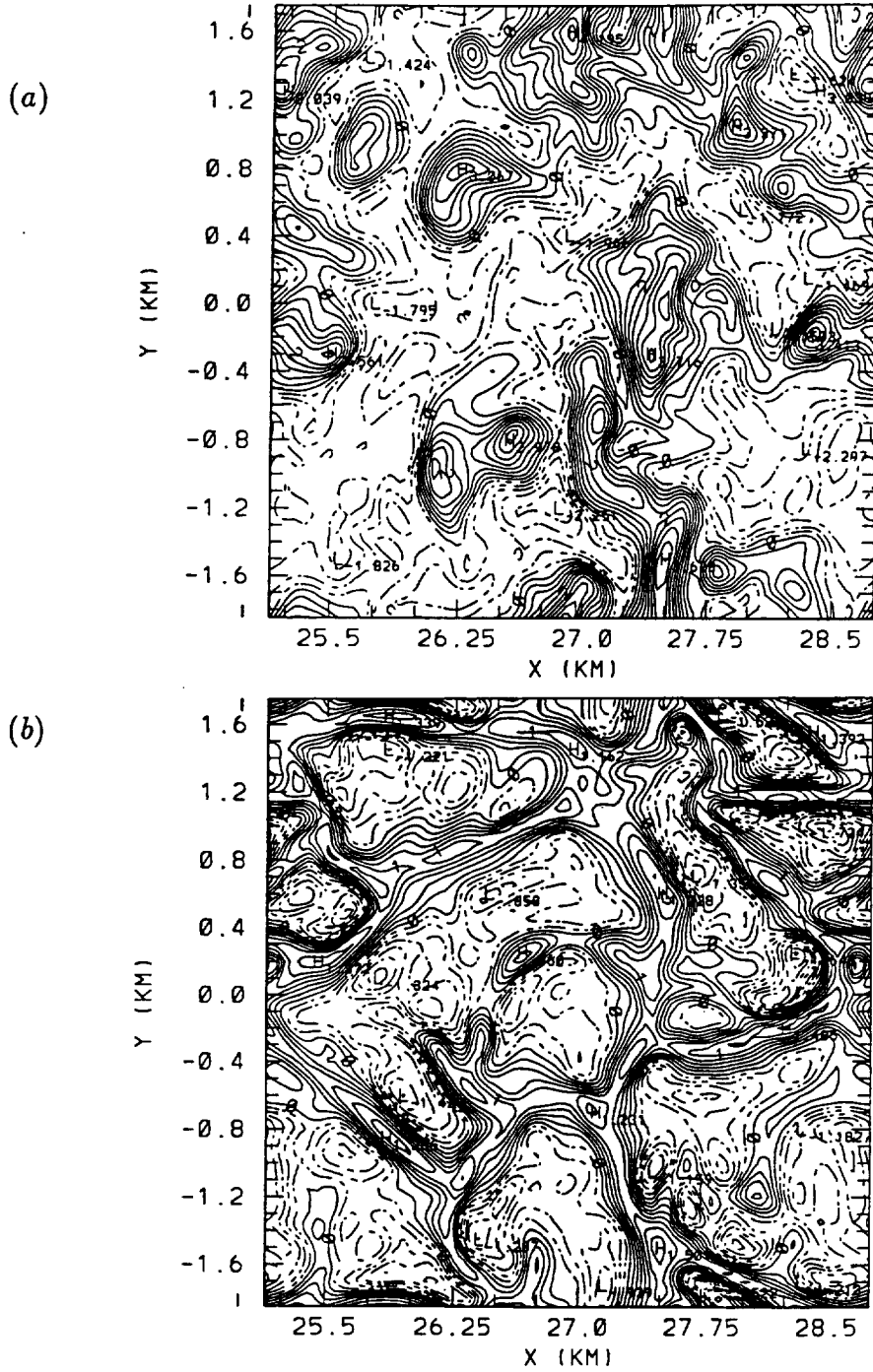
Figure 9: Contour plots of vertical velocity after 150 minutes of simulation time for case AGF. (a) $z/Z_i = 0.47$ (from -2.0 ms$^{-1}$ to 4.0 ms$^{-1}$ by 0.4) (b) $z/Z_i = 0.04$ (from -1.6 ms$^{-1}$ to 1.4 ms$^{-1}$ by 0.2).

Streamwise convective roll structures in the boundary layer have been documented (Rabin *et al.* 1982, Moeng and Sullivan 1994, Atlas *et al.* 1986). These usually occur, however, when shear and buoyancy are both important aspects of the flow. The present simulations have been highly convective. Asai's (1970) stability analysis showed that statically unstable fluid with an inflection point in the velocity profile ought to develop vortical flow structures *perpendicular* to the flow direction, rather than in the streamwise direction. It must be noted, however, that his analysis was linear and the current simulations as well as the flows in the above mentioned references were highly non-linear. A close look at Figure 3 and Table 2 reveals possible roll behavior for the February 26 case from Lenschow *et al.* Here, $Z_i/L = -13.2$, the smallest absolute value of all the cases, indicating that it was the least convective. Near the ground and near the inversion, $\langle v'v' \rangle$ is consistently larger than $\langle u'u' \rangle$, an observation indicative of streamwise rolls. For the present simulations, $Z_i/L = -301$, indicating highly convective conditions. Streamwise rolls would not be expected in this case. These appear to be an artifact of the lower boundary conditions in this particular simulation.

Figure 10 shows the drag coefficient for case ALT after 150 minutes of simulation time. The background shows the sign of the vertical velocity at 25 meters. By comparing with Figure 7(*b*), we observe the same vertical velocity structure in the background image. In addition, we see that the drag coefficient is highest primarily at the centers of the updraft regions and is lowest just outside of these regions. This is expected because the local velocity magnitude will be low in the centers of the updraft regions (this
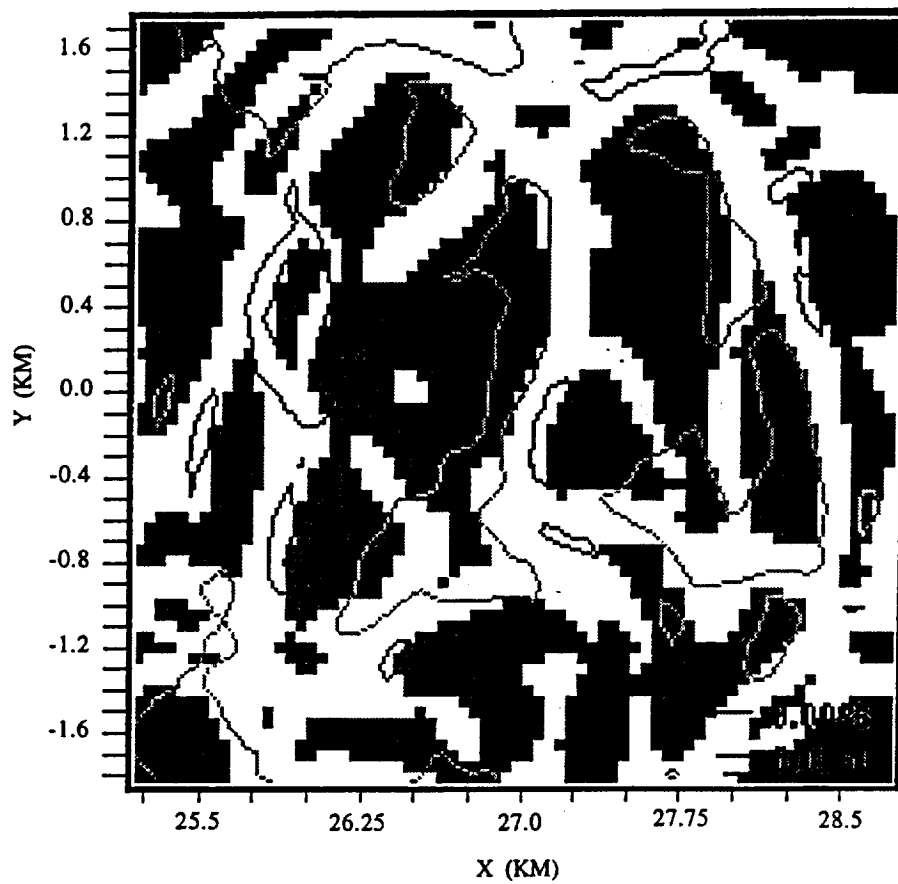
Figure 10: Contours of simulated surface drag coefficient after 150 minutes of simulation time for case ALT as a function of horizontal position. Black background indicates negative vertical velocity at $z = 25$ meters, while white background indicates positive vertical velocity.

23

leads to a smaller value of $u_*$ and, hence, a smaller absolute value of the Obukhov length by Equation 18). Thus, there is a larger drag coefficient in these regions in the local case. By the same principal, the drag coefficient is expected to be relatively low at the entrance to the thermal plumes where there are strong horizontal velocities.

It is common in problems of fluid mechanics to have streamwise streaks in regions of high shear because the ambient strain rate tilts cross-stream vorticity into the streamwise direction (see, for example Lin and Corcos' 1984 discussion of streamwise vortices in shear layers). Under convective conditions, however, we hypothesize that the drag at the surface is large enough to destroy these structures. When the drag coefficient is calculated locally, the drag becomes low enough just outside the updraft regions to allow such structures to exist. There they may combine with the thermal plume structures.

Figures 4 and 5 show that often the most dominant scale was the domain size. This is true even for $S_{11}$ in case AGF close to the ground. Because the anomalies typically scaled with the domain size, we believed that an increase in the horizontal extent of the domain may subdue the problem of the anisotropy with a local drag coefficient.

## 3.2   102 × 102 × 38 Domain

In these simulations, which are labeled as "B" in table 1, we have used the same grid resolution, but have increased the number of grid points horizontally such that the domain was 5100 m × 5100 m × 1900 m. This gave a horizontal extent of four times the boundary layer height during the aver-
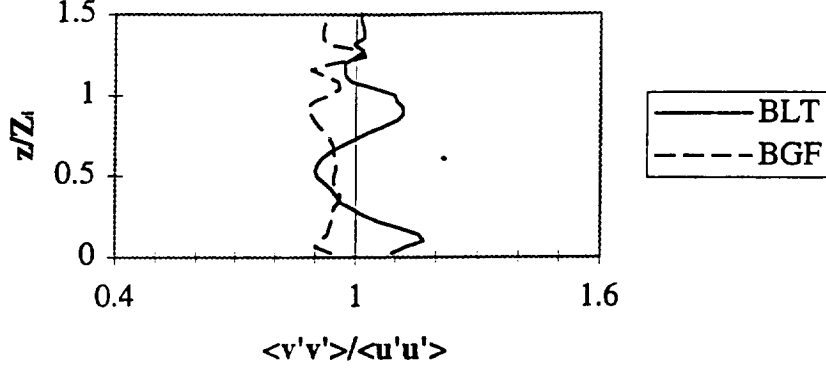
Figure 11: Horizontal anisotropy for cases BLT and BGF

aging period. Owing to the expense of running these simulations, we chose two boundary conditions to test for this domain. Case BLT employed a local drag coefficient and used a specified surface temperature. Case ALT showed the most severe anisotropies, so we felt it was important to look at the effect of domain size with the same boundary condition. We have not run a case in which the drag coefficient was local and the surface flux was specified because the results of case ALF were qualitatively similar to ALT, though the anisotropy was less severe. The second run for this domain was case BGF, in which the drag coefficient was calculated globally and the flux was specified. As in the smaller domain runs, the mean surface flux as a function of time was extracted from case BLT and used for case BGF.

Figure 11 shows the horizontal anisotropy for cases BLT and BGF. Note that case BLT is not as anisotropic as case ALT, but that the trend is the same. There remain large anisotropies close to the ground and just below the inversion. Spectra for these cases are shown in Figure 12. There is a well
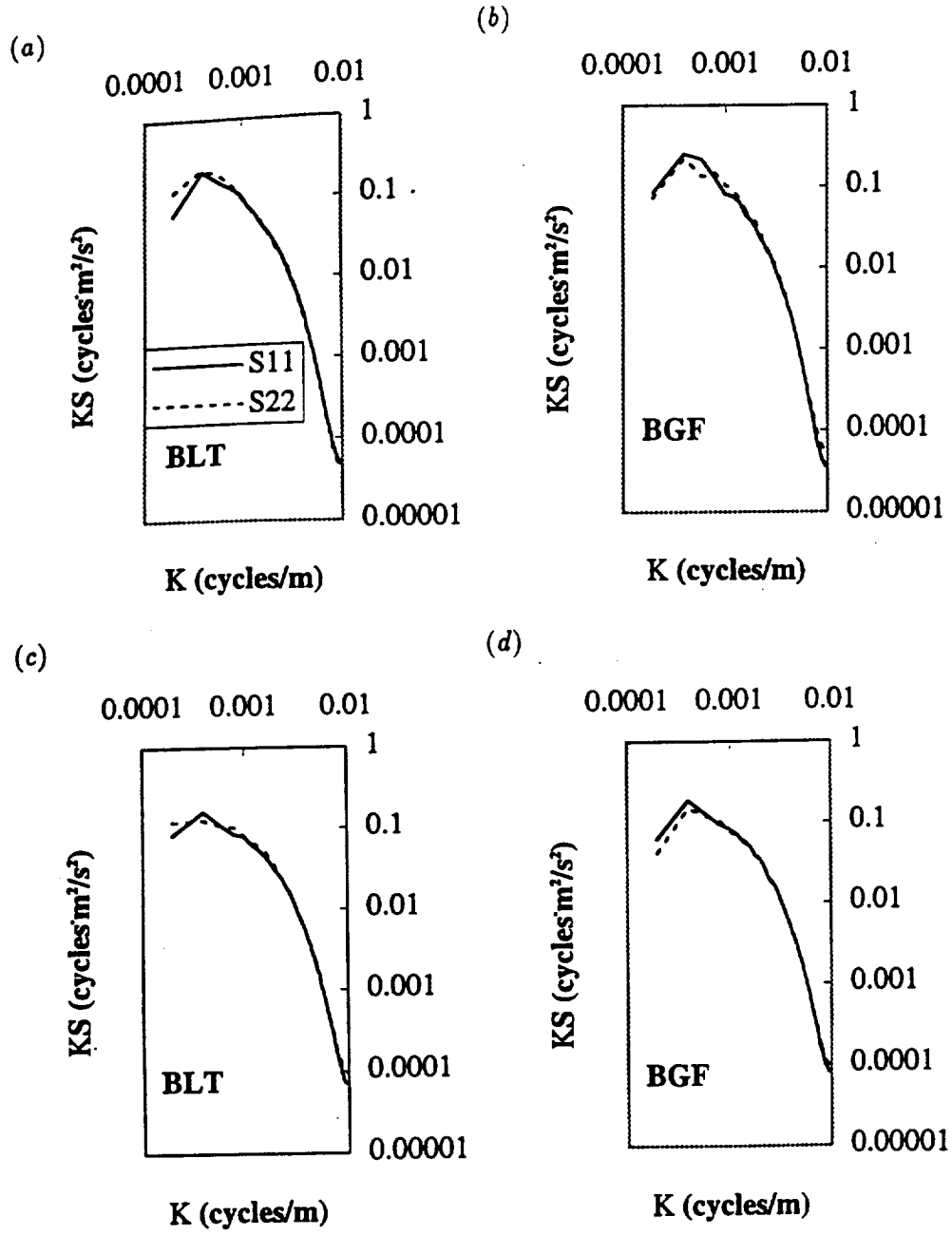
Figure 12: Longitudinal spectra for ($a$) case BLT at $z/Z_i = 0.12$, ($b$) case BGF at $z/Z_i = 0.12$, ($c$) case BLT at $z/Z_i = 0.86$, and ($d$) case BGF at $z/Z_i = 0.86$.

26

defined spectral peak for $S_{11}$ in all cases. In case BLT, however, the spectral peak is not as well defined for $S_{22}$ at $z/Z_i = 0.12$ and not at all defined for $z/Z_i = 0.86$. For case BGF, however, in which the drag coefficient was global, $S_{22}$ has a defined peak at both levels. Thus, increasing the size of the domain improved the local drag coefficient results, but did not eliminate the problem of the anomalous streamwise rolls.

Another parameter that we believed may have had an important effect was the vertical resolution of the grid mesh.

## 3.3  80 × 80 × 72 Domain

For these cases, labeled "C," the vertical grid resolution was increased to 25 meters. The first grid level was 12.5 meters above the surface. The horizontal resolution remained at 50 meters. Thus, the horizontal domain size was 4000 meters, about 3.1 times the inversion height during the averaging period. We believed that stress would be calculated more accurately with points closer to the surface. Again, only cases CLT (local drag coefficient calculation, surface temperature specified) and CGF (global drag coefficient, surface heat flux specified) were run, owing to the computational expense.

The anisotropy for these two cases is shown in Figure 13. Here we observe that this increased vertical resolution had a profound effect on the anomaly. Case CLT shows stronger anisotropy close to the ground, but CGF gives $\langle v'v' \rangle < \langle u'u' \rangle$ at two-thirds of the inversion height. At $z/Z_i = 1$, CLT again shows a positive anisotropy, but the magnitude is much smaller than for case BLT.

Figure 14, a contour plot of vertical velocity at $z/Z_i = 0.04$ for case CLT,

27
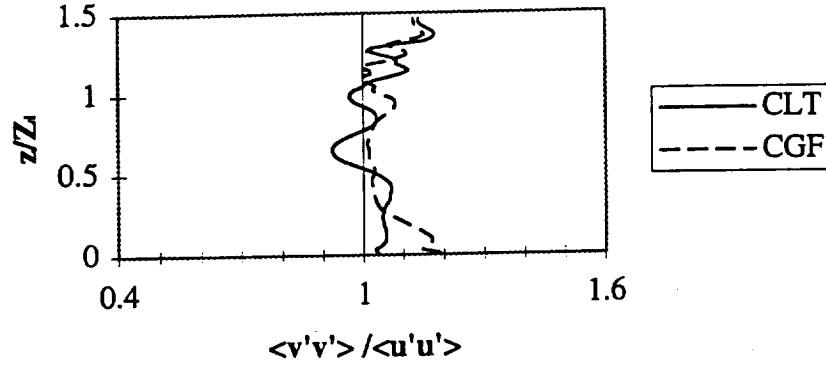
Figure 13: Anisotropy for cases CLT and CGF with increased vertical resolution.
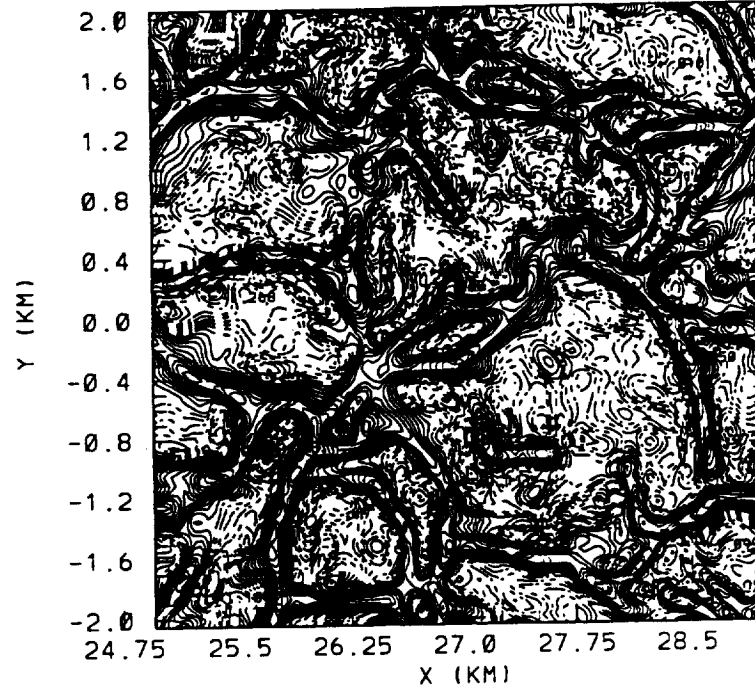


Figure 14: Contour plot of vertical velocity after 150 minutes of simulation time for case CLT at $z/Z_i = 0.04$ (from -1.4 ms$^{-1}$ to 1.4 ms$^{-1}$ by 0.1).

28
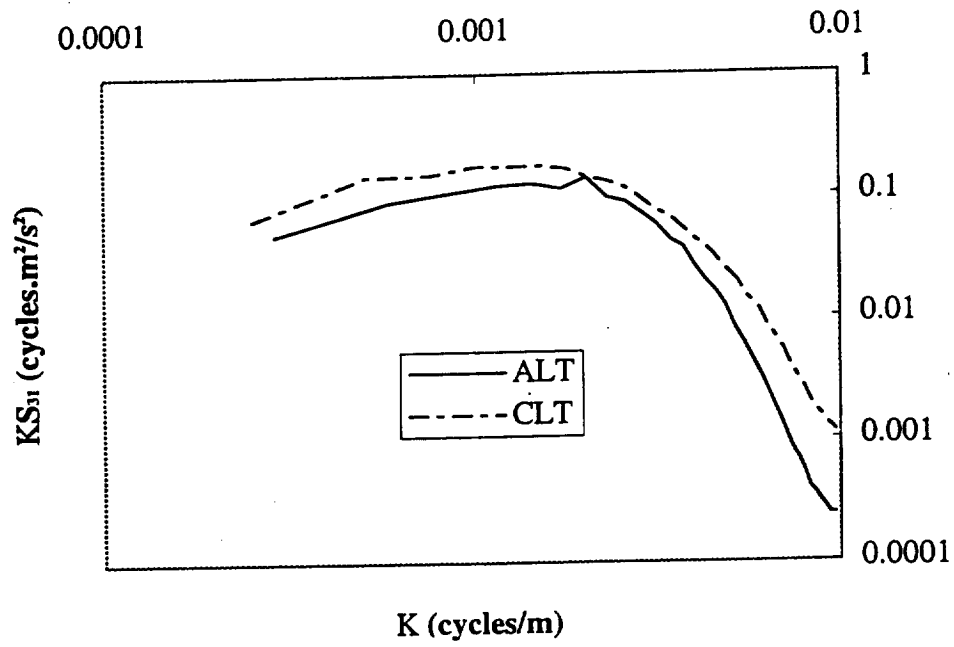
Figure 15: Longitudinal vertical velocity spectra, $S_{31}$ at $z/Z_i = 0.12$ for cases ALT and CLT.

presents a possible reason for this improved behavior. Upon comparison with Figure 7($b$) from case ALT, we note that there appears to be finer scale structures in case CLT, even though the horizontal resolution has remained constant. Indeed, the $S_{31}$ spectra in Figure 15 show this to be the case ($S_{31}$ being the spectrum of vertical velocity in the streamwise direction). The high wavenumber end of the spectrum contains considerably more energy at this height for case CLT. Thus, when the vertical grid spacing was large in case ALT, the flow close to the ground seemed to depend too strongly upon the similarity boundary condition and important scales of eddies were not resolved. It appears that the small scale eddies close to the ground in case CLT prevented the longitudinal rolls from dominating the flow structure.

# 4 Conclusions

In conclusion, we have observed that using a locally calculated drag coefficient at the surface of a large-eddy simulation model led to unrealistically large horizontal anisotropies in convective boundary layer turbulence, especially when coarse vertical resolution was used in combination with a small horizontal domain extent. This anisotropy was due to large scale streamwise rolls which are typically found in boundary layers in which shear and buoyancy are equally important. In the reported cases, however, buoyancy was clearly dominant and the rolls were not expected. The rolls occurred because the drag coefficient was smallest at the entrance to large scale thermal structures. Thus, the streamwise streak structure which is common in shear flows was not destroyed by the stress at the ground in those regions. It is

hypothesized that in these low drag coefficient regions close to the thermals, streamwise vortices are allowed to exist and combine with the plumes.

The dominance of these structures was most clear when the surface heat flux was nonhomogeneous and depended upon the local temperature difference between surface and atmosphere. It was noticeable, however, even when the surface heat flux was uniform but the drag coefficient was locally derived. Increasing the horizontal domain size such that it was four inversion heights wide improved the results. Increasing the vertical resolution such that the first grid point was 12.5 meters above the surface as opposed to 25 meters rendered the anisotropy almost imperceptable. This is likely owing to the finer scale resolved eddies which appeared close to the ground in this case. Thus, when the vertical grid spacing was too large, important scales of turbulence were unresolved, facilitating the formation of the more regular, longitudinal rolls.

In closing, we note that, although temperature specification led to a larger anomaly than did flux specification for the local drag coefficient cases, it made very little difference if the drag coefficient was global. A test case which could have been called AGT (global drag coefficient, surface temperature specified) was run and the results were not significantly different from case AGF. Thus, the temperature specification only affects the flow insofar as the local temperature differences lead to inhomogeneous surface heat fluxes and inhomogeneous drag coefficients.

# A  Calculation of surface heat flux from surface temperature

The details of calculating surface heat fluxes from surface temperatures are described below. The method was derived from equations in Arya (1988). First, the heat flux was defined globally or locally as

$$(\overline{w'\theta'})_s = -u_*\theta_* \tag{20}$$

where $u_*$ is defined by (17) or (19) and

$$\theta_* = \frac{k\{\theta_a - \theta_s\}}{\alpha_0\{\ln(z_a/z_s) - \Psi_H(z_a/L) + \Psi_H(z_s/L)\}}, \tag{21}$$

where we have used a value of 0.4 for $k$. $\theta_a$ is the potential temperature at the first grid level above the surface in the model. As in Section 2, local values of velocity and temperature were used for local drag coefficients and heat fluxes, but horizontally averaged values are used here in the global case. That is, for global calculation of $\theta_*$, $\langle\theta_a\rangle$ was used in place of $\theta_a$. In either case, $\theta_s$ is the given uniform potential temperature at $z_s$, some level between 0 and $z_a$. For $L$, the Obukhov length, (16) or (18) was used. We have used a value of 0.89 for $\alpha_0$, the surface turbulent Prandtl number. For the stability functions, we use the following relations:

$$\Psi_M(z/L) = \Psi_H(z/L) = -5z/L \qquad z/L \geq 0 \tag{22}$$

$$\Psi_M(z/L) = 2\ln(\frac{1+x}{2}) + \ln(\frac{1+x^2}{2})$$
$$- 2\arctan(x) + \pi/2 \qquad z/L < 0 \tag{23}$$

32

$$\Psi_H(z/L) = 2\ln(\frac{1+x^2}{2}) \qquad z/L < 0 \qquad (24)$$

where

$$x = (1 - 15z/L)^{1/4}. \qquad (25)$$

In the case of a local drag coefficient, a polynomial approximation to the above stability functions was used for computational efficiency.

# References

[1] Arya, S. P.: 1988, 'Introduction to Micrometeorology', Academic Press, San Diego.

[2] Asai, T.: 1970, 'Stability of a Plane Parallel Flow with Variable Vertical Shear and Unstable Stratification', *J. Meteor. Soc. Japan*, **48**, 129-139.

[3] Atlas, D., Walter, B., Chou, S.-H., Sheu, P.J.: 1986, 'The Structure of the Unstable Marine Boundary Layer Viewed by Lidar and Aircraft Observations', *J. Atmos. Sci.*, **43**, 1301-1318.

[4] Clarke, R. H., Dyer, A. J., Brook, R. R., Reid, D. G., and Troup, A. J.: 1971, 'The Wangara Experiment: Boundary Layer Data', CSIRO Div. of Meteorol. Phys. Tech. Paper No. 19.

[5] Deardorff, J. W.: 1973, 'Three-Dimensional Numerical Modeling of the Planetary Boundary Layer', *Workshop on Micrometeorology*, D. A. Haugen, ed., American Meteorology Society, 271-311.

[6] Deardorff, J. W.: 1974,'Three-Dimensional Numerical Study of Turbulence in an Entraining Mixed Layer', *Bound. Layer Meteor.*, **7**, 199-226.

[7] Hechtel, L. M., Moeng, C.-H. and Stull, R. B.: 1990, 'The Effects of Nonhomogeneous Surface Fluxes on the Convective Boundary Layer: A Case Study Using Large-Eddy Simulation', *J. Atmos. Sci.*, **47**, 1721-1741.

[8] Hinton, D. A.: 1995, 'Aircraft Vortex Spacing System (AVOSS) Conceptual Design', NASA Tech. Memo. 110184.

[9] Lenschow, D. H., Wyngaard, J. C. and Pennell, W. T.: 1980, 'Mean-Field and Second-Moment Budgets in a Baroclinic, Convective Boundary Layer', *J. Atmos. Sci.*, **37**, 1313-1326.

[10] Lin, S.J. and Corcos, G.M.: 1984, 'The Mixing Layer: Deterministic Models of a Turbulent Flow. Part 3. The Effect of Plane Strain on the Dynamics of Streamwise Vortices', *J. Fluid Mech.*, **141**, 139.

[11] Mason, P. J.: 1989,'Large-Eddy Simulation of the Convective Atmospheric Boundary Layer', *J. Atmos. Sci.*,**46**, 1492-1516.

[12] Mason, P. J., and Thomson, D. J.: 1992, 'Stochastic Backscatter in Large-Eddy Simulation of Boundary Layers', *J. Fluid Mech.*, **242**, 51-78.

[13] Moeng, C.-H.: 1984,'A Large-Eddy Simulation Model for the Study of Planetary Boundary Layer Turbulence', *J. Atmos. Sci.*, **41**, 2052-2062.

[14] Moeng, C.-H., and Sullivan, P. P.: 1994, 'A Comparison of Shear- and Buoyancy-Driven Planetary Boundary Layer Flows', *J. Atmos. Sci.*,**51**, 999-1022.

[15] Paulson, C. A.: 1970, 'The Mathematical Representation of Wind Speed and Temperature Profiles in the Unstable Atmospheric Surface Layer', *J. Applied Meteor.*, 9,857-861.

[16] Proctor, F. H.: 1988, 'Numerical Simulations of an Isolated Microburst. Part I: Dynamics and Structure', *J. Atmos. Sci.*, **45**, 3137-3159.

[17] Proctor, F. H., and Bowles, R. L.: 1992, 'Three-dimensional simulation of the Denver 11 July 1988 microburst-producing storm', *Meteorol. and Atmos. Phys.*, **49**, 107-124.

[18] Rabin, R. M., Doviak, R. J., and Sundara-Rajan, A.: 1982, 'Doppler Radar Observations of Momentum Flux in a Cloudless Convective Layer With Rolls', *J. Atmos. Sci.*, **39**, 851-863.

[19] Schmidt, H. and Schumann, U.: 1989, 'Coherent Structure of the Convective Boundary Layer Derived From Large-Eddy Simulations', *J. Fluid Mech.*, **200**, 511-562.

[20] Schowalter, D. G., DeCroix, D. S., Lin, Y.-L., Proctor, F. H., Arya, S. P., and Kaplan, M. L.: 1995. 'Turbulent Statistics in the Atmospheric Boundary Layer: A Comparison of Large Eddy Simulation With Observations.' *11th Symp. Bound. Layers Turb.*, American Meteorological Society, 552-555.

[21] Shen, S. and Leclerc, M. Y.: 1994, 'Large-Eddy Simulation of Small-Scale Surface Effects on the Convective Boundary-Layer Structure', *Atmosphere-Ocean*, **32**, 717-731.

[22] Shen, S. and Leclerc, M. Y.: 1995, 'How Large Must Surface Inhomogeneities Be Before They Influence the Convective Boundary Layer Structure? A Case Study', *Q.J.R. Meteorol. Soc.*, **121**, 1209-1228.

**Appendix C: Two Dimensional Wake Vortex Simulation in the Atmosphere: Preliminary Sensitivity Studies**

AIAA 97-0056

Two Dimensional Wake Vortex Simulations in
the Atmosphere:   Preliminary Sensitivity Studies

F. H. Proctor and D. A. Hinton
NASA Langley Research Center
Hampton, Virginia


J. Han, D. G. Schowalter, and Y.-L. Lin
North Carolina State University
Raleigh, North Carolina

35th Aerospace Sciences
Meeting & Exhibit
January 6-10, 1997 / Reno, NV

# TWO DIMENSIONAL WAKE VORTEX SIMULATIONS IN THE ATMOSPHERE: PRELIMINARY SENSITIVITY STUDIES

**F.H. Proctor[*] and D.A. Hinton[†]**
*NASA Langley Research Center*
*Flight Dynamics & Control Division*
*Hampton, VA 23681-0001*

**J. Han[‡], D.G. Schowalter[§], and Y.-L. Lin[¶]**
*Department of Marine, Earth & Atmospheric Science*
*North Carolina State University*
*Raleigh, NC 27695-8208*

## Abstract

A numerical large-eddy simulation model is currently being used to quantify aircraft wake vortex behavior with meteorological observables. The model, having a meteorological framework, permits the interaction of wake vortices with environments characterized by crosswind shear, stratification, and humidity. The addition of grid-scale turbulence as an initial condition appeared to have little consequence. Results show that conventional nondimensionalizations work very well for vortex pairs embedded in stably stratified flows. However, this result is based on simple environments with constant Brunt-Vaisala frequency. Results presented here also show that crosswind profiles exert important and complex interactions on the trajectories of wake vortices. Nonlinear crosswind profiles tended to arrest the descent of wake vortex pairs. The member of the vortex pair with vorticity of same sign as the vertical change in the ambient along-track vorticity may be deflected upwards.

## I. Introduction

As an element of NASA's Terminal Area Productivity (TAP) program, a significant effort is underway at NASA Langley to develop a system that will provide dynamical aircraft vortex spacing criteria to Air Traffic Control (ATC) automation. The system, called the Aircraft Vortex Spacing System[1,2] (AVOSS), will determine safe operating spacings between arriving/departing aircraft based on the observed/predicted weather state. In order to develop this system, research is being focused toward understanding how wake vortices interact with the atmosphere. The objectives of this research are to quantify wake vortex

behavior as related to the atmospheric conditions using validated numerical simulations, as well as observed data from recent and on-going field studies. NASA-Langley theoretical modelling efforts are expected to play a major role in the development of these algorithms.

Presented in this paper are results from a numerical large-eddy simulation model called the Terminal Area Simulation System[3,4] (TASS) which has been adapted for application to aircraft wake vortex simulations. The TASS model has a meteorological reference frame, a compressible non-Boussinesq equation set, subgrid turbulence closure, and a formulation for ground-friction. The TASS model is capable of simulating post roll-up wake vortices in both two and three dimensions. The model is applicable to a wide range of atmospheric conditions that include: vertical wind shear, stratification, atmospheric boundary layer turbulence, fog, and precipitation. Ongoing research using the two-dimensional (2-D) version of this model is presented in this paper while results using the

---

[*]Research Scientist, AIAA member
[†]AVOSS Team Group Leader
[‡]Research Assistant
[§]Visiting Assistant Professor
[¶]Associate Professor

three-dimensional (3-D) version are presented in an accompanying paper.[5] In a recent study we were able to achieve excellent comparisons of simulated vortex trajectories with field data.[4] We are now using 2-D TASS to investigate how meteorology affects vortex transport -- knowledge of which is crucial to the development and implementation of the AVOSS system. The advantage of the 2-D system is its ease in use and the relatively small amount of computer resources required per run. Our early investigation is primarily focused on understanding how stratification, crosswinds, and ground proximity affect the trajectory of wake vortices. We intend to use 3-D TASS to investigate vortex decay, vortex interaction with atmospheric turbulence, and the onset of three dimensional instabilities.

The TASS model results will be applied to the specific requirements of the AVOSS system design. In particular, prediction of the motion of wake vortices from initial generation until departure from the approach corridor is critical, while motion beyond the approach corridor is less critical. The dimensions of the AVOSS approach corridor are described in Hinton.[1,2] Laterally the corridor is 91.4 meters wide along the runway and out to a distance of about 859 meters from the runway. This is the location of the approach middle marker transmitter. The corridor lateral limits then widen to a width of 305 meters at a distance of 9272 meters (5 nm) from the runway. This is a typical location for the approach outer marker, where approaching aircraft transition from level flight to the glide slope. The approach corridor vertical dimension places a floor at ground level along the runway out to the middle marker location. Currently two options exist for the AVOSS corridor floor, and may be altered based on industry input. The most conservative option provides a floor that begins at ground level at the middle marker and rises at a shallower angle than the glide slope, so that the floor is 122 meters (400 feet) below the glide slope at the outer marker. No reduced separation credit is given for vertical wake motion very near the runway, so detailed wake bounce studies at this location are not required at this time. There is no vertical corridor limit above the glide slope, since vertical rising of the wakes is not assumed to be a viable mechanism for reduced separation of aircraft.

The requirements for AVOSS simplifies our task, somewhat, by limiting the application of our experiments to a confined region defined by the flight corridor. Any vortex that has drifted outside these lateral or vertical limits is no longer considered a factor to a following aircraft. The relationships determined with the TASS model must lead to simple rules or analytical

models that can reliably and accurately predict the time required for the wakes from many aircraft types to leave the corridor, in a wide range of atmospheric conditions. In weather situations that cannot reliably remove the wakes from the corridor in a period of about 1 to 2 minutes, the AVOSS system will either rely on decay predictions to reduce separations or maintain separation at the current standards in use today. Provided there is assurance that a wake cannot move back into the corridor, neither, the AVOSS system, nor the numerical models need to predict wake motion outside of the corridor. In determining wake sensitivity to various parameters this small range of motions must be considered. Application of AVOSS to parallel runway operations, however, may require study at a later date of wake drift over lateral distances of 400 to 900 meters as well as more detailed vertical motion studies at very low altitude.

## II. Previous Research

Many investigations, including experimental, theoretical, and field studies, of wake vortex phenomenon have been conducted over the past three decades. Important processes that affect wake vortex transport are well known and include stratification, turbulence, ground interaction, and ambient crosswind.

Numerous theoretical and experimental studies have examined the effect of stratification on wake vortices.[6, 7, 8, 9, 10, 11, 12, 13, 14, 15] The primary processes of how stable stratification affects the descent of wake vortices is well known. As a wake vortex pair descends due to the mutual induction of its circulation fields, temperature and buoyancy forces increase due to adiabatic compression. The positive buoyancy forces act to diminish the descent rate with time. The descending volume of fluid that encompasses the wake vortex pair, termed the vortex oval, develops temperature differences along its interface which act to generate counter-sign vorticity. Unresolved issues remain, such as whether the spacing between the vortices increases or decreases with time, and whether there is there a limiting descent altitude based on the magnitude of stratification.

Another characteristic of the atmosphere which can affect the motion of wake vortices is vertical shear of the ambient winds. Although wind shear is commonly known to occur near the ground due to the effects of surface drag, it exists at other altitudes due to vertical changes in horizontal gradients of atmospheric pressure. In addition, significant vertical changes of the wind can be found along fronts and inversions. For example,

strong vertical shears can exist along typical nocturnal inversions that divide stable air (produced by radiative cooling at the ground) and the residual atmospheric boundary layer air that lies above.[16] Vertical change in the crosswind, or "crosswind shear" is known to have some peculiar effects on wake vortices. From field measurements Brashears et al.[17] reported that crosswind shear acted to reduce the vortex sink rates. The reduction in sink rate was usually greater for the downstream vortex, resulting in tilting of the vortex pair. However, for strong shears there was an opposite trend, with the upstream vortex sometimes seen to rise. Most numerical investigators have concentrated on studying the effects of crosswind shear when the wake vortices were generated near the ground.[10,18,19] Generally they see a tilting (rotation) of the vortex pair in a direction opposite to that of the shear vorticity, with the downwind (downshear) vortex being at greater altitude than the upwind (upshear) vortex. Laboratory experiments by Delisi et al.[20] and numerical experiments by Robins and Delisi[14] show that strongly-stratified shear flow can tilt the wake vortex pair and lead to a solitary vortex. The vortex having vorticity opposite to that of the shear vorticity was dissipated leaving a strong solitary vortex with rotation in the same sense as the ambient shear. Robins and Delisi believed that the accelerated weakening of one of the vortices was responsible for the tilting of the vortex pair. Recent numerical experiments by Schilling[21] and Proctor[4] suggest that the influence of stratification on the vortex trajectories is secondary to crosswind shear, at least for wakes generated below 175 meters.

## III. Numerical Model

The TASS model is a multi-dimensional, large-eddy code developed within a meteorological framework. Grid-scale turbulence is explicitly computed while the effects of subgrid-scale turbulence are modeled by a Smagorinsky closure model that is modified for stratification. The TASS model has parameterizations for ground stresses that are a function of surface roughness, allowing for "in-ground effect" wake simulations with realistic ground interactions. The TASS model consists of 12 prognostic equations: three equations for momentum, one equation each for pressure deviation and potential temperature, six coupled equations for continuity of water substance (water vapor, cloud droplet water, cloud ice crystals, rain, snow and hail) and a prognostic equation for a massless tracer. The lateral boundary condition may be open or periodic, with the open condition utilizing a mass-conservative, nonreflective, radiation boundary scheme. Explicit

numerical schemes are used in TASS that are quadratic conservative, and have almost no numerical diffusion.[22] Ambient atmospheric conditions are initialized with a vertical profile of temperature, dew point, and wind velocity. The two dimensional simulations are initialized with a simple vortex system representative of the post roll-up velocity field. Details of the TASS model and wake initialization can be found in Proctor.[4]

All of the cases except those in Section VI assume that there is no preexisting grid-scale turbulence. As mentioned previously, subgrid-scale turbulence is treated by first-order closure. Section VI examines the sensitivity to grid-scale turbulence.

## IV. Stratification

The purpose of this set of experiments is to see how well TASS 2-D simulations compare with laboratory data for the case of wake vortices in a very stably stratified environment. The second goal of this set experiments it see how normalized results from different aircraft intercompare. The experiments are run with dimensional variables with the results normalized for space and time scales following Sarpkaya[12] as:

$$Z^* = \frac{z}{b_o}, \qquad T^* = t\frac{\Gamma_o}{2\pi b_o^2}$$

where $Z^*$ is the nondimensional height, $z$ dimensional height, $b_o$ initial vortex spacing, $T^*$ nondimensional time, $t$ dimensional time, and $\Gamma_o$ the initial circulation. The ambient lapse rate for temperature can be specified in terms of the nondimensional Brunt-Vaisala frequency as:

$$N^* = \frac{N}{T^*} = \frac{2\pi N b_o^2}{\Gamma_o} \qquad (1)$$

where the dimensional Brunt-Vaisala frequency $N$, is related to temperature $\tau$, and potential temperature $\theta$ (which is conserved for dry adiabatic processes):

$$N^2 = \frac{g}{\theta}\frac{\partial\theta}{\partial z} \approx \frac{g}{\tau}[\frac{\partial\tau}{\partial z} + \frac{g}{c_p}]$$

where $g$ is the acceleration due to gravity, and $c_p$ is the specific heat of air at constant pressure. Note, that if we assume the vortex separation remains constant, inviscid theory predicts that a vortex pair will descend to a maximum depth of order: $Z^* = \mathcal{O}(1/N^*)$; and for neutral stratification the vortex pair descends $Z^* = 1$ in time $T^*=1$.

**Table 1.** *Aircraft and parameters for N\*=1 comparisons.*

| Aircraft | $b_o$ (m) | $\Gamma_o$ (m²/s) | $N$ ($10^{-3}$ s$^{-1}$) |
|----------|-----------|-------------------|--------------------------|
| Fokker 28 | 19.69 | 160.8 | 66 |
| B 737-200 | 22.26 | 205.5 | 66 |
| B 757-200 | 29.80 | 306.9 | 55 |
| DC 10-10 | 37.18 | 573.0 | 66 |
| DC 10-30 | 39.60 | 492.7 | 50 |
| EA 330 | 46.78 | 378.1 | 27.5 |
| B 747-400 | 50.51 | 534.3 | 33.3 |

## Initial Conditions

The list of aircraft used in this set of experiments is shown in Table 1. The initial circulations ($\Gamma_o$) are based on typical weights and approach speeds for each specific aircraft. [For the DC-10-10 we assumed a higher weight than average, but within the maximum landing weight.] Each case assumes a lapse rate of temperature such that $N$\*=1. Although $N$\* is fixed, the values of $N$ differ for each airplane due to different initial vortex spacings ($b_o$) and circulations (e.g., see Eq. 1). The lapse rate for potential temperature needed to achieve $N$\*=1 ranges from about 2.3 times greater than for isothermal conditions for the *Airbus 330* to over 13 times greater than isothermal for the *Fokker 28-4000, Boeing 737-200,* and *DC 10-10.* Although the temperature lapse rates for some of the cases are unrealistically large, the set of experiments is useful in examining how non-dimensionalized results compare for vortices generated by different types of aircraft.

The experiments also assume a compressible atmosphere in which density and pressure decrease with height in accordance with the specified lapse rate for temperature. The domain width and depth is 4 $b_o$ and 6 $b_o$, respectively. The vortex generation height is approximately 3.5 $b_o$ above the ground. A constant grid resolution of $b_o$/50.5 is assumed in both vertical and horizontal directions. The model environments contain neither ambient wind nor grid-scale turbulence.

## Results and Comparisons

Results of the seven experiments are shown in Fig. 1. The non-dimensionalized descent rates for all seven are nearly identical and agree well Sarpkaya's laboratory measurements conducted in water at moderate
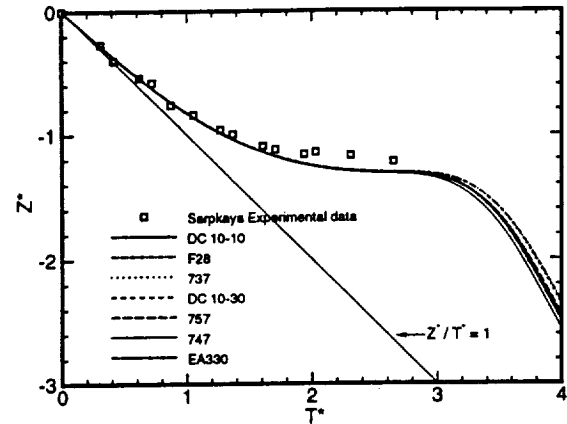


**Figure 1.** *Aircraft sensitivity to nondimensional height and time for N\*=1. TASS simulations for 7 aircraft (lines) compared with Sarpkaya's experimental data[12] (squares). Curve for dZ\*/dT\*=1 (thin line) shown also.*

Reynold's number for a delta-wing aircraft.[12] The results indicate that the vortex pair initially descend at $dZ$\*/$dT$\*=1, as is true in Sarpkaya's data. However, as the buoyancy forces increase due to compressional heating the descent rate slows, until at $T$\*=2, the vortex descent is halted. The lateral separation distance (not shown) between the two counter-rotating vortices remained nearly constant in the TASS simulations, then began to close together after $T$\*=2.5. This reduction in separation forced the simulated vortices to descend once again. Sarpkaya's experiments, which were at moderate Reynold's numbers, were unable track the weakening vortex pair after $T$\*=3. Spalart [15] recently published results from 2-D laminar simulations, which showed his vortices pausing then ascending after $T$\*=2.25, before again descending after $T$\*=4. TASS simulation results presented by Schowalter et al.[5] suggest that three-dimensional effects begin to influence the vortex after $T$\*=3, and the vortex descent following that time might be an artifact of the 2-D assumption.

Our model results for $N$\*=1 show that the stable stratification influences the descent of the vortex pair in

following way. Air from near the generation height is transported downward within the vortex oval (Fig. 2) and heats due to adiabatic compression. The increase in positive buoyancy from compressional heating has the most significant impact on the weaker tangential velocities at larger radii. Eventually the tangential velocities (and circulation) at radii greater than ½ $b_o$ are diminished. This weakens the mutual interaction of the vortices, and eventually causes them to stall (at ~1.25 $b_o$ below the generation height for $N^*$=1). Furthermore, our 2-D simulations at $N^*$=1, show that eddies generated
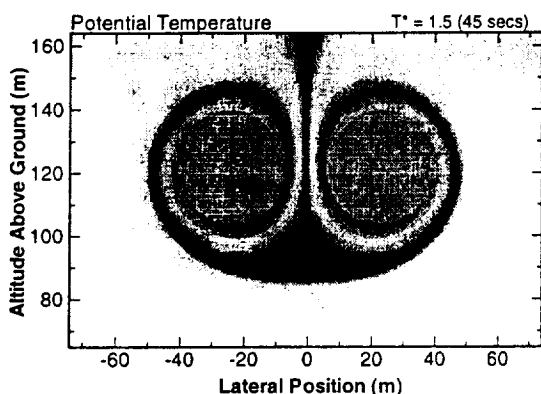


Figure 2. *Vertical cross section of the potential temperature filed associated with a descending vortex pair in stratified fluid. Darker colors represent warmer temperatures and delineate the vortex oval from the surrounding fluid.*

baroclinically at the vortex-oval periphery are transported upward and pinch the vortex pair closer together, resulting in the downward acceleration seen after $T^*$=3.

Another observation to be made from this set of experiments is the sensitivity of aircraft type to lapse rate. Although we have yet to do an extensive sensitivity study on the effects of stratification, it is obvious that wake vortices produced by large, wide-body aircraft such as the *B-747* and *EA-330* are much more sensitive to stable stratification than those produced from medium and light commercial jetliners. Mostly due to their smaller wingspans, rather large lapse rates are needed for the small and medium sized aircraft to achieve the same value for $N^*$ as that for the "Jumbos."

## V. Crosswind Shear

Although a number of researchers have examined the effects of crosswind shear on wake vortices, they usually have confined their experiments either to regions either close to the ground or simple shear profiles. In the experiments presented here, we look at the effect of narrow shear zones, such as one may find
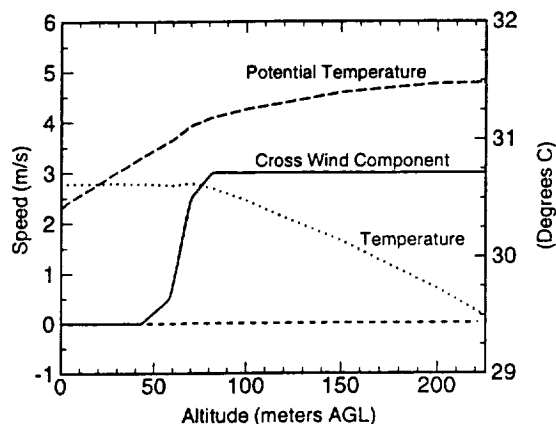


Figure 3. *Initial profiles for ambient temperature, potential temperature, and crosswind, for the shear-layer sensitivity experiments. [Only the wind profile for the 3 m/s crosswind change is show.]*

near a thermal inversion. In a second set of experiments, we examine wake vortex sensitivity to several types of shear profiles. For both sets of experiments we assume dimensional variables with initial wake conditions based on a *B-727-100* aircraft (Table 2).

### Sensitivity to Shear Layers.

The motivation behind the following set of experiments was our observation of Memphis 1994 and 1995 field data. Following sunset, many wake vortices tended either to stall or to be deflected when penetrating a region near the top of a low-level temperature inversion.[23] This inversion separated the radiatively-cooled air near the ground and the near-neutral residual boundary layer above. The measured levels of stratification, alone, were too weak to cause the observed levels of deflection. We postulate that pronounced shear can exist in the inversion zone due to changes in airmass characteristics. Unfortunately, high resolution wind data was not always available near the altitude of the inversion to confirm our suspicions.

In order to test the effect of shear zones on wake vortex descent, several experiments were conducted as

follows. An isothermal temperature profile was assumed below an altitude of 75 m, above which it transitions to a slightly-stable profile. Wind profiles were assumed to have no crosswind below an altitude of 50 m transitioning to a constant crosswind value above 80 m (e.g., Fig. 3). Hence, the crosswind change over 30 m was also equal to the crosswind above 80 m.

Six experiments were run with the initial conditions listed in table 2, with crosswind changes of: 0, 1, 2 ,3, 4 and 8 m/s. In order to evaluate any effects that the stable temperature stratification may be having, an additional experiment is conducted assuming a neutral temperature profile. An example of the profile for the 3 m/s crosswind change can be seen in Fig. 3.

A comparison of altitude vs lateral position for this set of experiments shows the sensitivity of the vortex trajectories to the shear zone (Fig.4). The descending wake vortices that encountered crosswind changes greater than 1 m/s were deflected downstream. Stronger shears also resulted in larger separations between the upstream
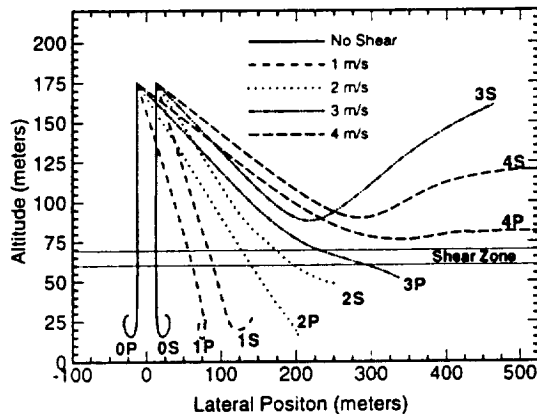


**Figure 4.** *Trajectories for the simulated wake vortices from the shear zone sensitivity experiments. Both port (P) and starboard (S) trajectories are shown for each shear profile. [The Starboard vortex (S) is downstream from the port vortex.]*

and downstream vortex. Crosswind changes of 3 m/s and larger were sufficiently strong to block the downward penetration of the vortices. The time height trajectories in Figs 5 and 6 show that a 2 m/s or greater crosswind shear significantly suppresses the sink rate of the vortices. Also, for a 3 m/s or greater shear the downstream vortex is deflected upwards.

**Table 2.** *Assumed values for initial parameters.*

| Initial Conditions | |
| --- | --- |
| **Parameter** | **Value** |
| Generation Height | 175 m |
| Circulation ($\Gamma_o$) | 250 m$^2$ s$^{-1}$ |
| Vortex Spacing ($b_0$) | 26 m |
| Core Radius | 1.75 m |
| Numerical Grid Size | 0.75 m |
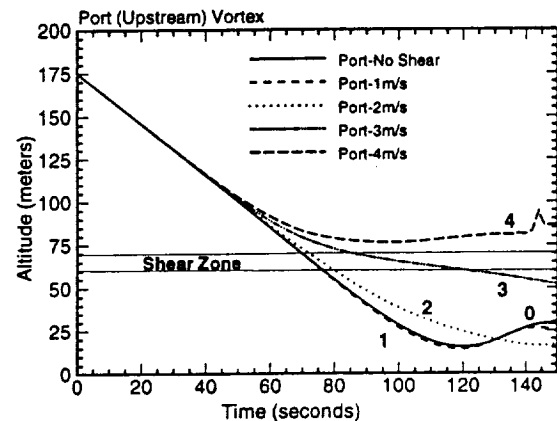


**Figure 5.** *Altitude vs time trajectory for upstream vortices in shear zone sensitivity experiments.*
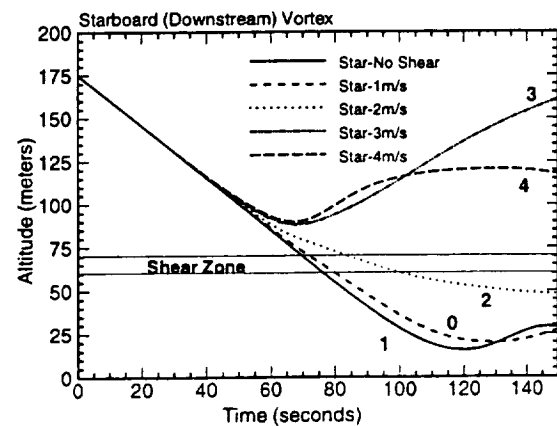


**Figure 6.** *Same as Fig. 5, but downstream vortices.*

The assumed crosswind shear profiles had the most direct influence on the downstream (starboard) vortex. As indicated in Figs. 4-6, this vortex was more sensitive and deflected to a higher altitude than its upstream counterpart. The deflection of the downstream vortex increased the separation distance from the upstream (port) vortex, thus weakening the mutual induction between the two vortices (see Fig. 4). Therefore, for the stronger shear cases the upstream vortex was left to drift near the altitude of the shear zone.

The mechanism responsible for this deflection is unclear to us at this time. The downstream vortex contains vorticity of opposite sign to that of the shear. However, there was no detectable preference for the downstream (or upstream) vortex to weaken at a greater rate.

An additional experiment was run with a neutral atmosphere rather than the temperature profile in Fig. 3. It gave nearly identical results to the experiment which assumed the sounding in Fig. 3, which implies that stratification played no role in the modification of the vortex trajectories. Note from Eq. (1) and assuming the specifications in Table 2, the ambient temperature would have to increase with altitude at $3.25^0$ C per 35 meters in order to suppress vortex descent within a 35 m thick zone.

A last point remains to be made about the trajectories in Fig. 4 for the 1 m/s and 2 m/s shear cases. There is a continued cross track drift of the vortices after they have descended below the shear layer into the air mass with no ambient crossflow. This effect is due to the downward transport of crossflow momentum with the descending vortex oval. Like potential temperature as shown in Fig. 2, crossflow momentum is transported from altitudes near the generation height (i.e. flight path). The consequence of this finding is that wind measurements near the surface may not always correlate with the lateral transport of the wake vortices.

Additional Crosswind Shear Experiments

To provide further insight into the role that shear may have on vortex transport, a second set of experiments are presented. This set consists of four experiments that are designed to test wake vortex sensitivity to environments with linear shear and transitioning shear. As with the previous set, the experiments assume the initial parameters in Table 2, but with neutral stratification and with the wind profiles shown in Fig. 7. Included, is a baseline experiment with no ambient wind (referred to as the No Shear case). As seen in Fig. 7, the
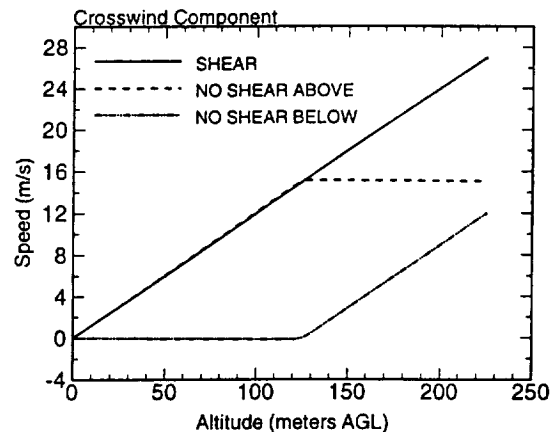


**Figure 7.** *Crosswind profiles used as input for crosswind shear experiments.*

constant linear shear case (Shear) has a crosswind profile that increases from no wind at the ground to 30 m/s at 250 m. This gives a constant magnitude of shear of $0.12 s^{-1}$. Also examined are two transitional cases, which assume an environment that transitions between constant shear and no shear. The wind profile for the "No Shear Above" case is identical to the linear-shear case, except that it transitions to a constant crosswind of 15 m/s above an altitude of 125 m.. On the other hand, the "No Shear Below" case has no crosswind below 125 m, but an increasing crosswind above this height with the same magnitude of shear as in the linear-shear case. In all cases the initial wake vortex is generated at an altitude of 175 m, which is 50 m above the transition altitude.

Time height profiles of the vortex trajectories are show for the port (upstream) vortex (Fig. 8) and the starboard (downstream) vortex (Fig. 9). The altitude vs lateral position trajectories are shown in Fig. 10. Note that the transition from shear to no shear and *vice versa* has a pronounced effect on the descent rate of the vortex trajectories. On the other hand, the descent rate for the vortex embedded in the linear shear was nearly identical to that of the vortex pair embedded in the no shear (no crosswind) environment. The trajectories of the vortex pair in the linear shear environment (Fig. 10) are convex in shape due to the decreasing wind speeds at lower altitudes. However, as for reasons described in the previous set of experiments, the vortex pair at lower levels translates faster than the mean winds for which they are embedded. Descent rates for the linear shear case were identical for both upstream and downstream vortex. Tilting of the vortex pair was not apparent.

Comparison of Figs. 7 and 8 show that the upstream vortex bounced highest when the shear is aloft, while downstream vortex bounces highest when the shear is near the ground. As indicated in Table 3, the bounce of the vortex is related to the vertical change in ambient shear (i.e. $\partial^2 U/\partial z^2$) rather than the environmental shear alone. In terms of the vorticity due to the ambient crosswind (crosswind vorticity), $\partial U/\partial z$, we see that the vortex with a sign of vorticity opposite to the sign of the vertical change in ambient vorticity, bounces highest. From these experiments, we see that vertical changes in the along-track component of ambient vorticity can preferentially reduce the descent rate of vortices, and may lead to vortex tilting and vortex rising. Linear shear (constant ambient vorticity) has no impact on the vortex descent rates.
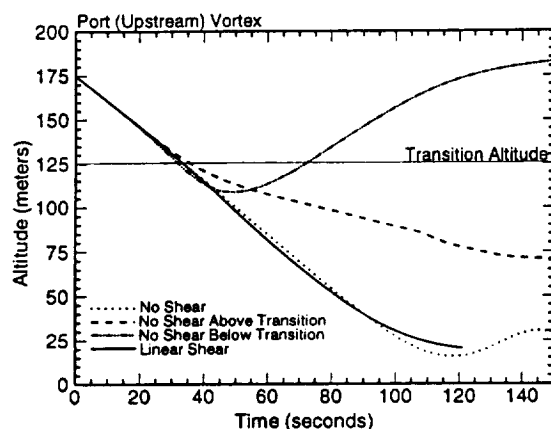


**Figure 8.** *Time-height trajectories for upstream vortex in crosswind shear experiments.*
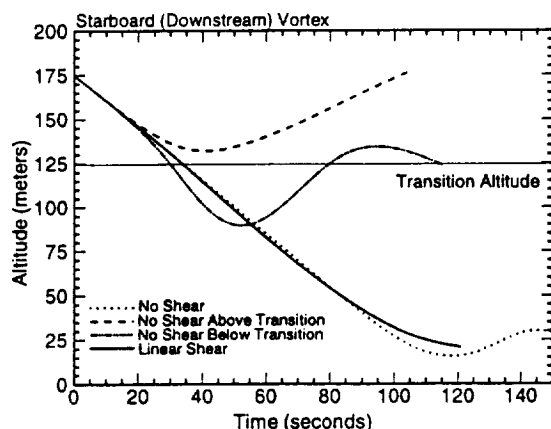


**Figure 9.** *Same as Fig. 8, but for downstream vortex.*
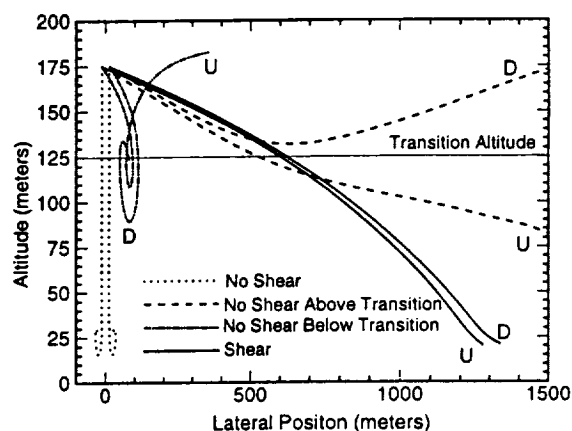


**Figure 10.** *Same as Fig. 4, but for crosswind shear experiments.*

**Table 3.** *Sign of crosswind vorticity vs vortex with highest bounce for each experiment*

| Case | Vorticity $\omega$ | $\partial \omega/\partial z$ | Vortex with Highest Bounce |
|---|---|---|---|
| No shear | 0 | 0 | same |
| Linear shear | + | 0 | same |
| No shear above | + | − | downstream |
| No shear below | + | + | upstream |

### IDF run 9 Case.

To give supporting confirmation to the above shear study, we have chosen a former TASS validation case[4] which compares simulated with measured trajectories. Input values for the simulation were based on known aircraft parameters and observed vertical distributions for ambient temperature and wind. Field measurements of wake vortex generated from a *B-757-200* (sponsored by the FAA) were taken at the Idaho Falls Field Center. The test aircraft was on a level flight at 70 m above ground level (AGL) in an early morning fly-by. The observed environmental profiles for potential temperature and crosswind are shown in Fig. 11. Note from the sounding that there is a pronounced zone of crosswind shear with a peak magnitude of 0.1 s$^{-1}$ located between 25 and 50 m AGL. The magnitude of the

crosswind change across this zone is slightly under 3 m/s. Measured data for this case was obtained from an instrumented tower,[24] Laser Doppler Velocimeter (LDV) and a Monostatic Acoustic Vortex Sensing System (MAVSS).[25, 26]
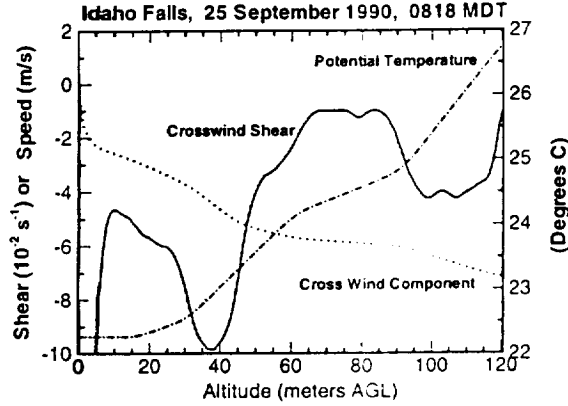


**Figure 11.** *Input sounding for Idaho Falls Run 9. Curves are for potential temperature (dash dot), crosswind (dotted) and crosswind shear (solid).*

Both the TASS model prediction and measured data show that the trajectory of the downstream (port) vortex is deflected as it encounters the zone of crosswind shear between 25-50 m AGL (Fig. 12). The crosswind vorticity in this shear region has opposite sign to that of the downstream vortex, while the change in vorticity with
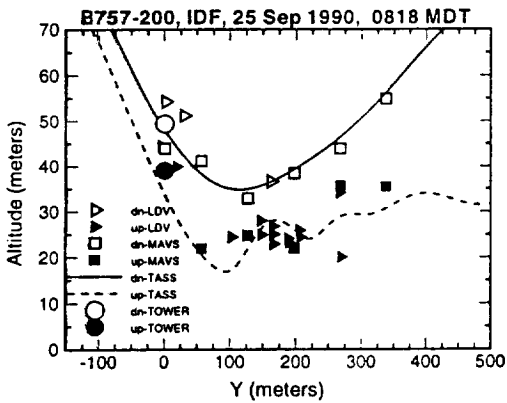


**Figure 12.** *Comparison of TASS predicted trajectories with filed data for Idaho Falls, B-757, Run 9 case. Field measurements are delineated by open (downstream vortex) and filled (upstream vortex) symbols. Model predictions are delineated by solid (downstream) and dashed (upstream) lines.*

height at the top of this layer is of the same sign as the vorticity in the downstream vortex. This interaction of the downstream vortex with the crosswind vorticity shear of the same sign eventually causes it to rise upward with increasing lateral separation from the upstream (starboard) vortex.

## VI. Sensitivity to Initial Turbulence

In a large eddy simulation of wake vortices, turbulence can be divided into several categories which include: 1) subgrid-scale turbulence, 2) resolvable-scale turbulence generated by the interaction of the vortex pair, 3) resolvable-scale turbulence generated by the interaction of the wake vortex with the ground and its environment, and 4) preexisting resolvable-scale turbulence. The simulations presented in the previous sections have ignored the existence of the latter category. In order to evaluate its sensitivity, we have developed a procedure for initiating background turbulence into our model. Turbulence initialization is accomplished through the use of a random streamfunction field in conjunction with a low-pass filter. The use of the streamfunction ensures incompressibility of the turbulent velocity field while the low-pass filter prevents the initial turbulent energy from being concentrated at the smallest scales. The three-dimensional streamfunction and velocity vectors are defined as:

$$\vec{\Psi} = (\psi_x, \psi_y, \psi_z)$$
$$\vec{V} = \nabla \times \vec{\Psi}$$
$$\nabla \cdot \vec{V} = \nabla \cdot \nabla \times \vec{\Psi} \equiv 0$$

In two dimensions, this reduces to:

$$\vec{\Psi} = (0, \psi_y, 0)$$
$$u' = -\frac{\partial \psi_y}{\partial z}$$
$$w' = \frac{\partial \psi_y}{\partial x}$$

where $u'$ and $w'$ are the added crosswind and vertical velocity fluctuations due to grid-scale turbulence.

At each grid point, $\psi_y$ is assigned a random number with a prescribed standard deviation. It is desirable to avoid having the largest velocity variations concentrated at the smallest scales, since that energy is quickly dampened by subgrid turbulence. Thus, a nine point filter is used to smooth the streamfunction before it is differentiated. An approximate relationship between the standard deviation of the streamfunction and the turbulence kinetic energy is used to prescribe the latter as

a function of height. After an initial development period, two-dimensional vortices are initialized by adding the usual initial vortex field to the background turbulent velocity field.

TKE profile for weaker background turbulence
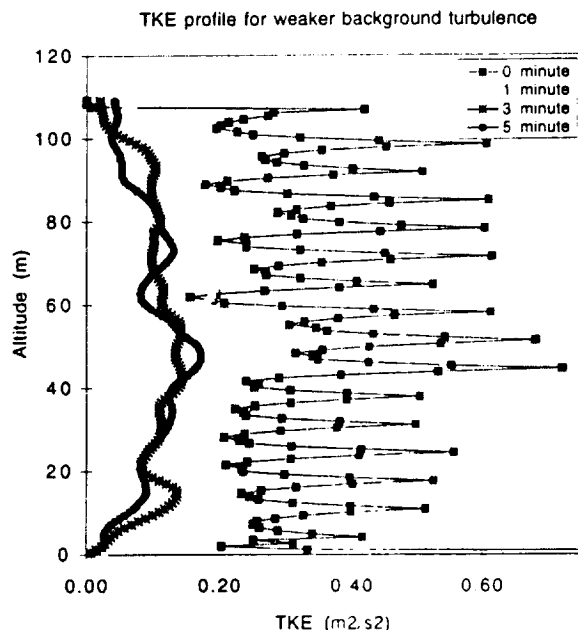


**Figure 13.** *Turbulence kinetic energy profiles for background turbulence at several model simulation times.*

In an initial test, we avoid the complicating effect of background wind shear and stratification by assuming that the atmosphere is neutrally stable and there is no background mean wind. We have chosen two strengths of turbulence for this case. The first case, labeled as "weaker turbulence," employs turbulence which is typical of convective conditions in the atmosphere (Stull,[16] pp. 359 and 371). The second case uses an order magnitude stronger turbulence than the first. The temporal variation of the turbulence kinetic energy profiles for the weaker case is shown in Fig. 13. In each case, the profile becomes smooth and nearly steady in time after about three minutes. It was at three minutes that vortices were initialized in the turbulent runs.

A vortex pair without background turbulence initialization (baseline run) descends initially due to the mutual interaction of their velocity fields with a constant initial separation. When they approach the ground, secondary vortices are induced due to the production of countersign vorticity at no-slip boundaries and force the primary vortices to rise up. Interactions with secondary

vortices result in a spiral path of the primary vortices. Four different random number generations were used in separate runs for both the weaker and stronger turbulence cases. Because of the symmetric nature of the flow in these cases with no background wind, this results in eight vortex trajectories for each turbulence strength from which we calculated averages and standard deviations. Time histories of lateral position, and altitude for the weaker turbulence case are shown in Fig. 14. A single curve is shown for the case without resolved turbulence, while three curves are shown for the turbulent case representing the mean, the mean plus one standard deviation, and the mean minus one standard deviation. We see from the figure that the resolved background turbulence has very little effect on the vortex transport in an ensemble sense. The main effect is a smaller amplitude of the oscillations caused by the secondary vortices. Although not shown, the effect on average circulation from including the initial background turbulence is even smaller.

Fig. 15 shows the same plots for ten times stronger turbulence. Here the results are similar but with two exceptions. The first is a larger spread for the positions for the turbulent runs. This indicates than any individual vortex history could be significantly different with very strong turbulence, but the average behavior is nearly the same. The second exception is a tendency for less lateral transport with very strong resolved turbulence after two minutes.

These results suggest that two-dimensional background turbulence does not play a significant role in vortex decay. Some well-known decay mechanisms, such as Crow instability and vortex bursting, are highly three-dimensional and cannot occur in a two-dimensional flow. Regarding wake transport, the turbulent eddies appear to cause stochastic variations in the vortex motions which become significant only for late times and very strong turbulence. In addition, the effect of the ground-induced secondary vortices appears to be somewhat weakened.

The turbulence field initialization was applied to several of the validation cases from the Idaho Falls field study. Values for the initial turbulence were estimated based on the turbulence velocity scale for the convective boundary layer[27] as derived from the observed sounding for each case. Cases were also run using 10 times the estimated value for turbulence. In these cases, no appreciable improvement was gained by including resolved two-dimensional turbulence. The strength of

**Altitude vs Time**



**Lateral Displacement vs Time**
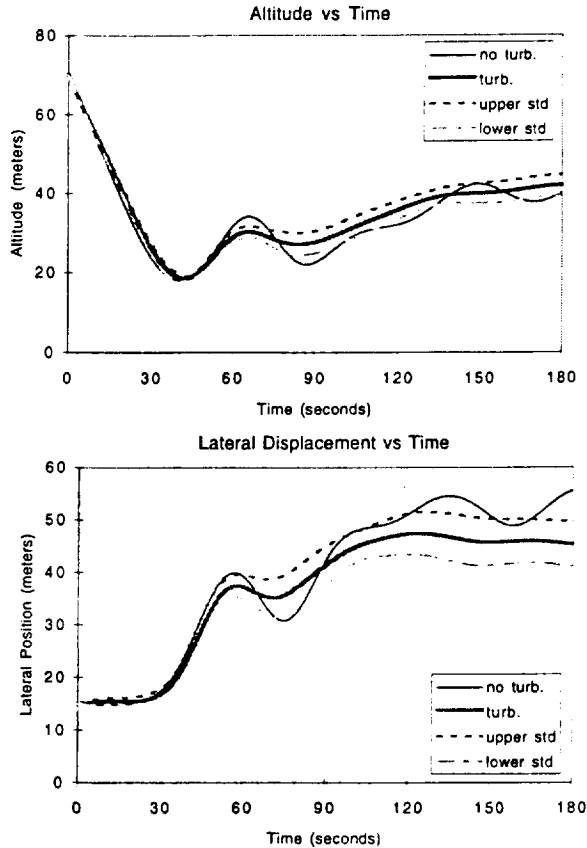


**Figure 14.** *A comparison of wake vortex behavior with and without weak resolved background turbulence. The mean (turb.), the mean plus the standard deviation (upper std.), and the mean minus the standard deviation (lower std.) are shown. (a) Altitude vs time ; (b) Lateral position vs time.*

the turbulence had virtually no effect on the 10-meter average circulation history.

In summary of the turbulence initiation experiments, moderately strong two-dimensional background resolved turbulence has, in general, a minor effect on wake vortex transport. Very strong turbulence, however, can result in significant chaotic motion of the individual vortices. Background resolved turbulence has insignificant effects on the 10-meter average circulation. However, we expect to see a much more pronounced effect when it is included in 3-D simulations of the wake vortices, since turbulence is more realistically treated and 3-dimensional vortex instabilities would be permitted.

## VII. Summary

Two-dimensional TASS simulations are shown to be useful for investigating the effects of stratification, wind shear, and turbulence on wake vortex transport. Simulations presented in this paper confirm that conventional nondimensionalizations work well for stratified environments in the absence of shear. The usefulness of their application to more complex environments is yet to be evaluated.

**Altitude vs Time**



**Lateral Displacement vs Time**
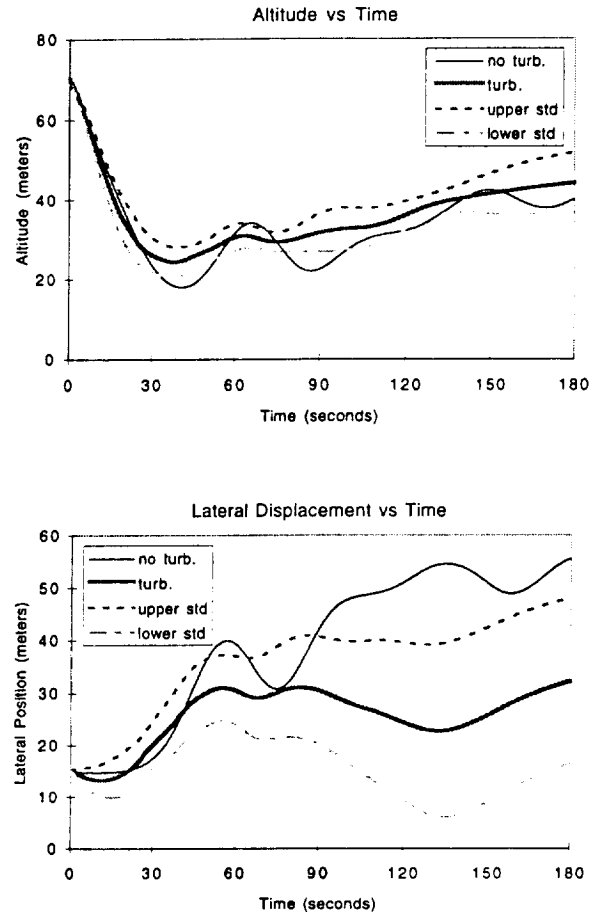


**Figure 15.** *Same as Fig. 14, but for strong turbulence.*

Our results show that wake vortex trajectories are very sensitive to the crossflow component of the wind. Changes in crosswind with altitude can affect the wake vortex trajectories in several ways. As a vortex descends through a sheared crossflow its lateral speed is affected, but may be different from the speed of the crossflow at a lower level. This is partly due to the downward transport of crossflow momentum from its generation point. Nonlinear shear of crossflow affects the vortex descent rates and may result in vortex tilting or

rising. The member of the vortex pair with vorticity of same sign as the vertical change in the ambient along-track vorticity, may be deflected upwards. These effects appear to be more sensitive than the affects of stable stratification. Zones with sharp vertical changes in the crosswind, like that associated with fronts or inversions, may be quite effective in altering the vortex trajectories. Detection of crossflow distributions may be critical to AVOSS and other similar prediction systems. This will require special sensor to monitor the winds aloft in the terminal area.

Our results also suggest that stable stratification must be quite strong in order to have the same affect as crosswind shear. Aircraft such as the large wide-body jetliners may be more susceptible to the stratification effect than small and medium range jet aircraft.

A procedure for initiating wake vortex simulations with grid-scale turbulence was described. For the cases examined, the addition of background resolved-scale turbulence had only minor effects on two-dimensional vortex transport. However, in three-dimensional simulations with unstable atmospheres, we expect significant sensitivity to background, resolved-scale turbulence.

### References

1. Hinton, D.A., "Aircraft Vortex Spacing System (AVOSS) Conceptual Design," NASA Tech Memo No. 110184, August 1995.

2. Hinton, D.A., "An Aircraft Vortex Spacing System (AVOSS) for Dynamical Wake Vortex Spacing Criteria, "AGARD 78th Fluid Dynamics Panel Meeting & Symposium, Trondheim, Norway, Paper No. 23, May 1996.

3. Proctor, F.H., "The Terminal Area Simulation System. Volume I: Theoretical Formulation," NASA Contractor Rep. 4046, DOT/FAA/PM-86/50, I, April 1987. [Available from NTIS]

4. Proctor, F. H., "Numerical Simulation of Wake Vortices Measured During the Idaho Falls and Memphis Field Programs," 14th AIAA Applied Aerodynamics Conference, Proceedings, Part-II, New Orleans, LA, AIAA Paper No. 96-2496, June 1996, pp. 943-960.

5. Schowalter, D.G., DeCroix, D.S., Switzer, G.F., Lin, Y.-L., and Arya, S.P., "Toward Three-Dimensional Modeling of a Wake Vortex Pair in the Turbulent Boundary Layer," AIAA 97-0058, January 1997.

6. Turner, J.S., "A Comparison Between Buoyant Vortex Rings and Vortex Pairs," *J. Fluid Mech.* Vol 7, 1960, pp. 451-464.

7. Scorer, R.S. and Davenport, R.S., "Contrails and Aircraft Downwash," *J. Fluid Mech.*, Vol 43, 1970, pp. 451-464.

8. Tombach, I., "Observations of Atmospheric Effects on Vortex Wake Behavior," *J. Aircraft*, Vol 10, 1973, pp. 641-647.

9. Hill, F.M.., "A Numerical Study of the Descent of a Vortex Pair in a Stably Stratified Atmosphere," *J. Fluid Mech.*, Vol 71, 1975, pp. 1-13.

10. Bilanin, A.J., Teske, M.E., and Hirsch, J.E., "The Role of Atmospheric Shear, Turbulence and A Ground Plane on the Dissipation of Aircraft Vortex Wakes," *AIAA Journal*, Vol 16, 1978, pp. 956-961.

11. Hecht, A.E., Bilanin, A.J., and Hirsch, J.E., "Turbulent Trailing Vortices in Stratified Fluids," *AIAA Journal*, Vol 19, 1981, pp. 691-698.

12. Sarpkaya, T., "Trailing Vortices in Homogeneous and Density-Stratified Media," *J. Fluid Mech.*, Vol 136, 1983, pp. 85-109.

13. Greene, G.C., "An Approximate Model of Vortex Decay in the Atmosphere," *J. Aircraft*, Vol 23, 1986, pp. 566-573.

14. Robins, R.,E. and Delisi, D.P., "Numerical Study of Vertical Shear and Stratification Effects on the Evolution of a Vortex Pair," *AIAA Journal*, Vol 28, 1990, pp. 661-669.

15. Spalart, P.R., "On the Motion of Aircraft Wakes in a Stably Stratified Fluid," to appear in *J. Fluid Mech.*, 1996.

16. Stull, R.B., *An Introduction to Boundary Layer Meteorology*, Kluwer Academic Publishers, 1988.

17. Brashears, M.R., Logan, N.A., and Hallock, J.N., "Effect of Wind Shear and Ground Plane on Aircraft Wake Vortices," *J. Aircraft*, Vol 12, 1975, pp. 830-833.

18. Robins, R.E., and D.P. Delisi, "Potential Hazard of Aircraft Wake Vortices in Ground Effect with Crosswind," *J. Aircraft*, Vol 30, 1993, pp. 201-206.

19. Zheng, Z.C., and Ash, R.L., "Study of Aircraft Wake Vortex Behavior Near the Ground," *AIAA Journal*, Vol 34, pp. 580-589.

20. Delisi, D.P., Robins, R.E., and D. Lucas, " Initial Laboratory Observations of the Evolution of a Vortex Pair in a Stratified Shear Flow," *Phys. Fluids*, Vol 3, 1991, pp. 2489-2491.

21. Schilling, V.K., "Motion and Decay of Trailing Vortices within the Atmospheric Surface Layer," *Beitr. Phys. Atmosph.*, Vol 65, No. 2, 1992, pp. 157-169.

22. Switzer, G.F., "Validation Tests of TASS for Application to 3-D Vortex Simulations," NASA Contractor Report 4756, 1996.

23. Matthews, M.P., Dasey, T.J., Perras, G.H., and Campbell, S.D., "Planetary Boundary Layer Measurements for the Understanding of Aircraft Wake Vortex Behavior," 7th Conf. on Aviation Weather Systems, Long Beach, CA, Amer. Meteor. Soc., February 1997.

24. Garodz, L.J., and Clawson, K.L., "Vortex Wake Characteristics of B757-200 and B767-200 Aircraft Using the Tower Fly-By Technique, Volumes 1 and 2," NOAA Tech. Memo. ERL ARL-199, Jan. 1993. [Available from NTIS]

25. Systems Research Corporation, "Atmospheric Description for Idaho Falls B-757 Run #9 on September 25, 1990," Volpe National Transportation Systems, Cambridge, MA, Jan. 1994.

26. Rudis, R.P., Burnham, D.C. and Janota, P., "Wake Vortex Decay Near the Ground Under Conditions of Strong Stratification and Wind Shear," 78th Fluid Dynamics Panel Meeting & Symposium, Trondheim, Norway, 20-23, May 1996.

27. Arya, S.P., "The Atmospheric Boundary Layer and its Parameterization," *Wind Climate in Cities*, J. E. Cermak, A. G. Davenport, E. J. Plate, and D. X. Viegas, Eds., Kluwer Academic Publishing, 1995, pp 41-66.

# Appendix D: Toward Three-Dimensional Modeling of a Wake Vortex Pair in the Turbulent Planetary Boundary Layer

# AIAA 97-0058

## Toward Three-Dimensional Modeling of a Wake Vortex Pair in the Turbulent Planetary Boundary Layer

D. G. Schowalter*, D. S. DeCroix*, G. F. Switzer[†]
Y.-L. Lin*, and S. P. Ayra*

*North Carolina State University
Raleigh, NC

[†]Research Triangle Institute
Hampton, VA

## 35th Aerospace Sciences Meeting & Exhibit
## January 6-10, 1997 / Reno Nevada

# TOWARD THREE-DIMENSIONAL MODELING OF A WAKE VORTEX PAIR IN THE TURBULENT PLANETARY BOUNDARY LAYER

D. G. Schowalter[*], D. S. DeCroix[†], G. F. Switzer[‡], Y.-L. Lin[§], and S. P. Arya[¶]

[*†§¶]*North Carolina State University*

[‡]*Research Triangle Institute*

## Abstract

A method for large-eddy simulation of aircraft wake vortices embedded in planetary boundary turbulence is outlined. A nested grid scheme and three-dimensional initial and boundary conditions are described and demonstrated. The nested grid scheme allows multiple one-way or two-way simulations using mass-conservative interpolation and averaging schemes along with radiative boundary conditions which lets unwanted wave energy pass out of the finer mesh domains. The three-dimensional wake vortex initial and boundary conditions enforce fully-developed wake vortices on the upstream boundary but permit the vortices within the domain to develop spatially and temporally. Future work will entail combining the two schemes for simulations of wake vortices embedded within the convective planetary boundary layer.

## 1. Introduction

Understanding the dynamics of aircraft induced wake vortices within the atmospheric boundary layer (ABL) is essential for improving forecasting systems responsible for air safety and efficiency. Our current research involves ABL and vortex modeling for the NASA wake vortex effort and the creation of the Aircraft Vortex Spacing System[1] (AVOSS). Observations and measurements of moving wake vortices show large variations with respect to ABL conditions, such as the background wind, wind shear, and stratification (e.g., Burnham[2]). For example, the vortex lifetime appears to be limited mainly by ambient turbulence effects in the planetary boundary layer[3]. Thus, it is important to study the evolution of wake vortices under different atmospheric conditions in the ABL. To date, however, very little significant work on the effect of ABL background turbulence on aircraft

wake vortex transport and decay has been accomplished.

Well known decay mechanisms for wake vortices are the Crow instability[4] and vortex breakdown[5]. The Crow instability results in vortex lines forming vortex rings and vortex breakdown or "bursting" is associated with rapid core expansion due to large variations in axial velocity. In unstable and convective boundary layers, there will be weak shear and vigorous turbulence, which should cause strong perturbations for the mechanisms mentioned above. Based on these considerations, we have been using a three-dimensional, high-resolution, nonlinear, nonhydrostatic large-eddy simulation (LES) model, the Terminal Area Simulation System[6,7] (TASS). We have shown the model to be adequate in the simulation of the atmospheric boundary layer under convective conditions during morning and mid-day[8,9]. In addition, the model has been validated for the evening transition period when the turbulence rapidly changes from being convection-dominated to shear-dominated[10].

Most vortex modeling relevant to aircraft wakes to date falls into two categories. The first category is two-dimensional studies of wake vortices in which turbulence within the vortices is modeled explicitly or parameterized. These models have been used to study wake vortices in the free atmosphere as well as their interaction with the ground. Examples are Bilanin et al.[11], Robins and Delisi[12], Schilling[13], Zheng and Ash[14], and Proctor[7]. The latter showed that the TASS model was accurate in the simulation of wake vortices in two-

[*]Visiting Assistant Professor, Dept. Marine, Earth & Atm. Sci., North Carolina State University, RALEIGH, NC, USA

[†]Research Assistant, Dept. Marine, Earth & Atm. Sci., North Carolina State University

[‡]Aeronautical Engineer, Research Triangle Institute, HAMPTON, VA USA

[§]Associate Professor, Dept. Marine, Earth & Atm. Sci., North Carolina State University

[¶]Professor, Dept. Marine, Earth & Atm. Sci., North Carolina State University

dimensions for stable conditions in which there is little or no background turbulence. The second category is three-dimensional models of infinite-length vortices which use idealized initial and boundary conditions. Usually, periodic or other simplified boundary conditions are used and there is no background turbulence or stratification. Examples of this category are Ragab and Sreedhar[15], Leonard and Chua[16].

To date, only a few studies have included resolved background turbulence. Spalart and Wray[17] studied the behavior of periodic vortex lines embedded in homogeneous isotropic turbulence, finding a relatively large spread in the destruction time for the wake vortices. Gerz and Ehret[18] found that weak large-scale atmospheric turbulence *above* the planetary boundary layer had a much stronger effect on the vortices than small-scale aircraft boundary layer turbulence. Corjon et al.[19] used direct numerical simulation to analyze the behavior of low Reynolds number vortices embedded in homogeneous isotropic turbulence. In agreement with Gerz and Ehret, they found that small scales of turbulence served only to cause small distortions in the vortices, while larger scales caused the large deformations which lead to Crow instability. Corjon et al. also found important three-dimensional effects in laminar ground interaction process. While these studies have made significant contributions to the knowledge of the effect of turbulence on three-dimensional vortices, there are further advances to be made with more realistic simulations. ABL turbulence is often quite anisotropic[8]. We are also interested in the behavior when the integral length scale is on the order of the vortex spacing as well as the behavior near the surface with background turbulence. Though useful for fundamental studies, periodic boundary conditions do not allow vortices to decay in space *and* in time as they do in the real atmosphere. We feel it is very important to develop fully three-dimensional high Reynolds number simulations with a realistic depiction of the atmospheric turbulence. Wake vortices have a horizontal scale on the order of 20 to 65 m, which cannot be properly resolved in a conventional large-eddy simulation of the ABL. Thus, we have developed a nesting procedure, whereby a simulation of the entire ABL with resolution of order 50 m can interact with a simulation of the small scale wake vortices with a resolution of order 2 m.

The nesting scheme and a three-dimensional vortex initialization procedure have been developed independently. The effects of stratification and turbulence in two-dimensional simulations are discussed in a companion paper[20]. Section 2 describes the grid-nesting while Section 3 describes the three-dimensional vortex initialization. Section 4 summarizes the results.

## 2. Three-dimensional nesting

### 2.1. Methods

We have used a nesting scheme similar to that used by Chen[21]. A fine mesh with high resolution overlaps a coarse mesh with low resolution. On the boundaries of the fine grid, this involves the interpolation of coarse grid variables. Like Clark and Farley[22], we have used a conservative interpolation scheme. In order to avoid wave reflection at the boundary, an additional radiative condition is employed for the fine mesh. On the lateral boundaries, as in Chen, the nested radiative condition corresponds to

$$\frac{\partial \phi}{\partial t} = \frac{\partial \Phi}{\partial t} - C_{\phi-\Phi} \frac{\partial(\phi-\Phi)}{\partial x},$$

where $\phi$ is a fine mesh variable, $\Phi$ is the same coarse mesh variable interpolated to the fine mesh position, and $C_{\phi-\Phi}$ is the gravity wave phase speed of $\phi-\Phi$, the *difference* between the fine mesh variable and the interpolated coarse mesh variable. At the top boundary, as in Chen again, we use a modified Klemp-Durran[23] condition:

$$(p-P)_k = \rho_0 \frac{N(w-W)_k}{\sqrt{k_x^2 + k_y^2}}.$$

Here, $p$ and $w$ are the fine mesh perturbation pressure and vertical velocity, respectively, and $P$ and $W$ are the corresponding variables for the coarse mesh. The $()_k$ notation indicates a two-dimensional horizontal Fourier transform at the top boundary and $k_x$ and $k_y$ are the wavenumbers in the $x$- and $y$-directions, respectively. $\rho_0$ is the local environmental density and $N$ is the Brunt-Vaisala frequency defined by

$$N^2 \equiv \frac{g}{\theta} \frac{\partial \bar{\theta}}{\partial z}.$$

Here, $g$ is the acceleration of gravity and $\bar{\theta}$ is the horizontally averaged potential temperature,

$$\theta \equiv T\left(\frac{P_0}{P}\right)^{R/C_p},$$

where, $P$ is the pressure, $P_0$ the reference pressure (1000 mb), $C_p$ is the specific heat of air at constant pressure, and $R$ is the gas constant for dry air. Variables other than $p$ and $w$ are simply interpolated from the coarse mesh at the top boundary. If $N$ is very close to zero at the top boundary, this radiative boundary condition is not required. In that case, a simple interpolation of $p$ is used and $w$ is determined by assuming incompressibility

at the boundary. Because the lower boundary corresponds to the ground in all nested meshes, no nested boundary condition is required there. The nested radiative boundary conditions described above impose the coarse grid flow on the boundaries, while allowing a relaxation such that unwanted wave energy travels outward from the nested mesh.

It is possible to use one-way or two-way nesting. With one-way nesting, the coarse grid is run independently of the fine mesh. The fine grid boundary points, however, are updated at every time step by the interpolation of the coarse grid points in that area. The fine mesh must use a smaller time step for stability. Thus, the boundary conditions for the fine mesh are interpolated in time as well as in space. Under two-way nesting, the variables in the fine mesh are averaged spatially to update the coarse grid variables in the overlapping region. One-way nesting is computationally more efficient, and usually works well when the dynamics within the fine mesh have a minimal impact upon the large scale dynamics of the coarse mesh. This is likely to be the case with aircraft wake vortices. It must be noted, however, that although the *net* energy cascade in a turbulent flow is from large scales to small scales, some energy does travel in the opposite direction. Thus, we have developed the capability of using either one-way or two-way nesting.

Figure 1 (a) and (b) show schematic diagrams of the spatial and temporal arrangement, respectively, of two nested grids. TASS uses an Arakawa C staggered mesh[24] so that velocity component values are stored in the center of the corresponding normal faces of the grid cells. So, for example, $u$, the velocity in the $x$-direction is stored in the center of grid faces oriented in $y$-$z$ planes. Scalar variables are stored in the center of the grid cells. Progressively finer grid meshes may be located inside of one another. In principle, the number of nested grids is unlimited. Boundary conditions are passed at the end of each coarse mesh time step for use by the fine mesh. As we can observe in

Figure 1 (b), when the fine mesh catches up with the coarse mesh temporally, the fine mesh data is averaged over the coarse mesh grid cells and used by the fine mesh if two-way nesting is implemented.

We have used message passing software to implement the nested grid scheme. This involved writing a master script program which spawns a TASS executable for each nested grid being used. Boundary conditions and synchronization information are communicated between grids using message buffers. In this way, we minimize complications involved in changing the entire TASS source code and it is necessary only to change the boundary conditions and to

synchronize the two modules. In addition, when running in one-way nesting mode, we may take advantage of parallel processing. In that case, each grid runs independently of the grids nested within for short periods of time, and the tasks may be spawned concurrently to more than one CPU, thereby increasing efficiency.

To demonstrate this nesting scheme we have simulated a rising symmetric temperature impulse and its interaction with a strong inversion. The potential temperature of the environment is set to be constant below about 900 m and constant above with a sharp 16 degree inversion between. The temperature impulse had an initial radius of 200 m with a peak amplitude of 2 °C. The coarse mesh domain is 50 X 50 X 75 with 40 m resolution in both horizontal directions and 20 m resolution in the vertical. This mesh is run for ten minutes of simulation time without any nesting. At this time, when the warm bubble comes into contact with the inversion, a fine mesh is spawned with a nesting ratio of two in each direction. The fine mesh domain size is 40 X 40 X 132 and has a common center with the coarse mesh. One-way nesting is employed.

## 2.2. Results

Figure 2 shows potential temperature contours in a central vertical plane of the simulation at 12 minutes and 16 minutes. At 12 minutes, we can observe the disturbance of the potential temperature contours caused by the impingement of the warm bubble on the strong inversion. Note that there is finer detail observable in the nested fine-mesh grid. Note, in addition, that the flow within the nested mesh remains symmetric about the horizontal origin. At 16 minutes, much of the potential temperature disturbance has passed out of the fine mesh without reflecting off the boundary, indicating the success of the nested radiative boundary condition.

In Figure 3 we observe contours of the $y$-component of vorticity on the same planes shown in Figure 2. The vortex ring from the rising bubble can clearly be seen in Figure 3 (a) and (b) at a vertical height of approximately 800 m and at a horizontal position of ±300 m. Slightly above this ring is an additional vortex ring of opposite sign. This vorticity is induced baroclinically from the tilting of the constant potential temperature surfaces in this region. By 16 minutes, part of the bubble vortex ring has passed out of the nested fine grid. This allows us to see how smoothly this ring moves across the boundary. The fine mesh gives better resolution of residual vorticity in the center of the domain as well as higher gradients in the baroclinic ring. These are precisely the types of details

which will be important for wake vortex numerical experiments.

## 3. Three-dimensional Vortex Initialization

### 3.1. Methods

The TASS model has been validated for two-dimensional wake vortex studies[7]. As described in Section 1, however, decay mechanisms tend mostly to be three-dimensional in nature and it is desirable to allow computational wake vortices to develop in both time and space. In addition, it is highly undesirable to simulate the roll-up process immediately behind the aircraft because of the prohibitive resolution requirements. For these reasons, we have chosen to impose fully developed vortices on the upstream domain boundary and to have this boundary move with the speed of the aircraft which is assumed to be 60 ms^{-1}. The initial velocity field throughout the domain corresponds to an axially homogeneous vortex pair. The downstream boundary condition is an open Orlanski boundary condition which is standard for meteorological finite-difference models[6]. Essentially, the Orlanski condition allows passage of gravity wave energy out of the boundary while allowing advection of external environmental variables into the domain. The velocity field associated with the wake corresponds to a Burnham-Hallock vortex profile[25]. No axial flow is allowed through the upstream boundary. A schematic representation of these initial and boundary conditions is shown in Figure 4. The x, y and z domain directions correspond to the axial, lateral and vertical directions of the vortex system, respectively, with the origin of the coordinate system being at the ground in the upstream boundary midway between the two vortices.

The TASS model has previously been validated for three-dimensional helical vortex flows[26]. Here, however, we demonstrate the three-dimensional *wake vortex* initialization discussed above. We have chosen a quiescent, very stable atmosphere with a constant lapse rate, $N^*=1$, where we define

$$N^* \equiv \frac{2\pi N b^2}{\Gamma_0},$$

where $\Gamma_0$ is the initial circulation of the vortices, $b$ is the initial vortex separation, and $N$ is the Brunt-Vaisala frequency. The value of $N^*=1$ represents an upper bound for the atmosphere. We have used dimensional values of $\Gamma_0=550$ m²s[-1] and $b=37$ m, values derived for a DC-10 aircraft with elliptical wing loading.

This particular case with no ambient wind enables the use of a symmetry boundary condition and necessitates the simulation of only one vortex (in this case, the starboard wake vortex). This symmetry boundary is located midway between the two vortices. Open boundaries are used to the starboard of the flight path in addition to the rear boundary.

### 3.2. Results

Figure 5 shows contours of the minimum pressure perturbation field in x-z and x-y planes after one minute of simulation time. For each two-dimensional position plotted, the contour represents the minimum pressure in the direction perpendicular to the plane shown. For example, for a given x-z position in Figure 5 (a), the contour represents the minimum of pressure perturbations for all y values at that x-z point. Note that the vortex develops spatially in this simulation. From the left-hand, or upstream boundary, the vortex slopes downward, indicating the descent of the wake after the passage of the aircraft. This slope decreases as the falling rate slows during the initial stages of ground effect and stratification effect.

Because two-dimensional wake vortex simulations have been quite successful in stably stratified environments[7], it is desirable to compare this three-dimensional simulation with a two-dimensional simulation. Figure 6 compares velocity vectors for two- and three-dimensional simulations at various dimensionless times, $t^*$, where

$$t^* \equiv t \frac{\Gamma_0}{2\pi b^2}.$$

The domain size and resolution in the spanwise and vertical directions are identical for the two-dimensional and three-dimensional simulations. In Figure 6, we notice that the simulations are remarkably similar up to $t^*=2.5$, after which there are some minor differences. It appears that, at $t^*=3.0$, there are differences in the locations of the secondary vortices which, in this case, are created baroclinically by the background stratification. The secondary vortex in Figure 6 (c) and (f) can be seen as a small region of fluid rotating in the opposite direction from the primary vortex. At this time, the two-dimensional secondary vortex is higher relative to the primary vortex and further inboard than the three-dimensional counterpart. It is likely that this difference in position is due to the sloping of the three-dimensional primary vortex in the axial direction.

Figure 7 shows the altitude histories for the two- and three-dimensional simulations. These are nearly identical up to about 48 seconds of simulation time ($t^*=3.1$). For both simulations, there is a rapid rate of descent until about 20 s. At this point, the vortices stall

due to the strong stratification. After about 48 s, the three-dimensional vortices begin to rise and the two-dimensional vortices begin to fall again. This difference in the transport of the vortices can be related back to the differences shown in Figure 6. In strong stable stratification, the wake vortex descent rate tends to slow due to an upward buoyant force from entrained warm air[3]. Because the two-dimensional secondary vortices are located higher and closer together, however, their induced velocity tends to push the primary vortices closer together. This eventually results in a higher downward velocity field between the primary vortices, which enables the pair to continue their downward motion after the stall. In the three-dimensional case, the secondary vortices are located at nearly the same level as the primary vortices. Thus, there is very little tendency to squeeze the primary vortices closer together. In addition, these secondary vortices induce a positive vertical velocity component at the primary vortex locations in the three-dimensional case. The upward buoyancy force, combined with the induction from the secondary vortices is strong enough to cause a slight upward motion of the pair.

Figure 8 shows the development of 10 m circulation and 10 m average circulation with time for two- and three-dimensional simulations. Average circulation at a radius $r_0$ from the vortex center is defined as

$$\overline{\Gamma_{r_0}} \equiv \int_0^{r_0} \Gamma(r)dr,$$

where the circulation, $\Gamma$, is

$$\Gamma(r) \equiv \oint_r \vec{u} \bullet d\vec{l}.$$

The histories are virtually identical until about 54 seconds of simulation time ($t^*=3.45$), at which point the two-dimensional circulations begin to drop off more rapidly.

Axial flow through the three-dimensional vortices is shown in Figure 9. The axial flow is strong and towards the aircraft in the core of the wake vortex and weak and directed away from the aircraft outside of the core. By looking at the pressure field in Figure 5, the cause of this secondary flow is evident. The vortices undergo a slow expansion due to turbulent diffusion as they fall further away from the upstream boundary. As discussed by Batchelor[27], this expansion reduces the pressure drop inside the vortex core. Thus, the core pressure is higher far away from the upstream boundary than near it, causing a secondary flow towards the

aircraft. To conserve mass, this flow must be balanced by a weak return flow outside of the core.

## 4. Summary

We have described the separate development of a nested grid technique and wake vortex boundary and initial conditions for large-eddy simulation. The nested grid technique employs mass-conservative interpolation and averaging routines along with radiation schemes which prevent wave reflection at fine-mesh boundaries. The scheme has been demonstrated with a simulation of a warm air bubble rising from the surface and interacting with a strong temperature inversion. This symmetric perturbation has been shown to lead to a symmetric solution using the nested grid, which is expected. In addition, disturbances are shown to pass out of the fine mesh properly. One-way and two-way nesting are possible.

Three-dimensional initialization of aircraft wake vortices along with upstream boundary conditions to sustain them have also been demonstrated. These boundary and initial conditions allow the wake vortices to develop spatially and temporally. Two-dimensional and three-dimensional simulations show similar results up to the time when baroclinically generated secondary vortices become important. Two-dimensional baroclinic secondary vortices were positioned higher than their three-dimensional counterparts. This positioning resulted in the pair descending after a stratification-induced stall for the two-dimensional simulation. In the three-dimensional case, however, the pair began to rise after the stall. An axial flow (which cannot be simulated in the two-dimensional experiments) develops which is directed toward the aircraft within the cores and weakly away from the aircraft outside of the cores. This axial flow is generated by a dilation of the vortex cores as they develop spatially away from the aircraft.

In the future, we plan to combine the nested simulations with the vortex simulations. This will involve a coarse mesh large-eddy simulation of the convective planetary boundary layer which will spawn a fine mesh nest. Vortices will be initialized within the fine grid which will, at that point, be suffused with realistic atmospheric turbulence.

(a)
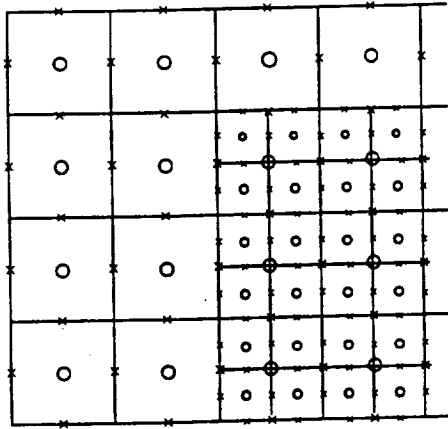
(b)
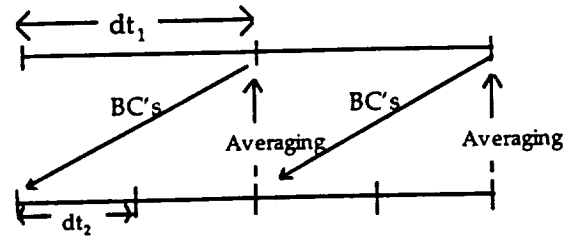


**Figure 1**: Schematic diagram of (a) spatial and (b) temporal arrangement of two nested grids. × denotes locations for velocity values and O denotes scalar locations on the Arakawa C staggered mesh. The nesting ratio is two for both directions shown. $dt_1$ is the time step for the coarse mesh and $dt_2$ for the fine mesh. Boundary conditions pass from the coarse mesh to the fine mesh and, if two-way nesting is specified, averaging information for the variables is passed back to the coarse mesh at the indicated times.

American Institute of Aeronautics and Astronautics
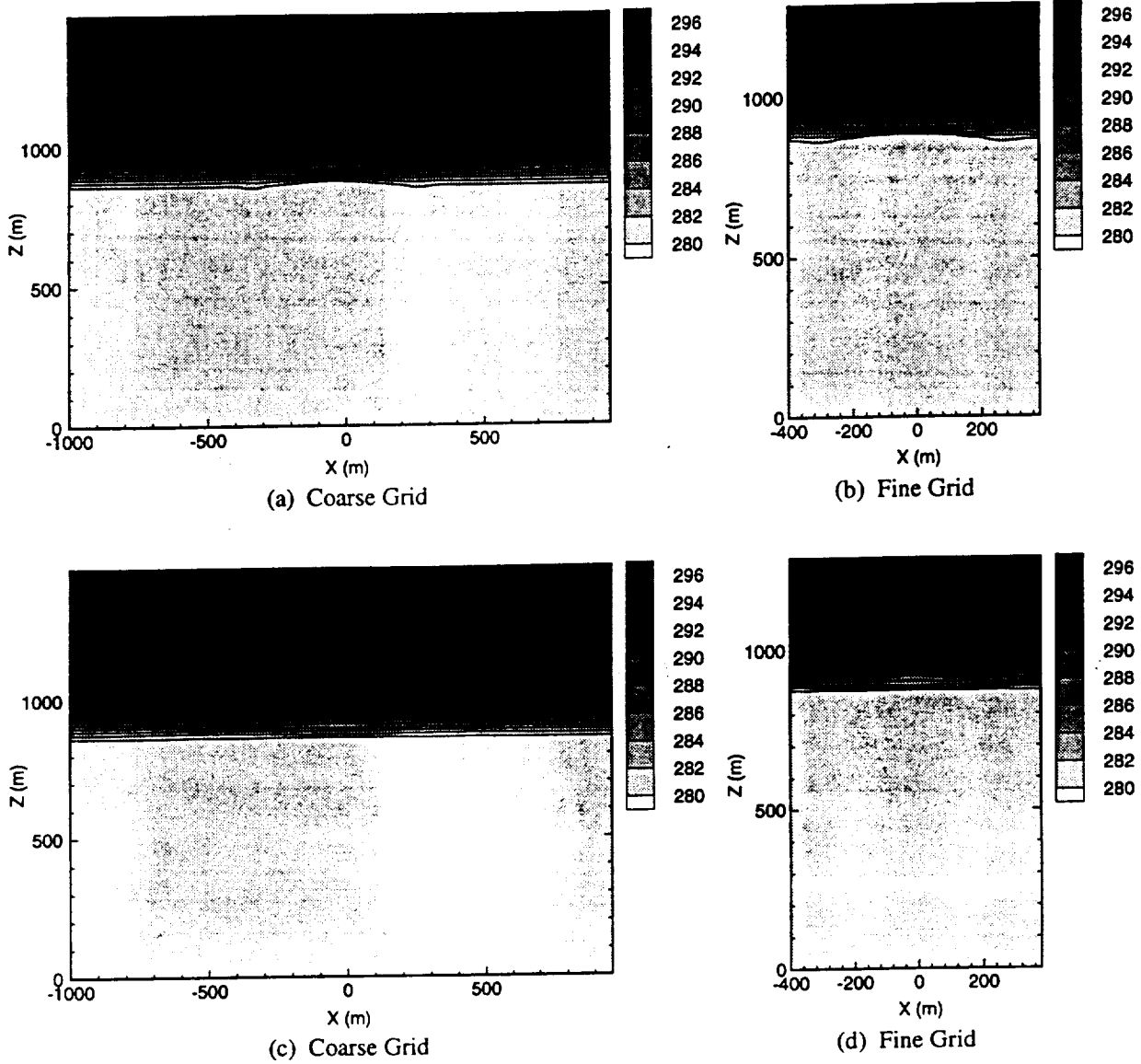
**Figure 2**: Contours of potential temperature for coarse and fine mesh simulations at 12.0 and 16.0 minutes of simulation time in the central $x$-$z$ plane, where $z$ is the vertical axis. (a) and (c) are for coarse mesh simulations while (b) and (d) are for fine mesh simulations. (a) and (b) are at 12.0 minutes of simulation time while (c) and (d) are at 16.0 minutes.
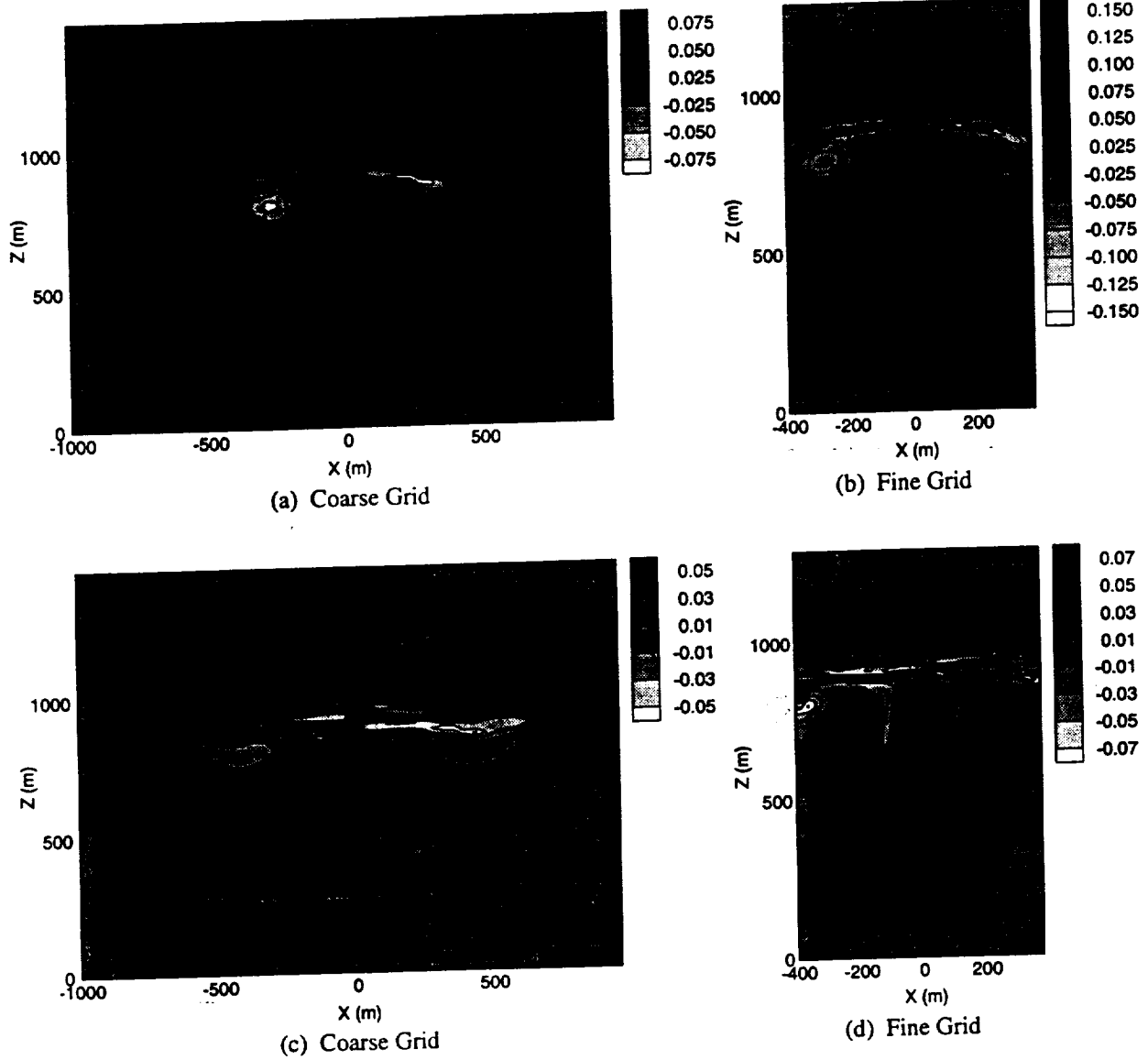
**Figure 3:** Same as Figure 2 but contours are for vorticity in the y-direction.
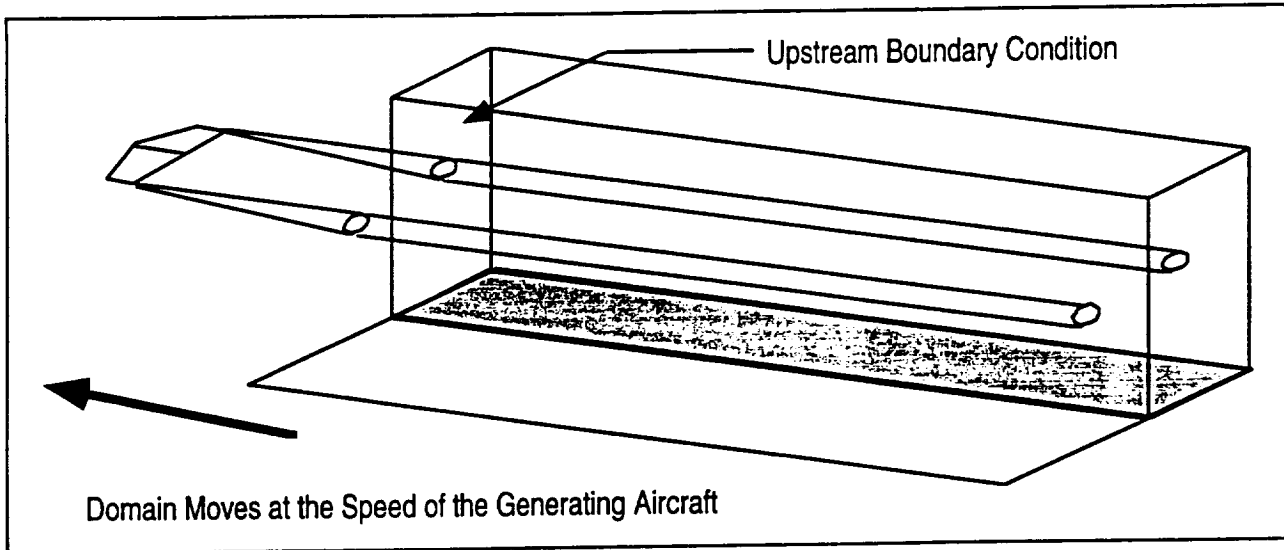
**Figure 4**: Schematic diagram of vortex initialization within the domain. Fully developed vortices are imposed on the upstream boundary and, initially, throughout the domain. Open radiation conditions are used on the downstream boundary. The domain moves at the aircraft speed.
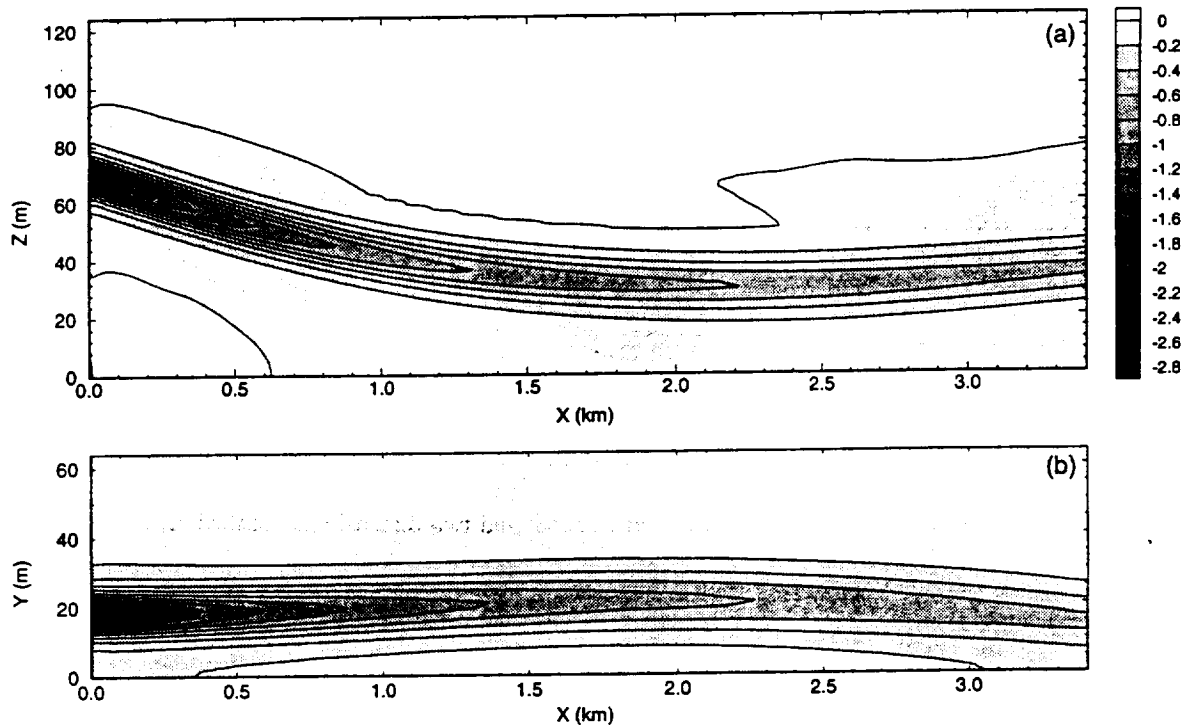


**Figure 5**: Minimum perturbation pressure field after one minute of simulation time. (a) Minimum pressure perturbation for $x$-$z$ coordinates. (b) Minimum pressure perturbation for $x$-$y$ coordinates. (938 meters corresponds to one non-dimensional unit of time)
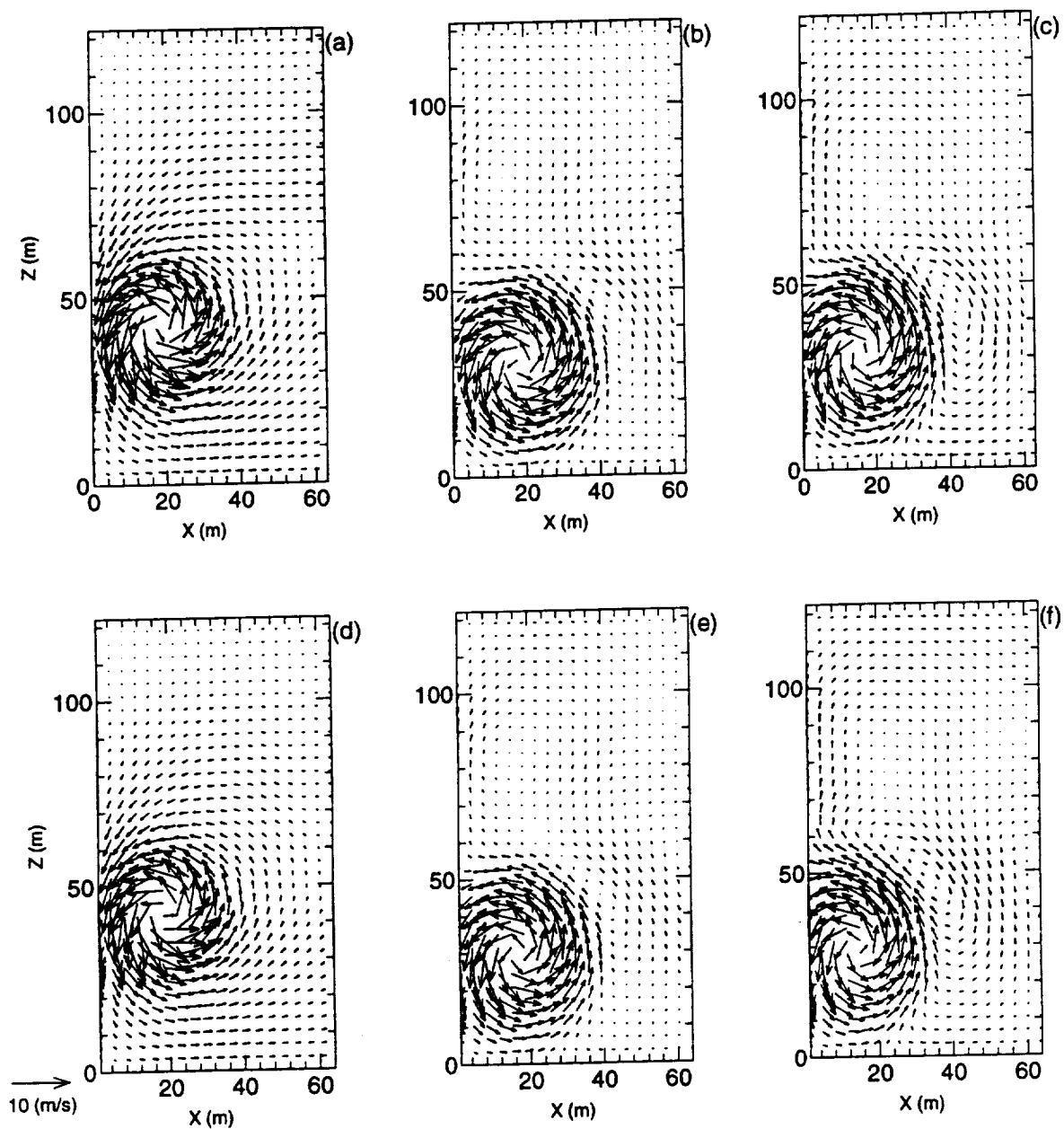
**Figure 6**: Velocity vectors in a $y$-$z$ plane for three-dimensional and two-dimensional simulations at various times. (a)-(c) from three-dimensional run and (d)-(f) for two-dimensional run. Times are (a) and (d) $t^*=1.0$, (b) and (e) $t^*=2.5$, and (c) and (f) $t^*=3.0$. Vectors are scaled as indicated.

American Institute of Aeronautics and Astronautics
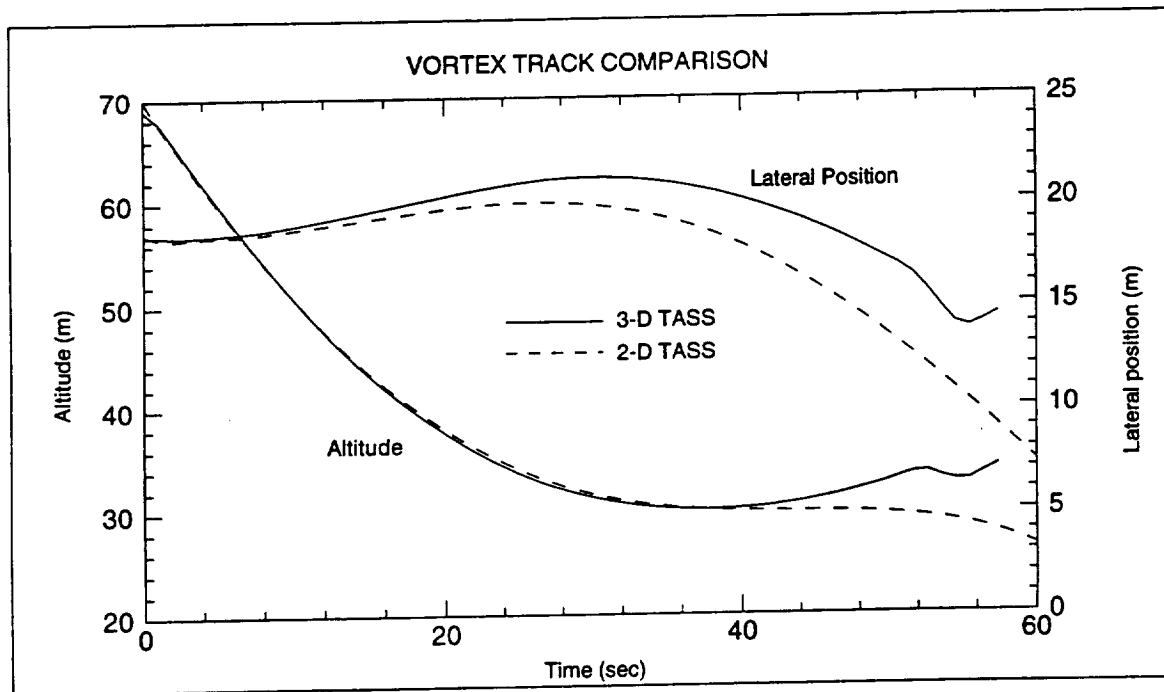
**Figure 7**: Development of vortex height and lateral position with time for two-dimensional and three-dimensional simulations. For the three-dimensional run, time is from forward boundary contact. (15.6 seconds corresponds to one unit of t*)
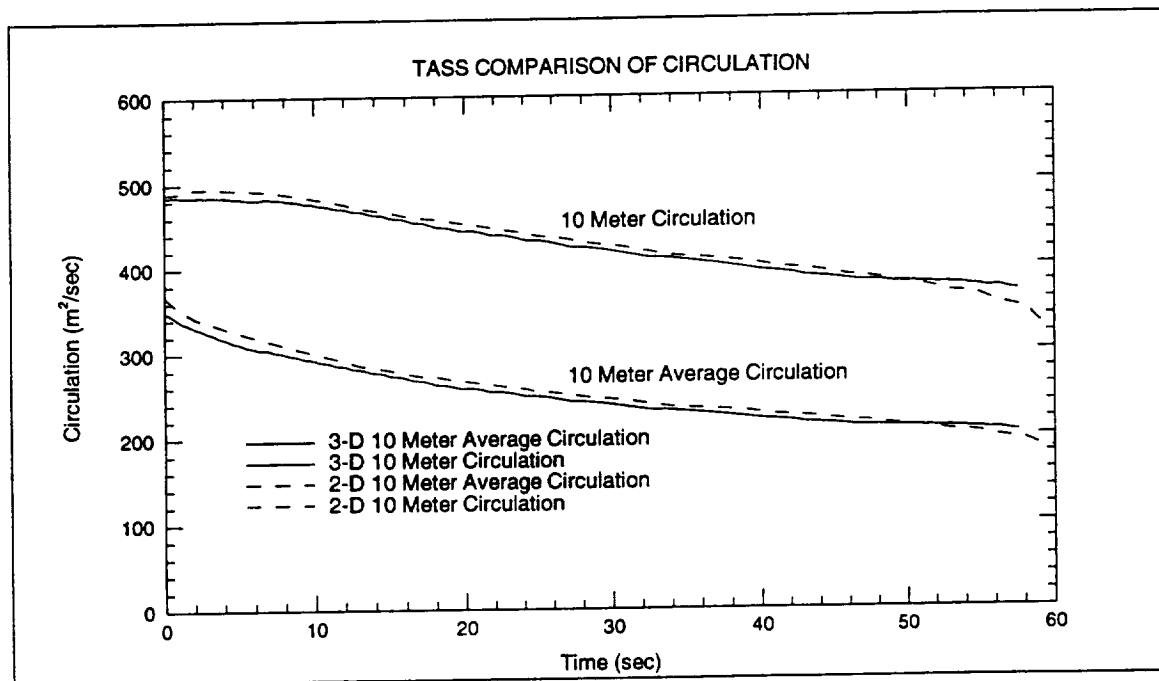


**Figure 8**: Same as figure 7, but for vortex circulation vs. time. Shown are 10 m circulation and 10 m average circulation.

11
American Institute of Aeronautics and Astronautics

Max=.146 Min=-1.15

Max=.083 Min=-1.13
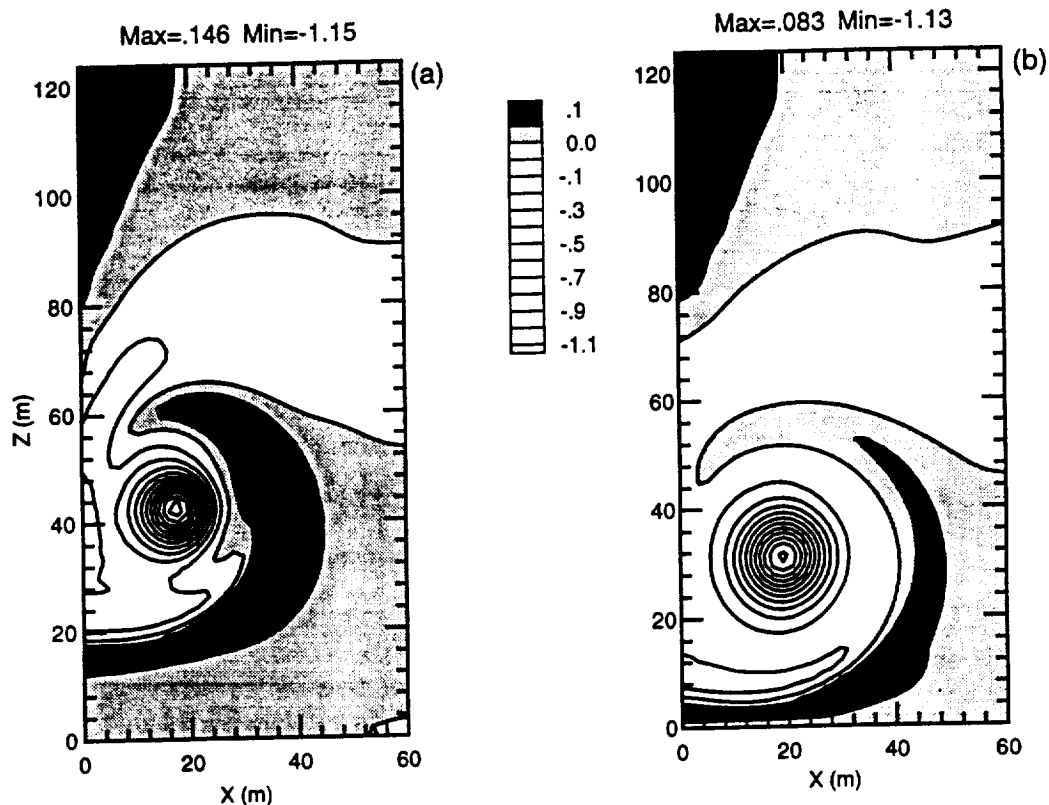


**Figure 9:** Contours of axial wake vortex flow for the three-dimensional simulation at (a) $t^*=1.0$ and (b) $t^*=2.0$. Velocity values greater than zero represent flow away from the aircraft and are shaded regions.

### References

1. Hinton, D. A., 1995: Aircraft Vortex Spacing System (AVOSS) Conceptual Design. *NASA Technical Memorandum 110184.*

2. Burnham, D. C., 1972: Effect of ground wind shear on aircraft trailing vortices. *AIAA J.,* **10**, 1114-1115.

3. Greene, G. C., 1986: An approximate model of vortex decay in the atmosphere. *J. Aircraft,* **23**, 566-573.

4. Crow, S. C., 1970: Stability theory for a pair of trailing vortices. *AIAA J.,* **8**, 2172-2179.

5. Hall, M. G., 1972: Vortex breakdown. *Ann. Rev. Fluid Mech.* **4**, 195-218.

6. Proctor, F. H., 1987: The Terminal Area Simulations System, Vol. I: Theoretical formulation. *NASA Contractor Report 4046,* DOT/FAA/PM-86/50, I.

7. Proctor, F. H., 1996: Numerical simulation of wake vortices measured during the Idaho Falls and Memphis field programs. *14th AIAA Applied Aerodynamics Conference,* Proceedings, Part- II, 17-20 June, New Orleans, LA, AIAA Paper No. 96-2496, 943-960.

8. Schowalter, D. G. , D. S. DeCroix, Y.-L. Lin, F. H. Proctor, S. P. Arya, and M. L. Kaplan 1995: Turbulent Statistics in the Atmospheric Boundary Layer: A Comparison of Large Eddy Simulation With Observations. *11th Symp. Bound. Layers Turb.,* American Meteorological Society, 552-555.

9. Schowalter, D. G., D. S. DeCroix, Y.-L. Lin, S. P. Arya, and M. L. Kaplan, 1996: Planetary boundary layer simulation using TASS. *NASA Contractor Report 198325,* 41pp.

10. Schowalter, D. G., Y.-L. Lin, and S. P. Arya 1996: The evening transition of the planetary boundary layer: A case study. Preprint, *First International Conference on Nonlinear Problems in Aviation and Aerospace.* Daytona Beach, Florida, May 9-11, 1996.

11. Bilanin, A. J. , M. E. Teske, and J. E. Hirsh 1977: Neutral atmospheric effects on the dissipation of aircraft vortex wakes. *AIAA J.*, **16**, 956-961.

12. Robins, R. E. and D. P. Delisi, 1988: Numerical study of vertical shear and stratification effects on the evolution of a vortex pair. *AIAA J.*, **28**, 661-669.

13. Schilling, V. K., 1992: Motion and decay of trailing vortices within the atmospheric surface layer. *Beitr. Phys. Atmos.*, **65**, 157-169.

14. Zheng, Z. and R. L. Ash 1993: Prediction of turbulent wake vortex motion near the ground. *FED*, **151**, 195-207.

15. Ragab, S. and M. Sreedhar, 1995: Numerical simulation of vortices with axial velocity deficits. *Phys. Fluids*, **7**, 549-558.

16. Leonard, A. and K. Chua, 1989: Three-dimensional interactions of vortex tubes. *Physica D*, **37**, 490-496.

17. Spalart, P. R. and Wray, A. A., 1996: Initiation of the Crow instability by atmospheric turbulence. *78th AGARD-FDP Symp. "The char. & modif. of wakes fr. lifting veh. in fluids,"* Trondheim, Norway, 20-23 May 1996.

18. Gerz, T. and Ehret, T. 1996: Wake dynamics and exhaust distribution behind cruising aircraft. *78th AGARD-FDP Symp. "The char. & modif. of wakes fr. lifting veh. in fluids,"* Trondheim, Norway, 20-23 May 1996.

19. Corjon, A., Risso, F., Stoessel, A. and Poinsot, T. 1996: Three-dimensional direct numerical simulations of wake vortices: Atmospheric turbulence effects and rebound with crosswind. *78th AGARD-FDP Symp. "The char. & modif. of wakes fr. lifting veh. in fluids,"* Trondheim, Norway, 20-23 May 1996.

20. Proctor, F. H., Hinton, D. A., Han, J., Schowalter, D. G. and Lin, Y.-L 1997: Two-dimensional wake vortex simulations in the atmosphere: Preliminary sensitivity studies. *AIAA Paper* 97-0056.

21. Chen, C. 1991: A nested grid nonhydrostatic, elastic model using a terrain-following coordinate transformation: the radiative-nesting boundary conditions. *Mon. Wea. Rev.* **119**, pp. 2852-2869.

22. Clark, T. L. and Farley, R. D. 1984: Sever downslope windstorm calculations in two and three spatial dimensions using anelastic interactive grid nesting: A possible mechanism for gustiness. *J. Atmos. Sci.*, **41**, 329-350.

23. Klemp, J. B. and Durran, D. 1983: An upper-boundary condition permitting internal gravity wave radiation in numerical mesoscale models. *Mon. Wea. Rev.*, **111**, 430-444.

24. Arakawa, A. 1966: Computational design for long-term numerical integration of the equations of fluid motion: Two-dimensional incompressible flow, Part I. *J. Comp. Phys.*, **1**, 119-143.

25. Burnham, D. C. and Hallock, J. N. 1982: Chicago Monostatic Acoustic Vortex Sensing System. Vol. 4 Wake Vortex Decay. Springfield, VA, NTIS.

26. Switzer, G. F. 1996: Validation tests of TASS for application to 3-D vortex simulations. *NASA Contractor Report 4756.*

27. Batchelor, G. K. 1964: Axial flow in trailing line vortices. *J. Fluid Mech.* **20**, pp. 645-658.

**Appendix E: Large Eddy Simulation of Aircraft Wake Vortices within Homogeneous Turbulence: Crow Instability**

# Large Eddy Simulation of Aircraft Wake Vortices Within Homogeneous Turbulence: Crow Instability

Jongil Han,[*] Yuh-Lang Lin,[†] David G. Schowalter,[‡] and S. Pal Arya[§]

*North Carolina State University, Raleigh, North Carolina 27695-8208*

and

Fred H. Proctor[¶]

*NASA Langley Research Center, Hampton, Virginia 23681*

Ambient atmospheric turbulence effects on aircraft wake vortices are studied using a validated large eddy simulation model. Our results confirm that the most amplified wavelength of the Crow instability and the lifetime of wake vortices are significantly influenced by ambient turbulence (Crow, S. C., "Stability Theory for a Pair of Trailing Vortices," *AIAA Journal*, Vol. 8, No. 12, 1970, pp. 2172–2179). The Crow instability becomes well developed in most atmospheric turbulence levels, but in strong turbulence the vortex pair deforms more irregularly due to turbulence advection. The most amplified wavelength of the instability decreases with increasing dimensionless turbulence intensity $\eta$, although it increases with increasing turbulence integral length scale. The vortex lifespan is controlled primarily by $\eta$ and decreases with increasing $\eta$, whereas the effect of integral scale of turbulence on vortex lifespan is of minor importance. The lifespan is estimated to be about 40% larger than Crow and Bate's predicted value (Crow, S. C., and Bate, E. R., "Lifespan of Trailing Vortices on a Turbulent Atmosphere," *Journal of Aircraft*, Vol. 13, No. 7, 1976, pp. 476–482) but in agreement with Sarpkaya's recent modification (Sarpkaya, T., "Decay of Wake Vortices of Large Aircraft," *AIAA Journal*, Vol. 36, No. 9, 1998, pp. 1671–1679) to Crow and Bate's theory. This larger lifespan is also supported by data from water tank experiments and direct numerical simulations. There appears to be a possibility that the scatter in vortex lifespans due to ambient turbulence alone decreases with increasing Reynolds number, whereas larger scatter of lifespans in flight tests may result from other factors such as stratification, wind shear, and inhomogeneous ambient turbulence.

## I. Introduction

E XISTING procedures for aircraft separations prevent unsafe encounters with hazardous wake vortices but are independent of ambient meteorology and can impact airport capacity. The development of a forecasting system that includes atmospheric variables can be useful for reducing aircraft separations, maintaining safety, and benefiting airport capacity. NASA is developing an automated system, called the Aircraft Vortex Spacing System (AVOSS),[1,2] that will determine safe operating spacing between arriving and departing aircraft as based on the observed or predicted weather conditions. To develop this system, research is being focused on understanding how wake vortices interact with the atmosphere. In the present work we focus on the effects of ambient atmospheric turbulence on the Crow instability[3] as well as vortex lifespan using a validated numerical model. Results from this work and parallel efforts are to provide support in the development of the AVOSS system.

Crow instability is an important mechanism that eventually brings about the destruction of wake vortices.[3] This instability is based on linear theory and was first analyzed in terms of mutual induction by Crow. Because of the Crow instability, the vortices undergo a symmetric and sinusoidal instability that grows exponentially and, finally, result in a linking into a series of crude vortex rings. This phenomenon has been observed by flight tests[4,5] and laboratory experiments,[6–8] as well as confirmed in numerical simulations.[9,10]

During development of the Crow instability, the vortex behavior is significantly influenced by atmospheric turbulence, stratification

and wind shear, and vortex core bursting, which are believed to be main causes of deviations from the predictions of the instability theory on the most amplified wavelength and vortex lifespan. Core bursting,[7,11] which falls outside the scope of the present study, is another dominant instability mechanism for vortex destruction, but it more often occurs toward the end of the vortex lifespan.

Turbulence, whose scale is smaller than vortex separation distance, can lead to an enhanced diffusion of the circulation of the vortices,[12–14] whereas strong and large turbulent eddy motion can cause a large distortion of the vortices.[5,10] The enhancement of vortex decay due to ambient turbulence is one important factor of the wake-prediction models developed by Donaldson and Bilanin[12] and Greene[13] and will be studied in more detail in a separate paper. On the other hand, the vortices may distort the ambient turbulence and cause departures from statistical homogeneity and isotropy. This nonlinear interaction between the vortices and the ambient turbulence may modify the predictions from the linear instability theory.

Crow and Bate[15] (CB) incorporate the effects of ambient turbulence to the Crow instability and then obtain the theoretical predictions for the vortex lifespan. They define the vortex lifespan as the time at which linking of a vortex pair occurs. Under the assumption that eddies of the relevant size lie in the Kolmogorov inertial subrange that is characterized by the turbulence energy dissipation rate $\epsilon$ and that the atmospheric turbulence is independent of the vortices, they predict that the dimensionless vortex lifespan,

$$\tau = (\Gamma_0/2\pi b_0^2)t^* \tag{1}$$

is only a function of the dimensionless turbulence intensity $\eta$:

$$\eta = (\epsilon b_0)^{\frac{1}{3}}/V_0, \qquad V_0 = \Gamma_0/2\pi b_0 \tag{2}$$

where $\Gamma_0$ is the circulation around the vortices, $t^*$ is the vortex lifespan, and $b_0$ is the initial separation distance of the vortex pair. Here, $\eta$ represents the ratio of the characteristic turbulent velocity scale at the scale of the vortex separation distance $[(\epsilon b_0)^{1/3}]$ to the speed of descent of the vortex pair by mutual induction, $V_0$, and is the appropriate dimensionless measure of turbulence intensity. The theoretical prediction function $\tau(\eta)$ appears to be in reasonable

agreement with data from field flight tests, but the scatter is large (about a factor of 3 in $\tau$ for fixed $\eta$), which may be due to other influences such as wind shear, stratification, and core bursting, as mentioned earlier.

On the other hand, from dimensional arguments, Sarpkaya and Daly[7] postulated a similarity relation

$$H = h/b_0 = f(T, \eta, L_{11}/b_0) \tag{3}$$

in the absence of wind shear and stratification, where $h$ is the descent distance of the vortices, $T$ is dimensionless time, that is,

$$T = V_0 t/b_0 \tag{4}$$

and $L_{11}$ is the longitudinal integral length scale in the axial direction of a vortex, defined as

$$L_{11} = \int_0^\infty \langle u(x)u(x+r)\rangle \Big/ \langle u^2\rangle \, dr \tag{5}$$

where $\langle\ \rangle$ is the domain average. Then, in the water tank experiments in which two biplanar grids were towed at a constant speed to produce isotropic turbulence, they found that the descent and demise of the vortices are controlled primarily by the dissipation rate of ambient turbulence, whereas the integral scale of turbulence plays only a minor role. Compared with flight tests, the water tank data displayed less scatter because the effects of ambient wind shear and stratification were avoided. Liu[8] performed similar experiments in a towing water tank. His results showed that, when the lifespan only due to vortex linking is considered, the scatter in lifespans is much less and that the dominant wavelength of the linking decreases with increasing turbulence intensity or dissipation rate.

The direct numerical simulation (DNS) results by Spalart and Wray,[10] in which a five by five array of vortex pairs is simulated in an initially isotropic turbulence without ambient wind shear and stratification, show a large scatter comparable with flight tests for the theoretical curve of CB. Because their DNS study showed no core bursting (to date, no numerical simulations of wake vortices have shown this phenomenon), the large scatter in their DNS results could be due to the variability of turbulence related to low Reynolds number flow characteristics intrinsic in any DNS study.

One way to investigate high-Reynolds-number flows, such as atmospheric boundary-layer turbulence, is through the use of a large eddy simulation (LES) model, which has become a useful tool for the study of interior turbulence structure.[16–18] In LES, the large-scale eddies are explicitly resolved, whereas small-scale eddies are parameterized through a closure model. One reason for the success of this approach is that the small-scale eddies tend to be more isotropic and universally similar and are, therefore, more amenable to parameterization than the large-scale eddies, which are much more dependent on the type of flow. The basic requirement of LES is that the grid size should be much smaller than the integral length scale to guarantee the isotropy of the subgrid-scale eddies. The numerical model used in the present study is a three-dimensional, nonlinear, compressible, nonhydrostatic LES model, namely, the Terminal Area Simulation System (TASS),[19,20] that has been adapted for simulation of interaction of wake vortices with the atmosphere.[20,21] We simulated only the post-rollup wake vortices; the rollup process falls outside the scope of the present study.

In Sec. II we describe our LES model and the modifications required for initial conditions. In Sec. III we present results from systematic numerical experiments in terms of dimensionless turbulence intensity and length scale. Finally, in Sec. IV we summarize our LES results and draw some conclusions.

## II. Model and Initial Conditions

### A. Model

The TASS model contains 12 prognostic equations: three for momentum, one each for pressure deviation and potential temperature, six coupled equations for continuity of water substance (water vapor, cloud droplet, cloud ice crystals, rain, snow, and hail), and one for a massless tracer (see Refs. 19 and 20 by Proctor for the whole TASS equation set). In the neutral and dry atmosphere neglecting

the Coriolis force, the model equations can be reduced to four prognostic equations given by

$$\frac{\partial u_i}{\partial t} + \frac{1}{\rho_0}\frac{\partial p}{\partial x_i} = -\frac{\partial u_i u_j}{\partial x_j} + u_i\frac{\partial u_j}{\partial x_j} + \frac{1}{\rho_0}\frac{\partial \tau_{ij}}{\partial x_j} + f \tag{6}$$

$$\frac{\partial p}{\partial t} + \frac{C_p P_0}{C_v}\frac{\partial u_j}{\partial x_j} = 0 \tag{7}$$

where $u_i$ is the component of velocity, $t$ is time, $p$ is deviation from the reference atmospheric pressure $P_0$, $\rho_0$ is the reference air density, $C_p$ and $C_v$ are the specific heats of air at constant pressure and volume, and $f$ is an artificial external forcing term to generate an isotropic turbulence. The equation for pressure deviation [Eq. (7)] has been derived from the mass continuity equation,[19] with the advection and subgrid eddy transport terms for pressure neglected in this study because of the dominance of the second term on the left-hand side of Eq. (7).

The dependent variables in TASS are treated as averages over the grid volumes, giving rise to subgrid stress terms. The subgrid stress $\tau_{ij}$ is approximated by using Smagorinsky first-order closure:

$$\tau_{ij} = \rho_0 K_m D_{ij} \tag{8}$$

where the velocity deformation $D_{ij}$ is defined as

$$D_{ij} = \frac{\partial u_i}{\partial x_j} + \frac{\partial u_j}{\partial x_i} - \frac{2}{3}\frac{\partial u_k}{\partial x_k}\delta_{ij} \tag{9}$$

and the subgrid eddy viscosity is given by

$$K_m = (c_s\Delta)^2|Def| \tag{10}$$

The subgrid length scale $\Delta$ is constant and related to the grid size as $\Delta = (2\Delta x 2\Delta y 2\Delta z)^{1/3}$, $|Def| = \sqrt{(\frac{1}{2}D_{ij}\cdot D_{ij})}$. The coeffcient $c_s = 0.075$ was used as the optimum value; this value was found to be large enough to damp out small-scale fluctuations but small enough to avoid too much damping of the turbulence energy in higher wave numbers.

The TASS model uses the time-splitting integration procedure (small time step for acoustically active terms and large time step for advection and diffusion[22]) that results in a substantial savings in computing time. Local time derivatives (both small and large time steps) are approximated by the second order Adams–Bashforth method. Space derivatives are approximated by central differences in quadratic-conservative form, which are fourth order for advective derivatives and second order for remaining derivatives. Details of the numerical formulation can be found in Refs. 19 and 20. The numerical schemes used in TASS produce accurate and stable results and have been shown to have almost no numerical dissipation.[23]

The vortex system is representative of the post-rollup wake velocity field and is initialized with the superposition of two counter-rotating vortices, with the velocity field for each vortex specified as[24,25]

$$V(r) = \Gamma_0/2\pi\big[r\big/(r_c^2 + r^2)\big] \tag{11}$$

where $V(r)$ is the vortex tangential velocity at radius $r$; $r_c$ is the core radius, that is, radius of peak tangential velocity; and $\Gamma_0$ is the circulation at $r \gg r_c$. In this study $r_c$ is fixed as 2 m.

Grid points used in our simulations are $324 \times 112 \times 112$ with grid size $(\Delta x, \Delta y, \Delta z) = (1.0, 0.75, 0.75\ \text{m})$, where $x$, $y$, and $z$ correspond to the axial, lateral, and vertical directions of the vortex system and corresponding velocity components are $u$, $v$, and $w$, respectively. Periodic boundary conditions are imposed at all domain boundaries. Two values of $b_0$, that is, $b_0 = 16$ and 8 m, are used for fixed-domain size. For the case of $b_0 = 16$ m, the domain size becomes $(L_x \times L_y \times L_z) = (20b_0 \times 5b_0 \times 5b_0)$. The domain size in the axial direction, $20b_0$, is large enough to simulate the most amplified wavelength of about $8.6b_0$ for Crow instability.[3] The domain size of $5b_0$ in the lateral and vertical directions is sufficiently large to minimize boundary influences. The strain rate of neighboring vortex pairs that are present outside of the domain when periodic boundary conditions are assumed is only a few percent of that exerted by one

vortex on the other in the vortex pair. This domain configuration is adequate, although a larger domain size would be preferable if not limited by computing resources. For the case of $b_0 = 8$ m, the domain size becomes much larger in terms of $b_0$. The core size 2 m used in our simulations is larger than the typical value (about 5% of the generating aircraft's wingspan[20]) observed behind aircraft. However, dependency of $r_c/b_0$ on the Crow instability is weak[3] and is examined further when our LES results are compared with the theoretical predictions in Sec. III.

### B. Initial Conditions

Because we want to study the effect of ambient turbulence on the Crow instability,[3] it is of crucial importance to obtain an initially homogeneous and isotropic turbulence field. Toward this purpose, the initial turbulence field is allowed to develop under an artificial external forcing at low wave numbers.[26] Because the TASS code uses a finite difference numerical scheme, the forcing is achieved by performing, first, a three-dimensional fast Fourier transform (FFT) at every large time step, then adding a constant amplitude $f$ to all of the modes with integer wave numbers whose magnitude is less than 3.0, and, finally, performing an inverse FFT back to the physical space. The wave number in the axial direction is normalized so that the axial wavelength has the same magnitude as that of the corresponding wave number in the lateral or the vertical direction. Because of viscous dissipation, the simulation can reach a statistically steady state in the sense that the mean turbulence kinetic energy (TKE) oscillates in time around a constant value. Figure 1 shows that the domain-averaged TKE and variances from resolved velocity fields reach a steady state around about 1000 s. The integral length scale is calculated as $L_{11} = 15.0$ m in a steady-state turbulence, and the large eddy turnover time, defined as

$$t_e = L_{11}/\langle u^2 \rangle^{\frac{1}{2}} \tag{12}$$

is estimated as $t_e = 56.2$ s. Thus, we obtain a statistically steady-state flow after integration over about 18 large eddy turnover times. The isotropy parameter $I$, defined as

$$I_1 = [\langle u^2 \rangle/\langle v^2 \rangle]^{\frac{1}{2}} \quad \text{or} \quad I_2 = [\langle w^2 \rangle/\langle v^2 \rangle]^{\frac{1}{2}} \tag{13}$$

fluctuates only a few percent around its expected value of 1 for isotropic turbulence. Therefore, our simulated turbulence is close to statistical isotropy.

Figure 2 shows the one-dimensional spectra of $u$ and $v$ in the statistically steady state as functions of wave number $\kappa_1$, where subscript 1 represents axial direction. Fairly extensive inertial subranges with

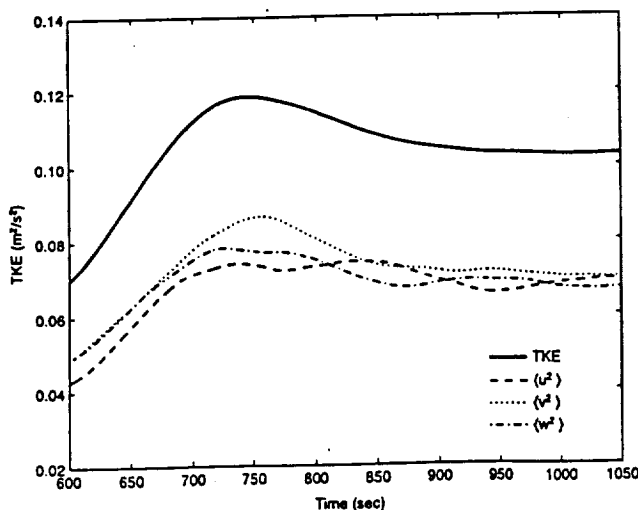$$F_{11}(\kappa_1)\kappa_1^{\frac{5}{3}}\langle\epsilon\rangle^{-\frac{2}{3}} = \alpha_1 \tag{14}$$



Fig. 1   Time evolution of turbulent kinetic energy and velocity vari-

Table 1   Characteristics of the numerical simulations

| Turbulence strength | $\eta$ | $b_0$, m | $r_c$, m | Domain size $(L_x \times L_y \times L_z)$ |
|---|---|---|---|---|
| Weak | 0.0316 | 16 | 2 | $20b_0 \times 5b_0 \times 5b_0$ |
|  |  | 8 | 2 | $40b_0 \times 10b_0 \times 10b_0$ |
|  | 0.0789 | 16 | 2 | $20b_0 \times 5b_0 \times 5b_0$ |
| Moderate | 0.1753 | 16 | 2 | $20b_0 \times 5b_0 \times 5b_0$ |
|  |  | 8 | 2 | $40b_0 \times 10b_0 \times 10b_0$ |
| Strong | 0.3506 | 16 | 2 | $20b_0 \times 5b_0 \times 5b_0$ |
|  |  | 8 | 2 | $40b_0 \times 10b_0 \times 10b_0$ |
|  | 0.5844 | 16 | 2 | $20b_0 \times 5b_0 \times 5b_0$ |
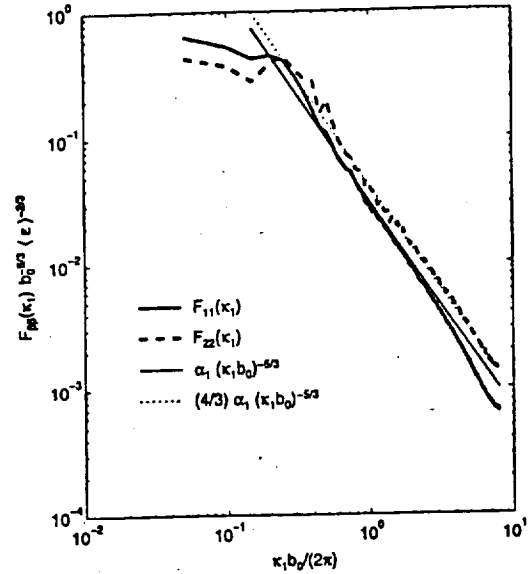


Fig. 2   One-dimensional energy spectrum in a steady-state turbulence before vortex injection.

$$F_{22}(\kappa_1)\kappa_1^{\frac{5}{3}}\langle\epsilon\rangle^{-\frac{2}{3}} = \frac{4}{3}\alpha_1 \tag{15}$$

are present, where $F_{11}(\kappa_1)$ and $F_{22}(\kappa_1)$ are one-dimensional longitudinal and transverse spectra, respectively, $\langle\epsilon\rangle$ represents a domain-averaged TKE dissipation rate, and $\alpha_1$ is a constant. If the Kolmogorov constant $\alpha$ is taken as 1.5 (e.g., see Ref. 27), then we can estimate $\langle\epsilon\rangle$ from a line fit of the theoretical relations of the spectra in the inertial subrange, that is, Eqs. (14) and (15) with $\alpha_1 = (\frac{18}{55})\alpha$, to the simulated spectra, as seen in Fig. 2. For our simulated turbulence field, the dissipation rate is calculated as $\langle\epsilon\rangle \approx 0.9897 \times 10^{-3}$ m$^2$ s$^{-3}$.

A two-dimensional counter-rotating vortex pair prescribed by Eq. (11) is initialized in every $y$–$z$ plane along the axial direction when the ambient turbulence reaches a steady state, that is, at 1020 s after integration. Five values for $\eta$ are obtained by varying the circulation to save computing time, rather than by varying $\langle\epsilon\rangle$, and can be divided into three turbulence strength groups, as seen in Table 1. The vortex injection time is the same for each $\eta$ value unless stated otherwise.

Except in one case, that is, the case of $\eta \approx 0.0$ described in Sec. III, the flow is turbulent with Reynolds numbers ($Re \equiv \Gamma/\nu$, where $\nu$ is kinematic viscosity) ranging from $2.88 \times 10^6$ to $5.33 \times 10^7$, which are appropriate for atmospheric wake vortices.

## III.   Results

### A.   Crow Instability

Figure 3 shows top and side views of the vortex pairs with increasing nondimensional time for six different nondimensional turbulence intensities. In the case of $\eta \approx 0.0$ (Fig. 3a), a constant viscosity is used for the subgrid stress ($Re \approx 1.66 \times 10^4$) and the instability is initiated by adding very small random velocity perturbations to the initial field. This case is representative of nearly laminar flow and is useful for comparing with the cases that have turbulence.

a) $\eta \approx 0.0$



b) $\eta = 0.0316$



c) $\eta = 0.0789$



d) $\eta = 0.1753$



e) $\eta = 0.3506$



f) $\eta = 0.5844$

Fig. 3  Top $(x, y)$ and side $(x, z)$ views of wake vortices at three nondimensional times for the case of $b_0 = 16$ m.

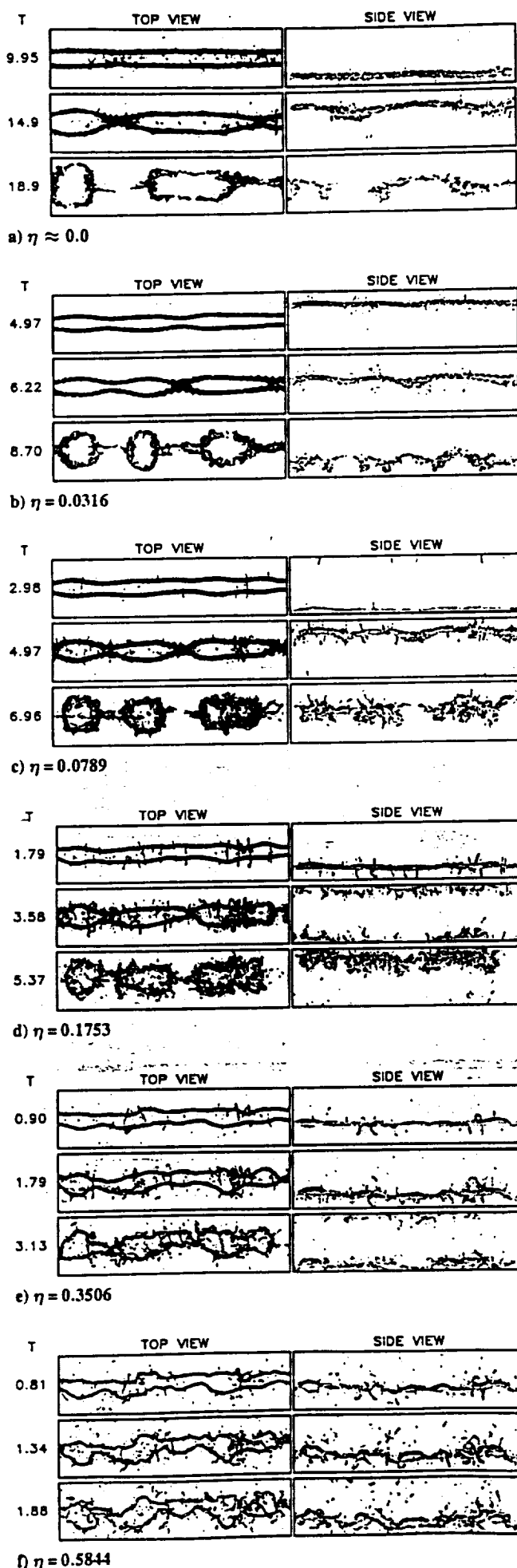of a vortex. They define a vortex in terms of the second negative eigenvalue $\lambda_2$ of the symmetric tensor $S^2 + \Omega^2$, where $S$ and $\Omega$ are, respectively, the symmetric and antisymmetric parts of the velocity gradient tensor $\nabla u$. Corjon et al.[29] applied this method for the identification of wake vortices and showed that an isosurface of negative $\lambda_2$ visualizes the vortices very well. In the present study, the top (side) view is taken from the $x$–$y$ ($x$–$z$) plane projection of the minimum negative $\lambda_2$ value along the $z(y)$ direction. A threshold $\lambda_2$ value to identify the vortex is arbitrarily determined. In the TASS code the vortex center position to estimate the most amplified wavelength is later calculated via the centroid of $\zeta_x \times p^6$, where $\zeta_x$ and $p$ represent axial vorticity and pressure perturbation, respectively.

Except for strong turbulence, most of the cases in Fig. 3 show clearly developing Crow instability. In agreement with observations, the vortex pair connects together as a result of the instability, forms a train of vortex rings, and then disintegrates into a turbulent state. In strong turbulence, the vortices are more irregularly distorted due to advection and nonlinear interaction with ambient turbulence. A sinusoidal instability still appears to develop even for a strong turbulence cases. This vortex behavior for strong turbulence was observed by Tombach[5] (e.g., see Fig. 4 in Ref. 5). Spalart and Wray's[10] DNS study also shows similar patterns, but their results for intense turbulence appear to be dominated by ambient turbulent flow advection without the indication of the sinusoidal development of Crow instability.[3]

The dimensionless vortex linking time, defining the vortex lifespan, decreases with increasing nondimensional turbulence intensity, which is consistent with previous studies.[5,7,8,10,15] Vortex lifespan will be discussed in detail later. Note that the vortex linking time for the case of $\eta \approx 0.0$ (Fig. 3a) is much larger than for cases with ambient turbulence (Figs. 3b–3f). The significant $\lambda_2$ values around the vortex pair may result from the stretching of the ambient turbulent eddies in the vertical direction by the velocity field induced by the vortices, as suggested in the Corjon et al.'s[29] DNS study. The circulation associated with the vortices can be weakened through this turbulence vorticity stretching process. The issues involving vortex decay will be discussed in a separate paper.

In the top views of Fig. 3, the most amplified wavelength (MAW) appears to decrease with increasing turbulence intensity. A quantitative estimate of the MAW can be obtained from the spectrum analysis of $y$ displacement of the vortex along the axial direction just before vortex linking (Fig. 4). The MAWs for $\eta = 0.0316$, $0.0789$, and $0.1753$ range from $4b_0$ to $7b_0$, showing higher value for weaker turbulence. For stronger turbulence, that is, $\eta = 0.3506$ and $0.5844$, a significant spectral energy of the displacement is seen in the smaller wavelength range. The case of $\eta \approx 0.0$ shows the largest MAW, that is, about $10b_0$. This trend that the MAW decreases with increasing turbulence intensity agrees surprisingly well with results of Liu's[8] laboratory experiments. It is noticeable that stronger turbulence tends to intensify more strongly smaller unstable wavelengths than larger ones.

According to Crow's linear instability theory,[3] both the MAW and the amplification rate depend only on $r_c/b_0$, though the dependency is weak. Crow obtained the MAW of $8.6b_0$ with $r_c/b_0 = 0.0985$, assuming that $d/(2r_c) = 0.321$ for vortices trailing from an elliptically loaded wing and that vorticity is uniformly distributed within the vortex core. Here, $d$ is the cutoff distance in the line integral representing self-induction. Because a value of $r_c/b_0 = 0.125$ is used in our simulations, the MAW predicted by Crow's theory is about $8.2b_0$, which is larger than any MAW obtained in our simulations with ambient turbulence. In laboratory experiments, Liu[8] obtained an average MAW of $7.8b_0$, whereas Spalart and Wray's[10] DNS results show an average MAW of $6.7b_0$. In Chevalier's[4] flight tests, the MAWs range from $5b_0$ to $10b_0$ in light atmospheric turbulence conditions, showing a large scatter about the average value of $8.4b_0$. A close inspection of his observations indicates that the MAW tends to decrease with increasing air speed. Because the circulation of the vortices is inversely proportional to the air speed [i.e., $\Gamma_0 = 4Mg/(\pi \rho V_a B)$, where $B$ is the span of the generating aircraft, $V_a$ is the air speed, and $M$ is the mass of the generating aircraft], $\eta$ becomes large as air speed increases. Thus, the observations by Chevalier indicate that, assuming the ambient turbulence intensity did not change much during the flight tests, the MAW tends
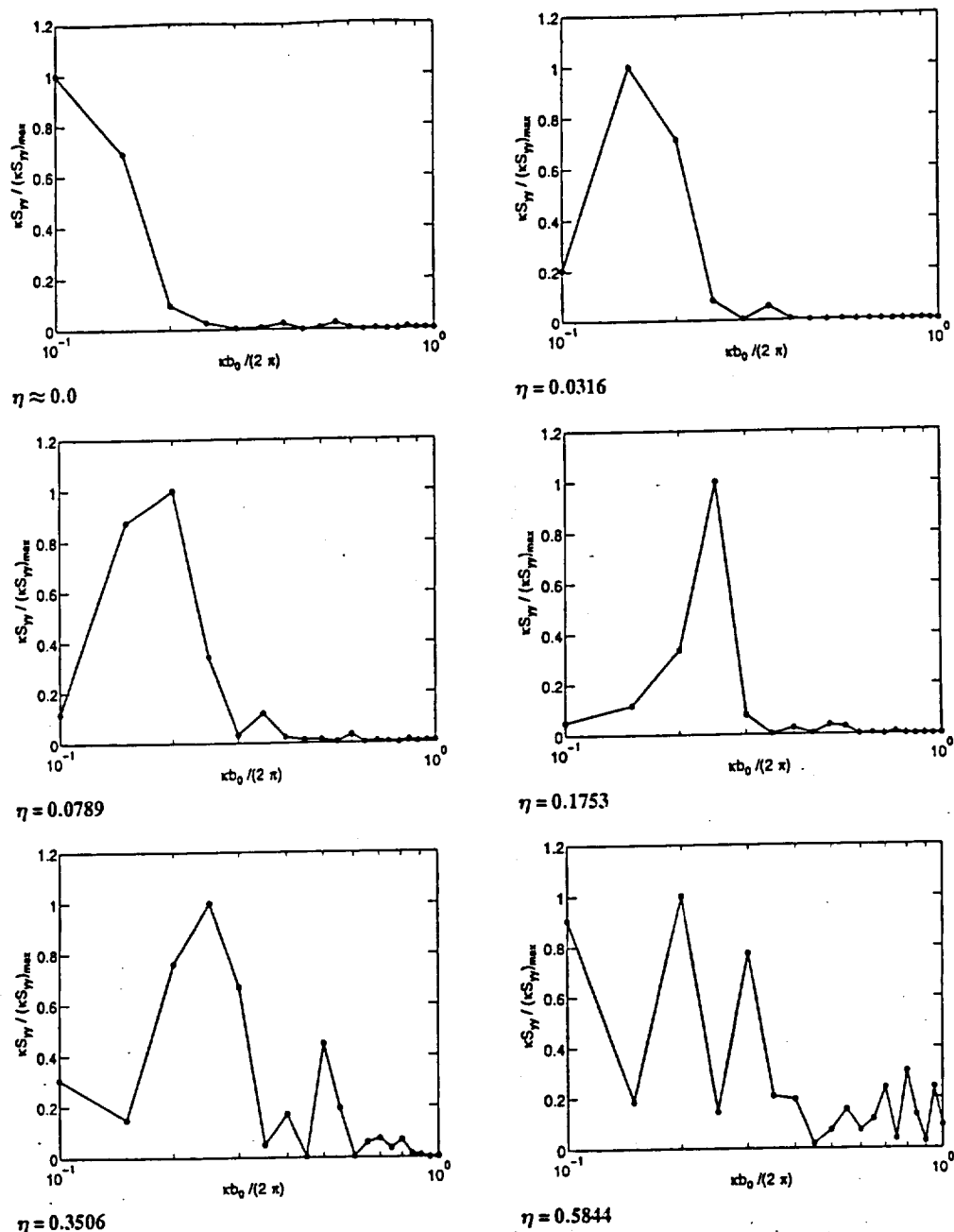
$\eta \approx 0.0$

$\eta = 0.0316$

$\eta = 0.0789$

$\eta = 0.1753$

$\eta = 0.3506$

$\eta = 0.5844$

Fig. 4  Spectrum of $y$ displacement of the vortex along the axial direction before vortex linking for the case of $b_0 = 16$ m.

to decrease with increasing nondimensional turbulence intensity, which is consistent with our results. However, the measurement errors and the absence of the turbulence dissipation rate measurement make it difficult to compare closely our results with those observations.

The smaller MAW compared with Crow's[3] linear theory in the case of $b_0 = 16$ m may come from the limited domain size used in the present study or the artificial external forcing added in a wavelength range of $1.7b_0$–$5b_0$ to maintain the ambient turbulence intensity. Another possibility is the difference of the vortex model used in the two studies; for example, unlike the Crow case, the vorticity within the vortex core in the present study decreases with increasing radial distance from the vortex center. Finally, the effect of the ambient turbulence length scale on the vortices must be considered. Although not shown in the figures, our previous test results have indicated that the artificial external forcing and the difference of the vortex model used are not relevant to the discrepancy between the Crow theory and the present results. For example, although the external forcing was deactivated at vortex injection time so that the ambient turbulence strength decreased with time, the instability development was almost identical to that with the external forcing, confirming the arguments by Corjon et al.[29] that the timescale of the ambient

turbulence compared to that of the vortex is sufficiently large to obtain the main characteristics of the effects of ambient turbulence on the wake vortices. We have also tested the instability development for the Rankine vortex model. The Rankine vortex model possessing uniform vorticity distribution within the vortex core is exactly the same that used in Crow's theory.[3] The instability development for the Rankine vortex model was also almost the same as that of the present model, indicating that the instability is very sensitive neither to the vortex model used nor to its core structure.

The much larger value of the MAW, that is, about $10b_0$, in the case of $\eta \approx 0.0$ indicates that our domain size is large enough to produce the Crow instability.[3] However, the problem for the limited domain size results because the scales of the ambient turbulence are limited by the domain size. Note that the Crow MAW, that is, $8.2b_0$ for $r_c/b_0 = 0.125$, is not within the inertial subrange (Fig. 2) but larger than the domain in the $y$–$z$ plane. Therefore, some sensitivity tests with $b_0 = 8$ m for $\eta = 0.0316$, $0.1753$, and $0.3506$ were conducted to see the effect of ambient turbulence length scale on the instability. In terms of vortex separation distance, the domain size in this case is enlarged to $(L_x \times L_y \times L_z) = (40b_0 \times 10b_0 \times 10b_0)$, that is, just twice of the case of $b_0 = 16$ m in each direction (Table 1). The integral length scale of the ambient turbulence also becomes about
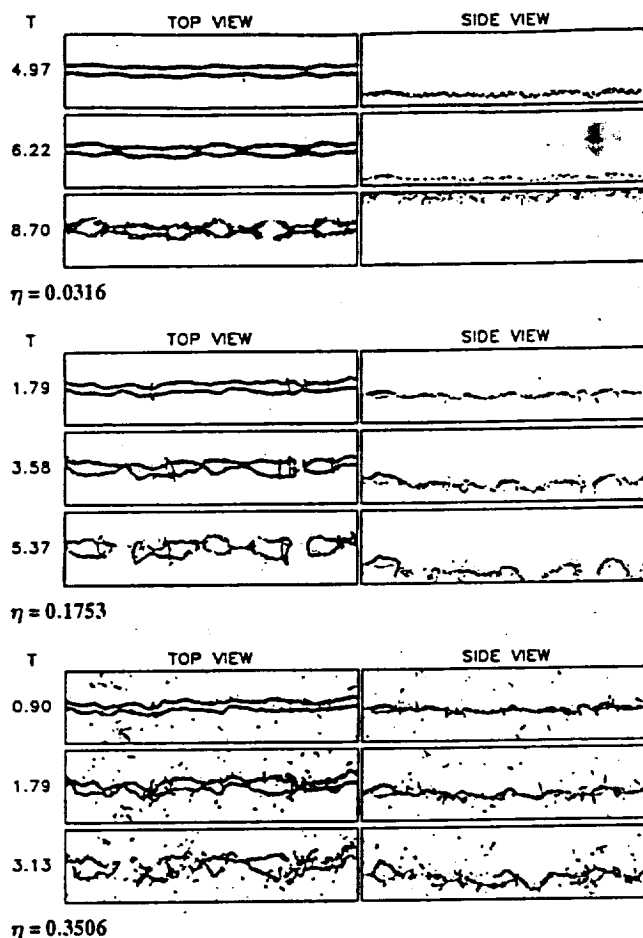
Fig. 5 Top $(x, y)$ and side $(x, z)$ views of wake vortices at three nondimensional times for the case of $b_0 = 8$ m.



$\eta = 0.0316$



$\eta = 0.1753$



$\eta = 0.3506$

Fig. 6 Spectrum of $y$ displacement of the vortex along the axial direction before vortex linking for the case of $b_0 = 8$ m.

twice the vortex separation distance. The MAW for the Crow instability based on the theory is estimated to be $6.9b_0$, which is quite well located in the middle of the inertial subrange of Fig. 2. (In this case the values on $\kappa_1$ axis of Fig. 2 should be divided by 2.) The top and side views and the $y$-displacement spectra for the larger integral length scale of turbulence are shown in Figs. 5 and 6, respectively. Because domain size in the axial direction is doubled, more vortex rings are formed (Fig. 5) compared with the case of $b_0 = 16$ m (Fig. 3). The vortex evolution appears to be similar to the previous case, but the MAW is a little larger, for example, the spectral peaks of $y$ displacements for $\eta = 0.0316$ and $0.1753$ are $8b_0$ and $5b_0$ compared to $7b_0$ and $4b_0$ in the preceding case, respectively. Although not shown in Fig. 6, the strongest spectral peaks of $y$ displacements for $\eta = 0.1753$ and $\eta = 0.3506$ are at $20b_0$, which may reflect the advection effect due to larger turbulent eddy motions but is not directly related to instability. Considering the theoretical MAWs in the cases of both $b_0 = 16$ and 8 m, that is, $8.2b_0$ and $6.9b_0$, respectively, the MAW in the case of $b_0 = 8$ m is relatively larger than that in the case of $b_0 = 16$ m. Therefore, larger scales of ambient turbulence tend to promote larger MAW. In addition, for the case of $b_0 = 8$ m, the theoretical MAW can be produced within our dimensionless turbulence strength range, especially in the weak turbulence case. The results with larger turbulence integral length scale are more consistent with Chevalier's[4] atmospheric observations and Liu's[8] laboratory experiments in that all include the theoretical MAW within the obtained MAW range.

## B. Vortex Lifetime

In this study, following CB's definition,[15] the vortex lifetime or lifespan is defined as the time at which linking of a vortex pair occurs. Using Crow's original theory,[3] CB developed a composite vortex lifespan function by considering the cases of both very strong and very weak turbulence.[15] Their expression for vortex lifespan was based on the assumptions that the ambient atmospheric turbulence is independent of the vortices and that turbulent eddies of size comparable to the MAW lie in the Kolmogorov inertial subrange.
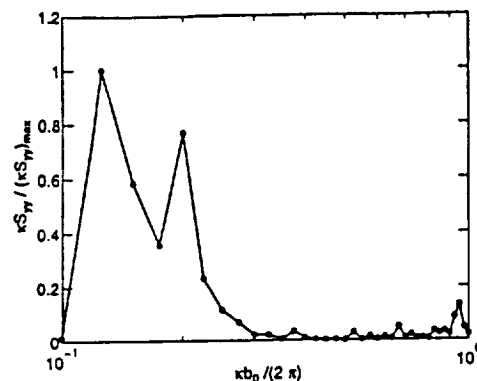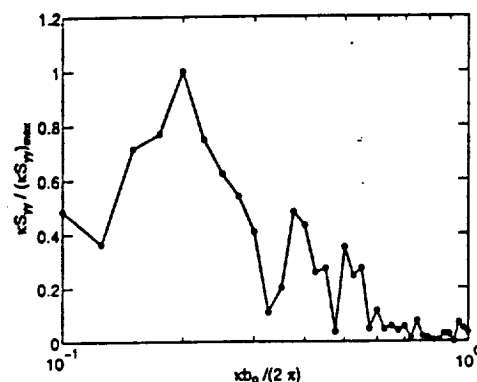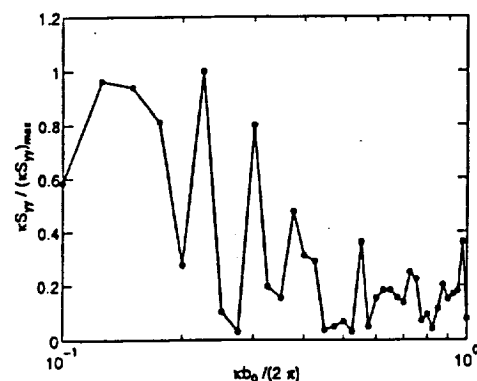
According to CB, the vortex lifespan in strong turbulence is given by

$$l = \left[ \frac{55}{81 \Gamma(\frac{1}{3})\alpha} \right]^{\frac{1}{2}} \frac{b_0}{(\epsilon b_0)^{\frac{1}{3}}} \tag{16}$$

In dimensionless form with the Kolmogorov constant $\alpha = 1.5$,

$$\tau = 0.41/\eta \tag{17}$$

CB also obtained an equation for vortex lifespan in weak turbulence as

$$b_0^2 = \frac{24}{55} \frac{\alpha \epsilon^{\frac{2}{3}} \kappa_m^{-\frac{2}{3}} e^{2a(\kappa_m)t}}{[a(\kappa_m) \tan \theta(\kappa_m)]^2} \left[ \frac{\pi}{|a''(\kappa_m)|t} \right]^{\frac{1}{2}} \tag{18}$$

where $\kappa_m$ is the wave number of the MAW mode, $a$ is the rate of displacement amplification, and $\theta$ is the angle of the vortex displacement from the horizontal plane. From the Crow theory,[3] $\kappa_m = 0.73/b_0$, $a(\kappa_m) = 0.83(\Gamma/2\pi b_0^2)$, $\tan \theta(\kappa_m) = 1.11$, and $|a''(\kappa_m)| = 3.12(\Gamma/2\pi)$. The $a''(\kappa_m)$ was evaluated from parabolic fit to the amplification rate curve for $r_c/b_0 = 0.0985$. Finally, the vortex lifespan

Fig. 7a Dimensionless amplification curve and its parabolic fit: ——, theoretical dimensionless amplication curve by Crow[3] for $r_c/b_0 = 0.0985$; ——, a parabolic fit to the amplification curve in present study; and ---, a parabolic fit to the amplification curve used by CB.[15]



Fig. 7b Composite dimensionless lifespans according to the formula for strong turbulence [Eq. (17)] and for weak turbulence [Eqs. (19) and (20)].

expression obtained by CB[15] for weak turbulence in dimensionless form becomes

$$\eta = 0.87\tau^{\frac{1}{4}}e^{-0.83\tau} \qquad (19)$$

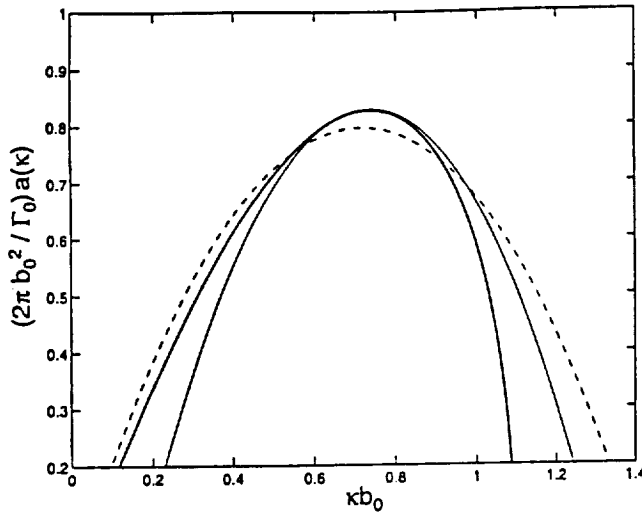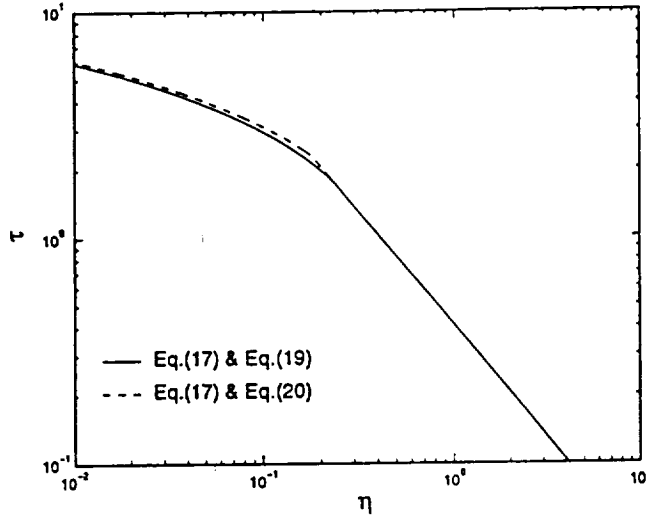We reevaluate $a''(\kappa_m)$ and find that the approximate coeffcient is about 4.90 instead of 3.12 from a parabolic fit to the amplification rate curve, as shown in Fig. 7a. With this refined value, the vortex lifespan for weak turbulence is

$$\eta = 0.98\tau^{\frac{1}{4}}e^{-0.83\tau} \qquad (20)$$

Figure 7b shows that the new expression gives a larger lifespan for given $\eta$ than the original one, but the difference between Eq. (19) and (20) is rather small. For example, the dimensionless lifespan from Eq. (20) at $\eta = 0.1$ is only about 5% larger than that of the lifespan from Eq. (19).

The vortex lifespan expression for the cases of $b_0 = 16$ and 8 m with a fixed $r_c = 2$ m is obtained following the method of CB[15] to compare with our LES results. It is estimated that, for the case of $b_0 = 16$ m, $\kappa_m = 0.77/b_0$, $a(\kappa_m) = 0.82(\Gamma/2\pi b_0^2)$, $\tan\theta(\kappa_m) = 1.10$, and $|a''(\kappa_m)| = 4.3(\Gamma/2\pi)$, whereas for the case of $b_0 = 8$ m, $\kappa_m = 0.91/b_0$, $a(\kappa_m) = 0.80(\Gamma/2\pi b_0^2)$, $\tan\theta(\kappa_m) = 1.10$, and $|a''(\kappa_m)| = 2.54(\Gamma/2\pi)$. Thus, with $\alpha = 1.5$, the vortex lifespan
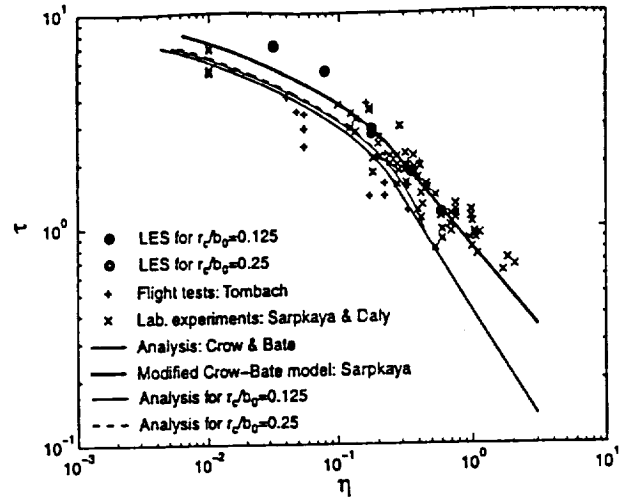


Fig. 8 Dimensionless vortex lifespans from numerical simulations, laboratory experiments, and flight tests.

for weak turbulence when $b_0 = 16$ m is approximated by

$$\eta = 0.97\tau^{\frac{1}{4}}e^{-0.82\tau} \qquad (21)$$

and when $b_0 = 8$ m is approximated by

$$\eta = 0.95\tau^{\frac{1}{4}}e^{-0.80\tau} \qquad (22)$$

For strong turbulence, Eq. (17) is used, and the vortex lifespan is independent of the ratio of $r_c$ and $b_0$.

As shown in Fig. 8, the difference of two curves is very small. In addition, the difference in lifespan between Eqs. (21) and (22) and the modified function of CB,[15] that is, Eq. (20), is also very small. For example, the dimensionless lifespan of the case of $b_0 = 8$ m at $\eta = 0.1$ is only about 2% larger than that of the case of $b_0 = 16$ m, and only about 4% smaller than that of the modified CB function. Note that $r_c/b_0$ of the case of $b_0 = 8$ m is about 2.5 times larger than that used by CB. This implies that the CB vortex lifespan expression is insensitive to the core radius for a fixed vortex separation.

To determine the lifespan in our simulations, we apply a simple equation formulated by Crow and Murman[30] and CB,[15] that is,

$$B(t) = \frac{b_{\max}(t) - b_{\min}(t)}{b_{\max}(t) + b_{\min}(t)} \qquad (23)$$

where $b_{\max}(t)$ and $b_{\min}(t)$ are the maximum and minimum vortex separation distance, respectively, and are estimated in the present study by considering only the $y$ displacement. The normalized amplitude $B(t)$ is zero in the absence of perturbation and becomes unity when the vortices link. Based on the top views of the vortices, the lifespan in the present study is determined as the time when $B(t) = 0.85$.

Dimensionless vortex lifespans from a total of eight simulations for cases of both $b_0 = 16$ and 8 m (see Table 1) are shown in Fig. 8 with those from Sarpkaya and Daly's[7] water tank experiments and Tombach's[5] flight tests. Sarpkaya and Daly's[7] data are the ones for vortex linking or core bursting among the entire data, and not more than 10% of the linking or bursting data set are due to bursting (personal communication with Sarpkaya, 1997). Figure 8 reveals clearly that stronger ambient turbulence enhances the demise of the vortices. The lifespan from our LES is about 40% larger on average than the theoretical value of CB.[15] Despite large difference in $Re$ between the LES and the water tank experiment, the LES results agree surprisingly well with Sarpkaya and Daly's data[7] of which lower bound appears to be the theoretical curve of CB.[15] Although not shown in Fig. 8, Liu's[8] data also indicate that the theoretical curve underpredicts the lifespans, especially when the lifespans only due to vortex linking are considered. DNS results of Spalart and Wray[10] also show that the CB[15] curve underestimates the average lifespans of the simulations (about 20%). This agreement between numerical simulations and laboratory experiments is encouraging because

wind shear and stratification are absent in these studies, and thus, only ambient turbulence effects are taken into account. The average lifespan in Tombach's[5] data (Fig. 8) appears to agree roughly with the CB[15] curve, whereas some other flight tests, for example, see CB's Fig. 8, display larger lifespans compared with the theoretical CB curve, which is consistent with our results. Because atmospheric observations of the lifespans are influenced by various sources such as nonhomogeneous atmospheric turbulence, wind shear, and stratification, however, it is difficult to differentiate only the ambient turbulence effect on the vortex lifespan from the others.

On the other hand, the CB[15] curve for weak turbulence is basically obtained using the turbulence strength of the scales of eddies comparable to the MAW that is assumed to reside in the inertial subrange, as mentioned before. Because in the case of $b_0 = 16$ m those excitatory eddies are not within the inertial subrange due to the limited domain size and their strength is much weaker than the turbulence strength if these eddies are within the inertial subrange (Fig. 2), one may anticipate that the lifespan would become larger. However, the lifespans for the case of $b_0 = 8$ m, in which the scales of eddies comparable to the MAW are within the inertial subrange, appear to be nearly the same as those for the case of $b_0 = 16$ m [see Fig. 8; LES results (solid and open circles) for $\eta = 0.0316$ and 0.3506 appear to be almost completely overlapped], implying that the turbulence length scale effects on the vortex lifespan is not important. This is consistent with the results from water tank experiments[7,8] in which the lifespan of the vortices in a turbulent environment are also controlled primarily by the dimensionless turbulence intensity $\eta$.

Recently, Sarpkaya[31] has revised the CB[15] model to allow for the variation of the wave length and the integral length scale that are not considered in the original CB analysis. The resulting vortex lifespans in strong and weak turbulence are given by

$$\eta \tau^{\frac{4}{3}} = \frac{3}{4} \quad \text{for} \quad \tau < 2.5 \quad (24)$$

$$\eta = \tau^{\frac{1}{4}} e^{-0.70\tau} \quad \text{for} \quad \tau > 2.5 \quad (25)$$

In Eq. (24), the interaction of strong turbulence with the vortices has been also taken into account. As shown in Fig. 8, our LES data agree very closely with Sarpkaya's[31] modified model rather than CB's.[15]

The normalized amplitude $B(t)$ in Eq. (23) is plotted with time to see the growth of the amplitude during the instability development in quantitative form. A plot of $B(t)$ in semilogarithmic coordinates will display the exponential growth of the instability as a straight line. Figure 9 shows the growth of the amplitude for the cases of $b_0 = 16$ and 8 m. It reveals that the growth is significantly reduced in the middle range of dimensionless time from the fast growth at earlier times. The simulation with larger integral length scale of turbulence, that is, the case of $b_0 = 8$ m, shows faster growth of amplitude in the middle range of dimensionless time than the case with smaller integral length scale, that is, the case of $b_0 = 16$ m, but in later stages the two curves tend to converge, producing nearly the same lifespan. A plot of $B(t)$ from an atmospheric observation by CB displays exponential growth from 30 to about 90 s (see Fig. 3 in Ref. 15), but they did not plot $B(t)$ at earlier times, that is, from 0 to about 30 s, when the growth of amplitude may be much faster than that after 30 s (Fig. 9).

To estimate the magnitude of scatter in the vortex lifespan due to the statistical fluctuations of turbulence, the vortices were injected at different times with about one eddy turnover time interval but still in a statistically steady-state turbulence field. Because the external forcing requires a significant computational effort and has been shown to have a negligible effect on the vortex evolution, it is deactivated after the vortices are injected. The results combined with the lifespans from our LES of Fig. 8 are shown in Fig. 10. The maximum deviations of the simulation results are about 7, 14, and 20% of their averages for $\eta = 0.0316$, 0.1753, and 0.3506, respectively. This increasing scatter with increasing $\eta$ is consistent with Spalart and Wray's[10] DNS result in which the standard deviation of the simulation results increased to about 20% of the mean for small $\eta$ and to about 40% of the mean for large $\eta$ showing much larger scatter in lifespans compared with our LES results. There appears



$b_0 = 16$ m
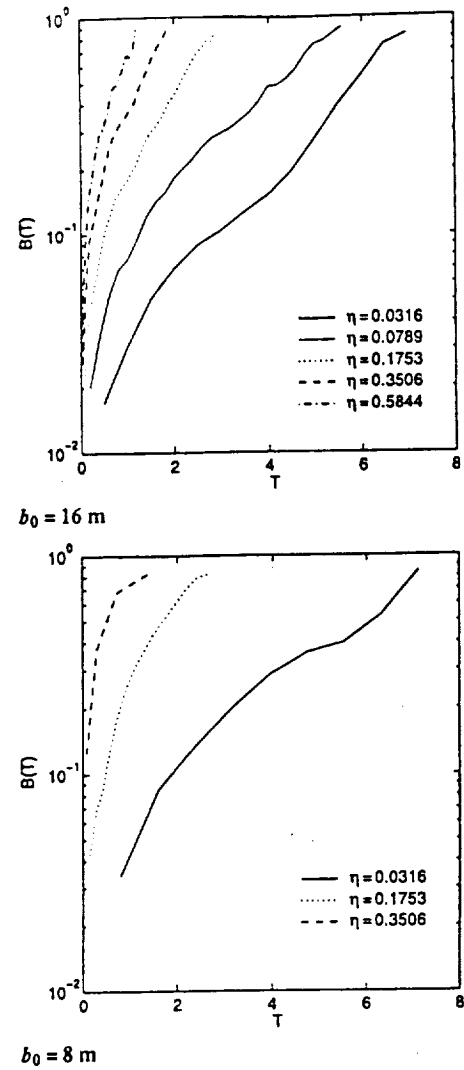


$b_0 = 8$ m

Fig. 9 Amplitude evolution of the instability with varying $\eta$ for the cases.
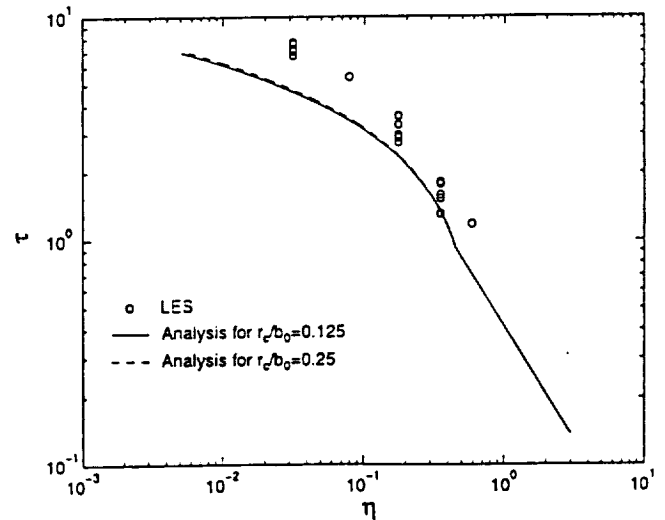


Fig. 10 Dimensionless vortex lifespans from numerical simulations; more lifespans for the case of $b_0 = 8$ m are obtained by injecting the vortices at varying time in a statistically steady-state turbulence with external forcing deactivated.

increasing Reynolds number. For example, the scatter of lifespans in laboratory experiments[7,8] appears to be somewhat larger than that in our simulations (Figs. 8 and 10), although Reynolds numbers in laboratory experiments are much lower than what is possible in the atmosphere. In addition, the Reynolds number in Spalart and Wray's DNS study[10] (about $1.7 \times 10^3$–$9 \times 10^3$) is an order of magnitude less than that in the water tank experiments of Sarpkaya and

in the DNS results is much larger than that in water tank experiments. However, a formal conclusion for this trend in the scatter of lifespans can be reached only by varying the Reynolds number over several DNSs. On the other hand, the larger scatter of lifespans in flight tests (Fig. 8, about a factor of 3 for fixed $\eta$) may result from other factors such as stratification, wind shear, and inhomogeneous atmospheric turbulence.

## IV. Conclusions

The effects of ambient atmospheric turbulence on aircraft wake vortices have been studied using a validated LES model. Our results reveal that the MAW of the Crow instability[3] and the lifetime of wake vortices are significantly influenced by ambient atmospheric turbulence. The following conclusions can be drawn from the results of numerical simulations.

1) The Crow instability[3] develops clearly at most atmospheric turbulence levels, but, in strong turbulence, the vortex pair deforms more irregularly due to turbulence advection.

2) The MAW of the instability decreases with increasing dimensionless ambient turbulence level, which are consistent with laboratory experiments[8] and atmospheric observations.[4]

3) Turbulence with smaller integral length scale ($b_0 = 16$ m), in which the theoretical MAW ($8.2b_0$) is not within the inertial subrange, leads to smaller MAW that is less than the theoretical value. On the other hand, turbulence with a larger integral length scale ($b_0 = 8$ m), in which the theoretical MAW ($6.9b_0$) is within the inertial subrange, leads to larger MAW.

4) Consistent with results of laboratory experiments,[7,8] vortex lifespan is primarily controlled by dimensionless turbulence intensity $\eta$ and decreases with increasing $\eta$, whereas the integral scale of turbulence is of minor importance to vortex lifespan.

5) The lifespan is estimated to be about 40% larger than that in the theoretical prediction by CB.[15] However, this larger lifespan agrees very well with the data from laboratory experiments and Sarpkaya's[31] modification to CB's theory.[15]

6) The maximum deviation in lifespan from the average value due to ambient turbulence alone is about 7% of the mean for small $\eta$ and about 20% of the mean for large $\eta$, showing much less scatter in lifespan compared with flight tests[5] and DNS.[10] There appears to be a possibility that the scatter in vortex lifespans decreases with increasing Reynolds number, although a formal conclusion can be reached only by varying Reynolds number over several DNSs. On the other hand, larger scatter of lifespans in flight tests may result from other factors, such as stratification, wind shear, and inhomogeneous ambient turbulence.

## Acknowledgments

## References

[1]Hinton, D. A., "Aircraft Vortex Spacing System (AVOSS) Conceptual Design," NASA TM-110184, 1995.

[2]Perry, R. B., Hinton, D. A., and Stuever, R. A., "NASA Wake Vortex Research for Aircraft Spacing," AIAA Paper 97-0057, Jan. 1997.

[3]Crow, S. C., "Stability Theory for a Pair of Trailing Vortices," AIAA Journal, Vol. 8, No. 12, 1970, pp. 2172–2179.

[4]Chevalier, H., "Flight Test Studies of the Formation and Dissipation of Trailing Vortices," Journal of Aircraft, Vol. 10, No. 1, 1973, pp. 14–18.

[5]Tombach, I., "Observations of Atmospheric Effects on Vortex Wake Behavior," Journal of Aircraft, Vol. 10, No. 11, 1973, pp. 641–647.

[6]Sarpkaya, T., "Trailing Vortices in Homogeneous and Density-Stratified Media," Journal of Fluid Mechanics, Vol. 136, 1983, pp. 85–109.

[7]Sarpkaya, T., and Daly, J. J., "Effect of Ambient Turbulence on Trailing Vortices," Journal of Aircraft, Vol. 24, No. 6, 1987, pp. 399–404.

[8]Liu, H.-T., "Effects of Ambient Turbulence on the Decay of a Trailing Vortex Wake," Journal of Aircraft, Vol. 29, No. 2, 1992, pp. 255–263.

[9]Lewellen, D. C., and Lewellen, W. S., "Large-Eddy Simulations of the Vortex-Pair Breakup in Aircraft Wakes," AIAA Journal, Vol. 34, No. 11, 1996, pp. 2337–2345.

[10]Spalart, P. R., and Wray, A. A., "Initiation of the Crow Instability by Atmospheric Turbulence," 78th AGARD-FDP Symposium on the Characterization and Modification of Wakes from Lifting Vehicles in Fluids, May 1996, pp. 18:1–18.

[11]Bisgood, P. L., "Some Observations of Condensation Trails," Royal Aeronautical Establishment, TM, FS-530, 1980.

[12]Donaldson, C. duP., and Bilanin, A. J., "Vortex Wakes of Conventional Aircraft," AGARDograph 204, May 1975.

[13]Greene, G. C., "An Approximate Model of Vortex Decay in the Atmosphere," Journal of Aircraft, Vol. 23, No. 7, 1986, pp. 566–573.

[14]Han, J., Lin, Y.-L., Schowalter, D. G., Arya, S. P., and Proctor, F. H., "Large-Eddy Simulation of Aircraft Wake Vortices: Atmospheric Turbulence Effects," 12th Symposium on Boundary Layers and Turbulence, 1997, pp. 237–238.

[15]Crow, S. C., and Bate, E. R., "Lifespan of Trailing Vortices on a Turbulent Atmosphere," Journal of Aircraft, Vol. 13, No. 7, 1976, pp. 476–482.

[16]Moeng, C.-H., "A Large Eddy Simulation Model for the Study of Planetary Boundary Layer Turbulence," Journal of Atmospheric Sciences, Vol. 41, No. 13, 1984, pp. 2052–2062.

[17]Mason, P. J., "Large Eddy Simulation of the Convective Boundary Layer," Journal of Atmospheric Sciences, Vol. 46, No. 11, 1989, pp. 1492–1516.

[18]Schmidt, H., and Schumann, U., "Coherent Structure of the Convective Boundary Layer Derived from Large Eddy Simulations," Journal of Fluid Mechanics, Vol. 200, 1989, pp. 212–248.

[19]Proctor, F. H., "The Terminal Area Simulations System, Volume 1: Theoretical Formulation," NASA CR 4046, DOT/FAA/PM-86/50, 1, 1987.

[20]Proctor, F. H., "Numerical Simulation of Wake Vortices Measured During the Idaho Fall and Memphis Field Programs," Proceedings of the AIAA 14th Applied Aerodynamics Conference, Pt. 2, AIAA, Reston, VA, 1996, pp. 943–960.

[21]Proctor, F. H., Hinton, D. A., Han, J., Schowalter, D. G., and Lin, Y.-L., "Two Dimensional Wake Vortex Simulations in the Atmosphere: Preliminary Sensitivity Studies," AIAA Paper 97-0056, Jan. 1997.

[22]Klemp, J. B., and Wilhelmson, R. B., "The Simulation of Three-Dimensional Convective Storm Dynamics," Journal of Atmospheric Sciences, Vol. 35, No. 6, 1978, pp. 1070–1096.

[23]Switzer, G. F., "Validation Tests of TASS for Application to 3-D Vortex Simulation," NASA CR 4756, 1996.

[24]Rosenhead, L., "The Spread of Vorticity in the Wake behind a Cylinder," Proceedings of the Royal Society of London, Series A: Mathematical and Physical Sciences, Vol. A127, 1930, pp. 590–612.

[25]Burnham, D. C., and Hallock, J. N., "Chicago Monostatic Acoustic Vortex Sensing System, Vol. 4: Wake Vortex Decay," National Technical Information Service, Springfield, VA, 1982.

[26]Vincent, A., and Meneguzzi, M., "The Spatial Structure and Statistical Properties of Homogeneous Turbulence," Journal of Fluid Mechanics, Vol. 225, 1991, pp. 1–20.

[27]Champagne, F. H., Friehe, C. A., LaRue, J. C., and Wyngaard, J. C., "Flux Measurements, Flux Estimation Techniques, and Fine-Scale Turbulence Measurements in the Unstable Surface Layer Over Land," Journal of Atmospheric Sciences, Vol. 34, No. 3, 1977, pp. 515–530.

[28]Jeong, J., and Hussain, F., "On the Identification of a Vortex," Journal of Fluid Mechanics, Vol. 285, 1995, pp. 69–94.

[29]Corjon, A., Risso, F., Stoessel, A., and Poinsot, T., "Three-Dimensional Direct Numerical Simulations of Wake Vortices: Atmospheric Turbulence Effects and Rebound with Crosswind," 78th AGARD-FDP Symposium on the Characterization and Modification of Wakes from Lifting Vehicles in Fluids, 1996, pp. 28:1–21.

[30]Crow, S. C., and Murman, E. M., "Trailing-Vortex Experiments at Moses Lake," Boeing Scientific Research Lab., Communication 009, The Boeing Co., Seattle, WA, Feb. 1970.

[31]Sarpkaya, T., "Decay of Wake Vortices of Large Aircraft," AIAA Journal, Vol. 36, No. 9, 1998, pp. 1671–1679.

S. K. Aggarwal
*Associate Editor*

# Appendix F: Numerical Study of Wake Vortex Decay and Descent in Homogeneous Atmospheric Turbulence

# Numerical Study of Wake Vortex Decay and Descent in Homogeneous Atmospheric Turbulence

Jongil Han,* Yuh-Lang Lin,† and S. Pal Arya‡
*North Carolina State University, Raleigh, North Carolina 27695-8208*
and
Fred H. Proctor§
*NASA Langley Research Center, Hampton, Virginia 23681-2199*

Numerical simulations are performed to isolate the effect of ambient turbulence on the wake vortex decay rate within a neutrally stratified atmosphere. Simulations are conducted for a range of turbulence intensities by injecting wake vortex pairs into an approximately homogeneous and isotropic turbulence field. Consistent with field observations, the decay rate of the vortex circulation increases clearly with increasing levels of ambient turbulence. Based on the results from the numerical simulations, simple decay models for the vortex pair are proposed as functions of nondimensional ambient turbulence intensity, nondimensional radial distance, and nondimensional time. For strong atmospheric turbulence, the model predictions are in reasonable agreement with the observational data. For weak turbulence with stable stratification, the model, based on turbulence dissipation alone, underestimates circulation decay with consistent overestimation of vortex descent, unless stratification effects are included.

## Nomenclature

$B$ = aircraft wingspan
$b_0$ = initial vortex separation distance, $\pi B/4$
$c_s$ = coefficient for filter width in the subgrid model, 0.16
$c_1, c_2$ = model coefficients for vortex decay, 0.13 and 0.08, respectively
$D$ = rate of velocity deformation
$d_1, d_2$ = model coefficients for vortex descent, 0.84 and 0.71, respectively
$F_{\beta\beta}$ = one-dimensional spectra
$H$ = nondimensional vortex descent distance, $h/b_0$
$h$ = vortex descent distance from initial vortex elevation
$I_1, I_2$ = isotropy parameters, $[\langle u^2 \rangle/\langle w^2 \rangle]^{1/2}$ and $[\langle v^2 \rangle/\langle w^2 \rangle]^{1/2}$, respectively
$K$ = subgrid eddy viscosity
$L_x, L_y, L_z$ = domain sizes in $x$, $y$, and $z$ directions, respectively
$L_{33}$ = integral length scale of turbulence in $z$ direction
$N$ = Brunt–Väisälä frequency
$q$ = turbulent velocity scale, $(\overline{u^2} + \overline{v^2} + \overline{w^2})^{1/2}$
$R$ = nondimensional radial distance from vortex center
$Re$ = circulation Reynolds number, $\Gamma/\nu$
$Ri_R$ = rotational Richardson number
$Ri_S$ = Richardson number due to stratification, $N^2/D^2$
$r$ = radial distance from vortex center
$r_c$ = initial core radius defined as radial distance of peak tangential velocity
$T$ = nondimensional time, $t V_0/b_0$
$t$ = time
$t_e$ = large-eddy turnover time, $L_{33}/\langle w^2 \rangle^{1/2}$
$u, v, w$ = velocities in $x$, $y$, and $z$ directions, respectively
$u'_n$ = fluctuation of velocity normal to the surface
$V$ = tangential velocity

$V_a$ = airspeed of generating aircraft
$V_0$ = initial vortex induction speed, $\Gamma_\infty/(2\pi b_0)$
$W$ = aircraft weight
$x, y, z$ = axial, lateral, and vertical space coordinate relative to initial vortex system
$\alpha$ = coefficient for $Ri_S$, 3.0
$\beta$ = coefficient for $Ri_R$, 1.5
$\Gamma$ = vortex circulation
$\Gamma_0$ = initial circulation
$\Gamma_\infty$ = initial circulation at $r \gg r_c$, $4W/(\pi B \rho V_a)$
$\Delta$ = filter width in the subgrid model, $(2\Delta x\, 2\Delta y\, 2\Delta z)^{1/3}$
$\Delta x, \Delta y, \Delta z$ = grid sizes in $x$, $y$, and $z$ directions, respectively
$\epsilon$ = turbulent kinetic energy dissipation rate
$\zeta$ = axial vorticity
$\zeta'$ = fluctuation of axial vorticity
$\eta$ = nondimensional ambient turbulence intensity, $(\epsilon b_0)^{1/3}/V_0$
$\Theta(z)$ = ambient potential temperature profile
$\kappa$ = wave number
$\Lambda$ = integral length scale of turbulence
$\nu$ = kinematic viscosity
$\nu_e$ = effective turbulent eddy viscosity
$\rho$ = air density
$\Omega$ = three-dimensional vorticity

## I.  Introduction

FOR the purpose of increasing airport capacity, a system is being developed under NASA's Terminal Area Productivity Program that will control aircraft spacing within the narrow approach corridors of airports. The system, called the Aircraft Vortex Spacing System,[1,2] will determine safe operating spacing between arriving and departing aircraft as based on the observed or predicted weather conditions. This system will provide a safe reduction in separation of aircraft compared to the now-existing flight rules, which are based on aircraft weight categories. To develop this system, research is being focused on understanding how aircraft wake vortices interact with the atmosphere. Previous studies indicate that transport and decay of wake vortices are strongly affected by ambient atmospheric parameters such as wind shear, stratification, and turbulence, as well as by proximity of aircraft to the ground.[3] In this study we focus on the effects of three-dimensional ambient atmospheric turbulence on vortex decay and descent using a validated large-eddy simulation (LES) model.

The mechanisms and causes for the decay of the wake vortices have been somewhat controversial.[4] Some researchers believe that vortices generally do not decay until three-dimensional instabilities such as Crow instability[5] lead to their sudden destruction.[6] However, this view is held in spite of the overwhelming observational evidence that vortices do decay at different rates depending on the ambient meteorological conditions.[3] and atmospheric turbulence plays a key role.[7,8] Recent analyses of field observation data by Sarpkaya[9] clearly show that vortex circulation decays much faster in the presence of strong turbulence than in weak turbulence. Using a second-order turbulence closure model. Bilanin et al.[10] show that the rate of decay of a vortex pair increases with increasing dissipation rate of background turbulence. From three-dimensional LES of wake vortices in a realistic atmospheric boundary layer, Corjon and Darracq[11] reveal that the vortices decay with time in a turbulent environment. Our analyses of LES data[3,12,13] also reveal that three-dimensional atmospheric turbulence enhances vortex decay. On the other hand, the descent speed of a vortex pair due to mutual induction decreases with decreasing circulation as long as the separation distance of a vortex pair remains constant. From the data obtained in their water tank experiments, Sarpkaya and Daly[14] find that the descent speed of vortices decreases with increasing dissipation rate of the ambient turbulence. This, in turn, implies that stronger turbulence yields larger reduction in circulation. Stable stratification [$\partial\Theta(z)/\partial z > 0$, where $\Theta(z)$ is the ambient potential temperature profile] can also hasten vortex decay through baroclinic generation of countersign vorticity along the vortex oval's periphery.[3,15,16] Because most of field observation data are subjected to the influence of both turbulence and stratification, it is difficult to distinguish each of their effects on circulation decay and vortex descent. In the present study, we consider only a neutrally stratified atmosphere, that is, $\partial\Theta(z)/\partial z = 0$, to isolate the effects of atmospheric turbulence on vortex decay. Our other ongoing investigations of wake vortex decay in nonneutral environments will be reported in a future paper.

The acceleration of vortex decay by ambient turbulence has been an important factor in several wake-vortex prediction models.[7,8] Donaldson and Bilanin[7] proposed a formula describing the relation between atmospheric turbulence and decay of vortex circulation:

$$\frac{d\Gamma}{dt} = -0.82\frac{q\Gamma}{b_0} \qquad (1)$$

Greene[8] incorporated Eq. (1) into his analytic model to account for the contribution of atmospheric turbulence effects on wake vortex motion and decay. Equation (1) implies that vortex circulation decays exponentially and depends only on ambient turbulence, represented by $q$, which is related to the turbulence kinetic energy (TKE $= q^2/2$). The TKE (or $q$) is primarily determined by the large energy-containing eddies. According to Eq. (1), large-scale eddies are involved in the decay of vortex circulation. Although large energy-containing eddies can lead to a large deformation and transport of vortices as well as to the development of the large-scale Crow instability.[3,17-19] it is the small-scale (order of $b_0$ and less) turbulent eddies that are directly associated with the decay of vortex circulation. These small scales of turbulent eddies are likely to be more homogeneous and isotropic and most often lie within the Kolmogorov inertial subrange that is characterized only by turbulent kinetic energy dissipation rate ($\epsilon$) (Ref. 20). Therefore, $\epsilon$ rather than $q$ is a more appropriate turbulence parameter for controlling the vortex decay.

In fact, $\epsilon$ has been commonly used in the literature[14,18,19,21,22] as an appropriate parameter to represent the effects of ambient turbulence on the lifespan of wake vortices. The strength of turbulence is often represented by the nondimensional turbulence intensity $\eta$ defined as

$$\eta = (\epsilon b_0)^{\frac{1}{3}}/V_0 \qquad (2)$$

where

$$V_0 = \Gamma_\chi/2\pi b_0 \qquad (3)$$

Note that $\eta$ is the ratio of the characteristic turbulent velocity scale at the scale of the vortex separation distance $(\epsilon b_0)^{1/3}$ to the initial descent speed of the vortex pair by mutual induction, $V_0$.

Our studies are focused on the far-field, postrollup stage of the vortex pair, in which each vortex possesses a well-developed structure. For later discussion, we define nondimensional parameters for time $t$, descent distance of the vortices, $h$, and radial distance $r$ as

$$T = V_0 t/b_0, \qquad H = h/b_0, \qquad R = r/b_0 \qquad (4)$$

In Sec. II. we describe the LES model and the modifications required for the initial conditions. In Sec. III. we present the results from systematic numerical experiments in terms of nondimensional turbulence intensity and also propose new vortex models for vortex decay and descent, based on the LES results. In Sec. IV, we apply the proposed models to available observation data. Finally, in Sec. V. we summarize our results and draw some conclusions.

## II.   Model and Initial Conditions

The model formulation and initial conditions must be chosen with great care when applied to the numerical simulation of wake vortices. Atmospheric wake vortices are three-dimensional, have very high Reynolds numbers, and are embedded within turbulent flow.[9] Hence, laminar simulations, especially at low Reynolds numbers, are inappropriate for studies of wake vortex decay. The numerical approximations assumed for wake vortex simulations should be stable, nondiffusive, and accurate, yet computationally efficient.

### A.   Model

The numerical model used in the present study is a three-dimensional, nonlinear, compressible LES model, called the terminal area simulation system[23] (TASS), which has been adopted for simulation of interaction of wake vortices with the atmosphere.[24-26] The TASS model contains 12 prognostic equations: 3 for momentum, 1 each for pressure deviation and potential temperature, 6 coupled equations for continuity of water substance (water vapor, cloud droplet, cloud ice crystals, rain, snow, and hail), and 1 for a massless tracer. In the present study, we use only four equations for momentum and pressure deviation because we assume statically neutral, dry atmosphere.

The TASS model uses the time-splitting integration procedure (small time step for acoustically active terms and large time step for advection and diffusion[27]) that results in a substantial savings in computing time. Local time derivatives (both small and large time steps) are approximated by the second-order Adams–Bashforth method. Space derivatives are approximated by central differences in quadratic-conservative form, which are fourth-order for advective derivatives and second-order for remaining derivatives. Details of the numerical formulation can be found by Proctor.[23,24] The numerical schemes used in TASS produce accurate and stable results and have been shown to have almost no numerical dissipation.[28] In Ref. 3 for a two-dimensional laminar simulation result with a very small constant viscosity ($Re \equiv \Gamma/\nu \sim 10^6$), it was shown that the tangential velocity does not change with time from the initial profile, indicating that TASS is essentially free of numerical dissipation.

Turbulence is strongly affected by the rotation of the swirling vortex flow. According to Rayleigh's well-known stability criterion,[29] perturbations are suppressed in an axisymmetric vortex if the circulation is increasing with radial distance, but perturbations would become unstable if the circulation is decreasing with radial distance. Because the circulation increases rapidly with radial distance in the vortex core region, any preexisting turbulence is suppressed there, and the vortex core (defined as the radius of maximum tangential velocity) expands very little with time.[9,16] In the present numerical model, an expression for the subgrid eddy viscosity that accounts for the flow rotation effects is used to avoid unrealistic core growth as described subsequently.

For subgrid turbulence. TASS currently uses a conventional Smagorinsky model[30] with modifications for stratification effects as

$$K = (c_s \Delta)^2 |D|(1 - \alpha Ri_S)^{0.5} \qquad (5)$$

Note that $Ri_S$ is included here, although it has no contribution because stratification is not considered in the present study.

A simple modification of the subgrid eddy viscosity for the effects of flow rotation has been developed in Ref. 31 following the suggestion by Rubinstein and Zhou.[32] In this formulation, rotation

acts to suppress subgrid turbulence, in a way that is analogous to the effects from stratification, and is given as

$$K = (c_s\Delta)^2|D|(1 - \alpha\,Ri_S - \beta\,Ri_R)^{0.5} \qquad (6)$$

Here rotational Richardson number $Ri_R$ is defined as

$$Ri_R = \Omega^2/D^2 + |\Omega|/|D| \qquad (7)$$

Equations (6) and (7) indicate that the eddy viscosity $K$ can be effectively reduced within the core of vortices due to large $|\Omega|/|D|$. Because the preceding formula cannot discriminate between shear flow and flow with coherent rotation, a discriminator function is applied that turns the formula off (defaulting to the original Smagorinsky model) in the absence of coherent rotation. Details of this formula may also be found in Ref. 31. The coefficient for $\beta$ is chosen empirically, with a value of 1.5. This value for $\beta$ was chosen large enough to suppress mixing across the vortex core and is assumed to be universal for all situations. This formulation, with $\beta = 1.5$, was also applied to a three-dimensional LES simulation of homogeneous turbulence with no detectable corruption of the energy spectrum. One of the beneficial consequences of the formulation is to prevent the vortex core from growing with time, as verified from field measurements.[9] In experiments with the unmodified Smagorinsky model [Eq. (5)], the vortex core was found to unrealistically expand with time.[33]

Periodic boundary conditions are imposed at all domain boundaries. The domain size used in our simulations is $(L_x, L_y, L_z) = (2.5b_0, 5b_0, 5b_0) = (80\Delta x, 160\Delta y, 160\Delta z)$, where $b_0 = 32$ m, the grid size $\Delta x = \Delta y = \Delta z = 1$ m, $x$, $y$, and $z$ correspond to the axial, lateral, and vertical directions of the vortex system, and the corresponding velocity components are $u$, $v$, and $w$, respectively. The smaller domain size in the axial direction, $2.5b_0$, which can save much computing time, suppresses the development of Crow instability of which the theoretical maximum wavelength is about $8.6b_0$ (Ref. 5), and thus, statistically homogeneous decay behavior is anticipated along the axial direction. The domain size of $5b_0$ in the lateral and vertical directions is sufficiently large to minimize boundary influences. Comparison with a test case assuming a larger domain width showed little difference, indicating that $5b_0$ width was sufficiently large for this experiment. Because of our limited computing resources and to allow the core to be resolved, the initial core size ($r_c = 4$ m) is somewhat larger than the typical value observed behind aircraft (less than about 5% of the wingspan[24]). Obviously, with the importation of a fully periodic condition, any effect from the ground is omitted from these simulations; thus, the results are applicable to the free atmosphere only.

## B. Initial Conditions

Because we want to study the effect of ambient turbulence on the vortex decay and descent within the free atmosphere, it is of crucial importance to obtain an initially homogeneous and isotropic turbulence field. Toward this purpose, the initial turbulence field is allowed to develop under an artificial external forcing at low wave numbers.[34] Because the TASS code uses a finite difference numerical scheme, the forcing is achieved by performing first a three-dimensional fast Fourier transform (FFT) at every large time step and then adding a constant amplitude to all of the modes with integer wave numbers whose magnitude is less than 3.0, and performing finally an inverse FFT back to the physical space. The wave number in the axial direction is normalized so that the axial wavelength has the same magnitude as that of the corresponding waves in lateral or vertical direction. Because of viscous dissipation, the simulation can reach a statistically steady state in the sense that the mean turbulence kinetic energy oscillates in time around a constant value.

Figure 1 shows the vertical velocity field and its one-dimensional longitudinal and transverse spectrum with $-\frac{5}{3}$ slope of Kolmogorov's spectrum when the turbulent flowfield reaches a statistically steady state. The calculated integral length scale is $L_{33} \approx 11.4$ m and the large-eddy turnover time, defined as $t_e = L_{33}/\langle w^2\rangle^{1/2}$, is estimated to be about 51.6 s. Here subscript 3 denotes the vertical direction and $\langle\,\rangle$ represents the domain average value. The isotropy parameter $I$, defined as $I_1 = [\langle u^2\rangle/\langle w^2\rangle]^{1/2}$
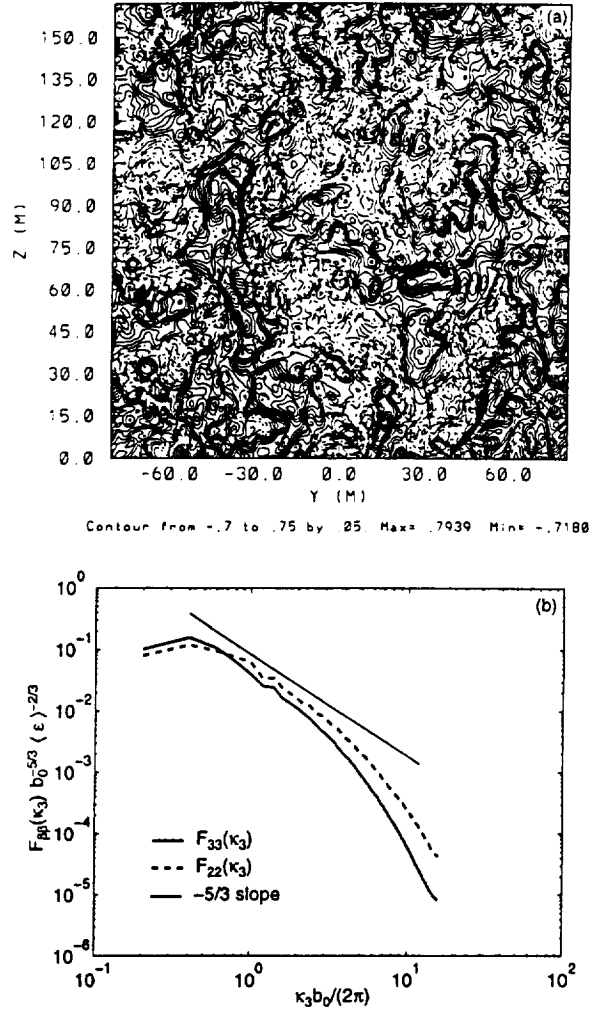


Fig. 1 Steady-state turbulence before vortex injection: a) vertical velocity field and b) its one-dimensional energy spectrum.

Contour from -.7 to .75 by .25 Max= .7939 Min= -.7188

or $I_2 = [\langle v^2\rangle/\langle w^2\rangle]^{1/2}$, fluctuates only a few percent around its expected value of one for isotropic turbulence. Therefore, our simulated turbulence is close to statistical isotropy. The TKE dissipation rate $\epsilon$ is estimated by fitting Kolmogorov's theoretical spectrum in the inertial subrange to the simulated spectra in Fig. 1.

The initial vortex system is representative of the postrollup, wake-vortex velocity field. A vortex model recently developed by Proctor[3] is adopted in our experiments. This model is empirical because it is based on field observations of several wake vortices measured early in their evolution. Its tangential velocity $V$ is represented as

$$V(r) = (\Gamma_\infty/2\pi r)\{1 - \exp[-10(r/B)^{0.75}]\} \qquad (8)$$

Note that the velocity field in Eq. (8) depends on the wingspan $B$ instead of the core radius $r_c$, which is not easy to accurately measure in field studies. Equation (8) is applicable only at $r > r_c$. For $r < r_c$, the model is matched with the Lamb model,[35] that is,

$$V(r) = (\Gamma_\infty/2\pi r)1.4\{1 - \exp[-10(r_c/B)^{0.75}]\}$$

$$\times\{1 - \exp[-1.2527\,(r/r_c)^2]\} \qquad (9)$$

The values assumed for initial vortex separation and circulation are derived from aircraft weight $W$, wingspan $B$, air density $\rho$, and airspeed $V_a$ according to the conventional assumption of an elliptically loaded wing, that is,

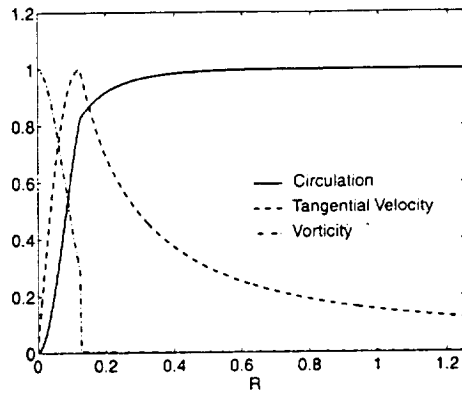$$b_0 = \pi B/4, \qquad \Gamma_\infty = 4W/\pi B\rho V_a$$

Fig. 2 Initial circulation, tangential velocity, and vorticity for each vortex normalized by their maximum values.

Normalized circulation, tangential velocity, and vorticity from the preceding model are shown in Fig. 2 as functions of the normalized radial distance $R = r/b_0$, assuming $r_c/b_0 = 0.125$.

A two-dimensional counter-rotating vortex pair following Eqs. (8) and (9) is initialized uniformly along the axial direction at the time when the ambient turbulence reaches a steady state after integration. To keep the vortices in the middle of the domain, the grid is allowed to translate downward at the speed of $0.9V_0$. Different values of nondimensional ambient turbulence strength $\eta$ are obtained by varying the initial circulation $\Gamma_\infty$ rather than by varying the initial turbulence field, that is, by varying $\epsilon$, to save computing time. Simulations are conducted with dimensional quantities, although the results are presented in nondimensional forms to make them more generally applicable and independent of individual dimensional variables. Assuming that $\Gamma_\infty = 400$ m$^2$ s$^{-1}$ and $b_0 = 40$ m, which are appropriate for large jet aircraft such as the DC-10, the range of values of $\eta$ in the lower atmosphere is estimated to be 0.01–0.5, with the maximum value occurring during early afternoon convective conditions and the minimum value during very stable conditions after midnight.[3] Simulations are conducted for six values of $\eta$, which are within the given range. These cases are divided into three turbulence strength groups: $\eta = 0.0302$ and $0.0702$ for weak turbulence, $\eta = 0.1006$ and $0.1509$ for moderate turbulence, and $\eta = 0.3018$ and $0.5031$ for strong turbulence. Generally, weak may represent the strength of typical boundary-layer turbulence during stable nighttime conditions and strong may represent typical strength during sunny daytime convective conditions. The simulated turbulence strengths represent a wide range of typical atmospheric conditions and aircraft sizes (note that $\eta$ also depends on aircraft wingspan and the far-field circulation of its vortices). To isolate the effect of atmospheric turbulence on vortex decay from that of thermal stratification, all simulations assume neutral stratification.

## III.  Numerical Results

Simulation results for six values of $\eta$ are presented. External forcing for maintaining ambient turbulence strength is deactivated to save computing time when the initial vortices are injected, but the difference in the results for maintaining or deactivating the forcing has been found to be negligible (not shown). This confirms the arguments by Corjon et al.[36] that the timescale of the ambient turbulence compared to that of the vortex is sufficiently large to obtain the main characteristics of the effects of ambient turbulence on the wake vortices.

During simulations, the vortices descend smoothly without any development of large-scale instabilities. As mentioned earlier, the Crow instability cannot occur in these simulations due to the small domain size in the axial direction.

The circulation at any radial distance $r$ can be easily determined from the area integral of the axial vorticity $\zeta$ over a region defined by the radial distance, that is,

$$\Gamma_r = \iint \zeta \, dA \qquad (10)$$

Table 1  Standard deviation of the circulation $\sigma_\Gamma$ (%) relative to its mean value at the end of simulation time

| $\eta$ | $T$ | $\sigma_\Gamma$ at $3r_c$ | $\sigma_\Gamma$ at $4r_c$ | $\sigma_\Gamma$ at $5r_c$ |
|---|---|---|---|---|
| 0.0302 | 7 | 2.8 | 2.0 | 2.1 |
| 0.0702 | 6 | 3.8 | 4.1 | 4.3 |
| 0.1006 | 6 | 3.5 | 4.5 | 4.6 |
| 0.1509 | 6 | 6.6 | 9.0 | 9.9 |
| 0.3018 | 3 | 10.1 | 9.6 | 8.5 |
| 0.5031 | 3 | 31.4 | 28.2 | 23.1 |

Obtained at a fixed radial distance are a total of 160 circulation values for a pair of vortices in 80 $y$–$z$ planes from which we have calculated averages and standard deviations. As shown in Table 1, the circulation fluctuations due to ambient turbulence increase with increasing turbulence level. The standard deviations appear to be small for most of turbulence levels (less than 10%) at least at the end of the simulation time, except for the strongest turbulence strength of $\eta = 0.5031$ for which the values are more than 20%. In the following, we consider only the average of circulations to deduce an appropriate model for vortex decay and descent.

### A.  Circulation Decay

Figure 3 shows the decay of circulation with time for varying radial distances, as well as varying ambient turbulence levels. As shown in Fig. 3, the decay rate of circulation increases clearly with increasing ambient turbulence level and appears to decrease with increasing radial distance, which is consistent with field observations.[9]

To investigate the vortex decay behavior in more detail for varying radial distances, the circulation evolution with a best-fitted function for each radial distance is plotted in Fig. 4 for relatively weak turbulence ($\eta = 0.0702$), in Fig. 5 for relatively moderate turbulence ($\eta = 0.1509$), and in Fig. 6 for strong turbulence ($\eta = 0.5031$). As evidenced in Figs. 4–6, the decay of the circulation appears to follow a Gaussian function $e^{-aT^2}$ for weak and moderate turbulence (model G), whereas for strong turbulence, it appears to follow an exponential function $e^{-bT}$ at smaller radial distances (model E) but a Gaussian function at larger radial distances, where $a$ and $b$ are functions of $\eta$ and radial distance. Although only partly shown in Figs. 4–6, the circulation at radial distances larger than $0.6b_0$ appears to follow the Gaussian decay for all levels of turbulence. An exponential decay formula [Eq. (1)] was first proposed by Donaldson and Bilanin,[7] with $q$ rather than $\epsilon$ as the turbulence parameter controlling the vortex decay. The Gaussian decay implies slower decay than the exponential decay during early evolution of the vortices. Based on our described LES results, two types of models (models E and G) are proposed for vortex decay and their formulations are given in the Appendix.

From the Appendix, Eqs. (A13) and (A17) can be rewritten in the nondimensional forms for model E as

$$\left.\frac{d\Gamma}{dT}\right|_{turbulence} = -c_1 \frac{\eta}{R^2} \Gamma \qquad (11)$$

and for model G as

$$\left.\frac{d\Gamma}{dT}\right|_{turbulence} = -2c_2 \frac{\eta^2 T}{R^2} \Gamma \qquad (12)$$

where $c_1$ and $c_2$ are empirical constants. Further integrations of Eqs. (11) and (12) with respect to nondimensional time (assuming ambient turbulence is only the process affecting vortex decay) yields for model E

$$\Gamma = \Gamma_0 \exp\left[-(c_1 \eta/R^2)T\right] \qquad (13)$$

and yields for model G

$$\Gamma = \Gamma_0 \exp\left[-(c_2 \eta^2/R^2)T^2\right] \qquad (14)$$

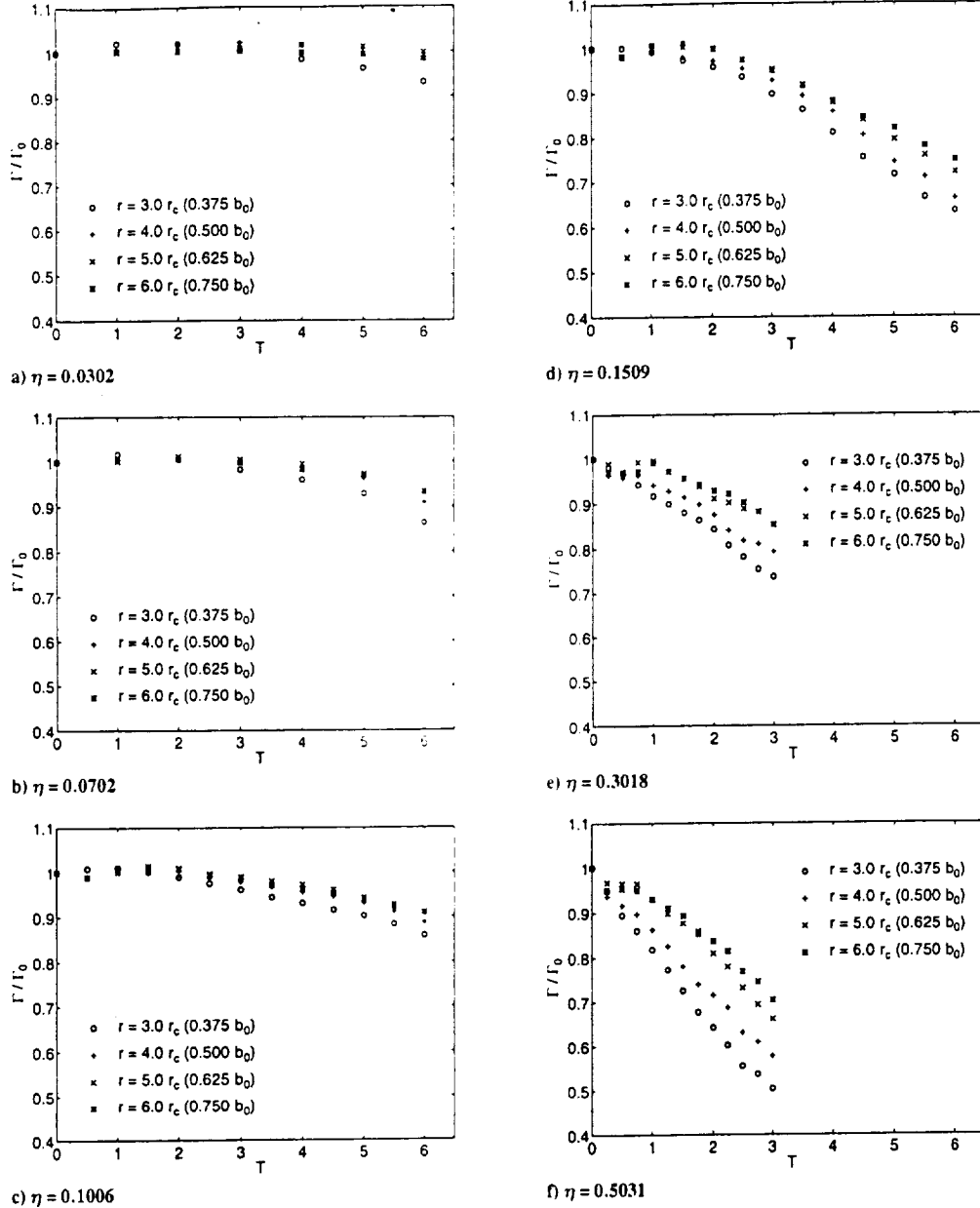(It is assumed that $\eta$ does not change with time.)

Fig. 3   Decay of circulation with time for varying radial distances and ambient turbulence strengths.

In a transition range from moderate to strong ambient turbulence levels, which is about $\eta = 0.25-0.30$ in the present study, the decay behavior of the vortices appears to be more complicated due to the dependency of the model types on radial distances. For example, in this range of $\eta$, the vortex decay follows model E in a smaller range of radial distances, whereas it follows model G in a larger range of radial distances: The range of radial distances for the applicability of model E increases with increasing ambient turbulence level but may not be a linear function of $\eta$. For a practical purpose, nevertheless, we propose a simple model in the transition range that is a composite of models E and G weighted linearly with varying $\eta$ $(0.25 < \eta < 0.30)$ as

$$\Gamma = [(\eta - \eta_1)/\Delta\eta]\Gamma_E + [(\eta_2 - \eta)/\Delta\eta]\Gamma_G \qquad (15)$$

where $\eta_1$ and $\eta_2$ are lower and upper limits of the transition range, $\Delta\eta = \eta_2 - \eta_1$, and $\Gamma_E$ and $\Gamma_G$ are the circulations given by Eqs. (13) and (14), respectively.

Previous investigators have quantified the strength of a vortex in terms of a parameter called average circulation that is defined as[24,37]

$$\bar{\Gamma}_{r_1,r_2} = \frac{1}{r_2 - r_1}\int_{r_1}^{r_2} \Gamma \, dr \qquad (16)$$

where $r_1$ and $r_2$ are the radial distances of the averaging interval. This parameter is desirable because it relates to the rolling moment of an encountering aircraft and provides a more stable measurement than the local circulation.[24,37] In particular, the average circulation within 15 m from the vortex center has been considered to be closely related to the hazard.[38,39] In the present study, we consider the average circulation from $R = 0.4$ to 0.6 because the circulation decay in this range of radial distances is not very sensitive to grid resolution. The average circulation in the following represents the circulation averaged over the range of $R = 0.4-0.6$ according to Eq. (16) unless stated otherwise.
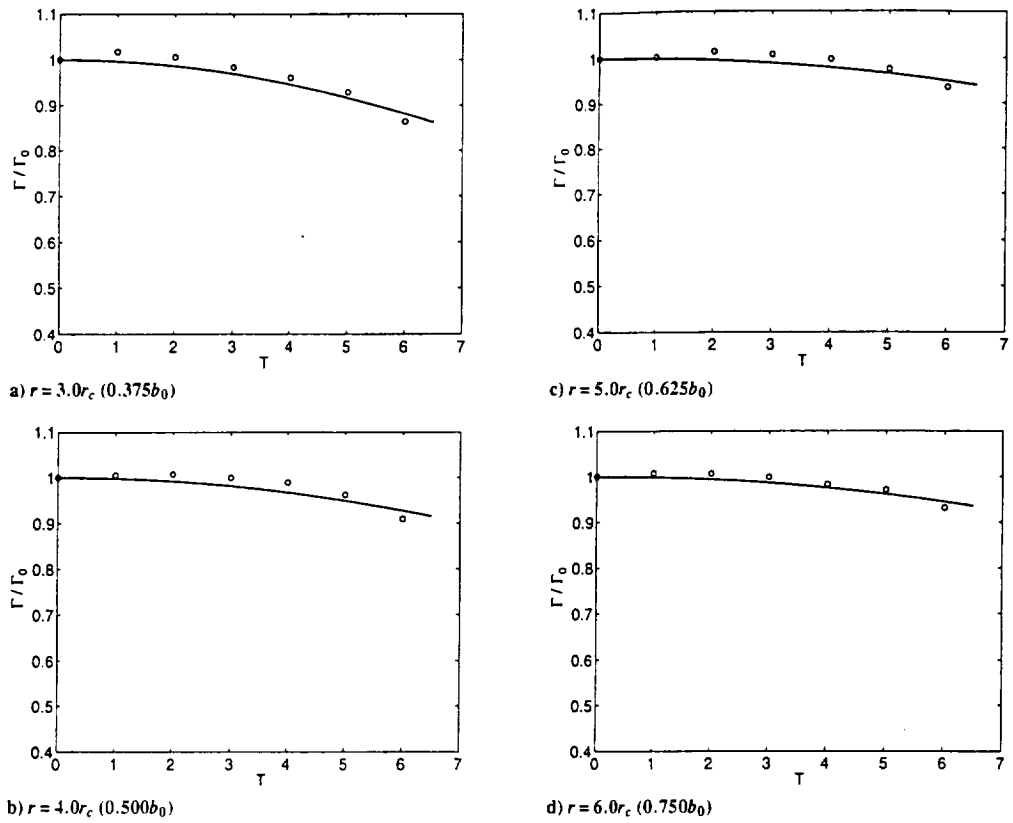
**Fig. 4** Circulation decay and best-fitted functions at four different radial distances for $\eta = 0.0702$ (weak turbulence): solid line indicates $e^{-aT^2}$, where $a$ is a function of $\eta$ and $R$.
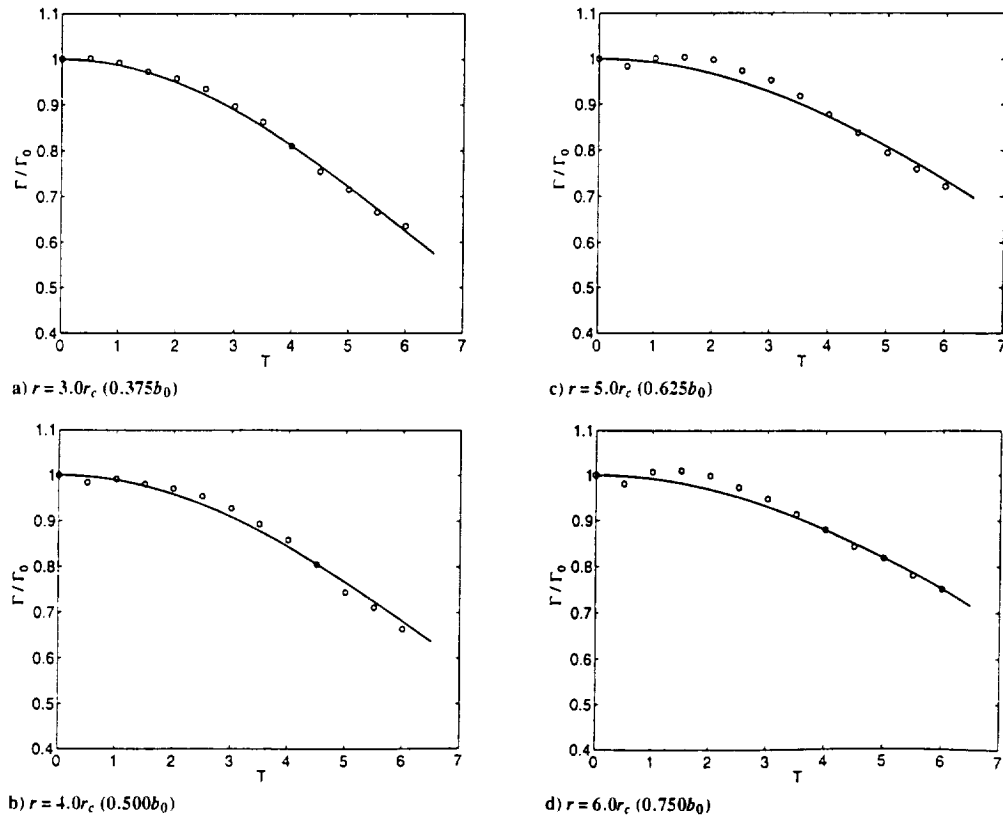


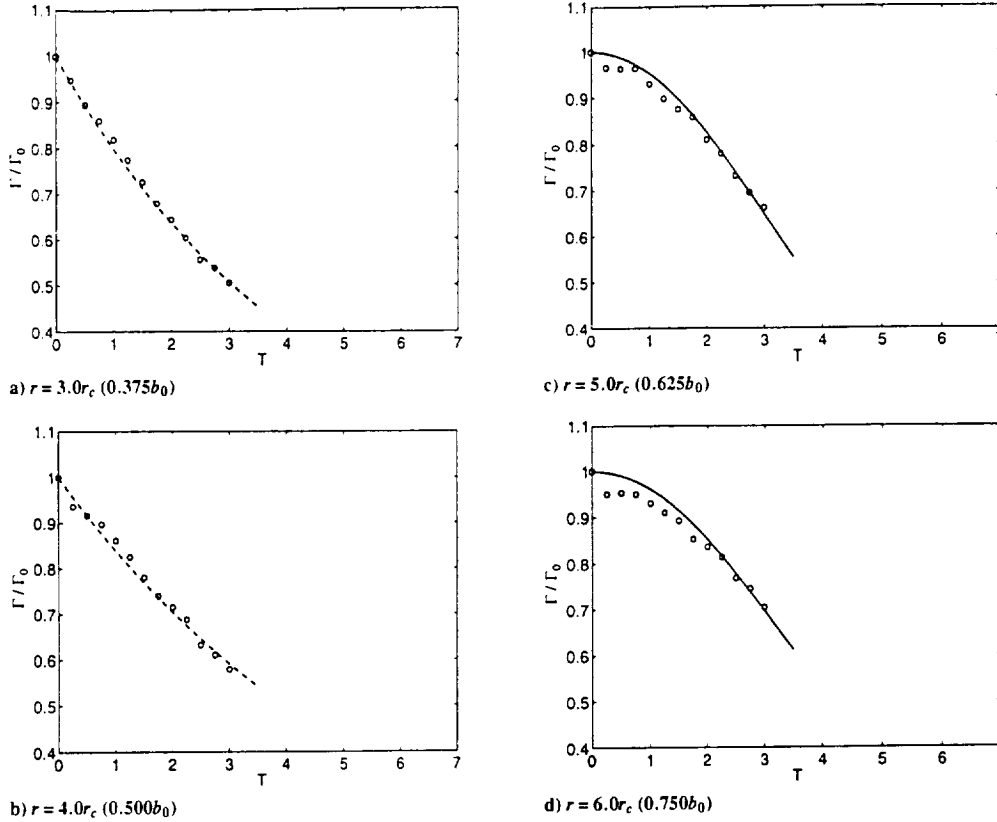Fig. 5    Same as Fig. 4 but for $\eta = 0.1509$ (moderate turbulence).

**Fig. 6** Same as Fig. 4 but for $\eta = 0.5031$ (strong turbulence): dashed line indicates $e^{-bT}$, where $b$ is a function of $\eta$ and $R$.

As can be seen from Fig. 7, the average circulations from the model predictions, that is, Eqs. (13) and (14), agree much better with the LES data than the local circulations, showing a Gaussian decay for weak and moderate turbulence but an exponential decay for strong turbulence. The model coefficients represented in Fig. 8 are obtained from the average circulation and do not appear to fluctuate significantly with varying $\eta$ in spite of the highly irregular nature of turbulence. To obtain a representative model coefficient, more experiments have been performed for different $\eta$ values and for different initial turbulence fields. The values of coefficients (Fig. 8) fluctuate with varying $\eta$ within the ranges of $c_1 = 0.06$–$0.09$ and $c_2 = 0.08$–$0.20$, respectively. The mean values of the coefficients, which can be considered as more representative, are $c_1 = 0.08$ for model E and $c_2 = 0.13$ for model G, respectively.

Using the given mean values of the coefficients, our model predictions at $R = 0.5$ for various ambient turbulence levels are plotted in Fig. 9. Crow instability is a well-known phenomenon in which the vortex pair undergoes a symmetric and sinusoidal instability that grows exponentially and finally results in a linking (merging) into a series of crude vortex rings. The vortex lifespans shown in Fig. 9, defined as the time at which linking of a vortex pair occurs as a result of the Crow instability, are obtained from a model recently developed by Sarpkaya,[9] where the linking time is given as only a function of $\eta$. This model is a revised one from the original Crow and Bate's[21] model and has been shown to agree well with data from water tank experiments[14] and LES predictions.[19] Figure 9 indicates that, until a linking of the vortices occurs, the circulation is reduced by only about 2% of its initial value for weak ambient turbulence ($\eta = 0.03$), whereas it may be reduced by as much as 20% for strong ambient turbulence ($\eta = 0.50$).

### B. Vortex Descent

The descent of an ideal vortex pair, where vorticity is concentrated in two parallel lines, will follow the relation of $H = T$ in an inviscid fluid. In the numerical simulation, however, descent rate of a pair of

the vortices can deviate from $H/T = 1$ due to the influence of image vortices implicit on the assumption of periodic boundary conditions and the use of a vortex model different from ideal line vortices. From a two-dimensional laminar simulation with the same domain size as the cross plane size of the preceding three-dimensional simulation and with a very small constant viscosity ($Re \sim 10^7$), the descent rate intrinsic in the present domain size and vortex model appears to be $H/T = 0.98$, slightly less than ideal one.

To develop a model for vortex descent due to ambient turbulence, we first assume that the vortex descent rate is proportional to the circulation, that is,

$$\frac{dh}{dt} \sim \frac{\Gamma}{2\pi b_0} \tag{17}$$

or in the nondimensional form

$$\frac{dH}{dT} \sim \frac{\Gamma}{\Gamma_\infty} \tag{18}$$

For weak and moderate turbulence, the circulation is expected to decay as a Gaussian function, as discussed in the preceding section. Thus, substituting Eq. (14) into Eq. (18), we obtain

$$\frac{dH}{dT} \sim \exp\left[-(d_1\eta T)^2\right] \tag{19}$$

where $d_1$ is an empirical coefficient. After integration, we finally obtain

$$H = (0.87/d_1\eta)\,\mathrm{erf}(d_1\eta T) \tag{20}$$

where erf is an error function and the proportionality constant 0.87 is an optimal value determined from our LES results. The preceding model for vortex descent has been applied to our LES results for weak and moderate turbulence. As shown in Figs. 10a–10d,
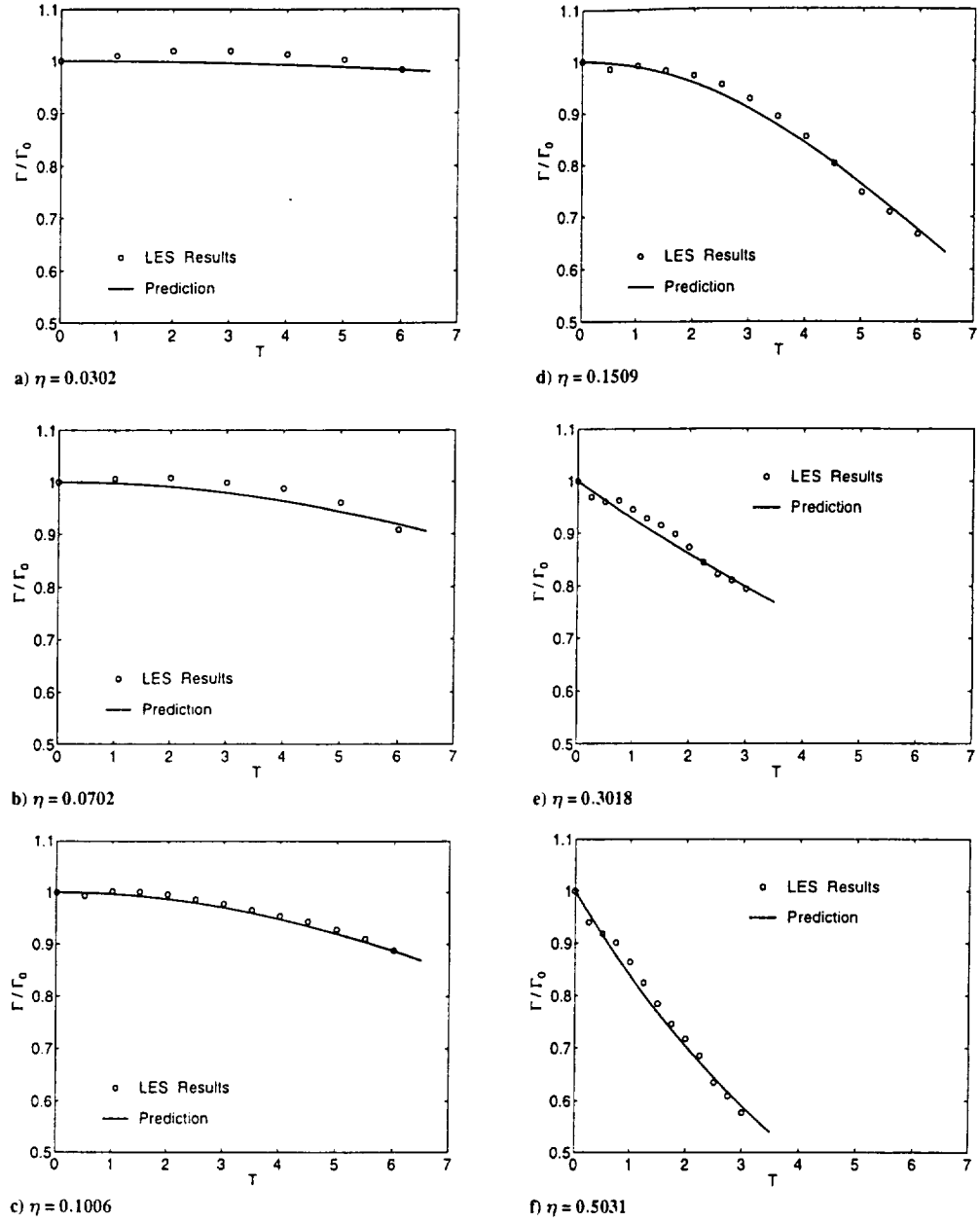
.

**Fig. 7** Evolution of the circulation averaged from $R = 0.4$ to 0.6 and corresponding model prediction with the coefficient adjusted for a best fit.

the model predictions agree well with the LES data, although the best-fitted coefficient $d_1$ appears to fluctuate with varying $\eta$ (Fig. 11).

For strong turbulence, however, an optimal value for $d_1$ could not be found. This may be because, for strong turbulence, the circulation decays exponentially over radial distances less than about $0.6b_0$, implying that circulations at smaller radial distances than $R = 0.6$ may also play significant role on the descent rate. Nevertheless, the modified form of Eq. (20)

$$H = (d_2/0.28\eta)\,\mathrm{erf}(0.28\eta T) \tag{21}$$

where $d_2$ is an empirical coefficient less than 0.87, can be matched with our LES results, as shown in Figs. 10e and 10f.

In the transition range from moderate to strong ambient turbulence levels, a simple model for $0.25 < \eta < 0.30$, similar to that for vortex decay, can be proposed:

$$H = [(\eta - \eta_1)/\Delta\eta]H_E + [(\eta_2 - \eta)/\Delta\eta]H_G \tag{22}$$

where $H_E$ and $H_G$ are the nondimensional vortex descent distance given by Eqs. (21) and (20), respectively.

The model coefficients $d_1$ and $d_2$ have been estimated the various LES cases covering a wide range of $\eta$ values and are shown in Fig. 11. The variations around their mean values of $d_1 = 0.84$ and $d_2 = 0.71$ are less than 20%.

Using the given mean values of the coefficients, the model predictions for the vortex descent for various ambient turbulence levels are plotted in Fig. 12 with the vortex lifespans obtained from Sarpkaya's[9] model. Figure 12 shows clearly that the descent rate of the vortices decreases with increasing ambient turbulence due to the increasing rate of decay of circulation with increasing ambient turbulence. On the other hand, for weak turbulence, the descent distance appears to closely follow the line $H = 0.98T$ before the vortex linking occurs.
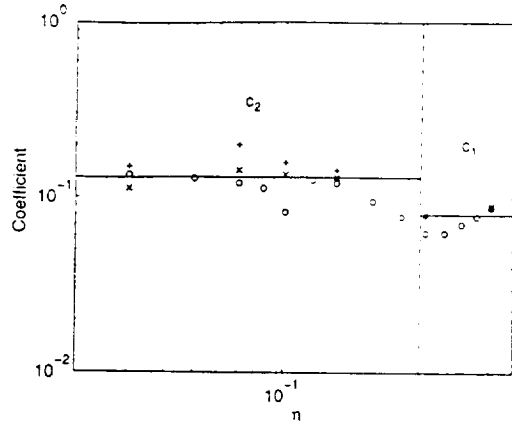
Fig. 8  Model coefficients with varying $\eta$ for the circulation decay in Eqs. (13) and (14) as obtained from numerical simulations; same symbols represent the results from same initial turbulence fields; solid lines indicate the average values of the coefficients for the Gaussian and exponential models distinguished by dashed line.
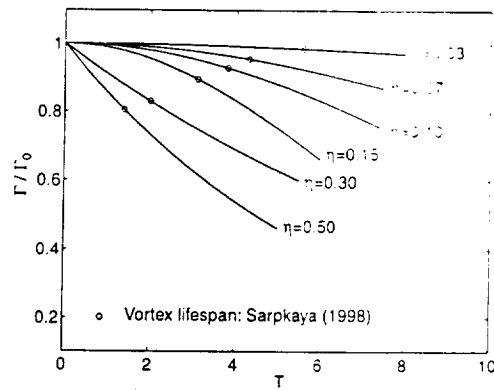


Fig. 9  Model prediction with varying $\eta$ for the circulation at $R = 0.5$ with vortex lifespan presented.

Table 2   Initial parameters for wake vortices for the flights analyzed

| Flight number | Aircraft type | $b_0$, m | $\Gamma_\infty$, $m^2 s^{-1}$ | Aircraft altitude, m | Atmospheric stability (observing time) |
|---|---|---|---|---|---|
| M-1252 | B-757 | 29.8 | 323 | 160.2 | Stable (midnight) |
| M-1273 | DC-10 | 39.6 | 416 | 149.9 | Stable (midnight) |
| M-1569 | DC-9 | 22.4 | 241 | 127.5 | Neutral (evening) |
| M-1573 | DC-9 | 22.4 | 245 | 103.8 | Neutral (evening) |
| M-1581 | B-757 | 29.8 | 297 | 166.1 | Unstable (noon) |
| M-1584 | DC-9 | 22.4 | 231 | 125.7 | Unstable (noon) |

Table 3   Turbulence energy dissipation rate[a]

| Flight number | $\epsilon$, $m^2 s^{-3}$ | $\eta$ |
|---|---|---|
| M-1252 | $0.212 \times 10^{-5}$ | 0.023 |
| M-1273 | $0.150 \times 10^{-6}$ | 0.012 |
| M-1569 | $0.584 \times 10^{-3}$ | 0.138 |
| M-1573 | $0.255 \times 10^{-3}$ | 0.103 |
| M-1581 | $0.302 \times 10^{-2}$ | 0.283 |
| M-1584 | $0.366 \times 10^{-2}$ | 0.265 |

[a]Measured at elevation of 40 m and corresponding nondimensional turbulence intensity

## IV.  Comparison of Observation Data and Model Predictions

In this section predictions of wake vortex decay and descent from the models proposed in the preceding sections are compared to observation from the Memphis Field Program.[40] As part of the NASA sponsored field program, Massachusetts Institute of Technology Lincoln Laboratory operated 10.6 $\mu$m $CO_2$ continuous wave laser Doppler radar [light detection and ranging (LIDAR)] and measured the line-of-sight velocities of the vortices in a plane perpendicular to the flight path of approaching or departing aircraft. Circulation values were estimated from the measured line-of-sight velocity field.[10]

In this study, six cases (Table 2) are chosen based on atmospheric stability conditions and number of data points. Some of the cases have been also analyzed by Sarpkaya[9] for a different purpose. The proposed models only address the effect of ambient turbulence on vortex decay and do not include the effect of thermal stratification. The initial conditions for the proposed models used the representative vortex separation and far-field circulation in Table 2, as well as the TKE dissipation rate $\epsilon$ measured at 40 m (Table 3). As seen from Table 3, the $\eta$ values calculated by the definition [Eq. (2)] are within the range of those used in our earlier LES.

Shown in Fig. 13 are the measured average circulations over the range of $R = 0.4$–0.6 with those from model predictions based on Eqs. (13) and (14) using the mean coefficients. The initial average circulation $\Gamma_0$ is determined from the present vortex model [Eq. (8)] with the theoretical circulation at $r \gg r_c$ ($\Gamma_\infty$) given in Table 2. The

data for times less than $T = 1$ have been discarded from the data set for all of the cases analyzed because the observed circulations at these times are subject to large trigonometry errors, for example, see Ref. 40.

As seen in Fig. 13, predictions by the proposed models appear to underestimate considerably the observations except for the stronger turbulence cases of M-1581 and M-1584 in which the model predictions appear to be in reasonable agreement with observations. The underestimation also appears to be larger with decreasing $\eta$. Significant differences in the rate of decay for the weaker turbulence cases between model predictions and observations may be caused by the following possibilities: 1) For the stable cases of M-1252 and M-1273, the interaction between the vortices and stable stratification, which is not included in the present numerical simulations, may enhance vortex decay as discussed in the Introduction. 2) There may be additional turbulence not taken into account in our simulations, such as self-generated internal turbulence that may originate with the vortices during the initial rollup process and may be confined only within the vortex oval. (The internal turbulence may be more effective on vortex decay for weaker ambient turbulence.) 3) There is uncertainty in measurement data especially for initial circulation $\Gamma_\infty$. (Note that the $\eta$ value and the rate of vortex decay in the observations are quite sensitive to the initial circulation.) 4) There is a discrepancy in the computation of the circulation between the numerical simulations and observations. (The circulation in the simulations is obtained directly by integrating the axial vorticity field, whereas the measured circulation is estimated from LIDAR line-of-sight velocities.)

For possibility 1, the effect of the stable stratification on vortex decay can be easily incorporated into Eqs. (11) or (12). According to Greene,[8] the rate of circulation decay due to the stable stratification is given by

$$\left. \frac{d\Gamma}{dt} \right|_{stratification} = -\frac{AN^2 h}{b_0} \qquad (23)$$

where $A$ is the wake oval area equal to $[\pi(1.73) \times (2.09)b_0^2]/4$. Because the ambient turbulence strength is generally weak in the stable atmosphere due to the suppression of ambient turbulence by stable stratification, for example see Table 2, Eq. (23) will be combined with model G [Eq. (12)] rather than model E [Eq. (11)] for a total vortex decay. Therefore, the total rate of circulation decay due to both ambient turbulence and stable stratification can be written in a nondimensional form as

a) $\eta = 0.0302$

b) $\eta = 0.0702$

c) $\eta = 0.1006$

d) $\eta = 0.1509$

e) $\eta = 0.3018$
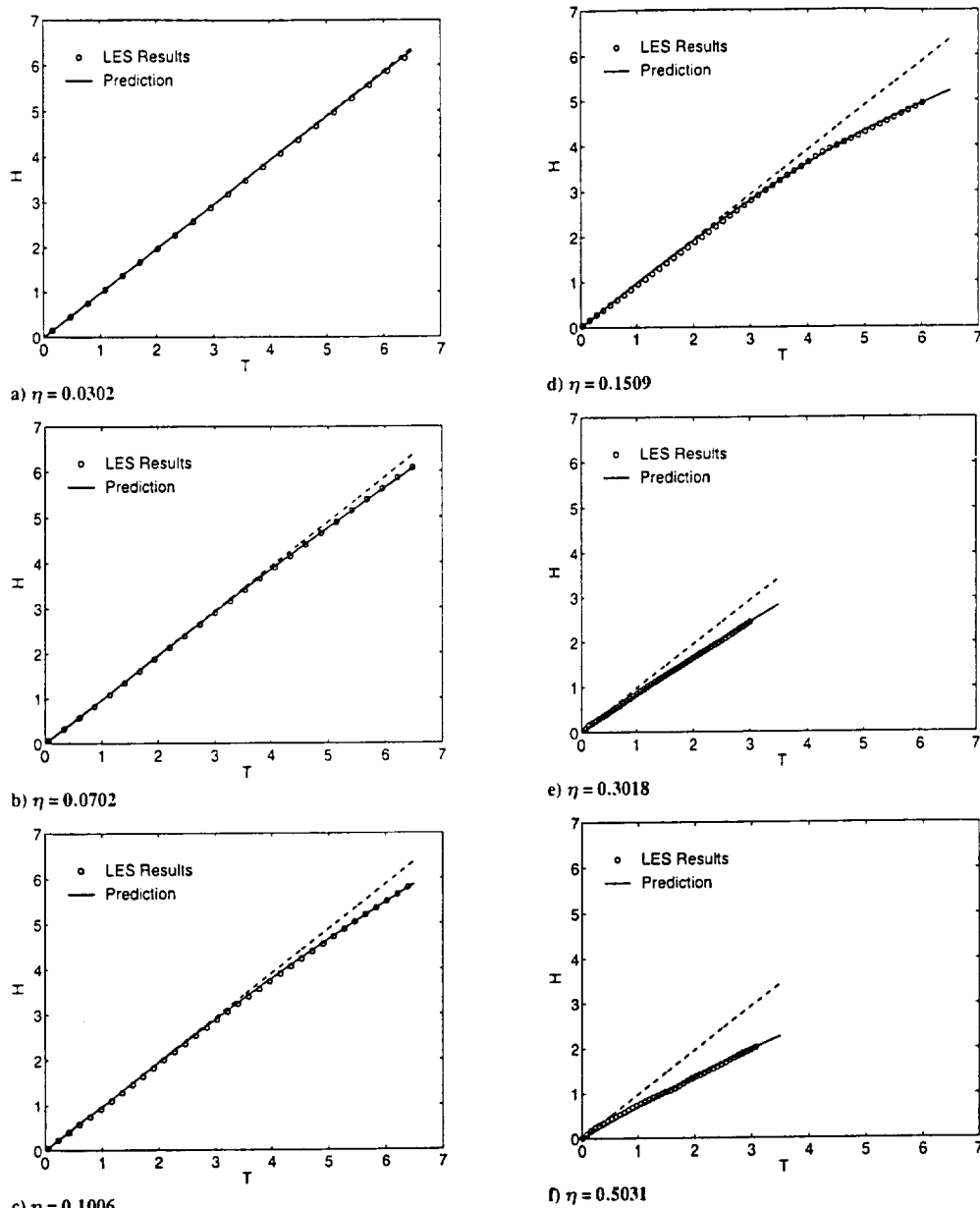
f) $\eta = 0.5031$

Fig. 10    Evolution of the descent distance in three-dimensional simulations compared with the theoretical model: dashed line $H = 0.98T$.



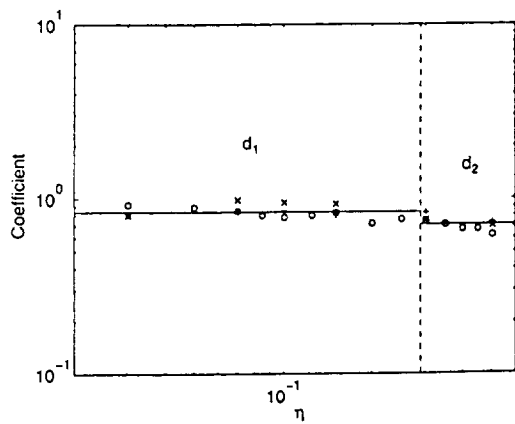Fig. 11    Same as Fig. 8 but for the vortex descent in Eqs. (20) and (21).
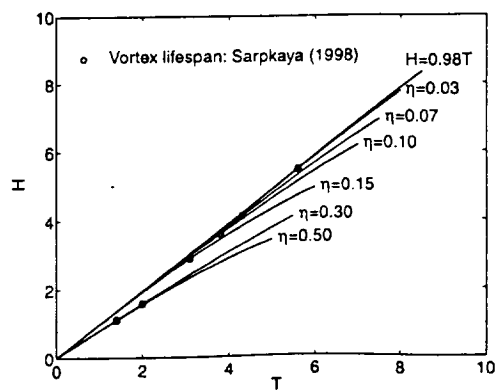


Fig. 12    Same as in Fig. 9 but for the vortex descent.

a) Stable environment, M-1252

b) Stable environment, M-1273

c) Neutral environment, M-1569

d) Neutral environment, M-1573

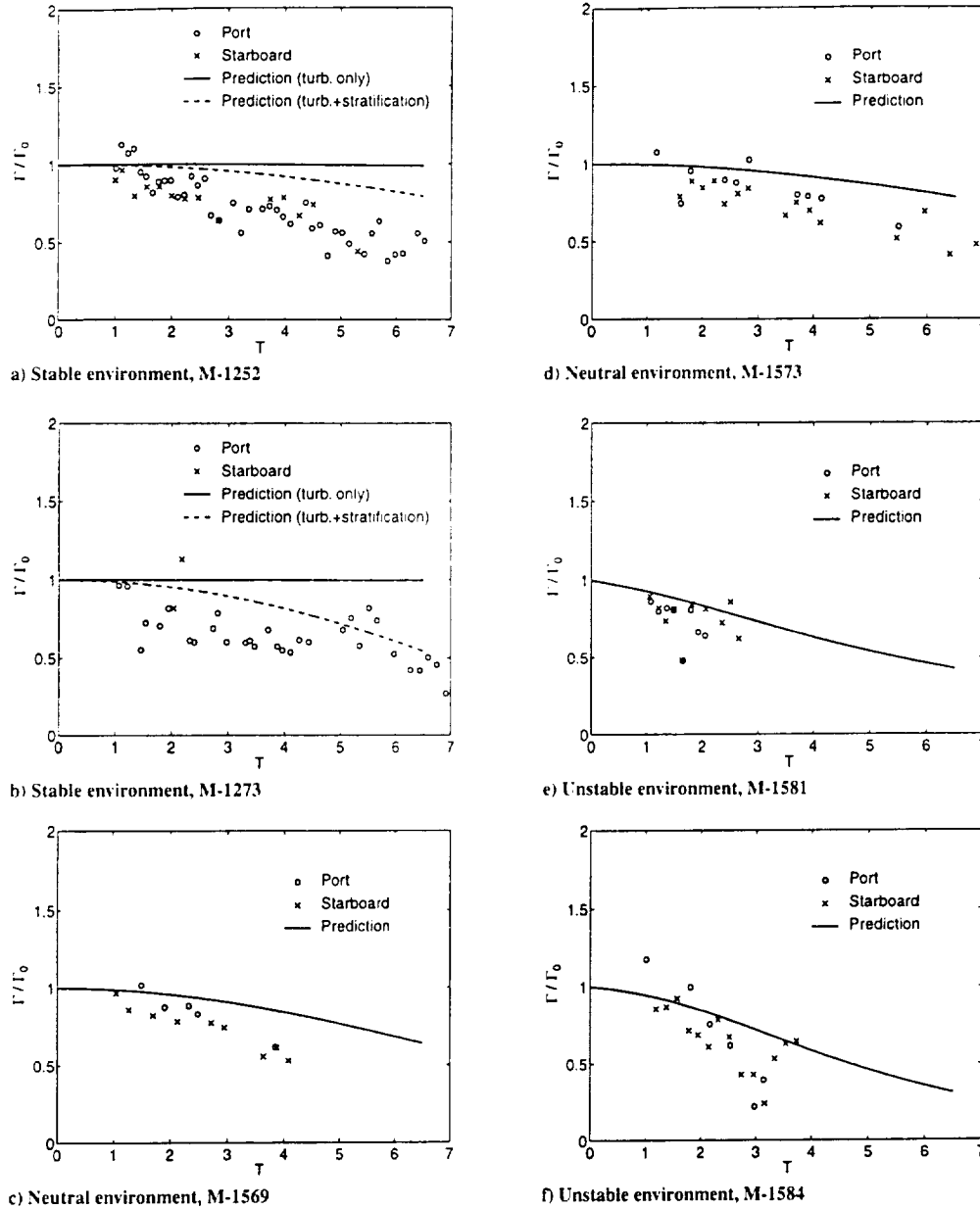e) Unstable environment, M-1581

f) Unstable environment, M-1584

Fig. 13   Comparison of field observations and model predictions for the average circulation over the range $R = 0.4-0.6$; solid (dashed) lines are model predictions for the circulation decay due to ambient turbulence only (due to both ambient turbulence and stable stratification).

$$\frac{d\Gamma}{dT}\bigg|_{turbulence} = \frac{d\Gamma}{dT}\bigg|_{turbulence} + \frac{d\Gamma}{dt}\bigg|_{stratification}$$

$$= -2c_2\frac{\eta^2 T}{R^2}\Gamma - \frac{b_0 A N^2 H}{V_0} \qquad (24)$$

On the other hand, the rate of vortex descent is given by

$$\frac{dH}{dT} = \frac{\Gamma}{\Gamma_0} \qquad (25)$$

Vortex decay and descent in Eqs. (24) and (25) have been computed through a numerical integration using a forward scheme in time, based on a vertically averaged $N$ from the observed ambient potential temperature profile [$N^2$ is defined as $(g/\Theta)(\partial\Theta/\partial z)$, where $g$ is the gravitational acceleration]. As shown in Figs. 13a and 13b, when the stratification effect is added in the model, the underestimation in vortex decay is significantly reduced, indicating that stratifica-

tion has an important influence on vortex decay for a weak ambient turbulence with stable stratification.

Shown in Fig. 14 are the measured vortex descents with model predictions based on Eqs. (20) and (21) again using the mean coefficients. In the calculation, the starting altitude of the vortices has been inferred from the LIDAR measurement as by Robins et al.[41] because the vortices appears to be located above the expected position, that is, the generating aircraft height in Table 2. Consistent with the large underestimation for the circulation decay, the model predictions in the weaker turbulence cases of M-1252 and M-1273 with stable stratification significantly overestimate the observed vortex descent, especially at later time periods. However, this overestimation in vortex descent is significantly reduced when the stratification effect is added in the model, consistent with reduction of the underestimation in circulation decay. The model predictions for the stronger turbulence cases of M-1581 and M-1584 appear to be in reasonable agreement with observations, which is also consistent with the agreement for the circulation decay.
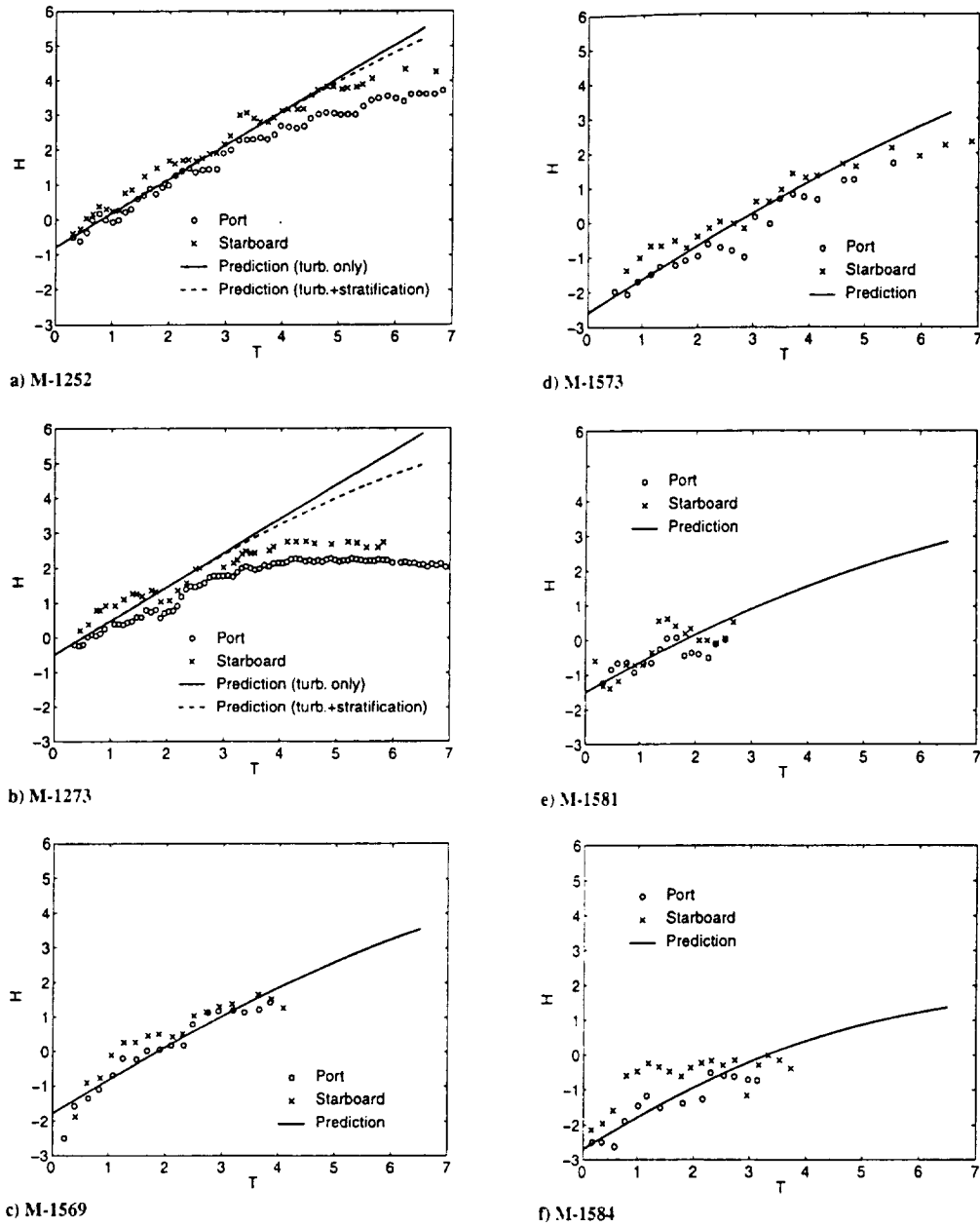
a) M-1252

b) M-1273

c) M-1569

d) M-1573

e) M-1581

f) M-1584

Fig. 14   Same as Fig. 13 but for the vortex descent.

## V.   Conclusions

This study represents a first step at understanding how wake vortices behave in the atmosphere by isolating the effects of ambient turbulence on vortex decay. LES simulations are conducted by first inducing a field of ambient turbulence that is nearly isotropic and spatially homogeneous. A vortex pair, representing aircraft trailing vortices, is introduced once the turbulence field reaches a statistically steady state. In these simulations, the Crow linking and its subsequent effect on vortex decay are suppressed by the selection of axial domain size.

Our results show that, consistent with field observations, the decay rate of the vortex circulation increases clearly with increasing levels of ambient turbulence and decreases with increasing radial distance. Based on the LES results, simple decay models for the vortex pair are proposed as functions of nondimensional ambient turbulence intensity $\eta$, nondimensional radial distance $R$, and nondimensional time $T$. Showing good agreement with the LES data, we propose a Gaussian type of vortex decay model for weak and moderate turbu-

lence, whereas an exponential type of vortex decay model is more appropriate for strong turbulence. The LES simulations and the fitted models show that the turbulence dissipation rate characterizes the level of ambient turbulence responsible for vortex decay. A model for the vortex descent based on the given vortex decay model is also proposed with functions of $\eta$ and $T$ and can be represented by an error function.

The proposed models for the vortex decay and descent are applied to available field data obtained from the Memphis airport. For a strong atmospheric turbulence, the model predictions appear to be in reasonable agreement with the observation data. For a weak atmospheric turbulence with stable stratification, the models largely underestimate the observed circulation decay with consistent overestimation of the observed vortex descent. However, this underestimation in vortex decay is significantly reduced with consistent reduction of the overestimation in vortex descent when the stratification effect is added in the models, indicating that stratification has an important influence on vortices for weak ambient levels of

turbulence under stably stratified conditions. The lack of agreement in the rate of decay for the weaker turbulence cases between model predictions and observations may also be caused by some other factors that are not taken into account in the comparison, such as the effect of internal turbulence on vortex decay, uncertainty in measurement data, and discrepancy in computation of the circulation between numerical simulations and observations.

## Appendix: Derivation of Decay Models

For high-Reynolds-number flows under the condition of neutral stratification, the equation that governs the rate of change for mean axial vorticity $\zeta$ due to turbulent motion can be given by

$$\frac{d\bar{\zeta}}{dt} = -\frac{\partial}{\partial x_j}\overline{u'_j\zeta'} \tag{A1}$$

Integration of Eq. (A1) over the region defined by the radial distance $r$ yields

$$\iint \frac{d\bar{\zeta}}{dt}\,dA = -\iint \frac{\partial}{\partial x_j}\overline{u'_j\zeta'}\,dA \tag{A2}$$

The area integral on the right-hand side of Eq. (A2) can be transformed into a line integral taken around the perimeter of the area using the Stoke's theorem, that is,

$$\frac{d\Gamma}{dt} = -\oint \overline{u'_n\zeta'}\,ds \tag{A3}$$

where $u'_n$ is the fluctuation of velocity normal to the surface. The line integral leads to

$$\frac{d\Gamma}{dt} = -2\pi r\langle\overline{u'_n\zeta'}\rangle \tag{A4}$$

where $\langle\,\rangle$ denotes an average around the perimeter with the radial distance $r$. From the down-gradient transport approximation,

$$\langle\overline{u'_n\zeta'}\rangle \sim -\nu_e \frac{\partial\langle\bar{\zeta}\rangle}{\partial r} \tag{A5}$$

where $\nu_e$ is an effective eddy viscosity. The radial gradient of mean axial vorticity may be approximated by

$$\frac{\partial\langle\bar{\zeta}\rangle}{\partial r} \sim -\frac{\langle\bar{\zeta}\rangle}{r} \tag{A6}$$

$$\langle\bar{\zeta}\rangle \sim \frac{\Gamma}{r^2} \tag{A7}$$

so that

$$\frac{\partial\langle\bar{\zeta}\rangle}{\partial r} \sim -\frac{\Gamma}{r^3} \tag{A8}$$

Note that $\partial\langle\bar{\zeta}\rangle/\partial r$ is assumed to be proportional to the difference of mean axial vorticity at the vortex center and that at the radial distance $r$. We are basically considering a vortex flow in which deviation from the axisymmetry due to ambient turbulence is small enough for the approximations of Eqs. (A5–A8) to be valid. Then Eq. (A4) can be expressed as

$$\frac{d\Gamma}{dt} \sim -\frac{\nu_e\Gamma}{r^2} \tag{A9}$$

The preceding derivations are almost the same as Donaldson and Bilanin's[7] (DB) except that the dependency of the circulation decay on the radial distance $r$ is considered in the present study, whereas $b_0$ is used instead of $r$ in DB's study because DB consider the decay rate of the circulation over an oval within which a pair of vortices resides.

From an equilibrium second-order closure theory, DB obtain the relation

$$\nu_e = 0.26\Lambda q \tag{A10}$$

where $\Lambda$ is a measure of the integral length scale of turbulence. Assuming that

$$\Lambda \simeq b_0/8 \tag{A11}$$

DB then obtain Eq. (1). However, their approximation of Eq. (A11) is not physically correct because $b_0$ has no relation with background atmospheric turbulence whose length scale varies significantly over day and night. As discussed in the Introduction, we use $\epsilon$, rather than $q$ and $\Lambda$, as the ambient turbulence parameter relevant to circulation decay.

For strong turbulence but at smaller radial distances where stronger the radial gradient of mean axial vorticity may exist, the parameterization of Eq. (A5) would be acceptable. The effective eddy viscosity in this case can be expressed in terms of effective turbulence velocity and length scales, that is,

$$\nu_e \sim (\epsilon b_0)^{\frac{1}{3}} b_0 \tag{A12}$$

Note that $(\epsilon b_0)^{1/3}$ is a characteristic turbulence velocity scale at the scale of the vortex separation distance $b_0$. Substituting Eq. (A12) into Eq. (A9), we obtain

$$\frac{d\Gamma}{dt} \sim -\frac{(\epsilon b_0)^{\frac{1}{3}} b_0}{r^2}\Gamma \tag{A13}$$

Thus, the decay rate of the circulation depends on both the turbulence energy dissipation rate $\epsilon$ and radial distance $r$, unlike DB's model [Eq. (1)].

For weak and moderate turbulence or at larger radial distances for strong turbulence where the radial gradient of mean axial vorticity may be weak, the parameterization of Eq. (A5) would not be appropriate. It is anticipated that the radial turbulent vorticity flux $\overline{u'_n\zeta'}$ in this case will be mostly influenced by turbulent diffusion of vorticity from the core region rather than by local diffusion as in Eq. (A5). This implies that $\overline{u'_n\zeta'}$ would be time dependent. We then hypothesize that the rate of change of $\langle\overline{u'_n\zeta'}\rangle$ in this case depends on turbulence velocity and mean axial vorticity gradient from vortex center to given $r$, that is,

$$\frac{\partial\langle\overline{u'_n\zeta'}\rangle}{\partial t} = f\left[(\epsilon b_0)^{\frac{1}{3}},\frac{\Gamma}{r^3}\right] \tag{A14}$$

From dimensional arguments,

$$\frac{\partial\langle\overline{u'_n\zeta'}\rangle}{\partial t} \sim \frac{(\epsilon b_0)^{\frac{1}{3}}\Gamma}{r^3} \tag{A15}$$

Integration of Eq. (A15) with respect to time leads to

$$\langle\overline{u'_n\zeta'}\rangle \sim [(\epsilon b_0)^{\frac{1}{3}} t\Gamma/r^3] \tag{A16}$$

where the initial value of $\langle\overline{u'_n\zeta'}\rangle$ is assumed to be zero. Substituting Eq. (A16) into Eq. (A4), we obtain

$$\frac{d\Gamma}{dt} \sim -\frac{(\epsilon b_0)^{\frac{1}{3}} t}{r^2}\Gamma \tag{A17}$$

## References

[1]Hinton, D. A., "Aircraft Vortex Spacing System (AVOSS) Conceptual Design," NASA TM-110184, Aug. 1995.
[2]Perry, R. B., Hinton, D. A., and Stuever, R. A., "NASA Wake Vortex Research for Aircraft Spacing," AIAA Paper 97-0057, Jan. 1997.
[3]Proctor, F. H., "The NASA-Langley Wake Vortex Modeling Effort in Support of an Operational Aircraft Spacing System," AIAA Paper 98-0589, Jan. 1998.
[4]Spalart, P. R., "Wake Vortex Physics: The Great Controversies," NASA First Wake Vortex Dynamic Spacing Workshop, NASA CP-97-206235, 1997, pp. 33, 34.

[5]Crow, S. C., "Stability Theory for a Pair of Trailing Vortices," *AIAA Journal*, Vol. 8, No. 12, 1970, pp. 2172–2179.

[6]Spalart, P. R., "Airplane Trailing Vortices," *Annual Review of Fluid Mechanics*, Vol. 30, 1998, pp. 1–35.

[7]Donaldson, C. duP., and Bilanin, A. J., "Vortex Wakes of Conventional Aircraft," AGARDograph 204, May 1975.

[8]Greene, G. C., "An Approximate Model of Vortex Decay in the Atmosphere," *Journal of Aircraft*, Vol. 23, No. 7, 1986, pp. 566–573.

[9]Sarpkaya, T., "Decay of Wake Vortices of Large Aircraft," *AIAA Journal*, Vol. 36, No. 9, 1998, pp. 1671–1679.

[10]Bilanin, A. J., Teske, M. E., and Hirsch, J. E., "Neutral Atmospheric Effects on the Dissipation of Aircraft Vortex Wakes," *AIAA Journal*, Vol. 16, No. 9, 1978, pp. 956–961.

[11]Corjon, A., and Darracq, D., "Three-Dimensional Large Eddy Simulation of Wake Vortices. Comparison with Field Measurements," AIAA Paper 97-2309, June 1997.

[12]Han, J., Lin, Y.-L., Schowalter, D. G., Arya, S. P., and Proctor, F. H., "Large-Eddy Simulation of Aircraft Wake Vortices: Atmospheric Turbulence Effects," *12th Symposium on Boundary Layers and Turbulence*, American Meteorological Society, Boston, 1997, pp. 237, 238.

[13]Han, J., Lin, Y.-L., Arya, S. P., and Kao, C., "Large-Eddy Simulation of Aircraft Wake Vortices: Atmospheric Turbulence Effects," *NASA First Wake Vortex Dynamic Spacing Workshop*, NASA CP-97-206235, 1997, pp. 131–144.

[14]Sarpkaya, T., and Daly, J. J., "Effect of Ambient Turbulence on Trailing Vortices," *Journal of Aircraft*, Vol. 24, No. 6, 1987, pp. 399–404.

[15]Sarpkaya, T., "Trailing Vortices in Homogeneous and Density-Stratified Media," *Journal of Fluid Mechanics*, Vol. 136, 1983, pp. 85–109.

[16]Hallock, J. N., and Burnham, D. C., "Decay Characteristics of Wake Vortices from Jet Transport Aircraft," AIAA Paper 97-0060, Jan. 1997.

[17]Tombach, I., "Observations of Atmospheric Effects on Vortex Wake Behavior," *Journal of Aircraft*, Vol. 10, No. 11, 1973, pp. 641–647.

[18]Spalart, P. R., and Wray, A. A., "Initiation of the Crow Instability by Atmospheric Turbulence," *78th AGARD-FDP Symposium on the Characterization and Modification of Wakes from Lifting Vehicles in Fluids*, 1996.

[19]Han, J., Lin, Y.-L., Schowalter, D. G., Arya, S. P., and Proctor, F. H., "Large Eddy Simulation of Aircraft Wake Vortices Within Homogeneous Turbulence: Crow Instability," *AIAA Journal*, Vol. 38, No. 2, 2000, pp. 292–300.

[20]Kolmogorov, A. N., "The Local Structure of Turbulence in Incompressible Viscous Fluid for Very Large Reynolds Number," *Doklady Akademii Nauk SSSR*, Vol. 30, 1941, pp. 9–13.

[21]Crow, S. C., and Bate, E. R., "Lifespan of Trailing Vortices on a Turbulent Atmosphere," *Journal of Aircraft*, Vol. 13, No. 7, 1976, pp. 476–482.

[22]Liu, H.-T., "Effects of Ambient Turbulence on the Decay of a Trailing Vortex Wake," *Journal of Aircraft*, Vol. 29, No. 2, 1992, pp. 255–263.

[23]Proctor, F. H., "The Terminal Area Simulations System, Volume 1: Theoretical Formulation," NASA CR 4046, Dept. of Transportation/Federal Aviation Administration/PM-86/50, 1, 1987.

[24]Proctor, F. H., "Numerical Simulation of Wake Vortices Measured During the Idaho Fall and Memphis Field Programs," *Proceedings of the AIAA 14th Applied Aerodynamics Conference*, Pt. 2, AIAA, Reston, VA, 1996, pp. 943–960.

[25]Proctor, F. H., Hinton, D. A., Han, J., Schowalter, D. G., and Lin, Y.-L., "Two-Dimensional Wake Vortex Simulations in the Atmosphere: Prelimi-

nary Sensitivity Studies," AIAA Paper 97-0056, Jan. 1997.

[26]Schowalter, D. G., Decroix, D. S., Switzer, G. F., Lin, Y.-L., and Arya, S. P., "Toward Three-Dimensional Modeling of a Wake Vortex Pair in the Turbulent Boundary Layer," AIAA Paper 97-0058, Jan. 1997.

[27]Klemp, J. B., and Wilhelmson, R. B., "The Simulation of Three-Dimensional Convective Storm Dynamics," *Journal of Atmospheric Sciences*, Vol. 35, No. 6, 1978, pp. 1070–1096.

[28]Switzer, G. F., "Validation Tests of TASS for Application to 3-D Vortex Simulation," NASA CR 4756, 1996.

[29]Lord Rayleigh, "On the Dynamics of Revolving Fluids," *Proceedings of the Royal Society of London Series A: Mathematical and Physical Sciences*, Vol. 93, 1916, p. 148.

[30]Smagorinsky, J., "General Circulation Experiments with the Primitive Equations: I. The Basic Experiments," *Monthly Weather Review*, Vol. 91, No. 3, 1963, pp. 99–164.

[31]Proctor, F. H., "A LES Subgrid Turbulence Model with Rotational Dampening," NASA TR, 1999.

[32]Rubinstein, R., and Zhou, Y., "The Dissipation Rate Transport Equation and Subgrid-Scale Models in Rotating Turbulence," NASA CR-97-206250, Inst. for Computer Applications in Science and Engineering, Rept. 97-63, Nov. 1997.

[33]Han, J., "Large Eddy Simulations of Aircraft Wake Vortices in a Homogeneous Atmospheric Turbulence," Ph.D. Dissertation, North Carolina State Univ., Raleigh, NC, 1998.

[34]Vincent, A., and Meneguzzi, M., "The Spatial Structure and Statistical Properties of Homogeneous Turbulence," *Journal of Fluid Mechanics*, Vol. 225, 1991, pp. 1–20.

[35]Lamb, H., *Hydrodynamics*, 6th ed., Cambridge Univ. Press, New York, 1932.

[36]Corjon, A., Risso, F., Stoessel, A., and Poinsot, T., "Three-Dimensional Direct Numerical Simulations of Wake Vortices: Atmospheric Turbulence Effects and Rebound with Crosswind," *78th AGARD-FDP Symposium on the Characterization and Modification of Wakes from Lifting Vehicles in Fluids*, 1996, pp. 28-1–28-21.

[37]Burnham, D. C., and Hallock, J. N., "Chicago Monostatic Acoustic Vortex Sensing System," Dept. of Transportation–TSC–Federal Aviation Administration Rept. DOT-TSC-FAA-79-103 IV, July 1982; available from National Technical Information Service.

[38]Hinton, D. A., and Tatnall, C. R., "A Candidate Wake Vortex Strength Definition for Application to the NASA Aircraft Vortex Spacing System (AVOSS)," NASA TM-110343, Sept. 1997.

[39]Tatnall, C. R., "An Investigation of Candidate Sensor-Observable Wake Vortex Strength Parameters for the NASA Aircraft Vortex Spacing System (AVOSS)," NASA CR-1998-206933, March 1998.

[40]Campbell, S. D., Dasey, T. J., Freehart, R. E., Heinrichs, R. M., Matthews, M. P., Perras, G. H., and Rowe, G. S., "Wake Vortex Field Measurement Program at Memphis, TN Data Guide," Project Report: NASA/L-2, Jan. 1997; available from National Technical Information Service.

[41]Robins, R. E., Delisi, D. P., and Greene, G. C., "Development and Validation of a Wake Vortex Predictor Algorithm," AIAA Paper 98-0665, Jan. 1998.

**Appendix G: Numerical Study of Wake Vortex Interaction with the Ground Using the Terminal Area Simulation System**

**AIAA 99-0754**

# Numerical Study of Wake Vortex Interaction with the Ground Using the Terminal Area Simulation System

Fred H. Proctor
NASA Langley Research Center
Hampton, VA

Jongil Han
North Carolina State University
Raleigh, NC

# 37th Aerospace Sciences Meeting & Exhibit
## January 11-14, 1999 / Reno, NV

# Numerical Study of Wake Vortex Interaction with the Ground Using the Terminal Area Simulation System

Fred H. Proctor*
*NASA Langley Research Center*
*Hampton, Virginia*

Jongil Han†
*North Carolina State University*
*Raleigh, NC*

## Abstract

*A sensitivity study for the "in-ground effect" on aircraft wake vortices has been conducted using a validated large eddy simulation model. The numerical results are compared with observed data and show good agreement for vortex decay and lateral vortex transport. The vortex decay rate is strongly influenced by the ground, but appears somewhat insensitive to ambient turbulence. In addition, the results show that the ground can affect the trajectory and descent-rate of a wake-vortex pair at elevations up to about 3 $b_o$ (where $b_o$ is the initial vortex separation). However, the ground does not influence the average circulation of the vortices until the cores descend to within about 0.6 $b_o$, after which time the ground greatly enhances their rate of demise. Vortex rebound occurs in the simulations, but is more subtle than shown in previous numerical studies.*

*Also described in this paper is the model formulation for surface stress, which is based on Monin-Obukhov similarity theory.*

---

*Research Scientist, Flight Management and Control Division, AIAA member

†Research Scientist, Department of Marine, Earth, and Atmospheric Sciences

## Nomenclature

| | |
|---|---|
| $B$ | aircraft wing span |
| $b_o$ | initial vortex separation - $\pi B/4$ |
| $g$ | acceleration due to gravity |
| $Z_i$ | initial height above ground of wake vortex |
| $M$ | mass of generating aircraft |
| $t$ | time coordinate |
| $T^*$ | nondimensional time - $t V_o / b_o$ |
| $V_a$ | airspeed of generating aircraft |
| $V_o$ | initial vortex descent velocity - $\Gamma_o / (2\pi b_o)$ |
| $z$ | vertical coordinate |
| $z_o$ | ground roughness coefficient |
| $\Gamma$ | vortex circulation |
| $\Gamma_o$ | initial circulation - $M g/(b_o \rho V_a)$ |
| $\rho$ | air density |
| $\epsilon$ | turbulence (eddy) dissipation rate |
| $\nu$ | kinematic viscosity |
| $\eta$ | nondimensional eddy dissipation - $(\epsilon b_o)^{1/3} V_o^{-1}$ |

## I. Introduction

The behavior of aircraft wake vortices is being investigated by NASA in order to develop a predictor system that will safely reduce aircraft spacing and increase airport capacity.[1,2] This system, the Aircraft VOrtex Spacing System (AVOSS), includes prediction algorithms[3] for wake vortex transport and decay. In order to protect the AVOSS approach/departure corridor, these algorithms must function in real time and at altitudes where the ground can affect vortex behavior. In order to develop this system, the influence of both the weather and the ground surface needs to be understood and quantified. Investigations with a Large Eddy Simulation (LES) numerical model are in progress and are intended to support the development of the predictor system.[4]

Some understanding of wake vortex behavior near the ground has been achieved in past research efforts,[5,6,7,8,9,10,11,12] but much more information is needed in order to develop prediction algorithms that can be applied successfully near the ground. Previous research has shown that, when near the ground, the transport of wake vortices is affected by both viscous and inviscid processes.[13] As a vortex pair descends toward the ground, inviscid processes cause the vortices to lose their vertical motion and diverge laterally.[14] This effect can be modeled mathematically by placement of image vortices beneath the ground plane so as to satisfy impermeable and free-slip conditions at the ground. However, this effect alone cannot explain the vortex rebounding that is often observed near the ground. A second influence is caused by the viscous retardation of the flow next to the ground. As the vortex circulation comes in contact with the ground, friction creates a shear layer of opposite sign vorticity, which is then swept upward and around the infringing vortex. This shear layer wraps into secondary vortices, which then act on the primary vortex causing it to rise or rebound upwards.[5] Another effect from the frictional retardation of the flow next to the ground is to weaken the coupling with the sub-surface images, which in turn, reduces the rate at which the vortices spread, as otherwise predicted by inviscid theory. Further complications for the prediction of the wake vortex trajectory are due to the presence of ambient crosswind near the ground which can influences the position and intensity of the secondary vortices.[10,11]

Vortex decay near the ground is known to be enhanced by proximity to the ground, but details are not well understood.[15] Little is known about the influence of environmental turbulence on wake vortex behavior near the ground. For aircraft wake vortices away from the ground, ambient atmospheric turbulence has been recognized to be a key factor for the enhancement of the vortex decay.[16,17,18,19,20,21] At low altitudes, however, the interaction of the vortices with the ground may be a more important factor for vortex decay.

Based on the previous wake vortex research efforts, Corjon et al[22] and Robins et al[3] have modified Greene's model[23] (which is applicable to the free atmosphere) for ground effects. Robins et al define a wake vortex to be "in-ground-effect" (IGE) when viscous effects with the ground are significant. This should occur when the vortex core descends to within $z < b_o$. They also define wake vortices to be "out-of-ground effect" (OGE) -- when the vortices are far from the influence of the ground; and "near-ground effect" (NGE) -- when the vortices are close enough to have some influence from the ground, but far enough not to generate secondary vorticity. The region defined by NGE is above where ground-viscous effects

are significant, but where inviscid process due to the ground can act to reduce the vortex sink rate ($b_o < z < 3 b_o$). The influence of the ground at these various altitudes must be carefully studied in order to insure the development of valid predictive algorithms.

In the present study, a three-dimensional numerical LES is conducted for a landing L-1011 which was observed at 20:09 UTC on 26 September 1997 at Dallas-Fort Worth (DFW) airport.[24] This specific case was chosen at the recommendation of Northwest Research Associates,[25] who are analyzing the NASA deployment data and are developing an AVOSS wake-vortex prediction model. Also presented are additional sensitivity experiments conducted for a wide range of ambient turbulence intensities and for a range of wake generation heights. Simulation results, including comparisons with Lidar measurements, are presented in section 3. The numerical model and initial conditions are briefly described in section 2, and the conclusions of this study are summarized in section 4.

## II. The Model and Initial Conditions

The numerical model used in the present study is a three-dimensional, compressible, nonhydrostatic LES model called the Terminal Area Simulation System[26] (TASS), which has been adapted for simulation of wake vortex interaction with the atmosphere.[27] Grid-scale turbulence is explicitly computed while the effects of subgrid-scale turbulence is explicitly modeled by a conventional 1st-order closure model with modifications for stratification and flow rotation. All simulations are conducted assuming rotational Reynolds numbers ($\Gamma_o/\nu$) of ~$10^7$. The numerical formulation of the TASS model is computationally efficient and essentially free of numerical diffusion.[28]

One feature of TASS, which enhances its ability to correctly simulate wake vortex behavior near the ground, is its formulation for the ground boundary condition. The formulation is based on Monin-Obukhov similarity theory, with the subgrid stress at the ground determined locally from the wind speed, surface roughness, and the local thermal stratification. Details of the formulation are described in the appendix.

In recent studies with the TASS model Han et al[21,29] have examined wake vortex decay and the development of Crow instability within a Kolmogorov spectrum of homogeneous atmospheric turbulence. In these studies, periodic boundary conditions are imposed at all domain boundaries in order to avoid the effects of the ground. In the present study, we include the ground surface, with periodic boundary conditions only at the horizontal

boundaries. As before, preexisting resolved-scale ambient turbulence is generated prior to injecting a wake vortex pair.

**Table 1.** *Initial vortex parameters.*

| Parameter | Value |
|---|---|
| Vortex spacing $(b_o)$ | 37 m |
| Generating height $(Z_i)$ | 14 m    $(0.38\ b_o)$ |
| Vortex circulation $(\Gamma_o)$ | 390 m$^2$ s$^{-1}$ |
| Vortex core radius | 3 m    $(b_o/12.3)$ |

The initial vortex system represents a post roll-up, wake-vortex velocity field as described in Proctor[4], and consists of a pair of counter-rotating vortices that have no initial variation in the axial direction. The initial vortex parameters (Table 1) are from the observed aircraft parameters for the L-1011. Note that the initial vortex elevation is less than half of initial vortex separation and is well within IGE.

**Table 2.** *Model domain parameters.*

| Parameter | Value |
|---|---|
| Crossplane width | 370 m    $(10\ b_o)$ |
| Crossplane height | 81 m    $(2.2\ b_o)$ |
| Axial length | 81 m    $(2.2\ b_o)$ |
| Crossplane grid resolution | 1.5 m    $(b_o/24.7)$ |
| Axial grid resolution | 2.0 m |
| Ground roughness $(z_o)$ | 0.1 m |

The model domain parameters are given in Table 2. The relatively small domain size in the axial direction is assumed in order to save computing time and simplify analysis of the results. This truncated size will suppress the development of Crow instability, which has a theoretical maximum wavelength of about 8.6 $b_o$.[30] Thus, statistically homogeneous wake vortex decay behavior is anticipated along the axial direction. The domain width of 10 $b_o$ in the crossflow direction is sufficiently large to minimize boundary influences. The domain size in the vertical direction (2.2 $b_o$) is large enough to investigate IGE, but bounds the largest resolvable turbulence eddy size, so that the effects of large turbulent eddies (such as thermals) on vortex transport are not taken into account.

**Table 3.** *Ambient turbulence energy dissipation rate and corresponding dimensionless turbulence intensity for the sensitivity cases (baseline case in bold).*

| $\epsilon\ (m^2\ s^{-3})$ | $\eta$ |
|---|---|
| $3.317 \times 10^{-8}$ | 0.0014 |
| $3.317 \times 10^{-5}$ | 0.0638 |
| **$1.654 \times 10^{-3}$** | **0.2349** |
| $6.671 \times 10^{-3}$ | 0.3739 |

The ambient temperature and velocity profiles for the selected case study are given in Figure 1. The atmosphere for this case has near-neutral stratification, with the static stability being very slightly unstable near the ground. The crossflow velocity is somewhat weak over the vertical depth of the simulation, with an average value of about 1 *m/s*.
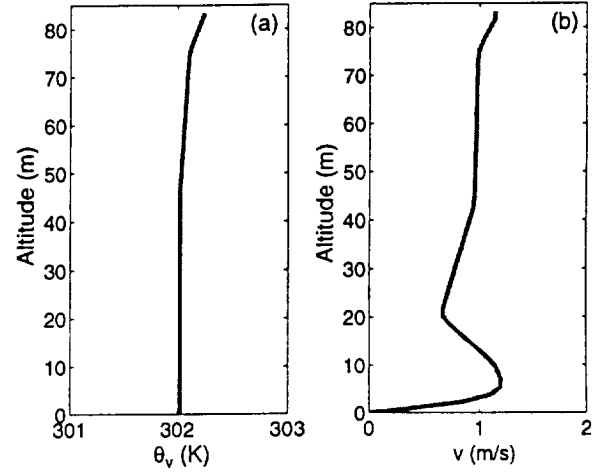


**Figure 1.** *Initial profile of a) ambient potential temperature and b) crosswind for DFW, 26 September 1997, 20:09 UTC.*

Prior to injecting the initial wake-vortex field, the initial turbulence field is allowed to develop under an artificial external forcing of horizontal velocity at low wavenumbers. The forcing is applied along each horizontal plane using a two-dimensional Fast Fourier Transform (see references [21, 29] for other details). At the same time, the horizontal domain average temperature and velocity fields are forced to maintain their initial vertical profiles by subtracting the difference every time step. This approach allows a well-developed turbulent flow field which possess Kolmogorov's inertial subranges, and maintains the ambient temperature and wind profile. Once the turbulence is well developed, the vortex system is injected into the simulation and the external forcing is discontinued. The above approach differs from the one used in a companion paper,[31] in which the resolved-scale ambient turbulence is grown by boundary layer forcing rather than by an artificial forcing function as in this paper.

In order to evaluate the sensitivity to environmental turbulence, ambient turbulence fields are generated for four levels of turbulence. Their associated values of turbulence energy (eddy) dissipation rate, $\epsilon$, are estimated from the well-known technique of fitting the inertial subrange of the simulated spectra. Their values and

corresponding nondimensional turbulence strengths, η, are given in Table 3. For the initial vortex parameters of this case, the range of values for η span typical values found in the lower atmosphere which range from about 0.01 in the nighttime to about 0.3 in the daytime.[4] The ambient turbulence field with a value of, ε =1.654 x 10$^{-3}$ $m^2 s^{-3}$ (η =0.2349), is close to the value observed at 40 $m$ elevation near the time of the L-1011 event. Thus, this numerical simulation can be directly compared with the Lidar wake-vortex measurements. [This case will be referred to as the baseline case.] Three-dimensional wake vortex simulations are carried out with each of the four turbulence fields identified in Table 3, with all other conditions identical. In addition to these experiments, a two-dimensional simulation is conducted with no ambient turbulence. In this experiment, the wake vortex can only decay from *two-dimensional turbulence* induced by the interaction of the vortex with the ground and atmosphere.
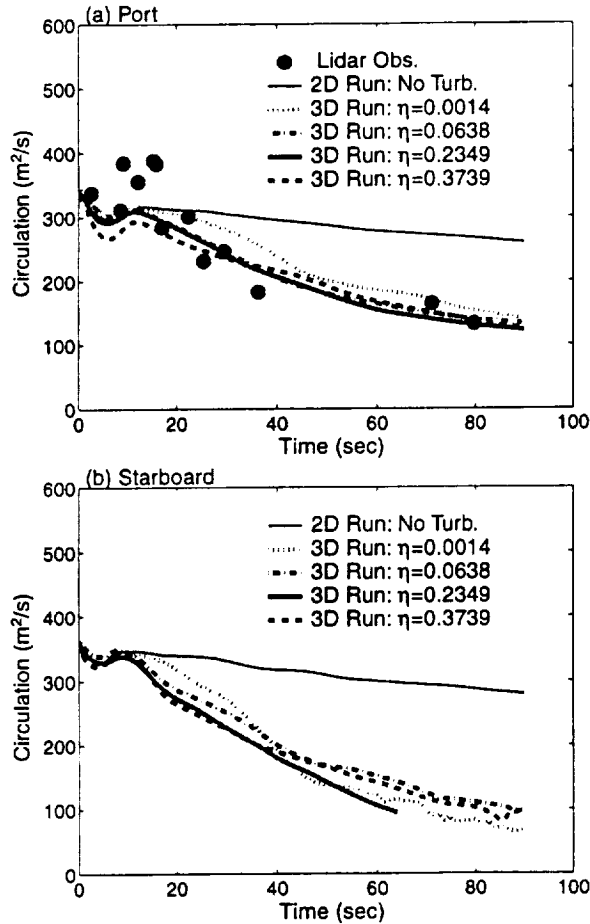


Figure 2. *Time evolution of 5-15 m averaged circulation for: a) port vortex and b) starboard vortex.*
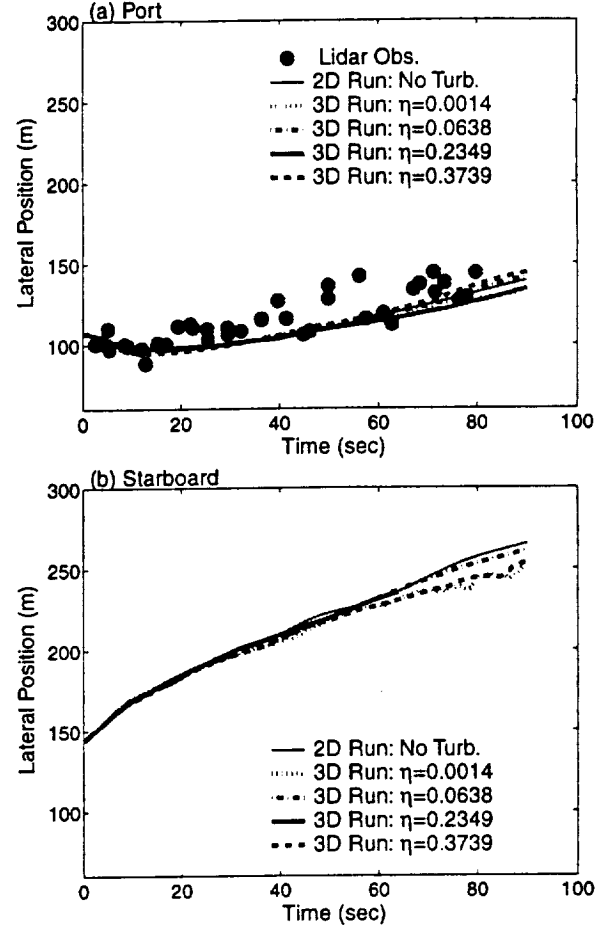


Figure 3. *Same as Fig. 2, but for lateral position.*

## III. Numerical Results

Results from the five experiments with the conditions listed in Tables 1-3 are compared in Figures 2-4. The profiles for both starboard and port vortices are shown since the light crosswind (Fig.1) causes slight differences in their behavior. Lidar observations for the port vortices are shown for comparison (observations for the starboard vortex were unavailable). The four 3-D cases with various levels of ambient turbulence only show minor differences, and are in agreement with the Lidar data for lateral position and circulation decay. Note that the port vortex essentially stalls near the flight path and may be hazardous to other aircraft trailing close behind.

Specifically, Fig 2 shows a comparison of the average circulation (averaged over a radius between 5 and 15 $m$ from the vortex center). A slight dip in average circulation occurs at early simulation times due to the vortex height being less than 15 $m$ (the calculation of

circulation from the TASS data is clipped at the ground). The initially large values of average circulation from the Lidar observation are known overestimates that frequently occur during the first several seconds of measurements.[32] Note from Fig. 2 that the circulation decay is quite significant, even for the very-weak ambient turbulence case ($\eta$=0.0014). However, for the 2-D case with no ambient turbulence, very little decay occurs. Therefore, it appears that some small perturbations are necessary in order to promote vortex decay within IGE, even though the rate of decay is very weakly related to the ambient level of turbulence.
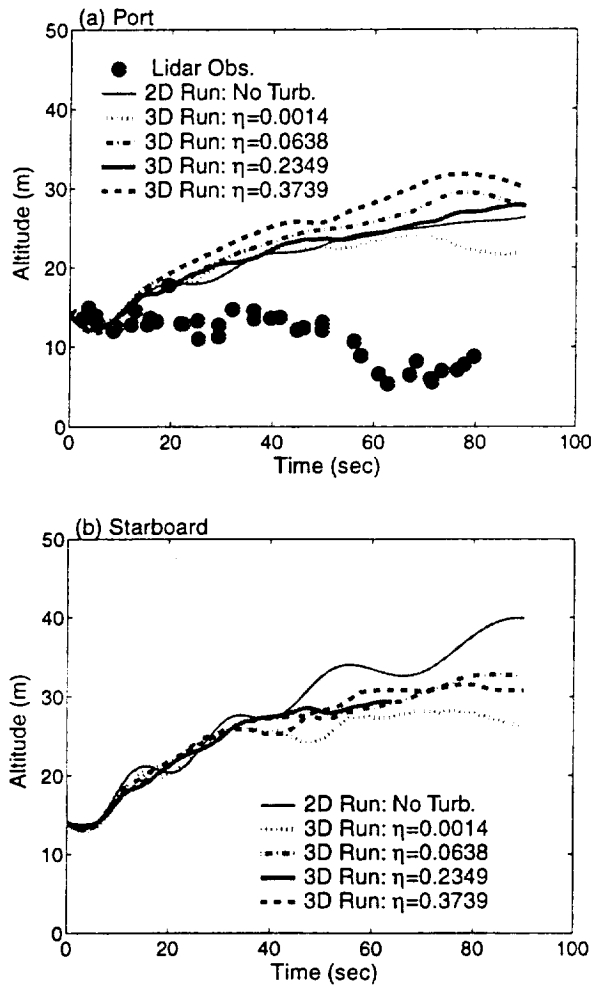


Figure 4. *Same as Fig. 2, but for vertical position.*

The lateral positions of the vortices are shown in Fig. 3. The Port (upstream) vortex initially travels upstream then slowly drifts downstream. However, its position remains within 30 *m* of the flight path during most of its lifetime. All of the simulations, including the 2-D no-turbulence run, produce similar lateral profiles, which are in good agreement with the measured data.

Note that the differences in lateral vortex positions for the numerical results are less than the size of scatter in the measured data.

The vertical position history of the vortices, in comparison with the observation, is shown in Figure 4. As expected, results from the two-dimensional simulation show pronounced oscillations in vortex altitude with time, indicating that significant secondary vortices are orbiting around the primary vortices. These oscillations are more significant for the starboard vortex than for the port vortex, since the secondary vortices around starboard vortex have the same sign vorticity to that induced by the ambient crosswind close to the ground. For the numerical simulations with strong turbulence (e.g., the cases with $\eta$=0.2349, and $\eta$=0.3739), however, the vertical oscillations in vortex positions are much less significant due to dissipation of the secondary vortices by the ambient turbulence. It appears that the vertical movement of the vortices is only weakly sensitive to the level of resolvable-scale turbulence. For example, the maximum difference between simulations for vortex height is only about 10 *m*, as is true for the maximum difference in lateral vortex position. On the other hand, while the observed vortex appears to descend slowly with time, those in the numerical simulations descend initially and then continuously rise almost to the end of simulation time. This discrepancy between observations and numerical results could be caused by the following possibilities: (1) the vortices are embedded in a large-scale downdraft (sinking air surrounding the thermals), note that the case was observed during the early afternoon; (2) the initial profile did not capture the crosswind shear that was local to the actual wake vortex (the gradient in vertical shear can effect the vortex sink rate[4]); (3) the roll-up process is more complex when in ground effect; (4) consequences due to loss-of-lift from the landing aircraft (touchdown occurs near the observing site) or (5) the Lidar observed height is incorrect. The sinking of the wake vortex with a lack of rebound was unexpected, and for this reason, this case was selected for examination. Several other cases observed near this time, showed a vertical trajectory similar to that of the simulations; i.e., rising motion with the vortex approaching a maximum height between $\frac{1}{2} b_0$ to $b_0$;[24] although according to Delisi,[33] several of the vortices from the DFW IGE cases (one-third to one half) did not appear to rise and remained close to the ground. However, we are unable to determine from our numerical experiments why the observed vortex remained very close to the ground for this event.

Figure 5 shows the time evolution of the axial vorticity field for the baseline case. Note that the magnitude of axial vorticity decreases with time, and by

$t = 77$ $s$, the starboard vortex has become almost indistinguishable from the background turbulence. Opposite sign vorticity is generated immediately after initiation by the surface stress at the ground, but the vorticity centers of the secondary vortices are difficult to distinguish from the background turbulence. Figures 6 and 7 show the evolution of the radial profiles for circulation and vorticity for the port vortex. Note that as the vortex decays with time, most of the vorticity remains confined to within a $5$ $m$ radius, and that the circulation maintains a more or less uniform radial profile as it decreases with time. However, at larger radii the profile of circulation rapidly diminishes with radius due to contact with the ground. We suspect that turbulence is intensified within this region by Rayleigh instability,[34] and becomes quite efficient in transferring vorticity away from the vortex core.

Sensitivity to Height of Vortex Generation

Three additional experiments are conducted with the height of vortex initiation, $Z_i$, equal to $2.5$ $b_o$, $b_o$, and ½ $b_o$ (or equivalently $92.5$ $m$, $37$ $m$, and $18.5$ $m$, respectively). The initial and domain parameters are, otherwise, the same as the previous cases (Tables 1 and 2), except that the crossplane domain width is $9.1$ $b_o$ and the crossplane domain height is $3.9$ $b_o$. In order to isolate and easily detect any influences due to the ground, a neutral stratification, a zero mean ambient crosswind, and a somewhat weak ambient turbulence field ($\eta=0.091$) are assumed. For comparison and ascertaining the influence of the ground, an additional simulation is conducted which assumes periodic bottom and top boundaries -- and hence, excludes any ground effect.

A comparison of the results (Figs. 7-10) show that the ground can influence the descent rates of vortices at altitudes up to $2.5$ $b_o$; but the $5$-$10$ $m$ averaged circulation is not affected until after the vortex *first* descends (or initiated) below $\sim0.6$ $b_o$. The results indicate that enhanced decay from ground-effect begins $5$-$10$ seconds after the vortices descend to their minimum height. After which time, the enhanced rate of decay continues, even as the vortices ascend.

For NGE, these results suggest that the descent rate of vortices may be reduced by the influence of the sub-surface vortex images, rather than by a reduction in the average circulation from the ground effect. Vortex decay at these altitudes is primarily influenced by stratification and ambient turbulence.

For IGE, the decay of average circulation is greatly enhanced following the descent of the vortices to their minimum altitude. Beyond this time, the decay process is dominated by the ground interaction, and ambient

turbulence has only a secondary influence. However, the ambient turbulence may play a role in reducing the amplitude of the vortex rebound. The amplitude of vortex rebound appears less than in other numerical experiments (cf. Schiling[9], Zheng and Ash[11], and Corjon and Poinsot[13]).
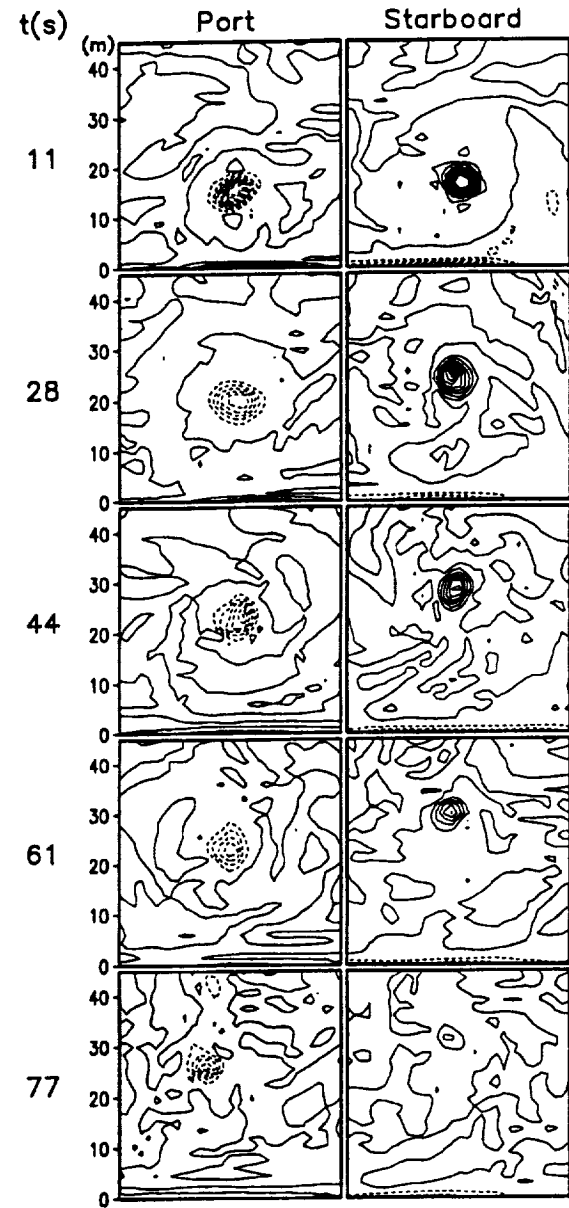


Figure 5. *Time evolution of the axial-component of vorticity within a crossplane for the baseline simulation ($\eta=0.2349$). The contour interval for vorticity is 1 $s^{-1}$.*

Sensitivity to Surface Roughness

In the last set of experiments, sensitivity due to surface roughness is examined. The surface roughness length, $z_o$, is related to the characteristic roughness of the

ground,[35] and its use in the TASS surface stress formulation is given in the appendix. The sensitivity of this parameter is evaluated by re-running the baseline case with $z_o$ decreased by an order of magnitude.
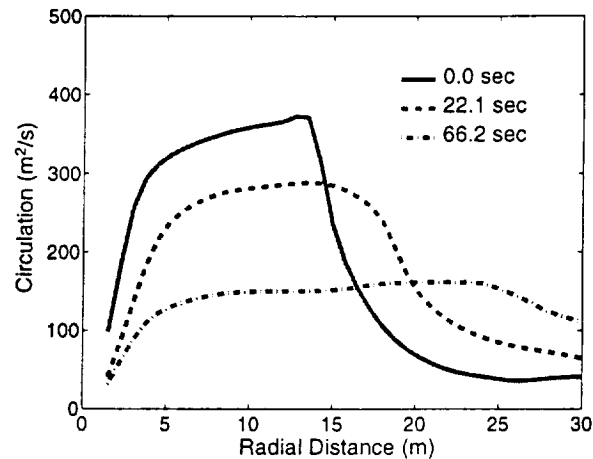


**Figure 6.** *Radial distribution of circulation for the port vortex of the baseline case at T\*=0, 1, and 3 (t = 0, 22, and 66 s). The ground is at radius of 14, 19, and 25m for the three respective times.*
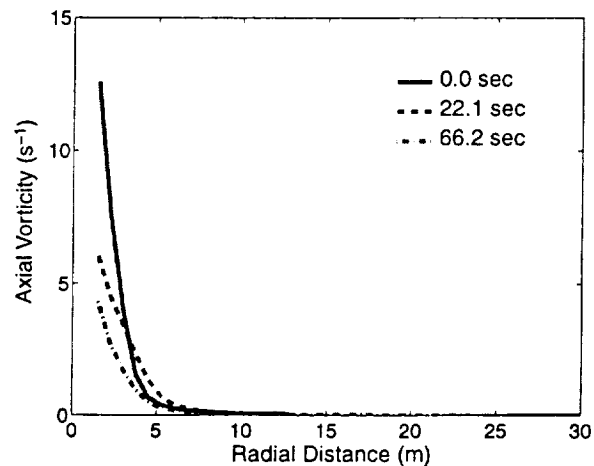


**Figure 7.** *Same as Fig. 6, but for azimuthal-averaged vorticity.*

The comparisons in Fig. 11 show that the results are weakly affected by an order-magnitude reduction in $z_o$. However, the results do indicate that a smoother ground weakens the rate of decay and dampens the amplitude of the rebound. A smaller surface roughness could not explain the relatively low vortex trajectory as observed by Lidar for this case.

## IV. Summary and Conclusions

A study of wake vortices initialized "in-ground effect," has been performed using a validated LES model. The study is performed with the following limiting assumptions: 1) Crow linking is suppressed due to the truncated axial length of the domain; 2) a simple, post roll-up vortex system is assumed for the initial conditions; 3) the wake vortices are of infinite length; 4) the ambient turbulence is horizontally homogeneous, with the largest scales restricted to the size of the model domain; and 5) the ground is flat with a uniform roughness. The numerical model used in this study differs from that in many previous investigations, in that: 1) time-dependent computations are carried out in three-dimensional space, 2) the computations are LES and at high Reynolds number, 3) realistic surface-stress and subgrid turbulence-closure formulations are assumed, 4) the numerical model has a compressible, non-Boussinesq formulation and a meteorological framework, 5) the model has been validated for real cases, and 6) the numerical formulation is stable, efficient, accurate, and essentially free of numerical diffusion.

Simulations with the three-dimensional LES and with environmental turbulence show strong decay of the vortex average circulation, which agrees very well with the observations, while a two-dimensional simulation without resolvable-scale ambient turbulence largely underestimates the observed rate of decay. For the 3-D cases, the circulation decay appears only weakly sensitive to ambient turbulence levels. The implication for IGE vortex predictions is that crude approximations of ambient turbulence level may be adequate for prediction of circulation decay.

Our LES results also indicate that the lateral and vertical transport of wake vortices is weakly influenced by ambient turbulence, and even a two-dimensional simulation may give good prediction of vortex transport behavior. This conclusion is premised on the absence of large eddy sizes, which can add uncertainty to the vortex trajectory prediction. The IGE numerical results do show good agreement with the measured data, except for the vortex altitude, which remained very, close to the ground in the observed case. Some uncertainties in vortex position data near the ground might be caused by either measurement error or effects from the unresolved features of the large-scale atmospheric flow. The primary conclusions of this study are:

1. Wake vortex transport can be influenced by the ground at altitudes up to 2.5 $b_o$.
2. Decay of the 5-15 $m$ average circulation is directly influenced by the ground following the initial descent below 0.6 $b_o$. The rate of decay becomes greatly enhanced several seconds after the vortex first reaches its minimum altitude; but prior to this time, the rate of decay is not affected by the ground.
3. Only a weak relation exists between the intensity of ambient turbulence and rate of decay during IGE.
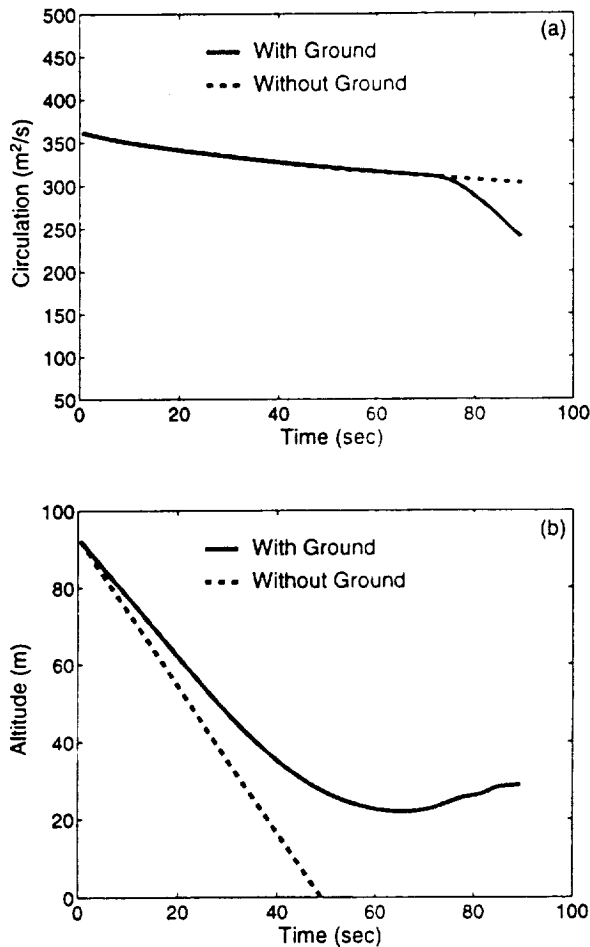


Figure 8. *Time evolution of a) 5-15 m averaged circulation, and b) vortex altitude, for simulation with vortex initiated at $Z_i$=2.5 $b_o$. The dashed line represents simulation without ground effect.*
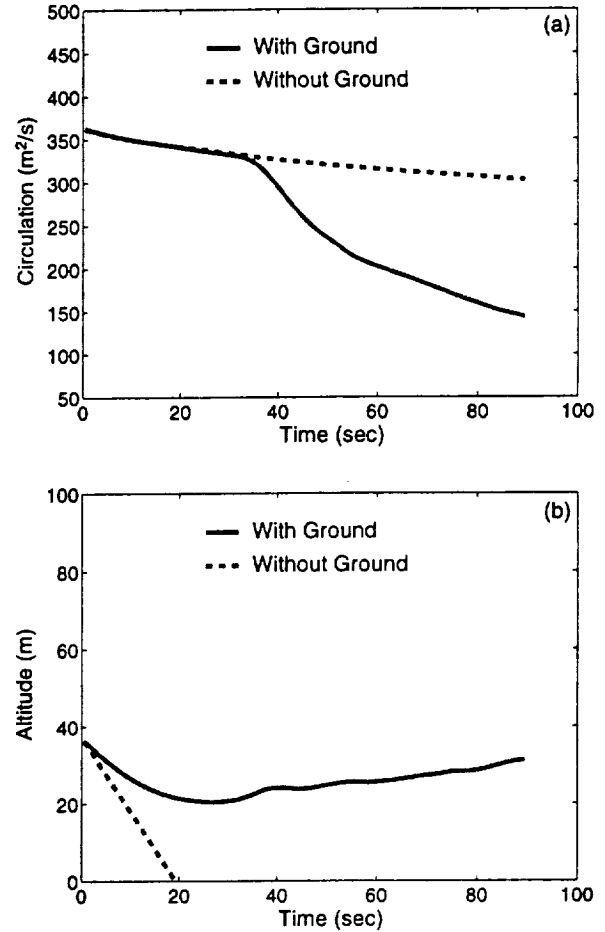


Figure 9. *Same as Fig. 8, but for simulation with wake initiated at $Z_i$= $b_o$.*

4. An increase in the surface roughness (and a corresponding increase in surface stress) acts to increase the rate of decay and increase the rebound height of the vortex.
5. Free slip conditions at the ground are inappropriate for models developed for IGE. Viscous stresses reduce the velocity near the surface and act to decouple the primary vortices from their sub-ground images. Ignoring this effect will result in unrealistic divergence of the vortex pairs.
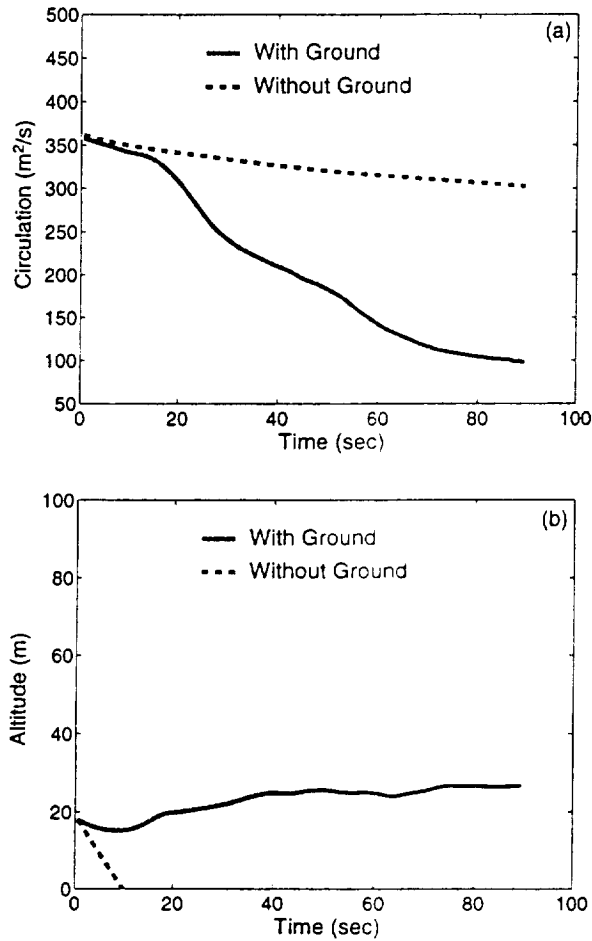
**Figure 10.** *Same as Fig. 8, but for simulation with wake initiated at $Z_i = 0.5 \, b_o$.*

## Acknowledgements

This research was sponsored by NASA's Terminal Area Productivity Program. One of the authors was funded under cooperative research grant NCCI-188. Numerical simulations were carried out on NASA and North Carolina Supercomputing Center supercomputers.

## Appendix

### Formulation for Surface Stress

The following formulation for surface stress was developed during an earlier NASA program and was originally applied to numerical studies of low-level wind shear. This formulation has been used in our wake vortex studies and is applicable to phenomenon having turbulent flow with strong local variations. [Other options for ground boundary conditions are available in TASS,[36] but are not used in our wake vortex simulations.]
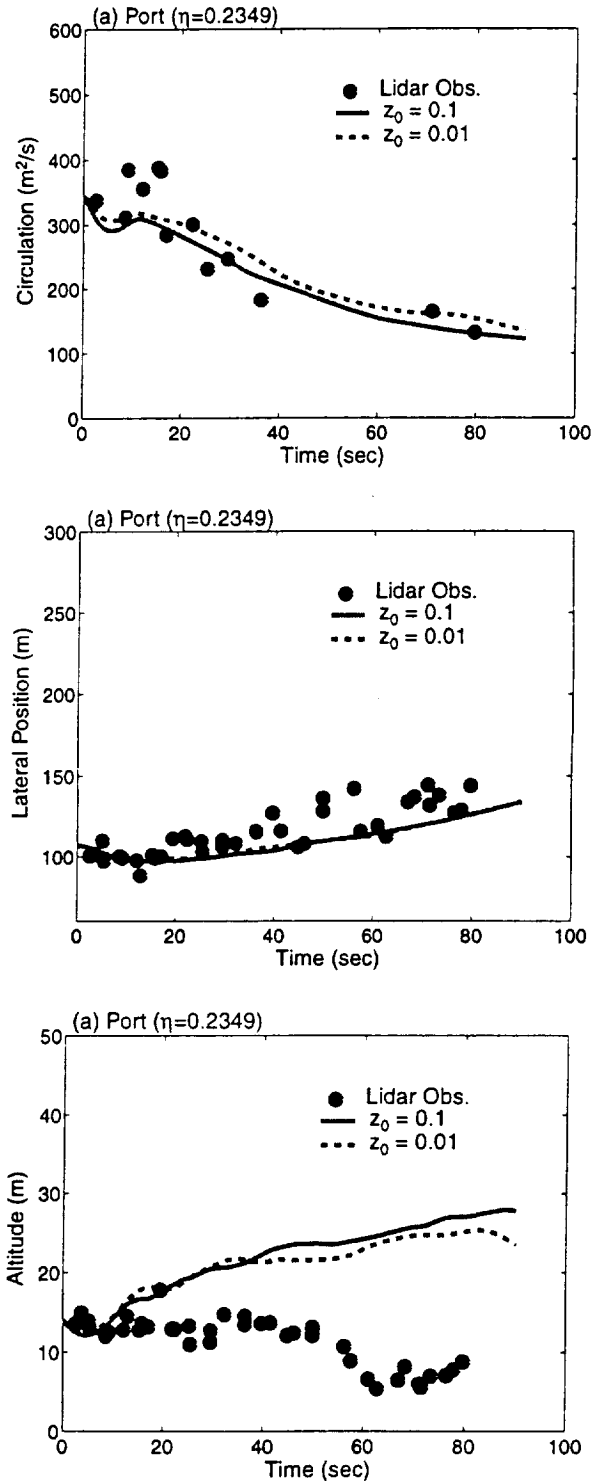


**Figure 11.** *Sensitivity to surface roughness parameter. Time evolution of a) 5-15 m averaged circulation, b) lateral position and c) vortex altitude for baseline simulation ($z_o = 0.1 m$) and simulation with $z_o = 0.01 m$.*

9
American Institute of Aeronautics and Astronautics

The surface stress formulation is used with a nonslip boundary condtion for velocity and a constant flux boundary condition for temperature and vapor. The subgrid stress at the ground $(z=0)$ is computed locally according to:

$$\tau_{uG} = \begin{cases} Max[\tau_u^*, \overline{\tau_u}(h_1)], & U(h_1) > 0 \\ Min[\tau_u^*, \overline{\tau_u}(h_1)], & U(h_1) \leq 0 \end{cases}$$

where,

$$\tau_u^* \equiv \overline{\tau_u}(h_1) + h_1 \frac{\overline{\tau_u}(h_2) - \overline{\tau_u}(h_1)}{h_2 - h_1},$$

and where, $\tau_{uG}$ is the subgrid stress at the ground for the $U$-component of horizontal velocity, $U(h_1)$ and $U(h_2)$ are the $U$-components at the first and second grid level above the ground, and $h_1$ and $h_2$ are the heights of the respective grid level.

In the above formulation, the local turbulence stresses at levels $h_1$ and $h_2$ are averaged horizontally over nine grid points. They are diagnosed as:

$$\tau_u(h) = \frac{\rho U(h) |\vec{V}(h)| k^2}{\left[ \ln(\frac{h - z_o}{z_o}) - \Psi(\frac{h - z_o}{L}) \right]^2}$$

where $k$ is von Karmen's constant $(=0.4)$, $|V|$ is the speed of the velocity vector, and $\Psi$ is a nondimensional stability parameter. The Monin-Obukhov (MO) length, $L$, is determined from the local Richardson number.

The stability parameter can be derived from the MO nondimensional shear functions presented in Hogstrom[37], for stable stratification $(L>0)$:

$$\Psi(x) = -5.3 x$$

and for unstable stratification $(L<0)$:

$$\Psi(x) = 2 \, ln\{[1+(1-19x)^{1/4}]/2\}+ln\{[1+(1-19x)^{1/2}]/2\}$$
$$-2 \tan^{-1}\{(1-19x)^{1/4}\} +\pi/2$$

where $x \equiv (h - z_o) / L$.

The above stability function for unstable stratification is approximated in a more computationally efficient form as:

$$\Psi(x) = -0.0627x^5 - 0.6067x^4 - 2.1689x^3 - 3.5874x^2 - 3.1536x$$

for $0 < x < -3.5$.

The surface stress for the $V$-component of horizontal velocity is computed in a similar fashion.

In the above formulation, the turbulence stress at the ground is a function of time and space. Note that either a decrease in the surface roughness, $z_o$, or an increase in stable stratification reduces the surface stress. Also, for either neutral stratification or strongly sheared flow, that $\Psi \sim 0$, and the surface stress depends only on the wind speed and $z_o$.

The above formulation was tested in a three-dimensional simulation of a thunderstorm downburst. The numerical simulation was set-up similar to the two-dimensional microburst simulations in Proctor.[38] Strong outflow is generated near the ground as the downdraft impinges upon the surface. An underestimate of the modeled surface stress will result in the outflow maximum being too close to the surface, while an overestimate will displace the maximum too high. Results from the numerical simulation are shown in Figures A1 and A2.

A vertical profile of the local outflow velocity is show in Figure A1. The profile is chosen at the outflow maximum and is compared with a field measurement and a laboratory wall jet. Following Bakke[39], the outflow velocity is normalized by its peak speed and the altitude is normalized by the half-velocity height. Note that the nondimensional profiles are in good agreement, showing the peak velocity at an elevation near 0.25.
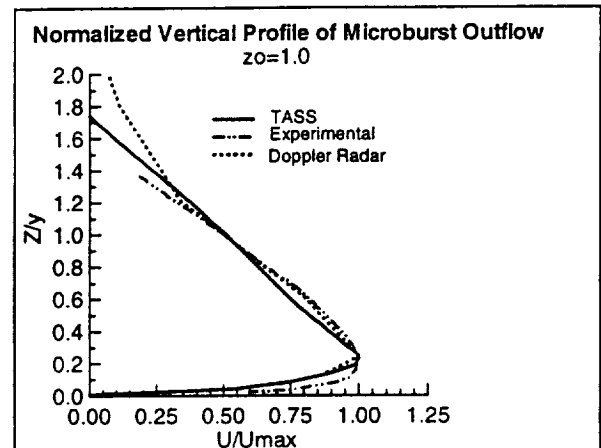


**Figure A1.** *Nondimensional vertical profile of downdraft outflow. Comparison of 3-D TASS with surface stress formulation with laboratory experiment[39] and a radar field measurement[40].*

In Fig. A2, the profile shows the outflow boundary layer is resolved by 4 grid points and the velocity profile exhibits a log variation with altitude. The intercept for $U = 0$ occurs at $z = 1m$ which agrees with the input

value assumed for $z_o$. The above comparisons lend support to the suitability of the stress formulation.
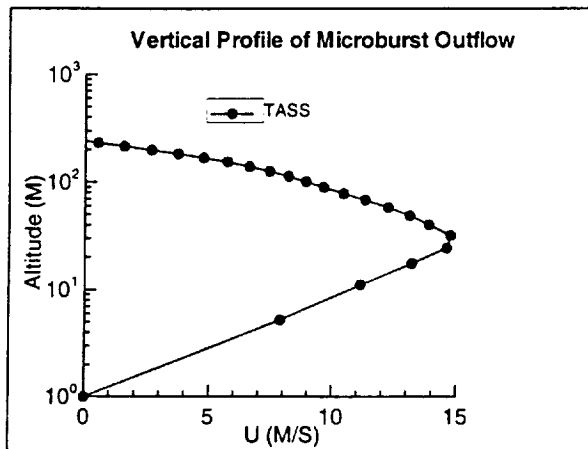


**Figure A2.** *Log-linear plot of altitude vs outflow speed for TASS simulation. Dots represent the vertical location of the grid points. The profile is chosen within the radius peak outflow.*
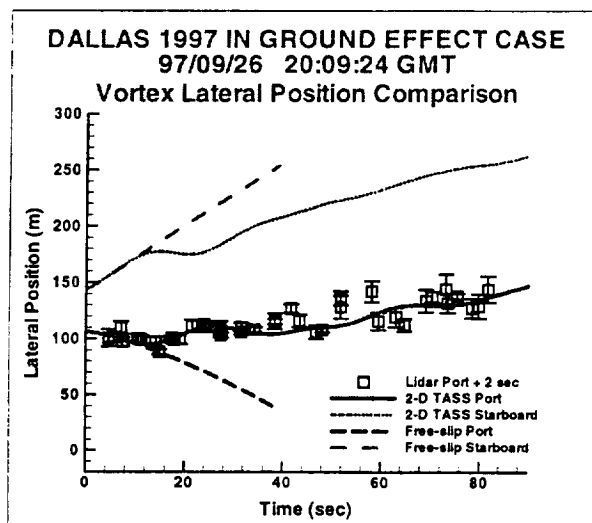


**Figure A3.** *Comparison of lateral time history for IGE 2-D simulations; results from free-slip (dashed) vs surface stress formulation (solid). Observed locations for the port vortex given by symbols.*

Free-slip vs Surface Stress Boundary Condition

The effects of the surface-stress formulation in comparison with a free-slip condition are evaluated for an IGE case in this section. Two experiments, one for each boundary condition, are conducted with the 2-D version of TASS. The experiments assume no ambient turbulence and a constant grid size of 0.5m, with other parameters as defined for the baseline case described in section 2.

A comparison of the time history for the lateral vortex position is shown in Figure A3. For the free-slip condition, the vortices rapidly diverge with the port vortex moving significantly upstream. For the simulation with the surface-stress formulation, the port and starboard vortices separate more slowly. Also, the port vortex moves little and shows good agreement with the location observed with Lidar. Vortex rebound does not occur with the free slip condition but does occur with the surfaces stress formulation. These experiments show that turbulence stress acting at the ground *significantly* affects lateral transport. The proper effects from surface stress should be included within any successful IGE prediction model.

**References**

[1]Hinton, D.A., "Aircraft Vortex Spacing System (AVOSS) Conceptual Design," NASA Tech. Memo No. 110184, August 1995, 27 pp.

[2]Hinton, D.A., Charnock, J.K., Bagwell, D.R., and Grigsby, D., "NASA Aircraft Vortex Spacing System Development Status," 37th Aerospace Sciences Meeting & Exhibit, Reno, NV,. AIAA-99-0753, January 1999, 17 pp.

[3]Robins, R.E., Delisi, D.P. and Greene, G.C., "Development and Validation of a Wake Vortex Prediction Algorithm," 36th Aerospace Sciences Meeting & Exhibit, AIAA-98-0665, January 1998, 10 pp.

[4]Proctor, F.H., "The NASA-Langley Wake Vortex Modelling Effort in Support of an Operational Aircraft Spacing System," 36th Aerospace Sciences Meeting & Exhibit, AIAA-98-0589, January 1998, 19 pp.

[5]Harvey, J.K., and Perry, F.J., "Flowfield Produced by Trailing Vortices in the Vicinity of the Ground," *AIAA Journal*, Vol. 9, No. 8, August 1971, pp. 1659-1660.

[6]Hallock, J.N., "Wake Vortex Decay Near the Ground," AIAA 8th Fluid and Plasma Dynamics Conf., Hartford, CN, AIAA-75-882, June 1975, 7 pp.

[7]Saffman, P., "The Approach of a Vortex Pair to a Plain Surface in Inviscid Fluid," *Journal of Aircraft*, Vol. 10, No. 11, November 1979, pp. 497-503.

[8]Atias, M. and Weihs, D., "Motion of Aircraft Trailing Vortices Near the Ground," *Journal of Aircraft*, Vol. 21, 1984, pp. 783-786.

[9]Schiling, V.K., "Motion and Decay of Trailing Vortices Within the Atmospheric Surface Layer," *Beitr. Phys. Atmos.*, Vol. 65, May 1992, pp. 157-169.

[10]Robins, R.E. and Delisi, D.P., "Potential Hazard of Aircraft Wake Vortices in Ground Effect with Crosswind," *Journal of Aircraft*, Vol. 30, No. 2, March-April 1993, pp. 201-206.

[11]Zheng, Z.C., and Ash, R.L., "Study of Aircraft Wake Vortex Behavior Near the Ground," *AIAA Journal*, Vol. 34, No. 3, March 1996, pp. 580-589.

[12]Corjon, A., and Stoessel, A., "Three-Dimensional Instability of Wake Vortices Near the Ground," 28th AIAA Fluid Dynamics Conf., Snowmass, CO, AIAA-97-1782, June-July 1997, 14 pp.

[13]Corjon, A. and Poinsot, T., "Behavior of Wake Vortices Near Ground," *AIAA Journal,* Vol. 35, No. 5, May 1997, pp. 849-855.

[14]Wickens, R.H., "A Technique for Simulating the Motion and Ground Effect of Aircraft Wake Vortices," *Canadian Aeronautics and Space Journal,* Vol. 26, No. 2, 1980, pp. 129-133.

[15]Burnham, D.C., and Hallock, J.N., "Measurements of Wake Vortices Interacting with the Ground," 36th Aerospace Sciences Meeting & Exhibit, AIAA-98-0593, January 1998, 12 pp.

[16]Tombach, I., "Observations of Atmospheric Effects on Vortex Wake Behavior," *Journal of Aircraft,* Vol. 10, November 1973, pp. 641-647.

[17]Donaldson, C. duP., and Bilanin, A.J., "Vortex Wakes of Conventional Aircraft," Advisory Group for Aerospace Research & Development, AGARDograph No. 204, May 1975.

[18]Sarpkaya, T., and Daly, J.J., "Effects of Ambient Turbulence on Trailing Vortices," *Journal of Aircraft,* Vol. 24, No. 6, June 1987, pp. 399-404.

[19]Liu, H.-T., "Effects of Ambient Turbulence on the Decay of a Trailing Vortex Wake," *Journal of Aircraft,* Vol. 29, No. 4, April 1992, pp. 255-263.

[20]Sarpkaya, T., "Decay of Wake Vortices of Large Aircraft," *AIAA Journal,* Vol. 36, No. 9, September 1998, pp. 1671-1679.

[21]Han, J., Lin, Y.-L., Arya, S.P., and Proctor, F.H., "Large Eddy Simulation of Aircraft Wake Vortices in a Homogeneous Atmospheric Turbulence: Vortex Decay and Descent," 37th Aerospace Sciences Meeting & Exhibit, AIAA-99-0756, January 1999, 21 pp.

[22]Corjon, A., Zheng, Z.C., and Greene, G.C., "Model of the Behavior of Aircraft Wake Vortices Experiencing Crosswind Near the Ground," 14th AIAA Applied Aerodynamics Conference, New Orleans, LA, AIAA-96-2519, June 1996, 7 pp.

[23]Greene, G.C., "An Approximate Model of Vortex Decay in the Atmosphere," *Journal of Aircraft,* Vol. 23, July 1986, pp. 566-573.

[24]NASA Langley Research Center, "Meteorological & Wake Vortex Data Set, Dallas-Fort Worth International Airport, September 15-October 3, 1997," November 1998, Compact Disc.

[25]Delisi, D.P. and Robins, R.E., Northwest Research Associates, personal communication, September 1998.

[26]Proctor , F.H., "The Terminal Area Simulation System, Volume 1: Theoretical Formulation," NASA Contractor Report 4046, DOT/FAA/PM-85/50, 1, April 1987, 176 pp.

[27]Proctor, F.H., "Numerical Simulation of Wake Vortices During the Idaho Falls and Memphis Field Programs," 14th AIAA Applied Aerodynamics Conference, Proceedings, Part-II, New Orleans, LA, AIAA-96-2496, June 1996, pp. 943-960.

[28]Switzer, G.F., "Validation Tests of TASS for Application to 3-D Vortex Simulations," NASA Contractor Report No. 4756, October 1996, 11 pp.

[29]Han, J., Lin, Y.-L., Schowalter, D.G., Arya, S.P., and Proctor, F.H., "Large Eddy Simulation of Aircraft Wake Vortices in a Homogeneous Atmospheric Turbulence: The Crow Instability," Accepted for publication in *AIAA Journal.*

[30]Crow, S.C., "Stability Theory for a Pair of Trailing Vortices," *AIAA Journal,* Vol. 8, No. 12, December 1970, pp. 2172-2179.

[31]Shen, S., Ding, F., Han, J., Lin, Y.-L., Arya, S.P., and Proctor, F.H., "Numerical Modeling Studies of Wake Vortices: Real Case Simulations," 37th Aerospace Sciences Meeting & Exhibit, AIAA-99-0755, January 1999, 16 pp.

[32]Campbell, S.D., Dasey, T.J., Freehart, R.E., Heinrichs, R.M., Matthews, M.P., Perras, G.H., and Rowe, G.S., "Wake Vortex Measurement Program at Memphis, TN, Data Guide," Project Report: NASA/L-2, January, 1997 (also in NASA CR-201690, April 1997).

[33]Delisi, D., Northwest Research Associates, personal communication, December 1998.

[34]Rayleigh, L., "On the Dynamics of Revolving Fluids," *Proc. Royal Soc. London,* A, Vol. 93, 1917, pp. 148-154 (also in *Scientific Papers,* Vol. 6, pp. 447-453).

[35]Stull, R.B., *An Introduction to Boundary Layer Meteorology,* Kluwer Academic Publishers, 1988.

[36]Schowalter, D.G., DeCroix, D.S., Lin, Y.-L., Arya, S.P., and Kaplan, M.L., "The Sensitivity of Large-Eddy Simulation to Local and Nonlocal Drag Coefficients at the Lower Boundary," NASA Contractor Report 198310, April 1996, 43 pp.

[37]Hogstrom, U., "Review of Some Basic Characteristics of the Atmospheric Surface Layer," *Boundary-Layer Meteorology,* Vol. 78, 1996, pp. 215-246.

[38]Proctor, F.H., "Numerical Simulation of an Isolated Microburst. Part I: Dynamics and Structure," *J. Atmos. Sci.,* Vol 45, No. 21, November 1988, pp. 3137-3160.

[39]Bakke, P., "An Experimental Investigation of a Wall Jet," *J. Fluid Mech.,* Vol. 2, 1957, pp. 467-472.

[40]Fujita, T.T., 1981, "Tornadoes and Downbursts in the Context of Generalized Planetary Scales," *J. Atmos. Sci.,* Vol. 38, 1981, pp. 1511-1534.

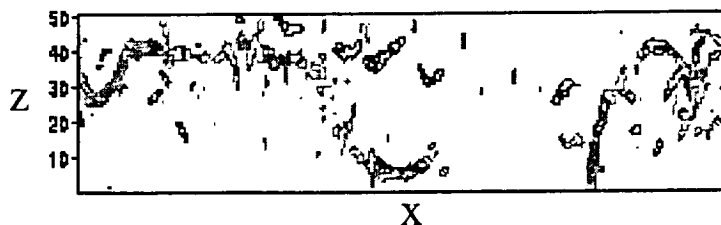**Appendix H: Wake Vortex Transport and Decay in Ground Effect: Vortex Linking with the Ground**

# AIAA 2000-0757

## Wake Vortex Transport and Decay in Ground Effect: Vortex Linking with the Ground

Fred H. Proctor and David W. Hamilton
NASA Langley Research Center
Hampton, VA

Jongil Han
North Carolina State University
Raleigh, NC

# 38th Aerospace Sciences Meeting & Exhibit
## January 10-13, 2000 / Reno, NV

# Wake Vortex Transport and Decay in Ground Effect: Vortex Linking with the Ground

Fred H. Proctor* and David W. Hamilton[†]
*NASA Langley Research Center*
*Hampton, Virginia*

Jongil Han[‡]
*North Carolina State University*
*Raleigh, NC*

## Abstract

*Numerical simulations are carried out with a three-dimensional Large-Eddy Simulation (LES) model to explore the sensitivity of vortex decay and transport in ground effect (IGE). The vortex decay rates are found to be strongly enhanced following maximum descent into ground effect. The nondimensional decay rate is found to be insensitive to the initial values of circulation, height, and vortex separation. The information gained from these simulations is used to construct a simple decay relationship. This relationship compares well with observed data from an IGE case study. Similarly, a relationship for lateral drift due to ground effect is constructed from the LES data. In the second part of this paper, vortex linking with the ground is investigated. Our numerical simulations of wake vortices for IGE show that a vortex may link with its image beneath the ground, if the intensity of the ambient turbulence is moderate to high. This linking with the ground (which is observed in real cases) gives the appearance of a vortex tube that bends to*

*become vertically oriented and which terminates at the ground. From the simulations conducted, the linking time for IGE appears to be similar to the linking time for vortices in the free atmosphere; i.e., a function of ambient turbulence intensity.*

## Nomenclature

| | |
|---|---|
| $B$ | aircraft wing span |
| $b_o$ | initial vortex separation - $\pi B/4$ |
| $g$ | acceleration due to gravity |
| $L_x, L_y$ | domain length in x and y directions, respectively |
| $L_z$ | domain depth |
| $M$ | mass of generating aircraft |
| $r$ | radius from vortex center |
| $r_c$ | radius of peak tangential velocity |
| $t$ | time coordinate |
| $T$ | nondimensional time - $t\,V_o/b_o$ |
| $T_G$ | T at $z = z_{min}$ |
| $V_a$ | airspeed of generating aircraft |
| $V_o$ | initial vortex descent velocity - $\Gamma_o/(2\,\pi\,b_o)$ |
| $x$ | horizontal coordinate along flight path |
| $y$ | horizontal coordinate lateral to fight path |
| $Y$ | nondimensional lateral coordinate - $y/b_o$ |
| $z$ | vertical coordinate |
| $z_{min}$ | minimum altitude achieved during vortex descent |
| $Z_i$ | initial height above ground of wake vortex |
| $\Gamma$ | vortex circulation |
| $\Gamma_o$ | initial vortex circulation - $M\,g/(b_o\,\rho\,V_a)$ |
| $\rho$ | air density |
| $\epsilon$ | ambient turbulence (eddy) dissipation rate |
| $\zeta_x$ | x-component of vorticity |
| $\nu$ | kinematic viscosity |
| $\eta$ | nondimensional eddy dissipation - $(\epsilon\,b_o)^{1/3}\,V_o^{-1}$ |

---

*Research Scientist, Airborne Systems Competency, AIAA member

[†]Research Scientist, Airborne Systems Competency

[‡]Research Scientist, Department of Marine, Earth, and Atmospheric Sciences, AIAA member

## I. Introduction

Aircraft wake vortices are formed when vorticity generated by lift rolls up into two primary trailing vortices. The two vortices have a characteristic initial separation, $b_o$, which is proportional to the wingspan of the generating aircraft. The wake vortices are considered to be "in ground effect" (IGE) when located within one initial separation of the ground (i.e., $z < b_o$).[1] The prediction for the location and intensity of these vortices is important for systems that are to manage safe aircraft spacings.

The complex influence of the ground on wake vortex behavior has been the focus of numerous investigations, including the observations by Harvey and Perry,[2] Hallock,[3] Kopp,[4] Hallock and Burnham,[5] Burhnam and Hallock,[6] and Rudis et al.,[7] as well as the numerical studies by Schiling,[8] Robins and Delisi,[9] Zheng and Ash,[10] Corjon and Poinsot,[11] Corjon and Stoessel,[12] and Proctor and Han.[13] Qualitative understanding of basic vortex transport mechanisms for IGE is known, but quantitative relationships are needed. Wake vortex decay is known to be enhanced by proximity to the ground, but much is to be learned about this behavior.[6]

Three-dimensional instability of wake vortices near the ground is largely unexplored. Lateral linking of the vortex pair associated with Crow instability[14] should be less likely due to the increased separation forced by the ground's presence. Ground linking -- the linking of a vortex with its image vortex beneath the ground plane -- has been observed,[15] but thought to be rare.[16] Linking instabilities can increase the uncertainty of a vortex's position and may affect the vortex decay rate as well.

Semi-empirical vortex prediction algorithms have been developed by Robins et al.[1] that include the ground's influence on lateral separation and vortex rebound. Similar algorithms[17] have been incorporated within NASA's Aircraft VOrtex Spacing System (AVOSS).[18,19,20] Improved accuracy of these prediction algorithms depend on the better understanding of vortex transport and decay near the ground. Numerical experiments with a Large Eddy Simulation (LES) model are being conducted in order to provide guidance for the enhancement of these prediction algorithms.[21]

This paper is a continuation of the three-dimensional LES study described in Proctor and Han,[13] with further focus on vortex decay within IGE. In Proctor and Han, we investigated the sensitivity over a wide range of ambient turbulence levels of a wake vortex for a landing L-1011 that was observed on 26 September 1997 at Dallas-Fort Worth (DFW) airport.[22] The simulations showed only a weak sensitivity to the level of ambient turbulence, and were in very-good agreement with Lidar-derived observations. The results indicated that enhanced decay from ground effect begins a few seconds after the vortices descend to their minimum height, with vortex decay prior to these times being primarily influenced by stratification and ambient turbulence. The study also found that vertical oscillations associated with vortex rebound were less prominent for higher levels of ambient turbulence, since the secondary vortices were more likely to be diminished by the stronger turbulence. Also addressed was the influence of ground stress on wake vortex transport. The study determined that viscous stress reduced the velocity near the ground and acted to decouple the primary vortices from their sub-ground images. If ground stress was ignored, unrealistic divergence of the vortex pairs ensued. The study, did not address Crow instability, or similar linking instabilities,

**Table 1. Salient Characteristics of TASS**

Primitive equation / non-Boussinesq equation set Time-dependent, nonhydrostatic, compressible.

Meteorological framework with option for either three-dimensional or two-dimensional simulations.

Large Eddy Simulation model with 1st-order subgrid scale turbulence closure -- Grid-scale turbulence explicitly computed, while effects of subgrid-scale turbulence modeled by Smagorinsky model with modifications for stratification and flow rotation.

Ground stress based on Monin-Obukhov Similarity theory.

Optional boundary conditions -- open conditions utilizes mass-conservative, nonreflective radiation boundary scheme.

Explicit numerical schemes, quadratic conservative, time-split compressible-- accurate as well as highly efficient, and essentially free of numerical diffusion. Space derivatives computed on Arakawa C-grid staggered mesh with 4th-order accuracy for convective terms.

Prognostic equations for vapor and atmospheric water substance (e.g. cloud droplets, rain, snow, hail, ice crystals). Large set of microphysical-parameterization models.

Model applicable to meso-γ and microscale atmospheric phenomenon. Initialization modules for simulation of convective storms, microbursts, atmospheric boundary layers, turbulence, and aircraft wake vortices.

since the assumed domain had a limited axial depth. In the present paper, we address the sensitivity of vortex decay for IGE, by conducting LES of wake vortices with different initial heights, separations and circulations. The results are normalized and a simple analytical representation for IGE decay is given. Similarly, a simple model based on the LES results is proposed for lateral drift due to ground effect. In the second part of this paper, we examine the occurrence of ground linking and its sensitivity to ambient turbulence.

## II. The Model and Initial Conditions

The numerical model used in this study is a three-dimensional LES model called the Terminal Area Simulation System[23] (TASS), which has been adapted for simulation of wake vortex interaction with the atmosphere.[24] The numerical model used in this study differs from that in many previous investigations, in that: 1) time-dependent computations are carried out in three-dimensional space, 2) the formulation is essentially free of numerical diffusion,[25] 3) the computations are LES and at high Reynolds number, 4) the experiments are initialized with realistic turbulence fields, and 5) realistic surface-stress and subgrid turbulence-closure formulations are assumed. Salient characteristics of TASS are listed in table 1.

### Model Equations

The TASS model contains a prognostic equation set for momentum, temperature and pressure, and employs a compressible time-split formulation. Omitting moisture and coriolis terms (which are not used in these simulations), the TASS equation set in standard tensor notation is as follows:

*Momentum:*

$$\frac{\partial u_i}{\partial t} + \frac{H}{\rho_o}\frac{\partial p}{\partial x_i} = -\frac{\partial u_i u_j}{\partial x_j} + u_i\frac{\partial u_j}{\partial x_j} + g(H-1)\delta_{i3}$$

$$+\frac{1}{\rho_o}\frac{\partial}{\partial x_j}\rho_o K_M\left[\frac{\partial u_i}{\partial x_j} + \frac{\partial u_j}{\partial x_i} - \frac{2}{3}\frac{\partial u_k}{\partial x_k}\delta_{ij}\right]$$

*Buoyancy Term:*

$$H = \left[\frac{\theta}{\theta_o} - \frac{p\,C_v}{P_o C_p}\right]$$

*Pressure Deviation:*

$$\frac{\partial p}{\partial t} + \frac{C_p P}{C_v}\frac{\partial u_j}{\partial x_j} = \rho_o\,g\,u_j\,\delta_{j3}$$

*Thermodynamic Equation (Potential Temperature):*

$$\frac{\partial \theta}{\partial t} = -\frac{1}{\rho_o}\frac{\partial \theta \rho_o u_j}{\partial x_j} + \frac{\theta}{\rho_o}\frac{\partial \rho_o u_j}{\partial x_j}$$

$$+\frac{1}{\rho_o}\frac{\partial}{\partial x_j}[\rho_o K_H \frac{\partial \theta}{\partial x_j}]$$

with the *Potential Temperature* defined as:

$$\theta = \tau\left(\frac{P_{oo}}{P}\right)^{\frac{R_d}{C_p}}$$

In the above equations, $u_i$ is the tensor component of velocity, $t$ is time, $p$ is deviation from atmospheric pressure $P$, $\tau$ is atmospheric temperature, $\rho$ is the air density, $C_p$ and $C_v$ are the specific heats of air at constant pressure and volume, $g$ is the earth's gravitational acceleration, $R_d$ is the gas constant for dry air, $P_{oo}$ is a constant equivalent to 1000 millibars ($10^5$ pascals) of pressure. Environmental state variables, e.g., $\rho_o$, $P_o$ and $\theta_o$, are defined from the initial input sounding and are functions of height only.

A modified Smagorinsky first-order closure is used for the subgrid eddy viscosity as:

$$K_M = l_s^2\sqrt{\frac{\partial u_i}{\partial x_j}\left(\frac{\partial u_i}{\partial x_j} + \frac{\partial u_j}{\partial x_i}\right) - \frac{2}{3}\left(\frac{\partial u_k}{\partial x_k}\right)^2}$$

$$\times\sqrt{1 - \alpha_1 Ri_s - \alpha_2 Ri_r}$$

The subgrid eddy viscosity for momentum, $K_M$, is modified by the Richardson numbers, for stratification, $Ri_s$, and for flow rotation, $Ri_r$, with $\alpha_1=3$ and $\alpha_2=1.5$.

The subgrid length scale, $l_s$, is determined from the grid volume and is matched to the appropriate length scale close to the ground where the flow is under-resolved. That is:

$$l_s = \begin{cases} \alpha\Delta & z \geq \alpha\Delta/k \\ \dfrac{\alpha\Delta\,[1+(\alpha\Delta/k\,z)^{m-1}]}{1+(\alpha\Delta/k\,z)^m} & \alpha\Delta/k > z > \Delta z/2 \\ k\,z & z \leq \Delta z/2 \end{cases}$$

where $k$ is von Karman's constant, and where $m$ and $\alpha$ are invariant constants with values defined as $m = 3$ and $\alpha = 0.15$. The filter width is based on the minimal resolvable scale:

$$\Delta = [\,2\Delta x\,2\Delta y\,2\Delta z\,]^{1/3}$$

where $\Delta x$, $\Delta y$, and $\Delta z$ are the numerical grid sizes in the respective $x$, $y$, $z$ direction.

The ground boundary is impermeable with nonslip velocity specifications. The surface stress due to the ground is determined locally from the wind speed, surface roughness, and the local thermal stratification. Details of the surface formulation are in the appendix of reference [13].

## Turbulence Initialization

Prior to vortex initialization, an initial field of resolved-scale turbulence is allowed to develop under an artificial external forcing at low wavenumbers.[26] The approach is similar to that in recent studies with TASS, where wake vortex decay and the development of Crow instability is examined within a Kolmogorov[27] spectrum of homogeneous turbulence (Han et al.[28,29]). The method, however, is slightly different for the present study, due to the inclusion of the ground. Since periodic boundary conditions are assumed only at the horizontal boundaries, the turbulence forcing is applied only to horizontal velocity over each horizontal plane. Nevertheless, the influence of the horizontal two-dimensional forcing spreads quickly to the vertical direction as well as to the vertical velocity through the mass continuity.
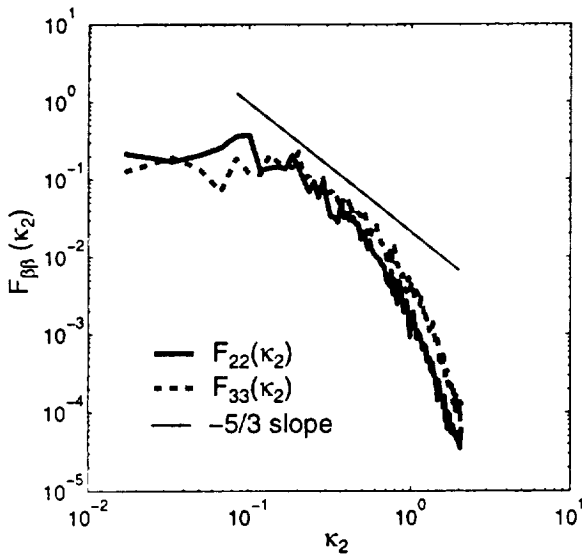


**Figure 1.** *Turbulence energy spectrum at z=14 m before vortex injection. Here, subscripts 2 and 3 denote crossflow and vertical directions, respectively.*

Because the TASS code uses a finite difference numerical scheme, the forcing is achieved by performing, first, a two-dimensional fast Fourier transform (FFT) at every large time step, then adding a constant amplitude to all the modes with integer wavenumbers whose magnitude

is less than 3.0, and finally, performing an inverse FFT back to the physical space. At the same time, the horizontal domain average temperature and velocity fields are forced to maintain their initial vertical profiles by subtracting the difference every time step. Due to subgrid dissipation, the simulation can reach a statistically steady state, in the sense that the mean turbulence kinetic energy oscillates in time around a constant value.

Figure 1 shows a one-dimensional energy spectrum with a -5/3 slope of Kolmogorov's[27] spectrum when the turbulent flow field has achieved a statistically steady state. Figure 1 indicates that our approach can produce a well-developed turbulent flow field that possesses Kolmogorov's inertial subrange. The eddy dissipation rate $\varepsilon$ is estimated from the well-known technique of fitting Kolmogorov's theoretical spectrum in the inertial subrange to the simulated spectra.

## Vortex Initialization

The initial wake vortex field is specified with a simple vortex system that is representative of the post roll-up, wake-vortex velocity field. The vortex system is initialized with the superposition of two counter-rotating vortices that have no initial variation in the axial direction. The tangential velocity, $V$, associated with each vortex, is determined from:

$$V(r) = \frac{\Gamma_\infty}{2\pi r}\left[ 1 - Exp\left(-10\left(\frac{r}{B}\right)^{0.75}\right)\right]$$

where, $r$ is the radius from the center of the vortex, $\Gamma_\infty$ the circulation at $r \gg r_c$, and $B$ is the span of the generating aircraft. The above formula is based on Lidar observations of wake vortices measured early in their evolution. The model is applied only at $r > r_c$ and is matched with a Lamb model profile for $r < r_c$. The values assumed for initial vortex separation and circulation are derived from an aircraft's weight, span, and airspeed according to conventional formula based on elliptical loading; i.e., $b_o = \pi B/4$, and $\Gamma_\infty = 4Mg/(\pi B\rho V_a)$. Appropriate vortex image conditions are applied to the initial wake field to ensure consistency and mass continuity at the TASS model boundaries.

Except when otherwise noted, the initial vortex parameters (table 2) are taken from the observed aircraft parameters for the L-1011, as was used in Proctor and Han.[13]

All simulations are conducted with dimensional variables and assume turbulent flow with a rotational Reynolds number ($\Gamma_o/\nu$) of ~$10^7$.

**Table 2.** *Initial vortex parameters (baseline).*

| Parameter | Value |
|-----------|-------|
| Vortex spacing $(b_o)$ | 37 m |
| Generating height $(Z_i)$ | 16 m    (0.432 $b_o$) |
| Vortex circulation $(\Gamma_o)$ | 390 $m^2 s^{-1}$ |
| Vortex core radius | 3 m    $(b_o/12.3)$ |

<u>Model Domain Parameters</u>

Two domain sizes are used for the experiments in this paper. A short domain, which has been truncated in the x-direction $(L_x, L_y, L_z = 81\ m, 370\ m, 81\ m)$, and a long domain $(L_x, L_y, L_z = 451\ m, 337\ m, 81\ m)$. For an assumed initial vortex separation of $b_o=37\ m$, this would translate into: $(2.2 \times 10 \times 2.2)\ b_o$ for the short domain and $(12.2 \times 9.1 \times 2.2)\ b_o$ for the long domain. Both long and short domains are resolved by the grid sizes listed in table 3.

**Table 3.** *Grid Resolution.*

| Parameter | Value |
|-----------|-------|
| Vertical resolution $(\Delta z)$ | 1.5 m |
| Lateral resolution $(\Delta y)$ | 1.5 m |
| Axial resolution $(\Delta x)$ | 2.0 m |

The advantage of the short domain is that it allows economical calculations of vortex behavior and simplifies the analysis of results. The longer domain, however, is less likely to hinder three-dimensional linking instabilities. A comparison of results from the two domain sizes is shown in the appendix.

<u>Determination of Vortex Position and Circulation</u>

Based on the vortex position in each crossflow plain, circulation is computed for each crossflow plane according to:

$$\Gamma_r(x) = \iint_r \zeta_x\ dydz$$

The circulation is not computed for any plane where the vorticity vector is beyond 30° of the x-axis.

A *5-15 meter* averaged-circulation, is computed according to:

$$\overline{\Gamma}^{a,b} = \frac{\int_a^b \Gamma_r dr}{\int_a^b dr}$$

where $a=5\ m$, and $b = 15\ m$. The *5-15 m* average circulation is chosen to characterize the intensity of the vortex, since it quantifies the hazard faced by an encountering aircraft[30,31]

A mean average circulation is reported for each time interval by computing a mean of the circulations from each crossflow plane:

$$\overline{\Gamma_{\bar{x}}}^{\,a,b} = \frac{1}{N}\sum_i^N \overline{\Gamma_i}^{\,a,b}$$

Similarly, a mean vortex position is reported for each time interval by averaging the positions from each crossflow plane.

### III. IGE Sensitivity

Three sets of experiments are conducted in order to determine the sensitivity of vortex decay within IGE. The short domain is assumed which will inhibit the occurrence of linking instabilities. All of the simulations assume neutral stratification, no mean ambient winds, and an ambient turbulence dissipation rate of $\epsilon = 9.6 \times 10^{-5}\ m^2\ s^{-3}$. Other initial conditions for the simulations are listed in tables 2 and 3.

<u>Sensitivity to Initialization Height</u>

Five experiments are conducted for a vortex initialization height $(Z_i)$ of: $0.32\ b_o$, $0.5\ b_o$, $0.65\ b_o$, $0.84\ b_o$, and $1.0\ b_o$. Comparisons of the experiments are shown in Fig. 2 as function of nondimensional time. Note that the time coordinate for each experiment is offset by the time of maximum descent into ground effect; i.e., by $T_G=T(z_{min})$. The curves for normalized $5\text{-}15\ m$ average circulation, as well as the normalized lateral positions tend to collapse, once the offset time $T_G$ is accounted for. As also shown in our previous study,[13] vortex decay is significantly enhanced following maximum penetration into IGE. In addition, these results show the decay rate to be more or less independent of the vortex initial height, with the enhanced level of decay beginning roughly $0.25$ nondimensional time units following $T_G$.

A formula for the decay of average circulation can be obtained from these results as

$$\frac{\Gamma}{\Gamma_{oo}} = Exp\{\frac{-2(T - T_{oo})^{2/3}}{5}\} \qquad (1)$$

where $T_{oo} = T_G +0.25$ (i.e., $0.25$ nondimensional time units following the time of maximum penetration into ground effect), and $\Gamma_{oo}$ is the circulation at nondimensional time $T_{oo}$. The above formula is independent of ambient turbulence and can only be applied for $T > T_G +0.25$.

Differentiating the above gives the rate of decay as:

$$\frac{1}{\Gamma_{oo}} \frac{d\Gamma}{dT} = -\frac{4}{15(T-T_{oo})^{1/3}} Exp\{\frac{-2(T-T_{oo})^{2/3}}{5}\}$$

A plot of the curve from *Eq. 1* is shown also in Fig. 2c and agrees very well with the LES results.

An empirical relationship for lateral spread within IGE can be determined from the LES results as well. The vortices, which start at a lateral distance from the flight path of $y = \pm \frac{1}{2}b_o$, diverge lateral with time due to the influence of the ground. Figure 2b indicates (in the absence of crosswind) that the vortices asymptote toward $y = 2b_o$; approaching a maximum separation of about $4b_o$. Based on these results, an empirical relationship for vortex drift due to ground effect is:

$$Y = 1.385 (T-T_G)^{0.227} \quad for \quad T > T_G + 0.25 \quad (2)$$

where $Y$ is the normalized lateral position from the flight path. The vortex separation, $b = 2Yb_o$, also can be predicted for IGE with Eq. 2. A plot of the curve from *Eq. 2* is compared with LES data in Fig. 2b.

The lateral drift rate can be determined by differentiating (2) giving:

$$V_G = \frac{dY}{dT} = 0.3173(T-T_G)^{-0.773} \quad for \quad T > T_G + 0.25$$

where $V_G$ is the nondimensional velocity for lateral drift due to ground effect (this velocity can be made dimensional by multiplying by the initial vortex sink rate, $V_o$).

<u>Sensitivity to Initial Vortex Spacing</u>

In order to further evaluate the sensitivity of our results and test the validity of *Eq. 1*, three additional experiments are conducted, which assume different initial vortex spacings $(b_o)$ as listed in table 4. An initial circulation of $400 \ m^2s^{-1}$ and an initial height of $Z_i = 0.432 \ b_o$ is assumed for each experiment. Values for $Z_i$ and nondimensional turbulence dissipation are slightly different in these experiments due to the variation in $b_o$.
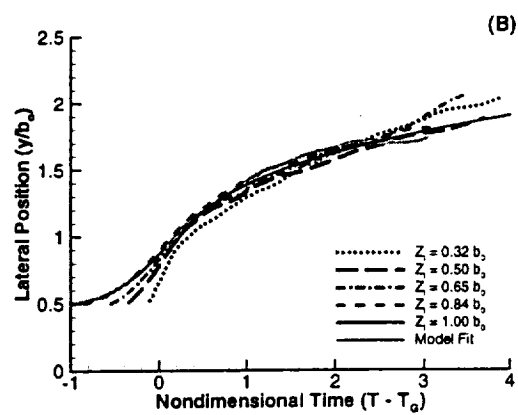
**Table 4.** *Initial vortex separation $(b_o)$ and corresponding initial altitude $(Z_i)$ and dimensionless turbulence intensity $(\eta)$ for sensitivity to initial vortex spacing cases.*

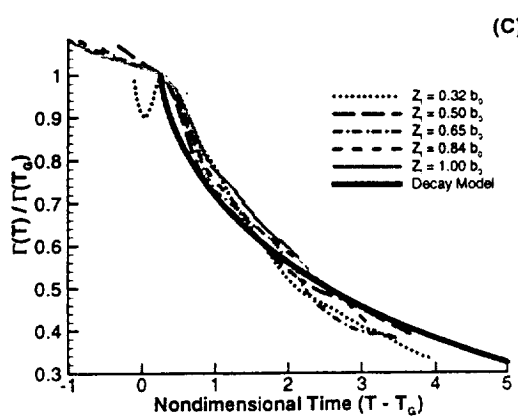| $b_o \ (m)$ | $Z_i \ (m)$ | $\eta$ |
|---|---|---|
| 30 | 13 | 0.0671 |
| 37 | 16 | 0.0897 |
| 49 | 21.2 | 0.1291 |
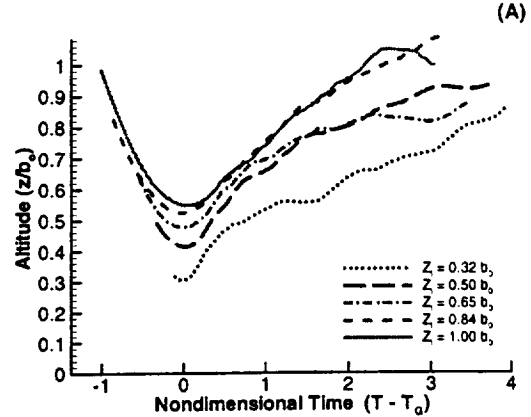


**Figure 2.** *Sensitivity to vortex initiation height. Nondimensional height (a), nondimensional lateral position (b), and nondimensional 5-15 m average circulation (c) vs nondimensional time. "Decay model" in (C) from Eq.1 and "Curve fit" in (B) from Eq.2.*
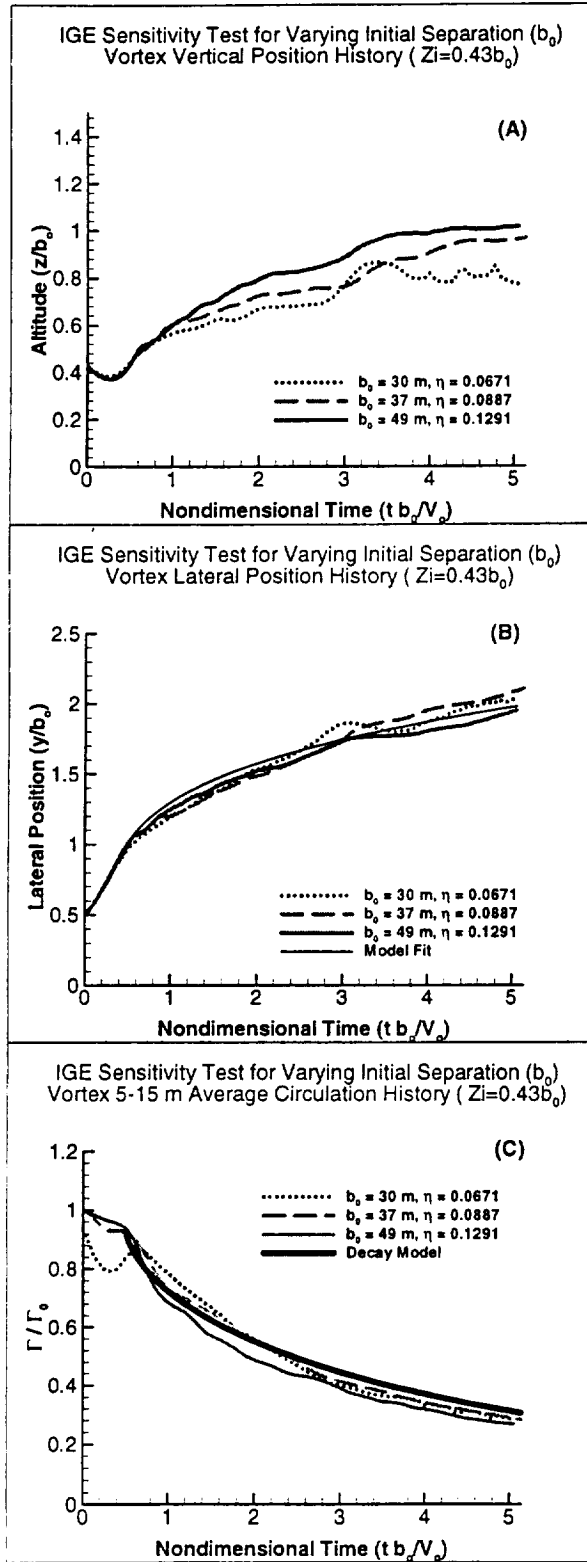
**Figure 3.** *Same as Fig. 2, but for sensitivity to initial vortex spacing.*
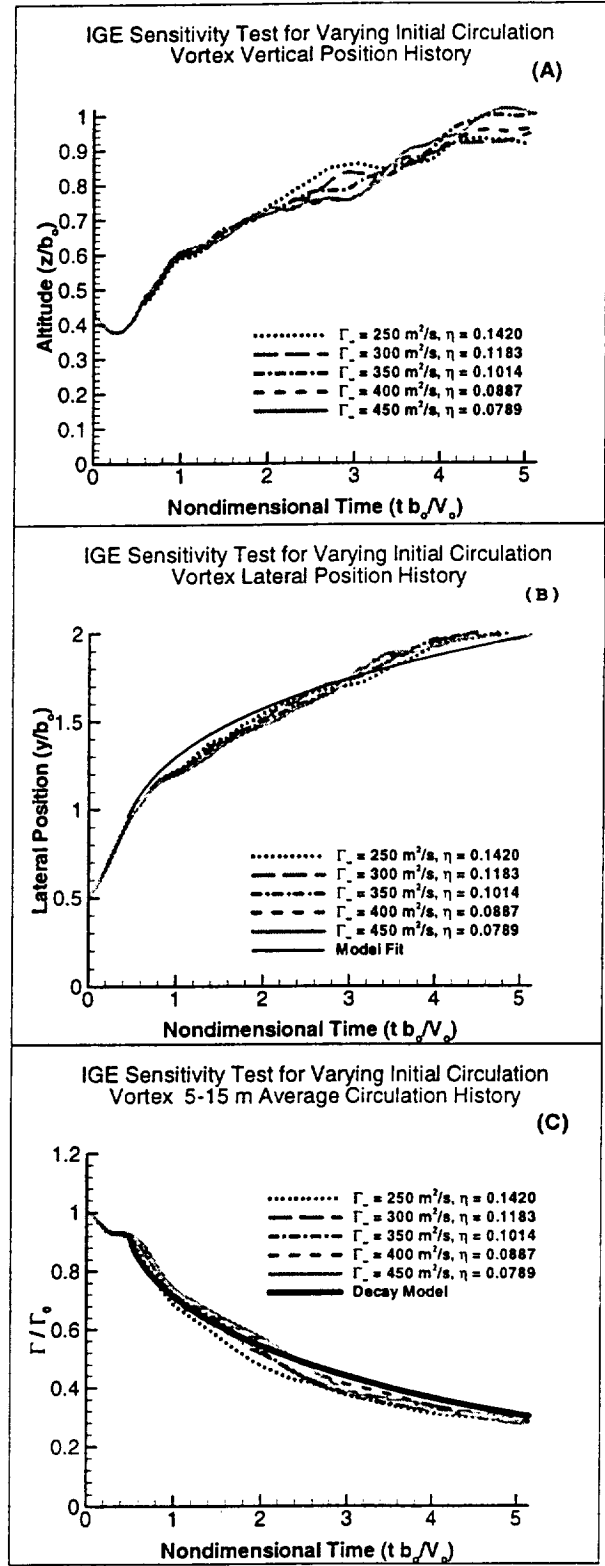


**Figure 4.** *Same as Fig.2, but for sensitivity to initial vortex circulation.*

The results presented in Fig. 3 show that the curves again collapse to a similar value when normalized, and that the proposed formulas for IGE decay and lateral drift are in excellent agreement with the LES results. Enhanced levels of decay due to IGE begin at $T=0.5$ (which is $T_G+0.25$) for all three cases.

## Sensitivity to Initial Circulation

In the third set of experiments, five simulations with different initial circulations are conducted (table 5). All else is assumed equal, with $\eta$ being different due to its dependency on $\Gamma_o$.

Again, the curves collapse with a tight spread (Fig. 4), and the proposed IGE decay and drift formulas are in excellent agreement with LES results.

**Table 5.** *Initial circulation ($\Gamma_o$) and corresponding dimensionless turbulence intensity for $\Gamma$ sensitivity cases.*

| $\Gamma_o$ ($m^2s^{-1}$) | $\eta$ |
|---|---|
| 250 | 0.1420 |
| 300 | 0.1183 |
| 350 | 0.1014 |
| 400 | 0.0887 |
| 450 | 0.0789 |

## IV. Comparison with Observed Case.

In this section, the new formula for IGE decay (Eq. 1) is compared with the LES simulation for a landing *L-1011*, which was observed at *20:09 UTC* on *26 September 1997* at Dallas-Fort Worth (DFW) airport. The input sounding for temperature and crosswind is shown in Fig. 5. The simulation is conducted with the short domain and with the parameters listed in tables 2 and 3. The simulation includes an ambient turbulence field with, $\epsilon =1.654 \times 10^{-3}\ m^2\ s^{-3}$ ($\eta =0.2349$), which is very close to the ambient value observed at $z=40\ m$. The average circulation from both the port and starboard vortices is show in Fig. 6. The slightly faster decay for the starboard vortex may be due to the opposite sign vorticity of the ambient crosswind. Also included in Fig. 6 for comparison, is measured Lidar data for the port vortex. The LES results and Lidar data show reasonable agreement with the circulation decay given by Eq. 1.

## V. Ground Linking Experiments

In the free atmosphere, the linking process begins as the counter-rotating circulations of a vortex pair connect, producing crude vortex rings. The time at which this linking takes place is a known function of the turbulence

intensity, or specifically, the eddy dissipation rate[28,32,33] The goal of the experiments in this section is to examine ground linking and any sensitivity that it may have to the level of ambient turbulence. All of the experiments assume the long domain so as to permit linking instabilities. The experiments also assume the parameters listed in tables 2 and 3, as well as the initial sounding in Fig. 5. The nondimensional turbulence strengths, $\eta$, used in these experiments, range from *0.233* to *0.75*. These values represent a typical range between moderate to very turbulent atmospheric boundary layers.
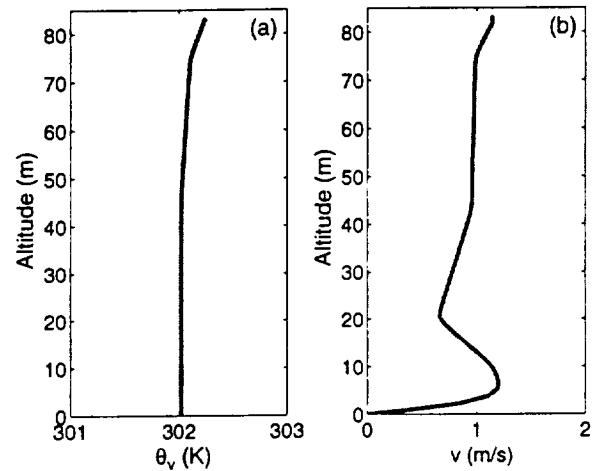


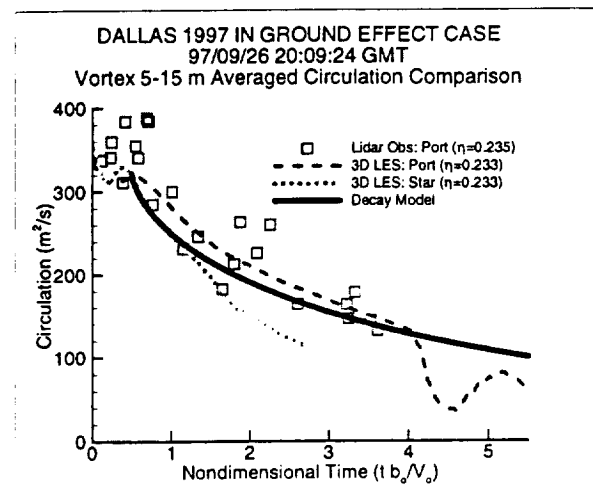**Figure 5.** *Initial profile of a) ambient potential temperature and b) crosswind for DFW, 26 September 1997, 20:09 UTC.*



**Figure 6.** *Average circulation vs nondimensional time for observed DFW case. Comparison of LES, Lidar, and IGE decay model (Eq. 1).*
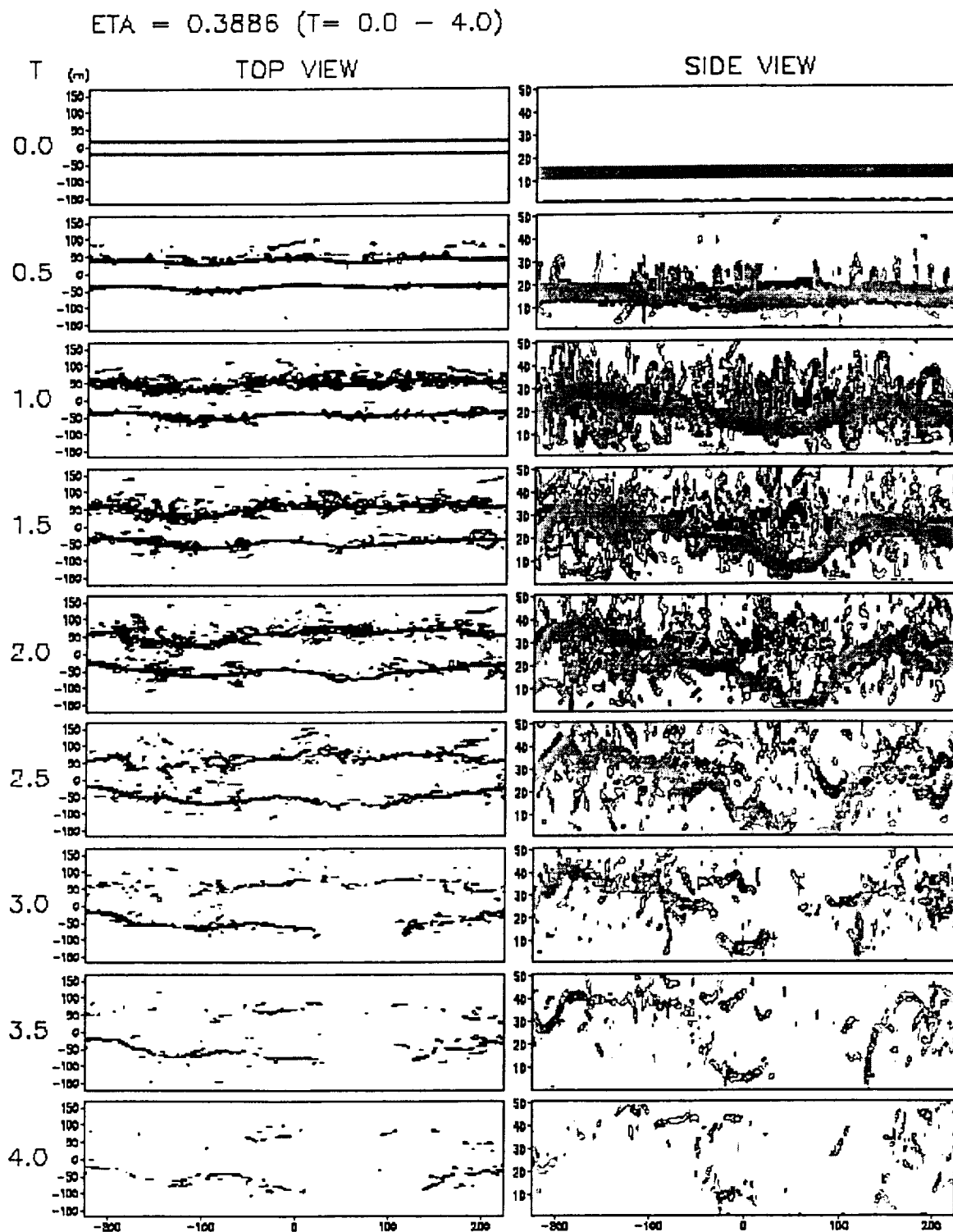
ETA = 0.3886 (T= 0.0 − 4.0)



**Figure 7.** *Time evolution within IGE of wake vortex pair for* $\eta = 0.388$. *Top* $(x,y)$ *and side* $(x,z)$ *view of wake vortices at increments 0.5 nondimensional time units.*
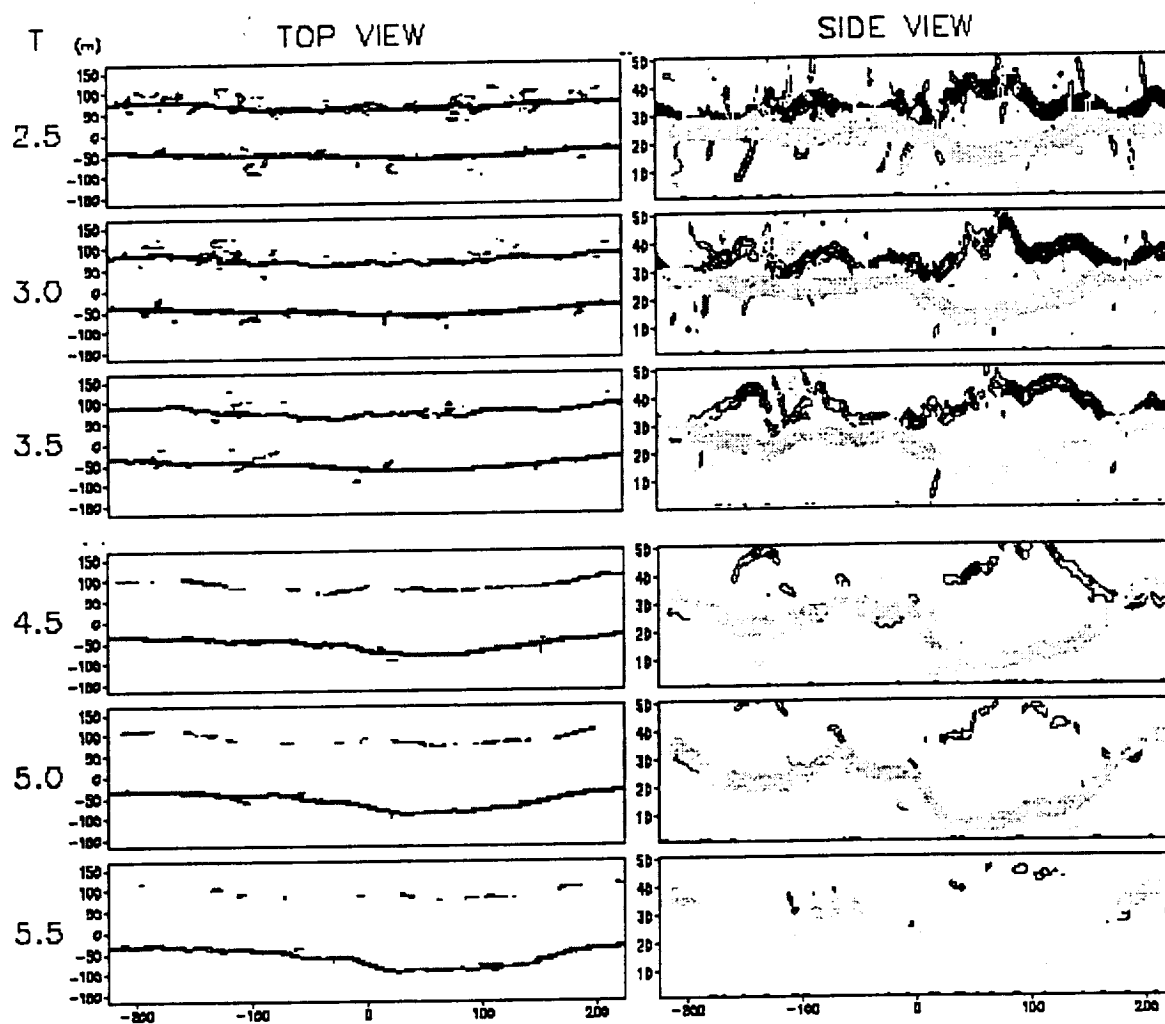
Figure 8. *Same as Fig. 7, but for* η = 0.233.

Results from these simulations showed obvious ground linking to occur when η exceeded 0.3 (e.g. Fig 7). For lower values of nondimensional turbulence intensity, pronounced vertical oscillations developed without obvious linking between the wake vortex and its ground image (e.g. Fig. 8). In none of the cases (which are all initiated well within IGE) did lateral linking occur. Influence of the very weak crosswind shear is unknown (see Fig. 5b), but ground linking only occurred with the port vortex.

The visualization of the simulated wake vortex as it links with the ground is shown in Fig. 7. The port vortex becomes nearly vertical as it links with the ground just after $T=2$. For comparison, a photograph of an actual ground link is shown in Fig. 9.
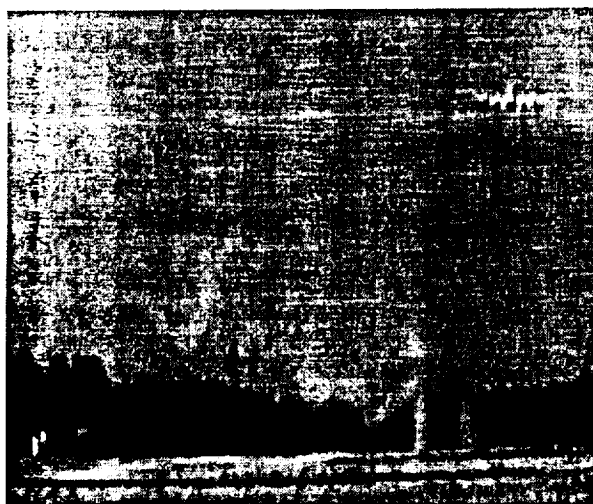


**Figure 9.** *Observed case of ground linking (from NASA Langley photo archives, photograph L 90-02905)*

Both port and starboard vortices in Fig. 7 rapidly dissipate after linking, becoming undistinguishable from background turbulence at $T=4$. Note that in the vicinity of where the ground connection is to occur, the starboard vortex is transported upward and the port vortex downward.

Figure 8 depicts the wake vortex system for a more moderate level of turbulence. Although an obvious link with the ground did not occur, a major portion of the port vortex remained parallel and very close to the ground. Again, note that the starboard vortex is at a relatively high altitude where the port vortex is closest to the ground.

A ground linking factor can be defined similarly to Crow's linking parameter[14] as:

$$\beta(t) = \frac{z_{max} - z_{min}}{z_{max} + z_{min}},$$

where $z_{max}$ and $z_{min}$ are respectively, the maximum and minimum altitude of one of the vortices. Either the port or starboard vortex may be considered linked with its ground image when the linking factor exceeds 0.85. Table 6 shows nondimensional times for β to exceed both 0.75 and 0.85 as a function of nondimensional turbulence intensity. Also included is the linking time as predicted by Sarpkaya's[17,34,35] re-derivation of Crow and Bate's[32] theoretical formula for vortex lifespan in the free atmosphere. In our experiments, ground linking did not occur for η < 0.388, although the vertical linking parameter did grow with time. Additional experiments were carried out for larger domain sizes assuming η =0.233, but little sensitivity was noted. Therefore, the linking time (or lack of linking) was not believed to be affected by our domain size. The influence of the crosswind shear on the suppression of linking for the lower turbulence levels is yet to be examined.

**Table 6.** *Sensitivity of Ground Linking to Ambient Turbulence (port vortex).*

| η | $T_{\beta=0.75}$ | $T_{\beta=0.85}$ | $T_{Sarp}$ |
|------|------|------|------|
| 0.233 | 4.3 | ------ | 2.4 |
| 0.30 | 2.90 | ------ | 2.0 |
| 0.388 | 1.90 | 2.10 | 1.71 |
| 0.50 | 1.47 | 1.63 | 1.43 |
| 0.75 | 0.98 | 1.14 | 1.11 |

Figure 10 shows a comparison of the time to ground link with experimental data[33] and theory[32,34] for vortex linking in the free atmosphere. The three simulations that had ground linking are in close agreement with Sarpkaya's formula,[34,35] even though the theory was developed for lateral vortex linking away from any ground influence.
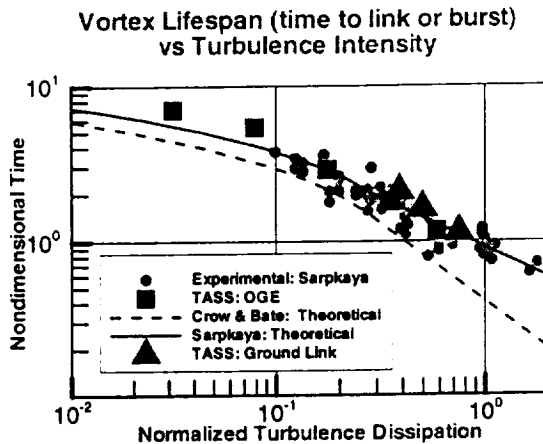
**Figure 10.** *Linking time vs nondimensional turbulence intensity. Time of ground linking from LES given by triangles, all other data for lateral linking (or vortex bursting) out of ground effect (OGE).*

## VI. Summary and Conclusions

A study of wake vortices initialized in-ground effect has been performed using a validated three-dimensional LES model. The simulations, which included environmental turbulence, show strong decay of wake vortices following maximum penetration into IGE. Wake vortex linking with its ground image was simulated for moderate to strong values of atmospheric turbulence.

The primary conclusions of this study are:

1. Wake vortex transport and decay for IGE can be nondimensionalized with conventional parameters.
2. Appropriate normalization of parameters reduces wake vortex sensitivity to initial circulation, initial separation, and generating height.
3. Vortex decay for IGE has minor sensitivity to the ambient turbulence level.
4. Based on the LES results, a formula for IGE decay is proposed. This formula, with few dependent parameters, should be easy to incorporate in wake vortex prediction models.
5. Also based on the LES results, a model for lateral drift rate due to ground effect is proposed.
6. Both the decay and drift models show very good agreement with the LES sensitivity results.

7. Ground linking is influenced by the level of ambient turbulence. Similar to lateral linking in the free atmosphere, the time to ground link is a function of the nondimensional eddy dissipation. However, ground linking did not occur for moderate to weak levels of turbulence.
8. The increased lateral separation of vortices from ground effect can suppress lateral vortex linking.

Future work needs to address the sensitivity of crosswind shear to the onset vortex linking, both in and out of ground effect.

### Appendix – Sensitivity of Domain Size

A number of experiments assume a truncated domain in the x-direction, so as to reduce computation time, inhibit crow instability and simplify analysis of the experiments. The consequence of shortening the domain is evaluated here. Two simulations are carried out with everything identical except for a short domain: $(L_x, L_y, L_z = 2.2\ b_o, 10\ b_o, 2.2\ b_o)$, and a long domain $(L_x, L_y, L_z = 12.2\ b_o, 9.1\ b_o, 2.2\ b_o)$. The ambient turbulence level is assumed as $\eta=0.2349$ and each are resolved by the grid sizes listed in Table 3. The ambient temperature and crosswind are from profiles observed at 20:09 UTC on 26 September 1997 at DFW (Fig. 5).

Comparison of the average circulations from the two simulations with different domain sizes is shown in Fig. A-1. Lidar observations from the L-1011 port vortex are also included. A comparison of lateral positions is shown in Fig. A-2. For this case, the figures indicate little sensitivity to domains size.
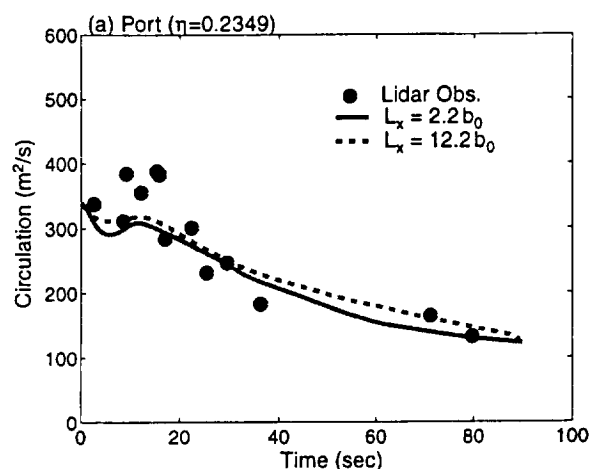
**Figure A-1.** *Time evolution of the 5-15 m averaged circulation for port vortex from short domain $(L_x=2.2b_o)$ and long domain $(L_x=12.2b_o)$ simulations.*
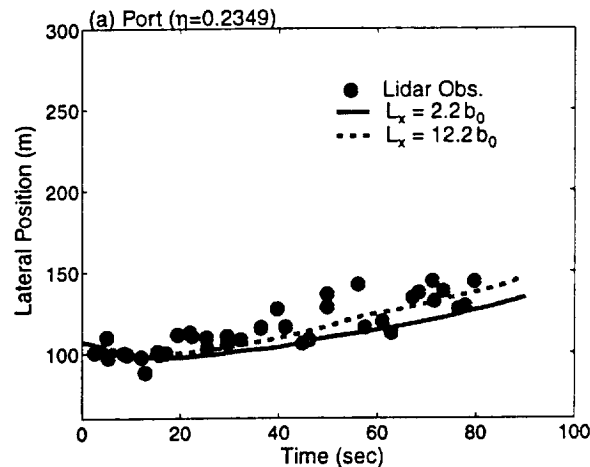


**Figure A-2.** *Same as Fig. A-1, but for lateral position of port vortex.*

## References

[1]Robins, R.E., Delisi, D.P. and Greene, G.C., "Development and Validation of a Wake Vortex Prediction Algorithm," 36th Aerospace Sciences Meeting & Exhibit, AIAA-98-0665, January 1998, 10 pp.

[2]Harvey, J.K., and Perry, F.J., "Flowfield Produced by Trailing Vortices in the Vicinity of the Ground," *AIAA Journal*, Vol. 9, No. 8, August 1971, pp. 1659-1660.

[3]Hallock, J.N., "Wake Vortex Decay Near the Ground," AIAA 8th Fluid and Plasma Dynamics Conf., Hartford, CN, AIAA-75-882, June 1975, 7 pp.

[4]Kopp, F., "Doppler Lidar Investigation of Wake Vortex Transport Between Closely Spaced Parallel Runways," *AIAA J.*, Vol. 32, April 1994, pp.805-810.

[5]Hallock, J.N., and Burnham, D.C., "Decay Characteristics of Wake Vortices from Jet Transport Aircraft," 35th Aerospace Sciences Meeting & Exhibit, AIAA-97-0060, January 1997, 11 pp.

[6]Burnham, D.C., and Hallock, J.N., "Measurements of Wake Vortices Interacting with the Ground," 36th Aerospace Sciences Meeting & Exhibit, AIAA-98-0593, January 1998, 12 pp.

[7]Rudis, R.P., Burnham, D.C., and Janota, P., "Wake Vortex Decay Near the Ground under Conditions of Strong Stratification and Wind Shear," AGARD Fluid Dynamics Panel Symposium, Trondheim, Norway, AGARD CP-584, November, 1996, pp. 11-1 to 11-10.

[8]Schiling, V.K., "Motion and Decay of Trailing Vortices Within the Atmospheric Surface Layer," *Beitr. Phys. Atmos.*, Vol. 65, May 1992, pp. 157-169.

[9]Robins, R.E. and Delisi, D.P., "Potential Hazard of Aircraft Wake Vortices in Ground Effect with Crosswind," *Journal of Aircraft*, Vol. 30, No. 2, March-April 1993, pp. 201-206.

[10]Zheng, Z.C., and Ash, R.L., "Study of Aircraft Wake Vortex Behavior Near the Ground." *AIAA Journal*, Vol. 34, No. 3, March 1996, pp. 580-589.

[11]Corjon A., and Poinsot, T., "Behavior of Wake Vortices Near Ground," *AIAA J.*, Vol. 35, No.5, May 1997, pp.849-855.

[12]Corjon, A., and Stoessel, A., "Three-Dimensional Instability of Wake Vortices Near the Ground," 28th AIAA Fluid Dynamics Conf., Snowmass, CO, AIAA-97-1782, June-July 1997, 14 pp.

[13]Proctor, F.H., and Han, J., "Numerical Study of Wake Vortex Interaction with the Ground Using the Terminal Area Simulation System," 37th Aerospace Sciences Meeting & Exhibit, AIAA-99-0754, January 1999, 12 pp.

[14]Crow, S.C., "Stability Theory for a Pair of Trailing Vortices," *AIAA Journal*, Vol. 8, No. 12, December 1970, pp. 2172-2179.

[15]Bisgood, P.L., Maltby, R.L., and Dee, F.W., "Some Work at the Royal Aircraft Establishment on the Behavior of Wake Vortices," In *Aircraft Wake Turbulence and Its Detection*, New York, Plenum, 1971.

[16]Spalart, P.R., "Airplane Trailing Vortices," *Ann. Rev. Fluid Mech.*, Vol 30, 1998, pp. 107-138.

[17]Sarpkaya, T., Robins, R.E., and Delisi, D.P., "Wake-Vortex Eddy-Dissipation Model Predictions Compared with Observations," 38th Aerospace Sciences Meeting & Exhibit, AIAA-2000-0625, January 2000.

[18]Hinton, D.A., "Aircraft Vortex Spacing System (AVOSS) Conceptual Design," NASA Tech. Memo No. 110184, August 1995, 27 pp.

[19]Perry, R. B., Hinton, D. A., and Stuever, R. A., "NASA Wake Vortex Research for Aircraft Spacing," 35th Aerospace Sciences Meeting & Exhibit, , Reno, NV, AIAA 97-0057, January 1997, 9 pp.

[20]Hinton, D.A., Charnock, J.K., Bagwell, D.R., and Grigsby, D., "NASA Aircraft Vortex Spacing System Development Status," 37th Aerospace Sciences Meeting & Exhibit, Reno, NV, AIAA-99-0753, January 1999, 17 pp.

[21]Proctor, F.H., "The NASA-Langley Wake Vortex Modelling Effort in Support of an Operational Aircraft Spacing System," 36th Aerospace Sciences Meeting & Exhibit, AIAA-98-0589, January 1998, 19 pp.

[22]NASA Langley Research Center, "Meteorological & Wake Vortex Data Set, Dallas-Fort Worth International Airport, September 15-October 3, 1997," November 1998, Compact Disc.

[23]Proctor, F.H., "The Terminal Area Simulation System, Volume 1: Theoretical Formulation," NASA Contractor Report 4046, DOT/FAA/PM-85/50, 1, April 1987, 176 pp.

[24]Proctor, F.H., "Numerical Simulation of Wake Vortices During the Idaho Falls and Memphis Field Programs," 14th AIAA Applied Aerodynamics Conference, Proceedings, Part-II, New Orleans, LA, AIAA-96-2496, June 1996, pp. 943-960.

[25]Switzer, G.F., "Validation Tests of TASS for Application to 3-D Vortex Simulations," NASA Contractor Report No. 4756, October 1996, 11 pp.

[26]Vincent, A. and Meneguzzi, M., "The Spatial Structure and Statistical Properties of Homogeneous Turbulence," *Journal of Fluid Mechanics*, Vol. 225, 1991, pp. 1-20.

[27]Kolmogorov, A.N., "The Local Structure of Turbulence in Incompressible Viscous Fluid for Very Large Reynolds Number," *Dokl. Akad. Nauk SSSR*, Vol. 30, 1941, pp 9-13.

[28]Han, J., Lin, Y.-L., Schowalter, D. G., Arya, S. P., and Proctor, F. H., "Large Eddy Simulation of Aircraft Wake Vortices within Homogeneous Turbulence: Crow Instability," *AIAA Journal*, Vol. 38, February, 2000.

[29]Han, J., Lin, Y.-L., Arya, S.P., and Proctor, F.H., "Numerical Study of Wake Vortex Decay and Descent within Homogeneous Turbulence." In press, *AIAA Journal*, Vol. 38, 2000.

[30]Burnham, D.C., and Hallock, J.N., "Chicago Monostatic Acoustic Vortex Sensing System, Volume IV: Wake Vortex Decay," Dept. of Transportation, Rep No. DOT/FAA/RD-79-103 IV, July 1982, 206 pp. (Available from NTIS]

[31] Hinton, D.A., and Tatnal, C.R., "A Candidate Wake Vortex Strength Definition for Application to the NASA Aircraft Vortex Spacing System (AVOSS)," NASA Tech. Memo. 110343, September 1997, 35 pp.

[32] Crow, S.C., and Bate. E.R., "Lifespan of Trailing Vortices in a Turbulent Atmosphere," *J. Aircraft*, Vol. 13, No. 7, 1976, pp. 476-482.

[33] Sarpkaya, T., and Daly, J.J., "Effect of Ambient Turbulence on Trailing Vortices," *J. Aircraft*, Vol. 24, No. 6, 1987, pp. 399-404.

[34] Sarpkaya, T., "Decay of Wake Vortices of Large Aircraft," *AIAA J.*, Vol. 36, No. 9, 1998, 1671-1679.

[35] Sarpkaya, T., "A New Model for Vortex Decay in the Atmosphere," 37th Aerospace Sciences Meeting & Exhibit, AIAA-99-0761, January 1999, 14 pp.

**Appendix I: Large Eddy Simulation of Wake Vortices in the Convective Boundary Layer**

# Large Eddy Simulation of Wake Vortices in the Convective Boundary Layer

Yuh-Lang Lin, Jongil Han, Jing Zhang, Feng Ding, S. Pal Arya
North Carolina State University
Raleigh, NC

Fred H. Proctor
NASA Langley Research Center
Hampton, VA

## 38th Aerospace Sciences Meeting & Exhibit
### January 10-13, 2000 / Reno, NV

# LARGE EDDY SIMULATION OF WAKE VORTICES IN THE CONVECTIVE BOUNDARY LAYER

Yuh-Lang Lin[*], Jongil Han[†], Jing Zhang[‡], Feng Ding[§], S. Pal Arya[¶]
Department of Marine, Earth and Atmospheric Sciences
North Carolina State University
Raleigh, NC 27695-8208

Fred H. Proctor[‖]
Airborne Systems Competency
NASA Langley Research Center
Hampton, VA 23681-2199

## Abstract

The behavior of wake vortices in a convective boundary layer is investigated using a validated large eddy simulation model. Our results show that the vortices are largely deformed due to strong turbulent eddy motion while a sinusoidal Crow instability develops. Vortex rising is found to be caused by the updrafts (thermals) during daytime convective conditions and increases with increasing nondimensional turbulence intensity $\eta$. In the downdraft region of the convective boundary layer, vortex sinking is found to be accelerated proportional to increasing $\eta$, with faster speed than that in an ideal line vortex pair in an inviscid fluid. Wake vortices are also shown to be laterally transported over a significant distance due to large turbulent eddy motion. On the other hand, the decay rate of the vortices in the convective boundary layer that increases with increasing $\eta$, is larger in the updraft region than in the downdraft region because of stronger turbulence in the updraft region.

[*]Professor, AIAA member

[†]Research Scientist, AIAA member

[‡]Research Scientist

[§]Research Assistant

[¶]Professor

[‖]Research Scientist, AIAA member

## Nomenclature

| | |
|---|---|
| $B$ | = aircraft wingspan |
| $b_0$ | = initial vortex separation distance, $\pi B/4$ |
| $H$ | = nondimensional vortex descent distance, $(z - h_0)/b_0$ |
| $h_0$ | = initial vortex elevation |
| $L$ | = domain size |
| $r$ | = radial distance from vortex center |
| $r_c$ | = initial vortex core radius |
| $S$ | = symmetric part of $\nabla u$ |
| $T$ | = nondimensional time, $tV_0/b_0$ |
| $t$ | = time |
| $t_*$ | = large-eddy turnover time, $z_i/w_*$ |
| $u, v, w$ | = velocities in $x$, $y$, and $z$ directions, respectively |
| $V_a$ | = airspeed of generating aircraft |
| $V_0$ | = initial vortex induction speed, $\Gamma_\infty/(2\pi b_0)$ |
| $W$ | = aircraft weight |
| $w_*$ | = convective velocity scale, $(\frac{g}{\Theta}\overline{(w'\theta')}_s z_i)^{1/3}$ $[\overline{(w'\theta')}_s$: surface heat flux] |
| $x, y, z$ | = axial, lateral, vertical space coordinate |
| $z_i$ | = depth of convective boundary layer |
| $z_0$ | = surface roughness length |
| $\Gamma$ | = vortex circulation |
| $\Gamma_0$ | = initial circulation |
| $\Gamma_\infty$ | = initial circulation at $r \gg r_c$, $4W/(\pi B\rho V_a)$ |
| $\Delta$ | = grid size |
| $\epsilon$ | = turbulence dissipation rate |
| $\eta$ | = nondimensional ambient turbulence intensity, $(\epsilon b_0)^{1/3}/V_0$ |
| $\Theta$ | = potential temperature |
| $\lambda_2$ | = the second negative eigenvalue of the symmetric tensor $S^2 + \Omega^2$ |
| $\rho$ | = air density |
| $\Omega$ | = antisymmetric part of $\nabla u$ |

1

# I. Introduction

NASA is developing an automated Aircraft Vortex Spacing System[1] (AVOSS) under its Terminal Area Productivity program. This system will determine safe operating spacing between arriving and departing aircraft as based on ambient weather conditions and provide a safe reduction in separation of aircraft compared to the now-existing flight rules. This system includes prediction algorithms[2,3] for transport and decay of aircraft wake vortices. To develop this system, research is being focused on understanding the interaction of wake vortices with the atmosphere.

A pair of wake vortices usually descends due to their mutual induction. The vortex descent rate is reduced as the vortices decay with time due to ambient turbulence and stratification.[3-5] In some cases, however, the vortices can rise. It has been shown[6,7] that the vortices can either stall or be deflected upwards as they penetrate a strong crosswind shear layer which often occurs just above a developing nocturnal stable layer. Vertical winds associated with weather phenomena such as vigorous fronts, gravity waves, and thermals may also cause the vortices to rise. Rising vortices have been observed during daytime convective conditions,[8] possibly due to strong thermals developing in the convective boundary layer (CBL). Figure 1 shows some observed vertical position histories of the vortices during typical convective conditions as taken from the Memphis Field Program.[9] The vortices are observed to remain on the flight level (Fig. 1a), rise (Fig. 1b), or even descend faster than an ideal line vortex pair in an inviscid fluid, for which the sinking rate is given by $dH/dT = -1$ (Fig. 1c). Numerical simulation results by Holzäpfel et al.[10] indicate that in the CBL some segments of the vortex pair that are placed on an updraft (thermal) area remain on or even rise up to 20 $m$ above their initial positions. As Holzäpfel et al. pointed out, this situation can be more hazardous for reduced spacing operations due to the increased possibility of encountering stalled vortices during aircraft approach.

The CBL is typically composed of broad regions of gentle downdraft surrounding smaller regions of strong updraft (thermal). The fractional areas are about 0.4 for the updraft and 0.6 for the downdraft.[11] Both the updraft and downdraft have horizontal scales of roughly 1.5 $z_i$,[12] where $z_i$ is the CBL depth (of the order of 1 $km$). Vertical velocities in thermals can reach 5 $m/s$ or more, although weaker updrafts of 1 to 2 $m/s$ are more common.[13] Therefore, one can expect a large difference in the behavior of wake vortices when they are exposed in the CBL, depending on whether they are placed on the updraft regions or the downdraft regions.

In the present study, we investigate the behavior of aircraft wake vortices in the CBL using a validated large eddy simulation (LES) model. In Sec. II, we describe the LES model and the initial conditions. In Sec. III,
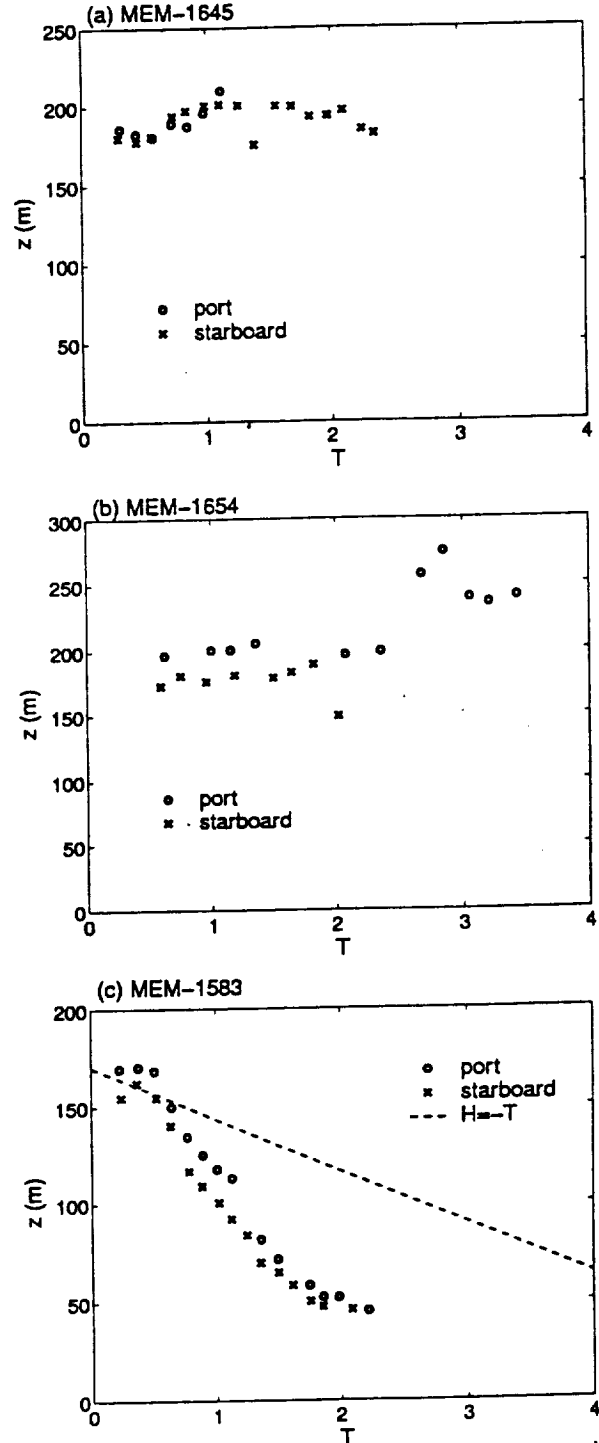


Figure 1: Time evolution of the observed vertical positions of the vortices during daytime convective conditions as taken from the Memphis Field Program.

2

we present the results from systematic numerical experiments in terms of nondimensional turbulence intensity. Finally, in Sec. IV, we summarize our results and draw some conclusions.

## II. Model and Initial Conditions

The numerical model used in the present study is a three-dimensional, nonlinear, compressible, nonhydrostatic LES model, called the Terminal Area Simulation System[14] (TASS). Numerous successful simulations of interaction of wake vortices with the atmosphere[5-7,15-18] and some within the CBL[19,20] have been conducted with this TASS code. In TASS-LES, grid-scale turbulence is explicitly computed while the effects of subgrid-scale turbulence are parameterized by a conventional first-order closure model with modifications for stratification and flow rotation.[5,21]

The initial vortex system represents a post roll-up, wake-vortex velocity field as described in Proctor,[7] and consists of a pair of counter-rotating vortices that have no initial variation in the axial direction. This vortex model has also been adopted for investigating the effects of ambient turbulence[5] and ground[16] on vortex decay and descent.

One of the major difficulties in numerical simulations of wake vortices is that very fine grid resolution is needed to resolve the vortex core whose size is of the order of $1\,m$, whereas horizontal domain size of at least four times larger than the CBL height (of the order of $1\,km$) is required to simulate large scale turbulence structure in the CBL. For current computer resources, it is almost impossible to simulate large scale structure of turbulence in the CBL and much smaller scale structure of aircraft wake vortices at the same time. However, the recent study by Holzäpfel et al.[10] indicates that the main characteristics of vortex behavior in the CBL can be obtained even when greatly reduced domain size (say, about $0.5\,km$) compared to the CBL scale is used.

In this study, in order to achieve a proper resolution of the characteristic scales of both the CBL and the wake vortices, we have chosen a domain size of $(L_x, L_y, L_z)$ = $(600m, 400m, 350m)$ = $(15b_0, 10b_0, 8.8b_0)$, with a grid size of $(\Delta x, \Delta y, \Delta z)$ = $(5.0m, 2.5m, 2.5m)$, where $b_0 = 40\,m$, and $x$, $y$ and $z$ correspond to the axial, lateral and vertical directions of the vortex system, respectively. Somewhat larger domain size in the axial direction ($15b_0$) can allow the development of Crow instability of which theoretical maximum wavelength is about $8.6b_0$.[22] The lateral domain size of $10b_0$ is sufficiently large to minimize boundary influences. The domain size in the vertical direction ($8.8b_0$) is large enough to investigate the effects of large turbulent eddies such as thermals on vortex transport. On the other hand, because of our limited computing resources and in order to allow the core to be resolved, the chosen initial core size of $r_c = 5\,m$ is somewhat larger than the typical value (less than about 5 %

of the wingspan[15]) observed behind aircraft. The initial vortices are placed on the height of $h_0 = 180m$ (4.5 $b_0$) above the ground.

Before the vortices are injected, the CBL is driven by a constant, spatially uniform heat flux on the bottom surface until a typical feature of the evolving CBL is well established. Periodic boundary conditions are employed in both horizontal directions. Free-slip and no-slip conditions are imposed at top and bottom boundaries respectively. The Monin-Obukhov similarity relations are used at the surface with surface roughness length, $z_0 = 0.1\,m$. Initial velocities are specified as zero. Initial potential temperature is vertically uniform. The turbulence is initiated by a small random temperature perturbations superimposed in five lower layers.

The vortices are injected at about 3.6 large-eddy turnover times (defined as $t_* = z_i/w_*$, where $w_*$ is the convective velocity scale), when the CBL is well developed although it is still evolving. Figure 2 shows vertical velocity fields on the horizontal $x - y$ plane of the initial vortex elevation and both vertical and lateral velocity fields on the vertical $x - z$ plane along the $y-$center line, with the location of the initial vortex pair indicated. As seen in Fig. 2a and b, the right part of the vortices is placed on an updraft area with stronger vertical velocity, whereas the left part is placed on a downdraft area with weaker vertical velocity. From this vertical velocity distribution, one can expect that the right part of the vortices may stay around the initial vortex elevation or rise, striving against the descent by mutual induction of the vortices, whereas the descent of the left part of the vortices may be accelerated. From Fig. 2c, on the other hand, in lower domain layers below the initial vortex elevation negative lateral velocities are more dominant, and thus, the vortices are expected to be transported mostly to the negative lateral direction during their descent.

To evaluate the sensitivity of vortex behavior to ambient turbulence, we generated five values of nondimensional turbulence strengths of $\eta$=0.20, 0.25, 0.30, 0.35, and 0.50 that are in a typical range of the CBL. These $\eta$ values are typically found during daytime convective conditions and obtained by varying the initial circulation ($\Gamma_\infty$) to save computing time, rather than by varying initial turbulence field. The associated value of turbulence energy dissipation rate $\epsilon$ is estimated by fitting the theoretical Kolmogorov spectrum in the inertial subrange to the simulated spectrum at the horizontal plane of the initial vortex elevation, as described in Han et al.[17] Three-dimensional wake vortex simulations are carried out with each of the five turbulence field, with all other conditions identical.

## III. Numerical Results

Figure 3 shows top and side views of the vortex pairs with increasing nondimensional time for three different
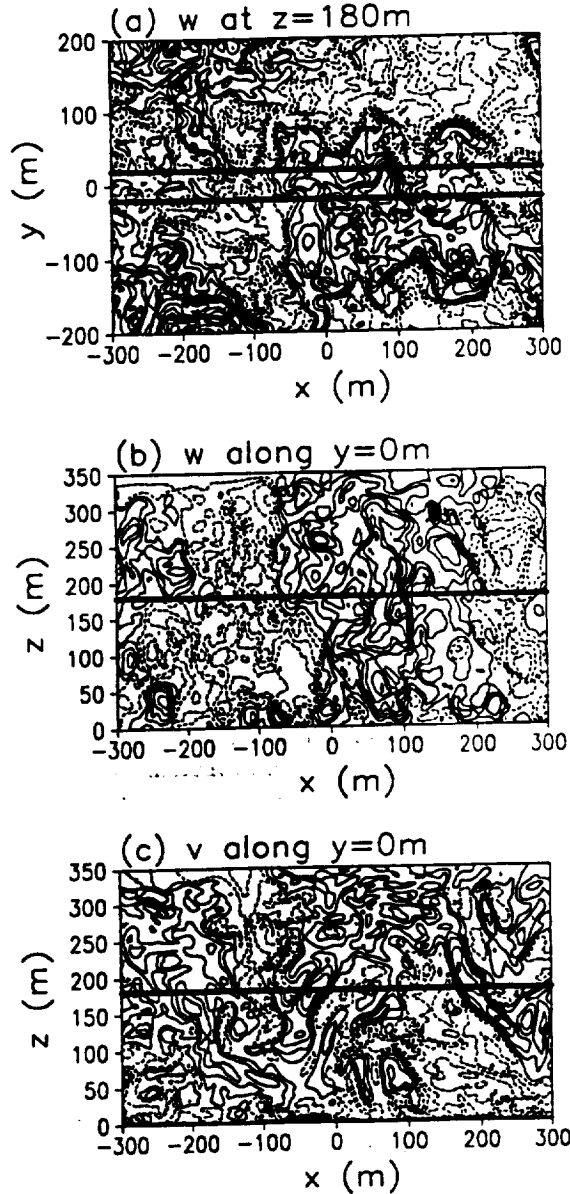
3

Figure 2: (a) Vertical velocity fields on the horizontal $x-y$ plane of the initial vortex elevation and both (b) vertical and (c) lateral velocity fields on the vertical $x-z$ plane along the $y$-center line, with the location of the initial vortex pair indicated (thick solid line). The contour interval for velocity is $0.4\,ms^{-1}$.

nondimensional turbulence intensities of $\eta = 0.2, 0.3,$ and 0.5. The method of Jeong and Hussain[23] is used for the identification of a vortex. They define a vortex in terms of the second negative eigenvalue $\lambda_2$ of the symmetric tensor $S^2 + \Omega^2$, where $S$ and $\Omega$ are respectively the symmetric and antisymmetric parts of the velocity gradient tensor $\nabla u$. The top (side) view of Fig. 3 is taken from $x - y$ $(x - z)$ plane projection of the minimum negative $\lambda_2$ value along $z$ $(y)$ direction. A threshold $\lambda_2$ value to identify the vortex is arbitrarily determined.
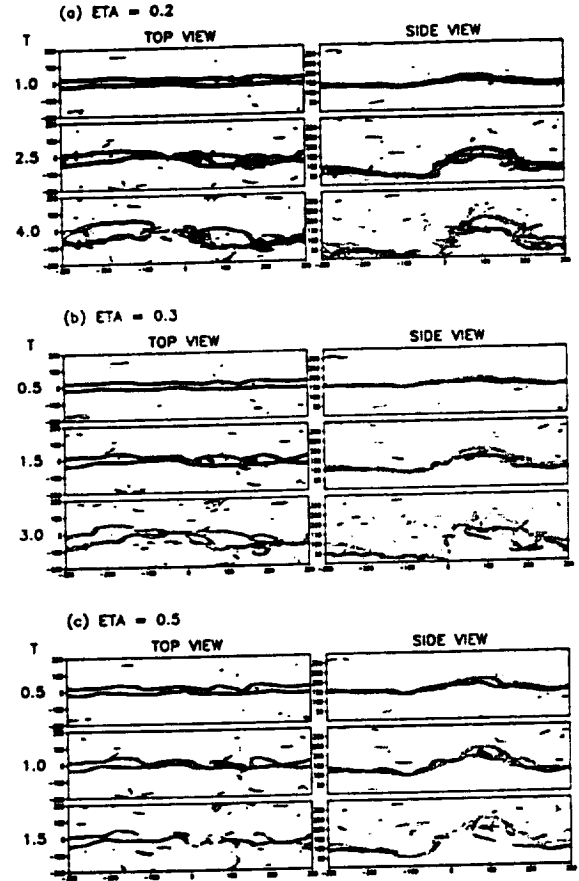


Figure 3: Top and side views for the cases of (a) $\eta=0.2$, (b) $\eta=0.3$, and (c) $\eta=0.5$. The unit for axis labels is $m$.

As shown in the top view of Fig. 3, because of larger axial domain size ($15b_0$) used, a sinusoidal Crow instability develops for all three cases, and then, the vortex pair connects together as a result of the instability and finally disintegrates into a turbulent state. In agreement with Han et al.'s[17] study, the linking of the vortex pair occurs earlier with stronger turbulence (that is, larger $\eta$). In addition, the vortices are strongly deformed especially for stronger turbulence due to large turbulent eddy motion. On the other hand, from the side view it is obvious

4

that the right part of the vortex pair rises due to strong thermal (updraft) developing in the CBL, whereas the descent of the left part vortex pair accelerates due to the downdraft.

Figure 4 depicts the evolution of maximum vertical vortex positions that are found in the updraft region. It is shown that vortex rise becomes more significant with stronger ambient turbulence strength. For the case of $\eta=0.5$, for example, at $T=1.5$ the vortex rises up to about $2\,b_0$ from its initial position and its coherent structure is destroyed. For the case of $\eta=0.2$, on the other hand, the vortex appears to stay at its initial height until about $T=2.5$ and then, rises further after its strength becomes much weaker due to dissipation by ambient turbulence.
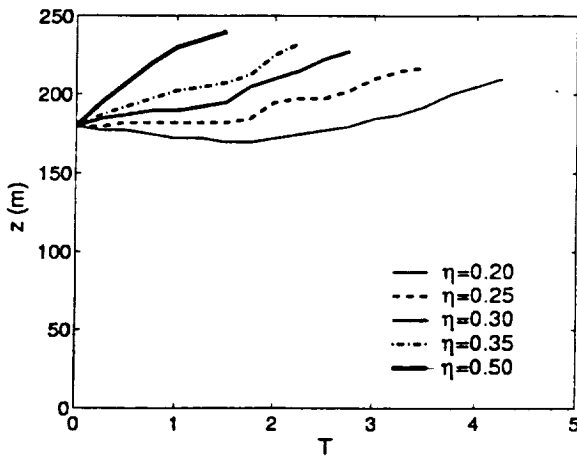


Figure 4: Time evolution of maximum vertical vortex positions for varying nondimensional ambient turbulence strengths.

Figure 5 depicts the evolution of minimum vertical vortex positions that are found in the downdraft region. It is shown that vortex sinking is accelerated due to the downdraft; for all the cases, the sinking rates of the minimum vertical vortex positions are larger than the theoretical sinking rate as given by mutual induction speed of an ideal line vortex pair in an inviscid fluid (that is, $dH/dT = -1$). The sinking rates increase with increasing ambient turbulence strength; for $\eta=0.5$ the sinking rate $dH/dT \sim -2.3$.

Figure 6 shows the evolution of vertical vortex positions averaged along the axial direction and their standard deviations. In an average sense, the vortices descend for all $\eta$ values rather than stay or rise as seen in Fig. 6, although they tend to stall at much later times when the vortices almost decay out. This is because the downdrafts not only occupy wider area (about 60%) than the updrafts, but also the vortex rising due to the updrafts has to counter the effect of sinking due to mutual induction. Unlike the behavior of the minimum vertical
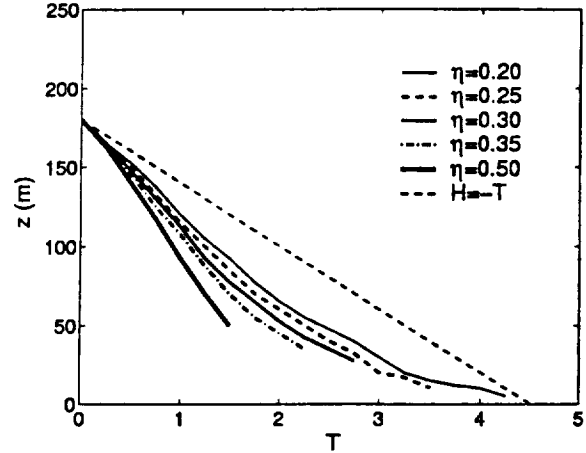


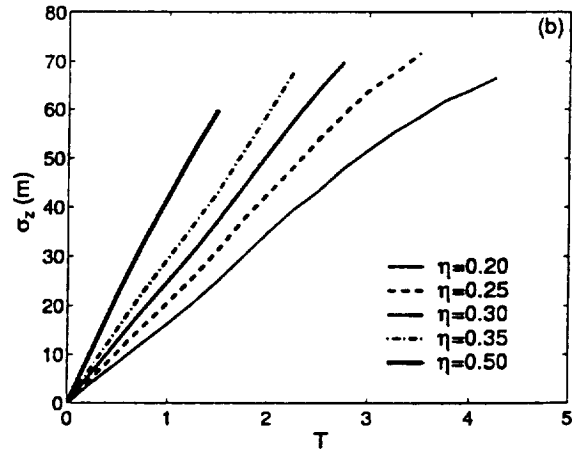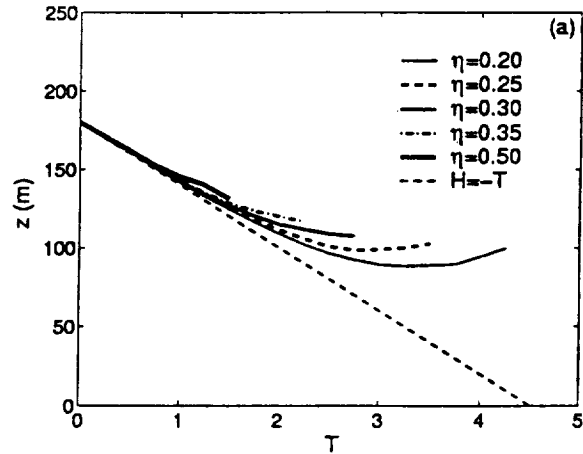Figure 5: Same as Fig. 4 but for minimum vertical vortex positions.





Figure 6: Same as Fig. 4 but for (a) mean vertical vortex positions along the axial direction and (b) standard deviations of vertical vortex positions.

vortex positions, however, the sinking rates of the average vertical vortex positions are smaller than the theoretical sinking rate of $dH/dT = -1$ and decrease with increasing ambient turbulence strength. On the other hand, the standard deviations of vertical vortex positions increase with increasing ambient turbulence strength, showing about $1.5\,b_0$ at $T=1.5$ for the extremely strong turbulence case of $\eta=0.5$.

Large turbulent eddies can also transport the vortices laterally over a significant distance, as indicated in the top views of Fig. 3. Figure 7 depicts the evolution of maximum and mean lateral vortex displacements from the initial positions and their standard deviations for five $\eta$ values. Although the maximum and mean lateral displacements and standard deviations appear to increase with increasing ambient turbulence strength, the differences among varying $\eta$ values are much smaller compared with those in vertical positions. Figure 7a indicates that for the case of $\eta=0.2$, that is, the most long-lived vortex in our experiments, the vortices can be transported up to about $2.5\,b_0$ at about $T = 4$ by large turbulent eddy motion of the CBL.

Figure 8 shows the decay of the average circulation (averaged over a radius between 5 and 15 m from the center) with time for varying ambient turbulence levels in both updraft (Fig. 8a) and downdraft (Fig. 8b) regions (in each region, the radius-averaged circulations are also averaged over 16 planes [80 m] along the axial direction where the vortex separation is the widest). As shown in Fig. 8, a rapid vortex decay behavior appears to be conspicuous due to buoyancy-driven strong turbulence typical in the CBL. The rate of vortex decay tends to increase with increasing ambient turbulence level, which is consistent with field observations[24] and our previous numerical simulations.[5] Vortex decay is more rapid in the updraft region (Fig. 8a) with stronger turbulence strength than in the downdraft (Fig. 8b) region with weaker turbulence strength.

## IV. Conclusions

This study presents the results of numerical simulations which were carried out for understanding how wake vortices behave in the CBL. LES simulations are conducted by introducing a vortex pair, representing aircraft trailing vortices, in a well-developed CBL. Although the domain size chosen is relatively smaller compared to large CBL turbulence scales, the main characteristics of vortex behavior in the CBL seem to be well captured. The following conclusions can be drawn from the results of numerical simulations:

1) In the CBL, the vortices are largely deformed due to strong turbulent eddy motion while a sinusoidal Crow instability develops. Consistent with previous studies, the linking of the vortex pair resulting from the instability occurs earlier with larger nondimensional turbulence intensity.
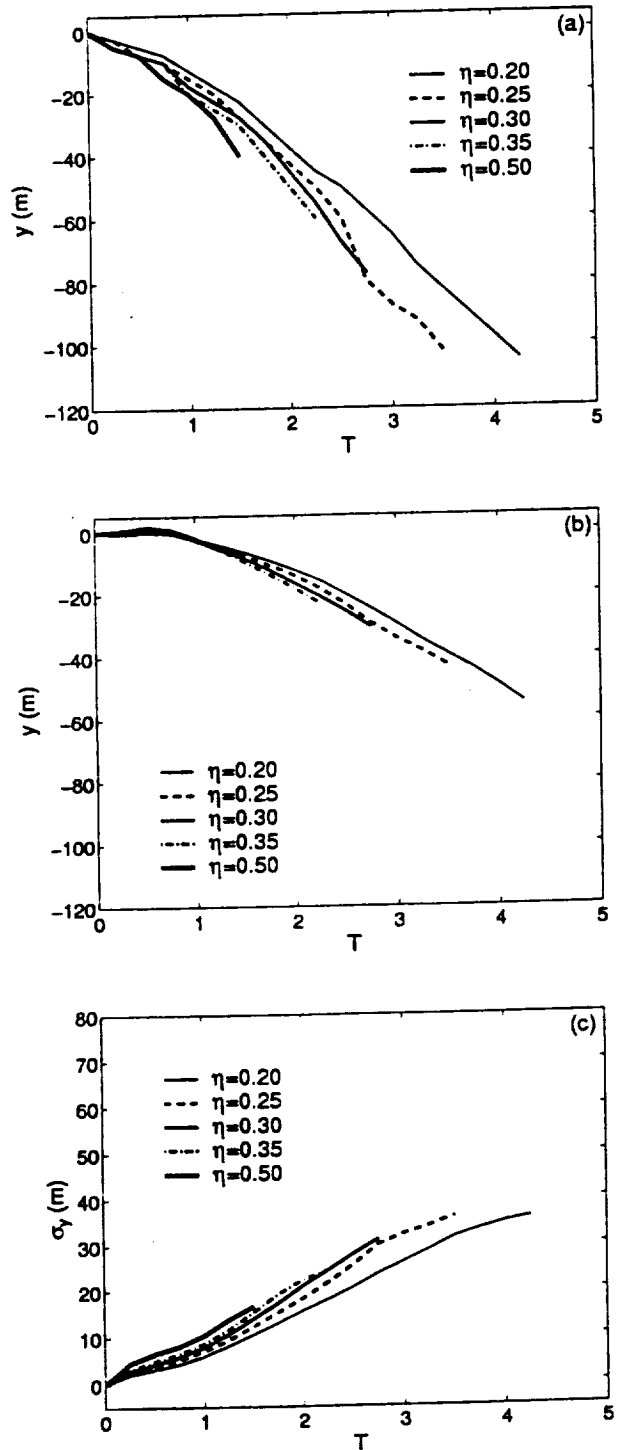


Figure 7: Same as Fig. 4 but for (a) maximum and (b) mean lateral vortex displacements from the initial positions and (c) standard deviations.

6

American Institute of Aeronautics and Astronautics

2) Vortex rise is caused by the updrafts (thermals) in the CBL, increases with increasing nondimensional turbulence intensity $\eta$, and can be as large as $H \sim 2$ at $T=1.5$ for the extremely strong turbulence case of $\eta=0.5$.
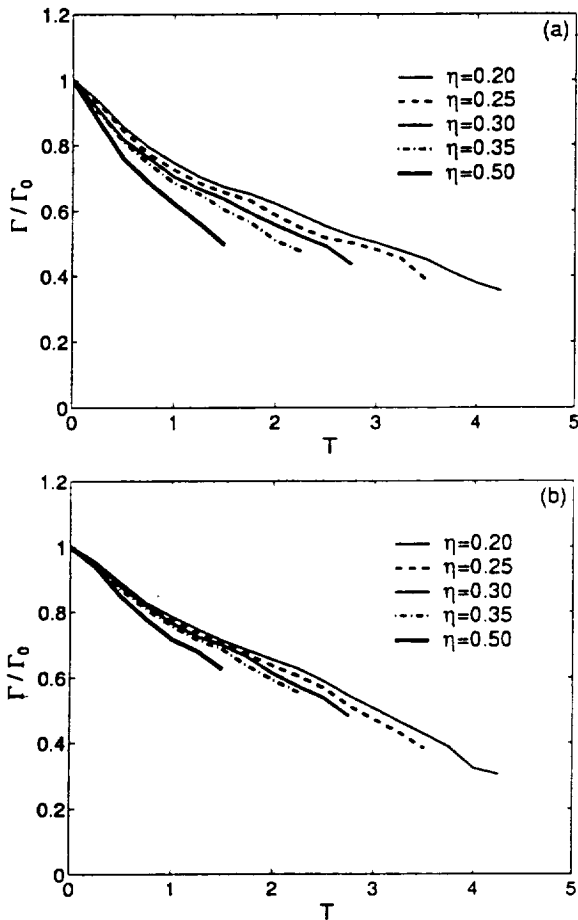


Figure 8: Same as Fig. 4 but for $5 - 15\,m$ averaged circulation in the (a) updraft and (b) downdraft regions.

3) In the downdraft region of the CBL, vortex sinking is accelerated; the sinking rate becomes larger than the theoretical value of $dH/dT = -1$, increases with increasing $\eta$, and can be as large as $dH/dT \sim -2.3$ for $\eta=0.5$.

4) Wake vortices can also be laterally transported over a significant distance due to large turbulent eddy motion in the CBL, and their lateral displacements from the initial positions increase with increasing ambient turbulence strength.

5) Wake vortices in the CBL decay rapidly because of strong turbulence intensity typical in the CBL, whereas the rate of decay increases with increasing $\eta$ and is larger in the updraft region than in the downdraft region.

These results could serve useful for adding a prediction of height and lateral variability in the AVOSS vortex trajectory forecast.

## Acknowledgments

## References

[1]Hinton, D. A., Charnock, J. K., Bagwell, D. R., and Grigsby, D., "NASA Aircraft Vortex Spacing System Development Status," *NASA TM-110184*, August 1995. *37th Aerospace Sciences Meeting & Exhibit*, Reno, NV, AIAA Paper No. 99-0753, January 1999.

[2]Robins, R. E. and Delisi, D. P., "Further Development of a Wake Vortex Predictor Algorithm and Comparisons to Data," *37th Aerospace Sciences Meeting & Exhibit*, Reno, NV, AIAA Paper No. 99-0757, January 1999.

[3]Sarpkaya, T., "A New Model for Vortex Decay in the Atmosphere," *37th Aerospace Sciences Meeting & Exhibit*, Reno, NV, AIAA Paper No. 99-0761, January 1999.

[4]Greene, G. C., "An Approximate Model of Vortex Decay in the Atmosphere," *Journal of Aircraft*, Vol. 23, No. 7, 1986, pp. 566-573.

[5]Han, J., Lin, Y. -L., Arya, S. P., and Proctor, F. H., "Numerical Study of Wake Vortex Decay and Descent in Homogeneous Atmospheric Turbulence," In press, *AIAA Journal*, Vol. 38, 2000.

[6]Proctor, F. H., Hinton, D. A., Han, J., Schowalter, D. G., and Lin, Y. -L., "Two-Dimensional Wake Vortex Simulations in the Atmosphere: Preliminary Sensitivity Studies," *35th Aerospace Sciences Meeting & Exhibit*, Reno, NV, AIAA Paper No. 97-0056, January 1997.

[7]Proctor, F. H., "The NASA-Langley Wake Vortex Modeling Effort in Support of an Operational Aircraft Spacing System," *36th Aerospace Sciences Meeting & Exhibit*, Reno, NV, AIAA Paper No. 98-0589, January 1998.

[8]Zak, J. A. and Rodgers, Jr., W. G., "Documentation of Atmospheric Conditions During Observed Rising Aircraft Wakes," *NASA Contractor Report 4767*, 1997.

[9]Campbell, S. D., Dasey, T. J., Freehart, R. E., Heinrichs, R. M., Matthews, M. P., Perras, G. H., and Rowe, G. S., "Wake Vortex Field Measurement Program at Memphis, TN Data Guide," *Project Report: NASA/L-2*, January 1997. [Available from NTIS]

[10]Holzäpfel, F., Gerz, M., Frech, M., and Dornbrack, A., "The Decay of Wake Vortices in the Convective Boundary Layer," *37th Aerospace Sciences Meeting &*

*Exhibit*, Reno, NV, AIAA Paper No. 99-0984, January 1999.     1671-1679.

[11] Weil, J. C., "Dispersion in the Convective Boundary Layer," *Lectures on Air Pollution Modeling*, A. Venkatram and J. C. Wyngaard, Eds., Amer. Meteor. Soc., Boston, 1988, pp. 167-227.

[12] Caughey, S. J., Kitchen M., and Leighton, J. R., "Turbulence Structure in Convective Boundary Layers and Implications for Diffusion," *Boundary-Layer Meteorol.*, Vol. 25, 1983, pp. 345-352.

[13] Stull, R. B., *An Introduction to Boundary Layer Meteorology*, Kluwer Academic Publishers, Dordrecht, 1988, 666 pp.

[14] Proctor, F. H., "The Terminal Area Simulations System, Volume 1: Theoretical Formulation," NASA Contractor Report 4046, DOT/FAA/PM-86/50, 1, 1987.

[15] Proctor, F. H., "Numerical Simulation of Wake Vortices Measured During the Idaho Fall and Memphis Field Programs," *14th AIAA Applied Aerodynamics Conference*, Proceedings, Part-2, New Orleans, LA, AIAA Paper No. 96-2496, June 1996. pp. 943-960.

[16] Proctor, F. H. and Han, J., "Numerical Study of Wake Vortex Interaction with the Ground Using the Terminal Area Simulation System," *37th Aerospace Sciences Meeting & Exhibit*, Reno, NV, AIAA Paper No. 99-0754, January 1999.

[17] Han, J., Lin, Y. -L., Schowalter, D. G., Arya, S. P., and Proctor, F. H., "Large Eddy Simulation of Aircraft Wake Vortices within Homogeneous Turbulence: Crow Instability," In press, *AIAA Journal*, Vol. 38, 2000.

[18] Schowalter, D. G., Decroix, D. S., Switzer, G. F., Lin, Y. -L., and Arya, S. P., "Toward Three-Dimensional Modeling of a Wake Vortex Pair in the Turbulent Boundary Layer," *35th Aerospace Sciences Meeting & Exhibit*, Reno, NV, AIAA Paper No. 97-0058, January 1997.

[19] Schowalter, D. G., DeCroix, D. S., Proctor, F. H., Lin, Y.-L., Arya, S. P., and Kaplan, M. L., "Turbulent Statistics in the Atmospheric Boundary Layer: A Comparison of Large Eddy Simulation with Observations," *11th Symposium on Boundary Layers and Turbulence*, Charlotte, NC, March 1995, pp. 552-555.

[20] Schowalter, D. G., DeCroix, D. S., Lin, Y.-L., Arya, S. P., and Kaplan, M. L., "Planetary Boundary Layer Simulation Using TASS," *NASA Contractor Report 198325*, 1996, 41 pp.

[21] Proctor, F. H., "A LES Subgrid Turbulence Model with Rotational Dampening," *Submitted as NASA Technical Report.*

[22] Crow, S. C., "Stability Theory for a Pair of Trailing Vortices," *AIAA Journal*, Vol. 8, No. 12, 1970, pp. 2172-2179.

[23] Jeong, J. and Hussain, F., "On the Identification of a Vortex," *Journal of Fluid Mechanics*, Vol. 285, 1995, pp. 69-94.

[24] Sarpkaya, T., "Decay of Wake Vortices of Large Aircraft," *AIAA Journal*, Vol. 36, No. 9, 1998, pp.

American Institute of Aeronautics and Astronautics

# Appendix J: Numerical Modeling Studies of Wake Vortices: Real Case Simulations

# AIAA 99-0755

# Numerical Modeling Studies of Wake Vortices: Real Case Simulations

Shaohua Shen, Feng Ding, Jongil Han,
Yuh-Lang Lin, S. Pal Arya
North Carolina State University
Raleigh, North Carolina

Fred H. Proctor
NASA Langley Research Center
Hampton, Virginia

# 37th AIAA Aerospace Sciences Meeting and Exhibit
## January 11-14, 1999 / Reno, NV

# NUMERICAL MODELING STUDIES OF WAKE VORTICES: REAL CASE SIMULATIONS

Shaohua Shen[*], Feng Ding[†], Jongil Han[‡], Yuh-Lang Lin[§], S. Pal Arya[¶]
Department of Marine, Earth and Atmospheric Sciences
North Carolina State University, Raleigh, NC 27695

Fred H. Proctor[||]
NASA Langley Research Center
Flight Dynamics and Control Division
Hampton, VA 23681-2199

## Abstract

A three-dimensional large-eddy simulation model, TASS, is used to simulate the behavior of aircraft wake vortices in a real atmosphere. The purpose for this study is to validate the use of TASS for simulating the decay and transport of wake vortices. Three simulations are performed and the results are compared with the observed data from the 1994-1995 Memphis field experiments. The selected cases have an atmospheric environment of weak turbulence and stable stratification. The model simulations are initialized with appropriate meteorological conditions and a post roll-up vortex system. The behavior of wake vortices as they descend within the atmospheric boundary layer and interact with the ground is discussed.

## 1. Introduction

To increase airport capacity while maintaining or increasing the present aviation safety levels, National Aeronautics and Space Administration (NASA) initiated the Aircraft Vortex Spacing System (AVOSS) project as an essential element of its Terminal Area Productivity (TAP) program to develop a real-time wake vortex forecasting system for Air Traffic Control (ATC)[1,2].

An accurate estimation of the lifetime and transport of the wake vortices trailing behind airplanes is truly crucial in developing the forecasting systems which are responsible for aviation safety and efficiency. A focal problem is to predict the behavior of wake vortices under different atmospheric environments. Results of field experiments as well as numerical simulations indicate that the atmospheric disturbances, such as turbulence, stratification and wind shear have strong influence on the evolution and transport of wake vortices[3-9].

The development of the forecasting system is based on both observed data and numerical simulations. During the past decades, great efforts have been made to understand the demise mechanism of wake vortices and the impact of ambient turbulence, stratification, wind shear and proximity effects on the vortices. These efforts included the laboratory and observed data as well as numerical modeling[9-15]. However, the behavior of wake vortices still remains elusive due to the intricate interaction of the wake vortex pair with its surrounding atmospheric boundary layer. On the other hand, systematic investigation of these processes is hampered by the environmental conditions. The numerical simulations become more practical with increasing computer power because they allow us to study the behavior of wake vortices in a wider range of meteorological conditions than those measured during field experiments which are restricted to a specific location (sometimes with a unique climatology) and relatively short period of time. But numerical models must be validated using these observational data.

In recent years, the large-eddy simulation (LES) models within the meteorological context have been widely used to study the behavior of wake

[*]Visiting Assistant Professor
[†]Research Assistant
[‡]Research Scientist
[§]Professor
[¶]Professor
[||]Research Scientist, AIAA member

vortices[15-21]. Numerical modeling efforts play a key role in the development of the AVOSS system. The Terminal Area Simulation System (TASS), a numerical large-eddy simulation model developed by Proctor[22,23], has been adapted to accomplish this objective. The model has been successfully used to investigate the effects of atmospheric turbulence, stratification, wind shear and fog on the decay of wake vortices in both two and three dimensional simulations[9,17]. Proctor[9] simulated the behavior of wake vortices measured during the Idaho Falls and Memphis field programs using the TASS model. His results showed that the TASS model was accurate in simulating transport of wake vortices in two dimensions for stable conditions in which there is little or no ambient turbulence. Han et al.[19-20] investigated the Crow instability and the effect of atmospheric turbulence on the vortex decay using three-dimensional TASS model. Their results agree well with other laboratory and field measurements. It is essential that all aspects of the model simulations be compared and validated with observed data although previous studies have shown that the TASS model is quite successful in simulating vortex decay.

Lidar measurements, coupled with the simultaneous recording of the meteorological data from the field measurements conducted at Memphis during December, 1994 and August, 1995 and at Dallas/Ft. Worth (DFW) Airport during 1997-1998, have provided us with the most reliable data base so far. These data sets contain the information on velocity, temperature, circulation and so on, which supply us enough information to carefully make assessment, validation, and improvement of various numerical models.

Ongoing studies with the TASS model are aimed at understanding and quantifying the decay of wake vortices. A determination of whether the simulations can realistically decay vortices is a necessary first step. The model must be validated before its results are used in developing predictor algorithms for an AVOSS system.

The purpose of this paper is to further validate the TASS model. Three dimensional simulations of cases 1252 and 1273 from the 1995 Memphis field experiments are conducted. Presented are TASS results and comparisons with the measurement data from both of the cases.

In this paper, we first briefly describe the TASS model in section 2. We then describe the initializa-

tion of the model and the experiments used to initialize the model in section 3. The results from the simulations are presented in section 4 and, finally, our studies are summarized in section 5.

## 2. The Model Description

### 2.1 The Numerical Model

The TASS model used in the present study is a three-dimensional, nonlinear, compressible, non-hydrostatic LES model. The TASS equation set in standard tensor notation is as follows[9,22]:

$$\frac{\partial u_i}{\partial t} + \frac{H}{\rho_0}\frac{\partial p}{\partial x_i} = -\frac{\partial u_i u_j}{\partial x_j} + u_i\frac{\partial u_j}{\partial x_j} + g(H-1)\delta_{i3}$$
$$+ \frac{1}{\rho_0}\frac{\partial \tau_{ij}}{\partial x_j} \tag{1}$$

$$H = \left[\frac{\theta}{\theta_0} - \frac{pC_v}{PC_p}\right] \tag{2}$$

$$\frac{\partial p}{\partial t} + \frac{C_p P}{C_v}\frac{\partial u_j}{\partial x_j} = \rho_0 g u_j \delta_{j3} \tag{3}$$

$$\frac{\partial \theta}{\partial t} = -\frac{\partial \theta u_j}{\partial x_j} + \theta\frac{\partial u_j}{\partial x_i} + \frac{1}{\rho_0}\frac{\partial \tau_{\theta j}}{\partial x_j} \tag{4}$$

where $u_i$ is the component of velocity, $t$ is time, $\theta$ is potential temperature and $\theta_0$ is the reference potential temperature. $p$ is deviation of pressure from the reference atmospheric pressure $P$, $\rho_0$ is the reference air density, $C_p$ and $C_v$ are the specific heats of air at constant pressure and volume, respectively. $H$ represents the ratio of the reference density of environment to the local density. $\delta_{i3}$ is the Kronecker delta. $g$ is the earth's gravitational acceleration and $\tau_{ij}$ and $\tau_{\theta j}$ are Reynolds stress and heat flux, respectively.

### 2.2 The Subgrid Turbulence Model

The dependent variables in TASS are treated as averages over the grid volumes which result in subgrid flux terms. The subgrid flux terms $\tau_{ij}$ and $\tau_{\theta j}$ are, respectively, approximated by using first-order closure:

$$\tau_{ij} = \rho_0 K_m D_{ij}, \tag{5}$$

$$\tau_{\theta j} = \rho_0 K_H \frac{\partial \theta}{\partial x_j}, \tag{6}$$

2

where the deformation tensor $D_{ij}$ is defined as

$$D_{ij} = \frac{\partial u_i}{\partial x_j} + \frac{\partial u_j}{\partial x_i} + \frac{2}{3}\frac{\partial u_k}{\partial x_k}\delta_{ij} \qquad (7)$$

For subgrid turbulence, TASS currently uses a conventional Smagorinsky model with modifications for stratification and rotation effects:

$$K_m = (c_s\Delta)^2 |D| (1 - \alpha\,Ri_S - \beta\,Ri_R)^{0.5} \qquad (8)$$

$$K_H = \alpha K_m, \qquad (9)$$

$$Ri_S = \frac{N^2}{D^2}, \qquad (10)$$

$$N^2 = \frac{g}{\theta}\frac{\partial\theta}{\partial z}. \qquad (11)$$

Here $K_m$ and $K_H$ are the subgrid scale eddy diffusivities of momentum and heat, respectively. $Ri_S$ is the Richardson number due to stratification, $N$ is the Brunt-Väisäla frequency, $\Delta = (2\Delta x 2\Delta x 2\Delta x)^{1/3}$ is the filter width, and $c_s = 0.16$ and $\alpha = 3$ are constants, and $\beta$ is a constant. The rotational Richardson number, $Ri_R$, represents the rotational effect on turbulence and is analogous to the effect of stratification.

This analogy between the rotation or streamline curvature and buoyancy was first suggested by Bradshaw[24]. An approximate expression for $Ri_R$ applicable to three-dimensional simulations is

$$Ri_R = \frac{\Omega^2}{D^2} + \frac{|\Omega|}{|D|}, \qquad (12)$$

where $\Omega$ is the magnitude of three-dimensional vorticity[25]. The above formulation does not require cylindrical coordinates or location of vortex axis, so it can be readily applied to fully three-dimensional systems. Equations (8) and (12) indicate that the eddy viscosity $K_m$ can be effectively reduced within the core of vortices when $Ri_R$ or $|\Omega|/|D|$ is large. Since the above formula cannot discriminate between a shear flow and flow with coherent rotation, a discriminator function is applied such that $Ri_R=0$ when no coherent rotation is present (thus defaulting to the original Smagorinsky model for pure shear flow[25]). Without Eq. (12), the Smagorinsky subgrid closure

model overpredicts the vortex decay rate in the vortex core region and causes unrealistic growth of the core size[26].

In the TASS model, a time-splitting integration scheme is used, in which the time integration is broken into small and large time steps. The acoustic term in the momentum and pressure equations are computed over the small time step, while other terms are calculated over the large time step. The space derivatives are approximated by central differences in quadratic conservative form with 4th-order accuracy for advection terms. Arakawa C grid staggered mesh is employed for all variables[27]. There is a choice of different surface boundary conditions by which one can specify the uniform surface temperature, the surface heat flux or the surface energy budget. There is also an option to choose either open or periodical lateral boundary conditions. A detailed description of the model was given by Proctor[9,22].

In our simulations, periodic boundary conditions are imposed in horizontal directions and zero gradient top boundary conditions and no slip bottom conditions are used in the vertical direction. Surface stresses are computed from similarity theory and the surface heat flux is prescribed.

## 3. Initialization

### 3.1 Vortex Initialization

A vortex model recently developed by Proctor[28] is used as an initial wake vortex field for three dimensional simulations. This model is empirical as it is based on field observations of several wake vortices measured early in their evolution and represents the post roll-up, wake-vortex velocity field. The model represents observed wake vortex tangential velocity profile much better than previous models, such as Lamb model. Its tangential velocity, $V$, is represented as

$$V(r) = \frac{\Gamma_\infty}{2\pi r}\left(1 - e^{-10(r/B)^{0.75}}\right), \qquad (13)$$

where $\Gamma_\infty$ is the circulation at $r \gg r_c$ ($r_c$ is the initial vortex core radius defined as radial distance of peak tangential velocity) and $B$ is the span of the generating aircraft. The values assumed for initial vortex separation and circulation are derived from aircraft weight $W$, wingspan $B$, air density $\rho$, and airspeed $V_a$, according to the conventional assump-

tion of elliptically-loaded wing, i.e.,

$$b_0 = \frac{\pi B}{4} \quad \text{and} \quad \Gamma_0 = \frac{4W}{\pi B \rho V_a}. \tag{14}$$

Note that the velocity field in $Eq.(13)$ depends on the wingspan $B$ instead of the core radius $r_c$ which may not be easy to measure with a good accuracy; $Eq.(13)$ is applied only at $r > r_c$. For $r < r_c$, the model is matched with the Lamb model, i.e.,

$$V(r) = \frac{\Gamma_\infty}{2\pi r} 1.4 \left(1 - e^{-10\,(r_c/B)^{0.73}}\right)$$

$$\cdot \times \left(1 - e^{-1.2527\,(r/r_c)^2}\right). \tag{15}$$

The results from Han et al.[26] show that this initialization procedure gives a good comparison with observation data even though it does not depend on the individual aircraft configuration.

### 3.2 Measurement Data

The data we used in our simulations come from the experiment conducted at the Memphis International Airport during August, 1995. The purpose of the field experiment was to measure wake vortex, meteorological and aircraft data together at an operational airport for use in validation of wake vortex models and in the development of the AVOSS prediction system. The wake vortex measurements were performed by a van-mounted 10.6 $\mu$m $CO_2$ CW lidar[29]. The lidar measured line-of-sight velocities in a plane perpendicular to the flight path in order to characterize vortices generated by approaching aircraft.

The atmospheric data sets were measured by several instruments, which included a 45m tower instrumented with various meteorological sensors for wind velocity, temperature and humidity, a radar profiler and acoustic sodar for measuring winds aloft, a Radio acoustic sounding system (RASS) for measuring temperature data, and the radiosonde balloon launches for the measurement of vertical profiles of wind speed and temperature[30]. The standard atmospheric variables and the atmospheric fluxes were measured at 1 Hz and 10 Hz, respectively.

In the Memphis field experiment, most of the turbulence data come from the tower measurements at 5 and 40m, the turbulence kinetic energy (TKE) and the energy dissipation rate, $\epsilon$, are only available at

heights of 5 and 40m ($\epsilon$ was calculated by estimating the spectral energy density). Here, the turbulence intensity is defined as weak, mild or strong in terms of the TKE or $\epsilon$ at a height of 40m[31]. From these data sets, cases 1252 and 1273 were chosen for the validation of the TASS model. Both cases have a stable stratification with weak wind shear. The values of wind shear and stratification at the surface and initial vortex height for both cases are given in Table 1.

| Flight No. | M-1252 | M-1273 |
|------------|--------|--------|
| $(\partial V/\partial z)_s$ | $9.3\times10^{-2}$ | $1.56\times10^{-1}$ |
| $(\partial V/\partial z)_h$ | $4.0\times10^{-3}$ | $-3.0\times10^{-3}$ |
| $N^*_s$ | $4.1\times10^{-2}$ | $1.12\times10^{-1}$ |
| $N^*_h$ | $-6.8\times10^{-4}$ | $2.50\times10^{-3}$ |

Table 1. Values of wind shear and stratification for Memphis cases 1252 and 1273

In Table 1, subscript "s" and "h" represent the values at the surface ($z = 3m$) and the initial vortex height, respectively. The vertical shear of crosswind, $\partial V/\partial z$, changes with height, and the nondimensional Brunt-Väisälä frequency is $N^*=2\pi b_0^2/\Gamma_0$, where $\Gamma_0$ is the initial circulation of the vortices.

The values of the vortex parameters and flight data of the generating aircraft were obtained from the Memphis data set[29]. The flight type, initial circulation, vortex core radius, vortex separation, initial vortex height and sink rate of vortex are shown in Table 2.

| Flight No. | M-1252 | M-1273 |
|------------|--------|--------|
| Aircraft | B-757 | DC-10 |
| $\Gamma_0$ $(m^2/s)$ | 345 | 489 |
| $r_c$(m) | 1.5 | 2.5 |
| $b_0$(m) | 29.8 | 39.6 |
| $h_0$(m) | 175.0 | 169.5 |
| $V_0$(m/s) | 1.87 | 1.97 |
| $b_0/V_0$(s) | 16.1 | 20.1 |

Table 2. Aircraft type and vortex parameters

### 3.3 Grid/Domain Configuration

The TASS model with the three-dimensional option is chosen to perform all simulations in this paper. The model domains, along the axial, lateral and vertical directions, are 75 × 150.75 × 237m and 104 × 202 × 200m for the cases 1252 and 1273, re-

spectively. As shown in Table 2, the initial separation distance of the vortex pair, $b_0$, is 29.8m in case 1252 and 39.6m in case 1273. The domain size in the axial direction is about $2.5b_0$ for cases 1252 and 1273. Such a small domain size in the axial direction may suppress the development of Crow instability of which theoretical maximum wavelength is about $8.6b_0$ [10] and cause homogeneous vortex decay along this direction in a statistical sense, but it can save much computing time without destroying the main vortex decay mechanism[15]. The domain sizes in lateral directions are approximately $5b_0$ for both cases. The domain sizes in lateral and vertical directions are reasonable for a vortex pair separation of $b_0$, because the strain rate of neighboring periodic vorices is only a few percent of that exerted by one vortex on the other in the vortex pair.

To save computing time, the TASS model with two meshes of different grid resolution is used to perform our simulations. We first ran the TASS model with a coarse mesh to generate a steady state turbulence. Then all variables are interpolated to fine mesh to simulate the vortex decay. Both coarse and fine meshes cover the same domain. A detailed description of this procedure will be given in the next subsection.

The grid points are, respectively, $50 \times 102 \times 136$ in the coarse mesh and $50 \times 201 \times 316$ in the fine mesh, with grid size $(\Delta x, \Delta y, \Delta z) = (1.5\,m, 1.5\,m, 1.5\,m)$, and $(\Delta x, \Delta y, \Delta z) = (1.5m, 0.75m, 0.75m)$ for case 1252. In case 1273, the grid points are $52 \times 100 \times 100$ and grid sizes are $(\Delta x, \Delta y, \Delta z) = (2m, 2m, 2m)$ in the coarse mesh, while the grid points are $52 \times 202 \times 200$ with grid sizes $(\Delta x, \Delta y, \Delta z) = (2m, 1m, 1m)$ in the fine mesh. The $x$, $y$ and $z$ correspond to the axial, lateral and vertical directions of the vortex system and corresponding velocity components of $u$, $v$ and $w$, respectively.

### 3.4 Turbulence Initialization

To simulate the behaviour of wake vortices in a real atmosphere, it is of crucial importance to get an initial field which is analogous to real atmospheric environments. One of the major difficulties in initializing the model for real cases is obtaining a representative ambient turbulence field. The difficulty arises from the intricate interaction of the atmospheric turbulence, stratification and wind shear. In case 1252 and 1273, the turbulence is weak due to stable strat-

ification, especially for case 1252. It is difficult for the model to generate or maintain the observed initial turbulence field under stable stratification conditions without an external forcing because the computational domain in the model does not cover the whole atmospheric boundary layer and there is no energy source to maintain the turbulence.

In our simulations, we first generated a turbulence field in coarse mesh through the surface heating. After turbulence reaches a steady state, we then interpolated the values of all variables in the coarse mesh to the fine mesh. At that time, the wind and temperature profiles deviated from their initial values beause of the surface heating and mixing turbulence. To maintain the initial wind and temperature profiles, we continued to run the model and forced the mean wind and temperature profiles back to their initial values at each time step through the surface cooling. During this period, we monitor the decrease in turbulence kinetic energy (TKE) with time at a height near 40m. The wake vortex pair was injected into the simulation when the TKE at this height was approximately equal to the observed TKE measured at 40m

In this paper, three simulations were performed using the three dimensional TASS model and the cases 1252 and 1273 in the Memphis field measurements were used to validate the model. The first two simulations were designed to further simulate the vortex decay in case 1273 and 1252, respectively. The third simulation was designed to examine the simulation of case 1252.

The vertical profiles of measured temperature and wind velocity that represent the air mass surrounding the wake vortices were used to initialize the simulations (Figs. 1 and 2). We assumed that the ambient temperature and wind velocity are homogeneous in horizontal directions and the ambient velocity along the axial direction of wake vortex (u component)is zero.

The energy dissipation rates and turbulence intensities of the measurements and the three simulations for both case 1252 and 1273 are given in Table 3.

Here $\eta=(\epsilon b_0)^{1/3}/V_0$ and $V_0=\Gamma/2\pi b_0$. "ob" and "sm" represent the values from the observation and simulation, respectively. A second simulation for case 1252 (referred as M-1252-II) is a re-simulation of the first simulation, but with somewhat larger tur-
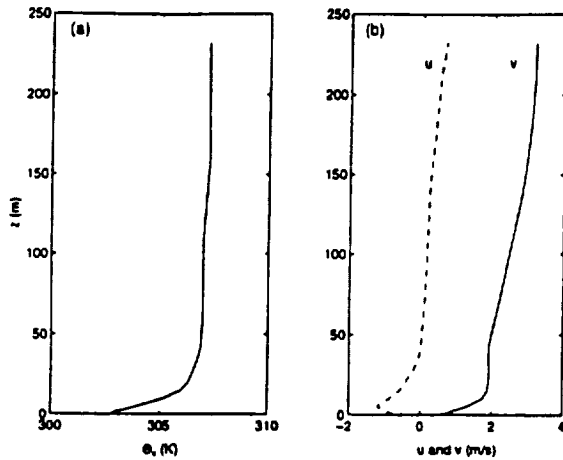
-Figure 1. The vertical profiles of (a) virtual potential temperature and (b) wind velocities for case 1252. $u$ (dashed line) and $v$ (solid line) are wind velocity in axial and lateral (crosswind) directions, respectively.



Figure 2. Same as Fig. 1, but for case 1273.

| flight No. | M-1273 | M-1252 | M-1252-II |
|---|---|---|---|
| $\epsilon$(ob) | $3.18\times10^{-4}$ | $1.35\times10^{-6}$ | $1.35\times10^{-6}$ |
| $\epsilon$ (sm) | $2.95\times10^{-4}$ | $6.27\times10^{-6}$ | $4.30\times10^{-5}$ |
| $\eta$ (ob) | $1.21\times10^{-1}$ | $1.84\times10^{-2}$ | $1.84\times10^{-2}$ |
| $\eta$ (sm) | $1.42\times10^{-1}$ | $3.05\times10^{-2}$ | $5.85\times10^{-2}$ |

Table 3. Turbulence intensity

bulence intensity than was observed.

## 4. Results and Discussion

### 4.1 Case 1273

In case 1273 a wake vortex is generated by a DC-10 at an elevation of 170 m. The vortices descend through weak crosswind and low turbulence and are not influenced by the ground until after 60 s. The atmospheric temperature profile is weakly stable above 50 m elevation, but becomes increasing stable toward the ground. Results from this case are shown in Fig. 3-6.

Figure 3 shows the radial distribution of normalized circulation for 3-D simulation and Lidar measurement data for case 1273 at t= 15, 45 and 75 second. Comparison of the profiles shows that the circulation computed from the model agrees generally with that measured by the Lidar. Both the simulations and observations show that the circulation decreases with time and the core radius remains a constant.

The circulation decays more or less uniformly with radius as shown in Fig. 3. At t=75s, the vortex has descended to about 35m above the ground (see Fig. 6), where the stratification becomes more stable and the ground begins to interact strongly with the vortex pair.

Figure 3 also indicates that the modeled circulation, in some degree, deviates from the observed circulation. One of the reasons is that the modeled circulation was obtained directly by integrating the vorticity field and then averaging the circulations at all cross-sections along axial direction, while the measured circulation was estimated from Lidar line-of-sight velocities at one cross-section.

The radial distribution of tangential velocity from the simulation and Lidar measurement at t=15, 45 and 75s is shown in Figure 4. It is clear that the tangential velocity decays with increasing time and radial distance. At t=75s, the tangential velocity near the edge of the core radius is reduced to about 30% of its initial value. The rapid decay is caused by the ambient turbulence and stratification, rather than by molecular diffusion and core expansion which need more than several hours to undergo a similar decay. In fact, Fig. 4c shows that the core radius only increase to 3.0m from its initial value of 2.5m. These results agree well with the estimates of Sarpkaya[31].

The averaged circulations of 3-10m and 5-15m are plotted in Figure 5. The 3-10m averaged circulation is well matched with measurements, except for the time less than 10s when the observed circulation was larger than the modeled circulation. In our simula-
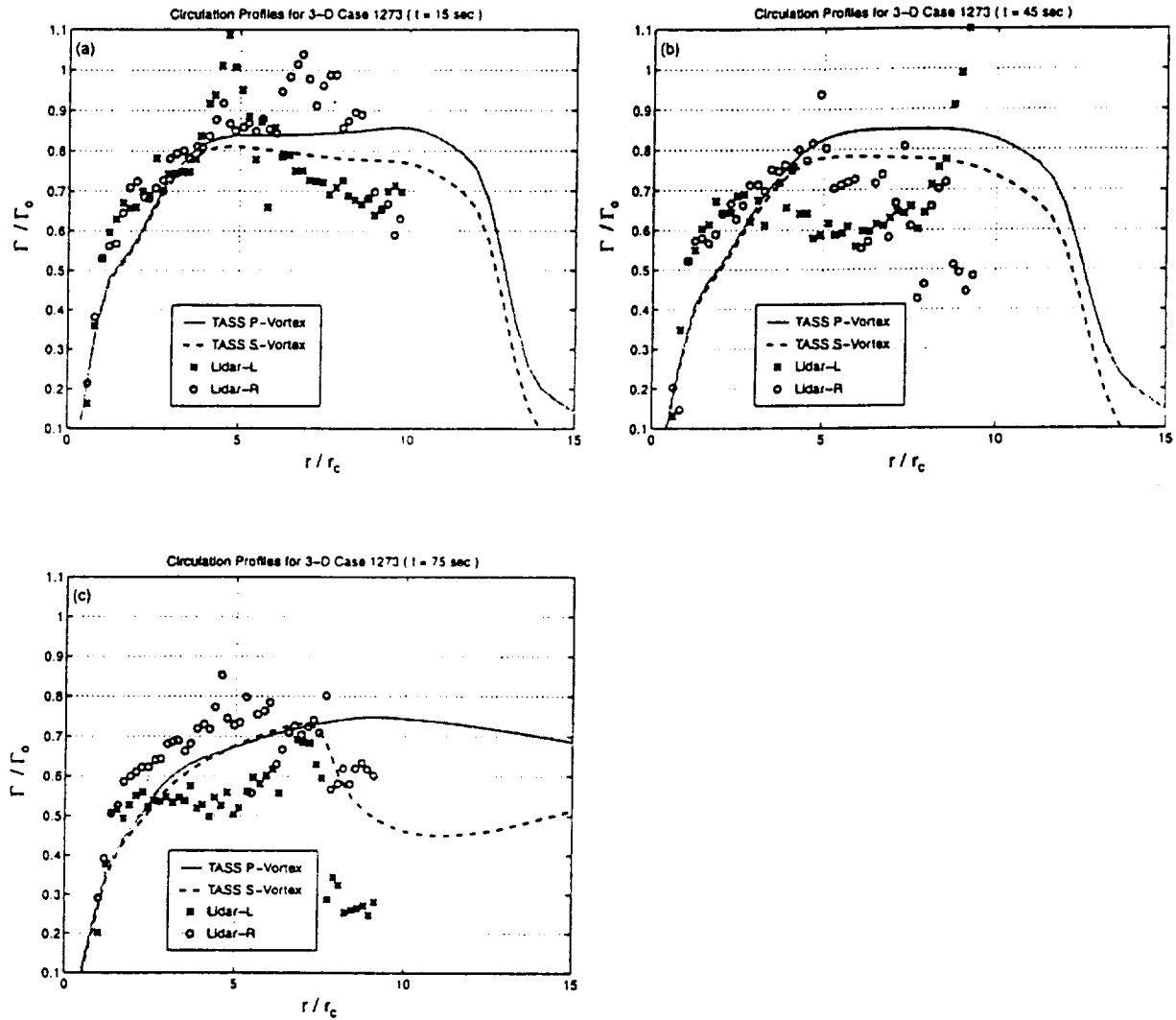
Figure 3. The radial distribution of circulation from the TASS simulation and Lidar measurements for case 1273 at (a) t=15s, (b) 45s and (c) 75s. Circulation is normalized by the initial theoretical circulation, and radius is normalized by the initial core radius (rc=2.5 m). Symbols represent Lidar measurements of left and right sides of port vortex. Solid and dashed lines represent the simulated Port and Starboard vortices, respectively.
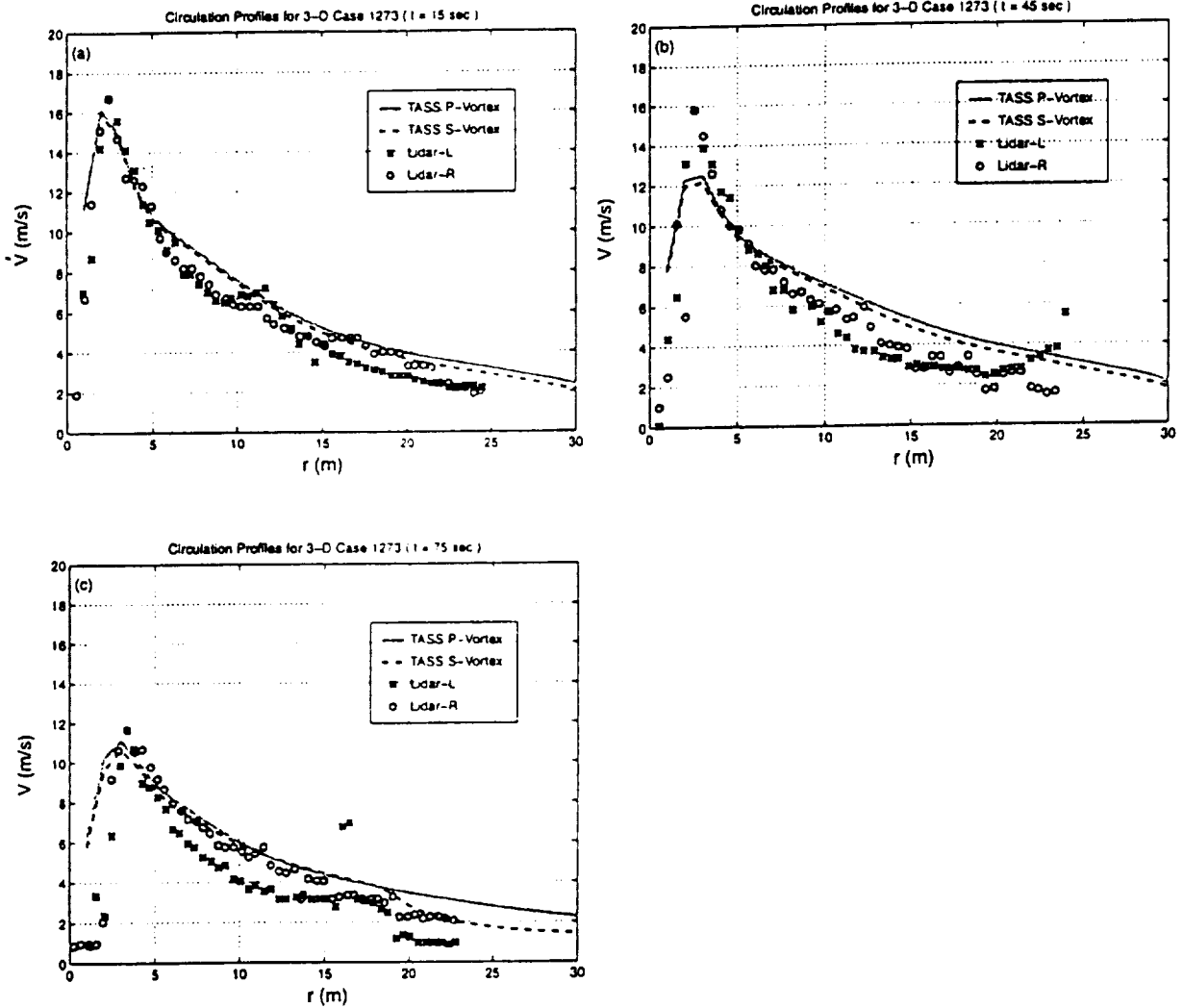
American Institute of Aeronautics and Astronautics

Figure 4. The radial distribution of tangential velocity from the TASS simulation and Lidar measurement for case 1273 at (a) t=15s, (b) 45s and (c) 75s. Symbols represent Lidar measurements of left and right sides of port vortex. Solid and dashed lines represent the simulated port and starboard vortices, respectively.
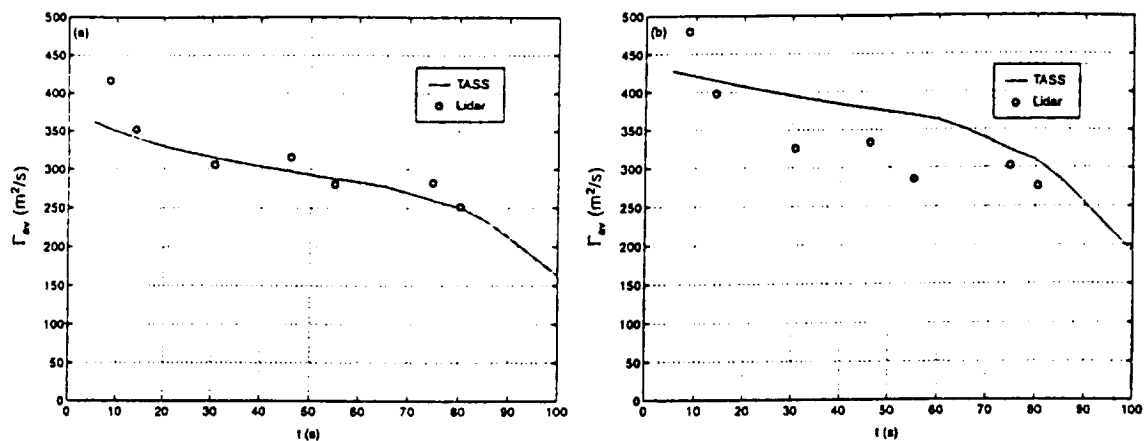
Figure 5. The 3-10m and 5-15m average circulations versus time from both the simulation and measurements for case 1273. (a) the 3-10m average circulation; (b) the 5-15m average circulation.
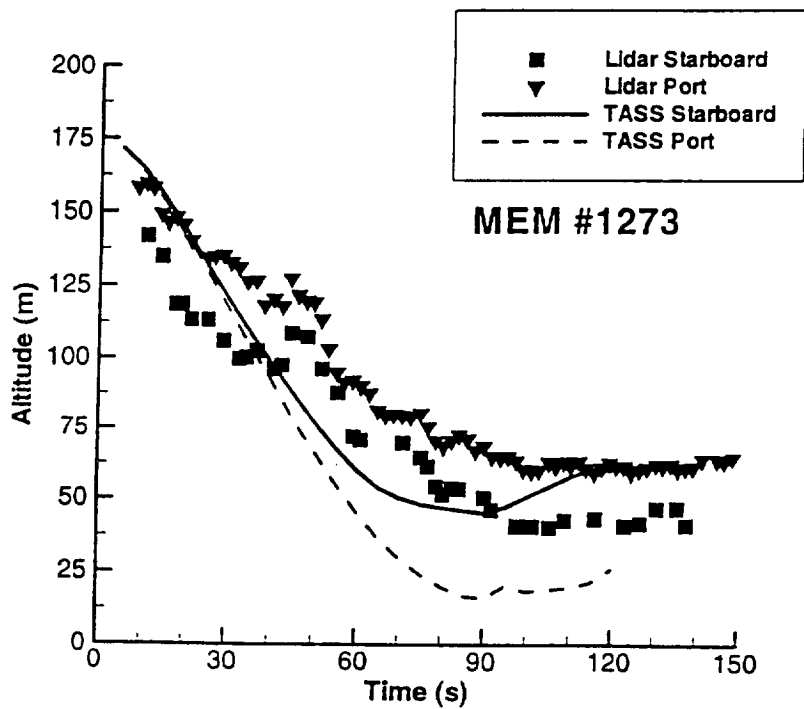


Figure 6. The vortex height history from the simulation and field measurements for case 1273. Symbols represent Lidar measurements. Solid and dashed lines represent the simulated port and starboard vortices, respectively.

American Institute of Aeronautics and Astronautics

tion, the 5-10m averaged circulation decays slowly before t=60s and more rapidly after that time (Fig. 5b). Although the modeled circulations are slightly larger than the observed circulation, the differences are within 20%. The discrepancy at early times may be caused by measurement error, since Campbell et al.[32] have found that the measured Lidar circulations were overestimated during initial times.

Comparisons of the modeled results with field measurements of the vortex trajectories are shown in Figure 6. It can be seen that the development of the vortex height with time from both the simulation and observation is in reasonably good agreement. The vortices linearly descend until at t=60s when they stall due to the stable stratification, windshear, and ground effect. The vortices descended to an average height of 55m at about t=85s. After that time, they rise slightly.

As shown in Fig. 6, the port vortex is deflected to a higher altitude than its starboard counterpart, and the mutual induction between the two vortices is weakened because of the increasing separation between the two vortices. Our simulation is consistent with Proctor's two-dimensional simulation[17], regarding the influence of crosswind shear on vortex descent. Compared with the measurement data (Fig. 6), the starboard vortex descended a lower altitude (about 25m) than that observed (about 40m) during later time of the experiment.

## 4.2 Case 1252

Case 1252 is somewhat similar to 1273 except that the wake is generated by a B-757 in an environment of slightly weaker stratification and turbulence. Both the simulated and observed wakes descend to the top of the stable layer at 40m in about 100s.

The radial distribution of normalized circulation and tangential velocity from the 3-D simulation and Lidar measurement data for case 1252 at t= 15, 30 and 80s are shown in Figures 7-8. The modeled circulation decays slower than the measured circulation, particularly at t<40s or r/rc > 5. The tangential velocity is well matched with the observation data, except near the core radius where the model under predicts the tangential velocity.

Figure 9 shows the averaged circulations of 3-10m and 5-15m at different times. The model predicts the decay of the 3-10m averaged circulation very well,

but under predicts the decay of the 5-15m averaged circulation. Measurement shows decay more rapidly before t=40s. One possible reason for the under prediction of the decay could be an underestimation in the intensity of the ambient turbulence. Therefore, an additional simulation has been run using a slightly higher value of turbulence and will be presented later in this section.

The vortex trajectories from the simulation and observation are shown in Figure 10, and it can be seen that the vortex trajectories are well predicted. Unlike in case 1273, the vortices do not show any rising motion prior to ground interaction. Fig. 10a shows the wake vortices linearly descending with a velocity of 1.8m/s before 70s, but slowly descending after 70s apparently due to the strong stratification and ground effects. The effect of the crosswind is clear in Fig. 10b. Both vortices are transported in the same direction. They move away from the position of generation before 45s and turn back to their original position during later time. This is partly due to the downward transport of crossflow momentum from their generation point. It is worthy to note that the effect of the crosswind is not simple advection since the slope of the lateral position vs time relation is different for both vortices.

To investigate whether the relatively faster decay from the Lidar measurements might have been associated with an under-reported level of turbulence intensity, we have rerun case 1252 with a slightly larger value for ambient turbulence. Otherwise, all conditions are identical with those in the previous simulation, with $\epsilon$ now set to $4.3 \times 10^{-5} m^2/s^3$.

The radial distribution of normalized circulation and tangential velocity for the simulation and Lidar measurement data at t= 30 are shown in Figure 12. It can be seen that the modeled circulation and tangential velocity are well matched with the Lidar measurements. Comparing with Figs. 8-9, the circulation decay is much faster at all radii for the larger intensity of ambient turbulence.

Figure 12 shows that the averaged circulations of both 3-10m and 5-10m are well predicted except that the model slightly over-predicts the decay of the 3-10m averaged circulation after t=60s due to slightly stronger turbulence. Compared with Fig. 9, we can see from Fig. 12 that this simulation better reproduced the behavior of wake vortices. The vortices decay rapidly for the time less than 40s and decay slowly after that time. A possible explanation for
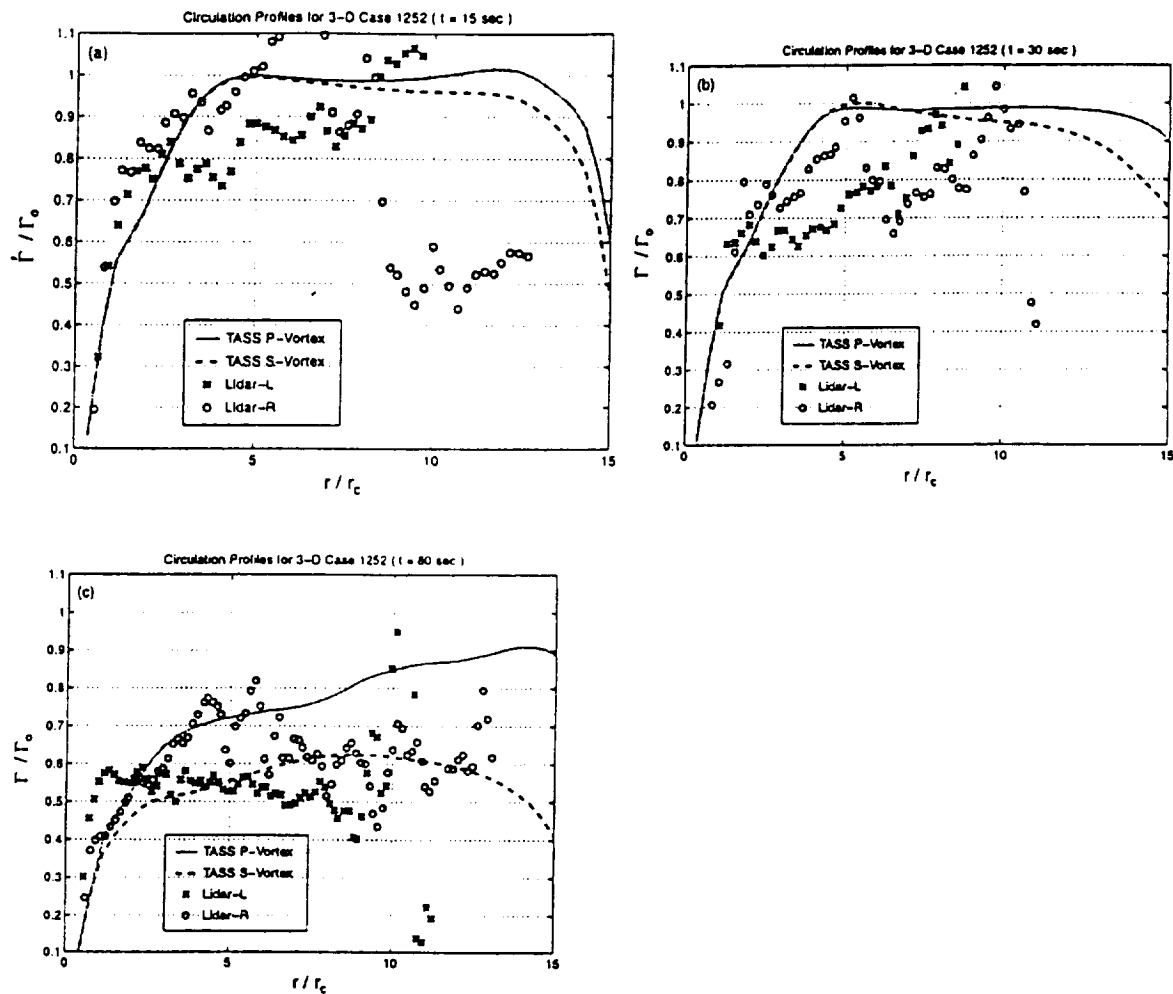
Figure 7. The radial distribution of circulation from the TASS simulation and Lidar measurements for case 1252 at (a) t=15s, (b) 30s and (c) 80s. Circulation is normalized by the initial theoretical circulation, and radius is normalized by initial core radius (rc=1.5 m). Symbols represent Lidar measurements of left and right sides of port vortex. Solid and dashed lines represent the simulated port and starboard vortices, respectively.
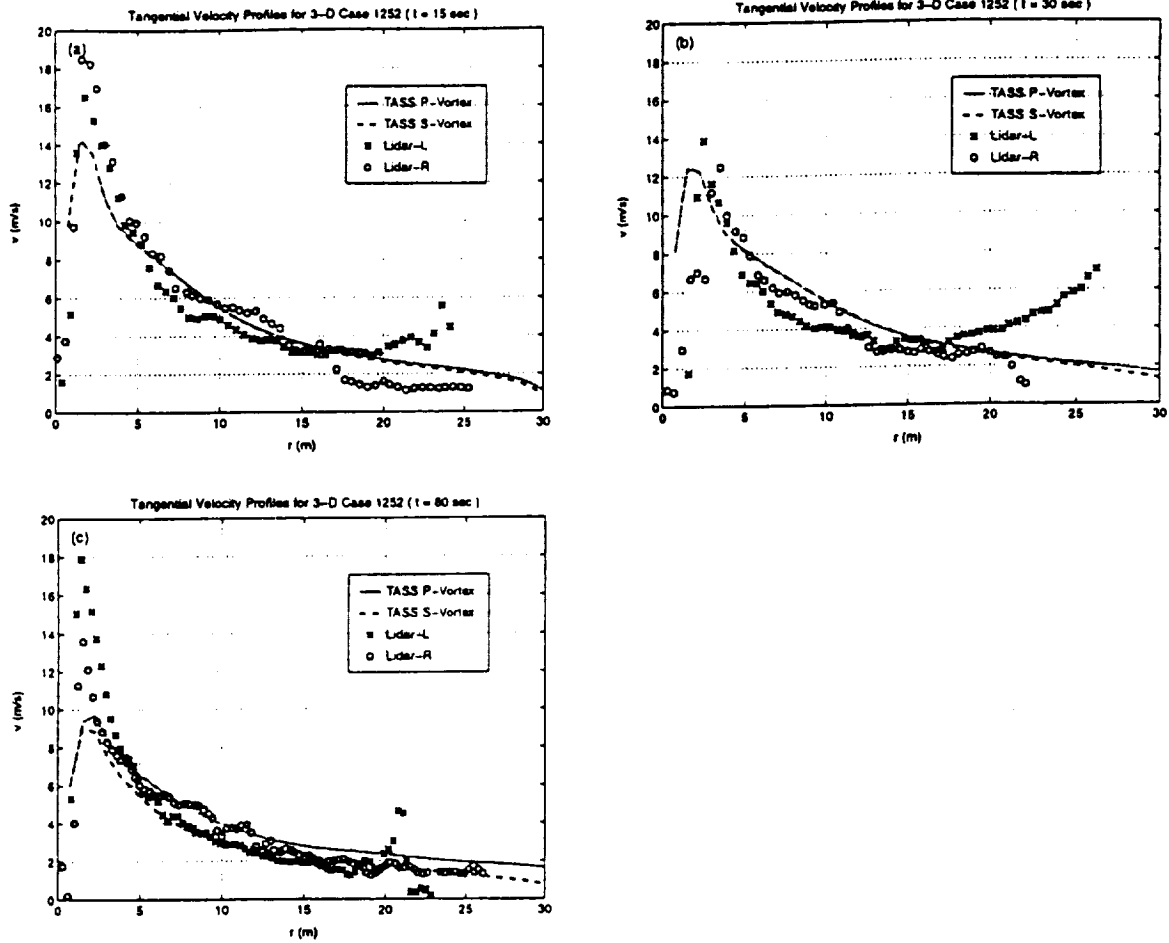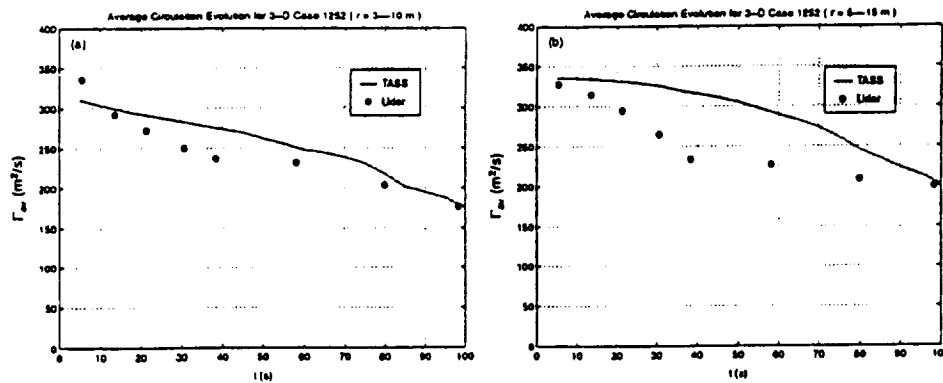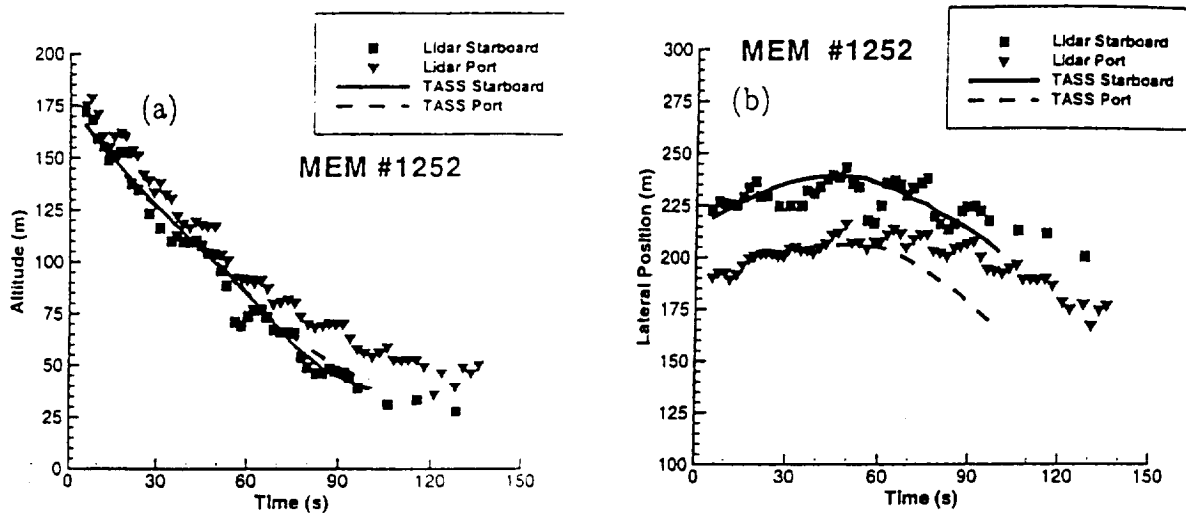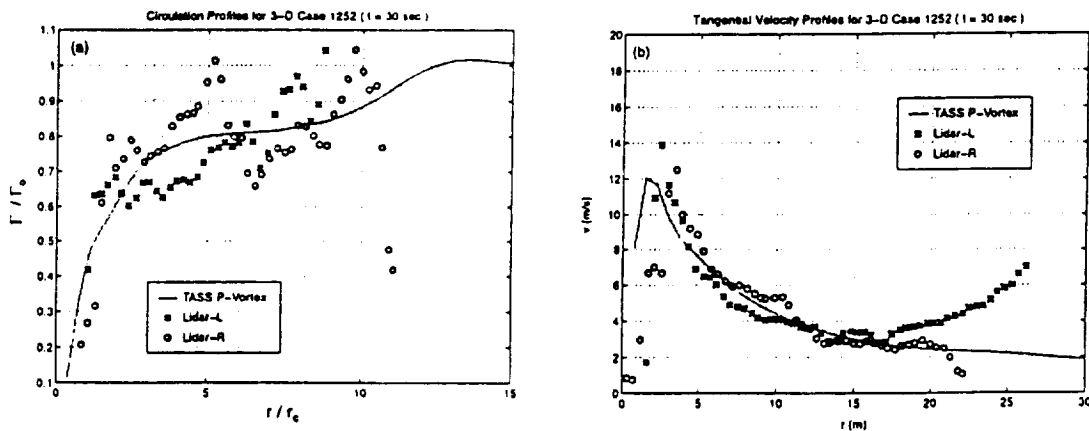
Figure 8. The radial distribution of tangential velocity from the TASS simulation and Lidar measurements for case 1252 at (a) t=15s, (b) 30s and (c) 80s. Symbols represent Lidar measurements of left and right sides of port vortex. Solid and dashed lines represent the simulated port and starboard vortices, respectively.



Figure 9. The 3-10m and 5-15m average circulations versus time from both the simulation and measurements for case 1252. (a) the 3-10m average circulation; (b) the 5-15m average circulation.

Figure 10. The vortex trajectories from the simulation and Lidar measurements for case 1252. (a) vortex height history; (b)vortex lateral position. Symbols represent Lidar measurements. Solid and dashed lines represent the simulated port and starboard vortices, respectively.



Figure 11. The radial distribution of (a) circulation and (b) tangential velocity from the TASS simulation and Lidar measurements at t= 30s. Circulation is normalized by the initial theoretical circulation, and $r_c$ is initial core radius. Symbols represent Lidar measurements of left and right sides of port vortex. Solid line represents the simulated port vortex.
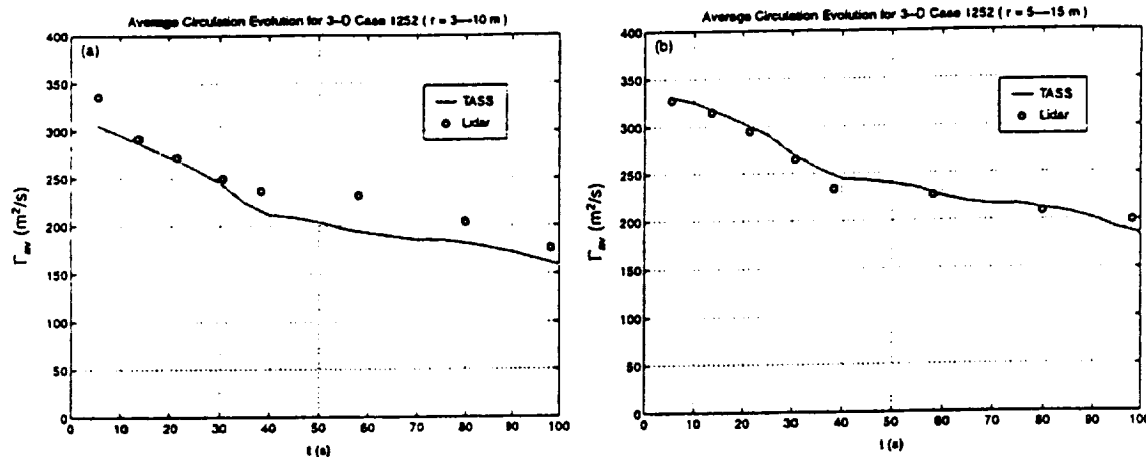
Figure 12. The 3-10m and 5-10m average circulations versus time from the simulation and Lidar measurements. (a) the 3-10m average circulation; (b) the 5-10m circulation.

this good agreement is that the measured dissipation rate was under-estimated or that the value observed at 40 m did not characterize the turbulence intensity at other altitudes.

## 5. Summary

To validate the application of LES to wake vortex decay, three-dimensional simulations in a realistic atmospheric boundary layer were performed using NASA's TASS model. Two case studies were presented which were initialized from and compared with Memphis fields measurements.

Our results indicate that the TASS model successfully predicted the behavior of aircraft wake vortices within environments representing a transitioning atmospheric boundary layer following sunset. Good agreement was obtained between simulations and measurements for the wake vortex trajectories. Exceptional agreement with the measurements was obtained for vortex decay. The three-dimensional simulations suggest that ambient turbulence, stratification and wind shear play important roles in the decay and transport of wake vortices. Ambient turbulence significantly influences the vortex decay. Study on the specific roles of wind shear, stratification and turbulence on vortex behavior pertinent to these two cases are in progress.

## Acknowledgments:

## References

[1] Hinton, D. A., "Aircraft Vortex Spacing System (AVOSS) Conceptual Design," NASA TM-110184, August 1995.

[2] Perry, R. B., Hinton, D. A., and Stuever, R. A., "NASA Wake Vortex Research for Aircraft Spacing," 35th Aerospace Sciences Meeting & Exhibit, Reno, NV, AIAA Paper No. 97-0057, January 1997.

[3] Tombach, I., "Observations of Atmospheric Effects on Vortex Wake Behavior," Journal of Aircraft, Vol. 10, 1973, pp. 641-647.

[4] Hecht, A. M., Bilanin, A. J., and Hirsh, J. E., "Turbulent Trailing Vortices in Stratified Fluids," AIAA Journal, Vol. 19, 1981, pp. 691-698.

[5] Sarpkaya, T., "Trailing Vortices in Homogeneous and Density-Stratified Media," Journal of Fluid Mechanics, Vol. 136, 1983, pp. 85-109.

[6] Sarpkaya, T. and Daly, J. J., "Effect of Ambient Turbulence on Trailing Vortices," Journal of Aircraft, Vol. 24, 1987, pp. 399-404.

[7] Liu, H. -T., "Effects of Ambient Turbulence on the Decay of a Trailing Vortex Wake," *Journal of Aircraft*, Vol. 29, 1992, pp. 255-263.

[8] Robins, R. E. and Delisi, D. P., "Numerical Study of Vertical Shear and Stratification Effects on the Evolution of a Vortex Pair,"

[9] Proctor, F. H., "Numerical Simulation of Wake Vortices Measured During the Idaho Fall and Memphis Field Programs," *14th AIAA Applied Aerodynamics Conference*, Proceedings, Part-2, New Orleans, LA, AIAA Paper No. 96-2496, June 1996. pp. 943-960. *AIAA Journal*, Vol. 28, 1990, pp. 661-669.

[10] Crow, S. C., "Stability Theory for a Pair of Trailing Vortices," *AIAA Journal*, Vol. 8, 1970, pp. 2172-2179.

[11] Crow, S. C. and Bate, E. R., "Lifespan of Trailing Vortices on a Turbulent Atmosphere," *Journal of Aircraft*, Vol. 7, 1976, pp. 476-482.

[12] Sarpkaya, T. and Daly, J. J., "Effect of Ambient Turbulence on Trailing Vortices," *Journal of Aircraft*, Vol. 24, 1987, pp. 399-404.

[13] Greene, G. C., "An Approximate Model of Vortex Decay in the Atmosphere," *Journal of Aircraft*, Vol. 23, 1986, pp. 566-573.

[14] Atias, M. and Weihs, D., "Motion of Aircraft Trailing Vortices Near the Ground," *Journal of Aircraft*, Vol. 21, 1984, pp. 783-786.

[15] Schiling, V. K., "Motion and Decay of Trailing Vortices Within the Atmospheric Surface Layer," *Beitr. Phys. Atmos.*, Vol. 65, 1992, pp. 157-169.

[16] Corjon, A., Risso, F., Stoessel, A., and Poinsot, T., "Three-Dimensional Direct Numerical Simulations of Wake Vortices: Atmospheric Turbulence Effects and Rebound with Crosswind," *78th AGARD-FDP Symposium on The Characterization and Modification of Wakes from Lifting Vehicles in Fluids*, Trondheim, Norway, May 1996.

[17] Proctor, F. H., Hinton, D. A., Han, J., Schowalter, D. G., and Lin, Y. -L., "Two-Dimensional Wake Vortex Simulations in the Atmosphere: Preliminary Sensitivity Studies," *35th Aerospace Sciences Meeting & Exhibit*, Reno, NV, AIAA Paper No. 97-0056, January 1997.

[18] Schowalter, D. G., DeCroix, D. S., Switzer, G. F., Lin, Y. -L., and Arya, S. P., "Toward Three-Dimensional Modeling of a Wake Vortex Pair in the Turbulent Boundary Layer," *35th Aerospace Sciences Meeting & Exhibit*, Reno, NV, AIAA Paper No. 97-0058, January 1997.

[19] Han, J., Lin, Y. -L., Schowalter, D. G., Arya, S. P., and Proctor, F. H., "Large-Eddy Simulation of Aircraft Wake Vortices: Atmospheric Turbulence Effects," *12th Symposium on Boundary Layers and Turbulence*, Vancouver, Canada, July-August 1997, pp. 237-238.

[20] Han, J., Lin, Y. -L., Arya, S. P., and Kao, C., "Large-Eddy Simulation of Aircraft Wake Vortices: Atmospheric Turbulence Effects," *NASA First Wake Vortex Dynamic Spacing Workshop*, Proceedings, Hampton, VA, NASA CP-97-206235, May 1997, pp. 131-144.

[21] Darracq D., Corjon, A., Ducros F., Keane M. and Buckton D., "Three-dimensional Numerical Simulation of Wake Vortex Detection with the MELAME 2 micron Lidar." *36th Aerospace Sciences Meeting & Exhibit*, Reno, NV, AIAA Paper No. 98-0666, January 1998.

[22] Proctor, F. H., "The Terminal Area Simulations System, Volume 1: Theoretical Formulation," NASA Contrator Report 4046, DOT/FAA/PM-86/50, April 1987. [Available from NTIS]

[23] Schowalter, D. G., DeCroix, D. S., Proctor, F. H., Lin, Y.-L., Arya, S. P., and Kaplan, M. L., "Turbulent Statistics in the Atmospheric Boundary Layer: A Comparison of Large Eddy Simulation with Observations," *11th Symposium on Boundary Layers and Turbulence*, Charlotte, NC, March 1995, pp. 552-555.

[24] Bradshaw, P., "The Analogy between Streamline Curvature and Boyancy in Turbulent Shear Flows," *Journal of Fluid Mechanics*, Vol. 36, 1969, pp. 177-191.

[25] Proctor, F.H., "'A LES Subgrid Turbulence Model with Rotational Dampening," *to be submitted as a NASA Tech Report*, 1999.

[26] Han, J., "Large Eddy Simulations of Aircraft Wake Vortices In a Homogeneous Atmospheric Turbulence,", Ph. D. Dissertation.

15

North Carolina State University.

[27] Arakawa, A., "Computational design for long-term numerical integration of the equations of fluid motion: Two-Dimensional Incompressible Flow, Part I., *J. Comp. Phys.*, Vol. 1, 1966, pp. 119-143.

[28] Proctor, F. H., "The NASA-Langley Wake Vortex Modeling Effort in Support of an Operational Aircraft Spacing System," *36th Aerospace Sciences Meeting & Exhibit*, Reno, NV, AIAA Paper No. 98-0589, January 1998.

[29] Heinrichs, R. Rm., Dasey, T.J., Matthews, M.P, Campbell, S. D., Freehart, R. E., Perras, G. H., and Salamitou, P., " Measurements of Aircraft Wake Vortices at Memphis International Airport with a CW $CO_2$ Coherent Laser Radar," *Proc. SPIE 10th International Aerosense Symposium, Air Traffic Control Technologies II.* Vol 2737, , 1996, pp. 122-133.

[30] Matthews, M., Dasey, T.J., Perras, G. H., and Campbell, S. D., " Planetary Boundary layer Measurements for the Understanding of Aircraft Wake Vortex Behavior," *Pro. Seventh AMS Conference on Aviation Weather Systems*, Feb. 2-7, 1997, Long Beach, CA.

[31] Sarpkaya, T., "Decay of Wake Vortices of Large Aircraft," *AIAA Journal*, Vol. 36, 1998, pp. 1671-1679.

[32] Campbell, S. D., Dasey, T. J., Freehart, R. E., Heinrichs, R. M., Matthews, M. P., Perras, G. H., and Rowe, G. S., "Wake Vortex Field Measurement Program at Memphis, TN Data Guide," *Project Report: NASA/L-2*, January 1997. [Available from NTIS]

American Institute of Aeronautics and Astronautics

# Appendix K: An Estimation of Turbulent Kinetic Energy and Energy Dissipation Rate Based on Atmospheric Boundary Layer Similarity Theory

NASA Contractor Report

# An Estimation of Turbulent Kinetic Energy and Energy Dissipation Rate Based on Atmospheric Boundary Layer Similarity Theory

Jongil Han, S. Pal Arya, Shaohua Shen, and Yuh-Lang Lin

*Department of Marine, Earth and Atmospheric Sciences*
*North Carolina State University*
*Raleigh, NC 27695-8208*

# Abstract

Algorithms are developed to extract atmospheric boundary layer profiles for turbulence kinetic energy (TKE) and energy dissipation rate (EDR), with data from a meteorological tower as input. The profiles are based on similarity theory and scalings for the atmospheric boundary layer. The calculated profiles of EDR and TKE are required to match the observed values at 5 and 40 $m$. The algorithms are coded for operational use and yield plausible profiles over the diurnal variation of the atmospheric boundary layer.

# Contents

# List of Tables

# List of Figures

iv

# Nomenclature

| | | |
|---|---|---|
| $e$ | $=$ | turbulence kinetic energy |
| $f$ | $=$ | Coriolis parameter |
| $g$ | $=$ | gravitational acceleration |
| $h$ | $=$ | height of atmospheric boundary layer |
| $L$ | $=$ | Obukhov length |
| $k$ | $=$ | von Karman constant, 0.4 |
| $Ri$ | $=$ | gradient Richardson number |
| $T_0$ | $=$ | reference temperature |
| $\bar{u}$ | $=$ | mean velocity in the direction of the wind |
| $u_*$ | $=$ | friction velocity |
| $u', v'$ | $=$ | horizontal velocity fluctuations |
| $w_*$ | $=$ | convective velocity scale |
| $w'$ | $=$ | vertical velocity fluctuation |
| $z$ | $=$ | elevation above the ground |
| $\epsilon$ | $=$ | turbulent kinetic energy dissipation rate |
| $\zeta$ | $=$ | Monin-Obukhov stability parameter, $z/L$ |
| $\bar{\theta}_v$ | $=$ | mean virtual potential temperature |
| $\theta_v'$ | $=$ | virtual potential temperature fluctuation |
| $\phi_h$ | $=$ | dimensionless potential temperature gradient in the surface layer |
| $\phi_m$ | $=$ | dimensionless wind shear in the surface layer |

# 1   Introduction

To safely reduce aircraft spacing and increase airport capacity, NASA is developing a predictor system, called the Aircraft VOrtex Spacing System (AVOSS: Hinton, 1995; Hinton et al., 1999; Perry et al., 1997). This system includes prediction algorithms for aircraft wake vortex transport and decay. Semi-empirical vortex prediction algorithms have been developed and incorporated within the AVOSS (Robins et al., 1998; Sarpkaya et al., 2000). One of the key input elements for the AVOSS prediction algorithms is the atmospheric boundary layer (ABL) turbulence of which the intensity can be represented by turbulent kinetic energy (TKE) or eddy energy dissipation rate (EDR). While the prediction algorithms require the vertical profiles for the TKE and EDR at least up to the vortex generation height, the observational data for the TKE and EDR are available only from a meteorological tower at the heights of 5 and $40\,m$ above the ground.

In supporting the AVOSS project of NASA Langley Research Center, the wake vortex research group at North Carolina State University (NCSU) has developed algorithms and software which can generate the vertical profiles of TKE and EDR. These algorithms are based on the ABL similarity relations (Arya, 1988, 1995, 2000; Caughey et al., 1979; Rao and Nappo, 1998; Sorbjan, 1989; Stull, 1988) and available experimental data.

Section 2 describes the ABL similarity relations with respect to the vertical profiles of the TKE and EDR that are dependent upon the ABL stability. Section 3 contains a detailed description of the software. In Section 4, estimates from the similarity relations are compared with the observed data. Section 5 provides information on running the software. Finally, the summary of this study is given in Section 6.

1

# 2 Similarity Relations for the TKE and EDR Profiles

ABL observations frequently show consistent and repeatable characteristics from which empirical similarity relationships have been obtained for the variables of interest such as TKE and EDR. Similarity theory is based on the organization of variables into dimensionless groups that come out of the dimensional analysis. The dimensional analysis is a technique used in science and engineering to establish a relationship between different quantities. The functional relationships between dimensionless groups are referred to as similarity relations, because they express the conditions under which two or more flow regimes would be similar. Similarity relationships that have certain universal properties are usually designed to apply to equilibrium (steady-state) situations. One of the well-known similarity relations is the logarithmic velocity profile law observed in surface or wall layers under neutral stratification.

The proposed similarity relationships for TKE and EDR are fundamentally based on the Monin-Obukhov similarity (Monin and Obukhov, 1954) and mixed-layer similarity (Deardorff, 1972) theories. The former is applied to a stratified surface layer and is sometimes called the surface-layer similarity theory, whereas the latter is applied to mixed layers that often develops during daytime convective conditions. These similarity theories have provided the most suitable and acceptable framework for organizing and presenting the ABL data, as well as for extrapolating and predicting certain ABL information where direct measurements of the same are not available.

Using the framework of these similarity theories, a variety of similarity relationships have been suggested to describe the vertical profiles of mean and turbulence fields as functions of the dimensionless groups $z/L$ and/or $z/h$, covering whole ABL including the surface layer (Arya, 1988, 1995, 2000; Caughey et al., 1979; Hogstrom, 1996; Rao and Nappo, 1998; Sorbjan, 1989; Stull, 1988). Occasionally, various investigators have suggested different values for the empirical coefficients. Based on the similarity scaling in the atmospheric surface layer and boundary layer under different stability conditions, the expressions and parameterizations for the vertical profiles of TKE and EDR and related characteristic scales

are suggested in the following subsections; some of the expressions are adopted directly from those references, whereas the others are derived using the similarity relationships of turbulence variables other than TKE and EDR.

## 2.1 Neutral and Stable Boundary Layers ($z/L \geq 0$)

The boundary layer may be subdivided into a surface layer (in which stress is nearly constant with height) and an outer layer. A separate set of algorithms is assigned to each sublayer as follows.

### 2.1.1 Surface Layer ($z \leq 0.1h$)

In the surface layer, the TKE ($e$) and EDR ($\epsilon$) are given by (Hogstrom, 1996; Rao and Nappo, 1998)

$$e = 6u_*^2, \tag{1}$$

$$\epsilon = \frac{u_*^3}{kz}\left(1.24 + 4.3\frac{z}{L}\right), \tag{2}$$

where $k \simeq 0.4$ is von Karman constant. The friction velocity, $u_*$, is defined as

$$u_*^2 = \left[(\overline{u'w'})_s^2 + (\overline{v'w'})_s^2\right]^{1/2}, \tag{3}$$

where the right hand side of $Eq.$ (3) represents the total vertical momentum flux near the surface (the subscript $s$ denotes the ground surface). The Obukhov length $L$ depends on both the momentum and heat fluxes near the surface and is defined later; the ratio $z/L$ is the fundamental similarity parameter of the Monin-Obukhov similarity theory.

### 2.1.2 Outer Layer ($z > 0.1h$)

Expressions for the outer layer can be assigned according to the level of stratification.

**(1) Neutral and Stable Boundary Layer**

In the neutral and moderately stable boundary layer, the TKE and EDR are given by (Hogstrom, 1996; Rao and Nappo, 1998)

$$e = 6u_*^2\left(1 - \frac{z}{h}\right)^{1.75}, \tag{4}$$

$$\epsilon = \frac{u_*^3}{kz}\left(1.24 + 4.3\frac{z}{L}\right)\left(1 - 0.85\frac{z}{h}\right)^{1.5}. \tag{5}$$

Alternatively, $Eqs.$(4) and (5) may also be used for the entire boundary layer, including the surface layer.

**(2) Very Stable and Decoupled Layers**

In the very stable boundary layer and decoupled layers, the TKE and EDR can be expressed by extension of $Eqs.$(1) and (2) as

$$e = 6u_L^2, \tag{6}$$

$$\epsilon = 4.3\frac{u_L^3}{kL_L}, \tag{7}$$

where $u_L$ is the local (friction) velocity scale and $L_L$ is the local buoyancy length scale. Under very stable conditions, the elevated layers of turbulence are decoupled from the surface and the local fluxes and scales cannot be reliably estimated. Perhaps, an empirical relationship between the overall turbulence intensity ($e^{1/2}/\bar{u}$) and Richardson number should be explored. It is worthwhile to note that some experimental results show that $Eq.$(5) can be still used to estimate $\epsilon$ even in a very stable boundary layer.

## 2.2    Unstable Boundary Layer ($z/L < 0$)

The unstable ABL such as during daytime surface heating can be divided into three regimes depending upon the stability parameter, $z/L$ or $h/L$.

### 2.2.1   Strongly Unstable (Convective) Regime ($|z/L| > 0.5$)

The structure of the convective regime is dominated by buoyancy. The mean wind velocity and potential temperature profiles are nearly uniform with height. For this reason, the convective outer layer is called the "mixed layer." The mixed layer is topped by an inversion layer in which temperature increases with height. A broad maximum of TKE is usually found in the middle of the mixed layer, while EDR decreases slightly with height.

**(1) Surface Layer ($z \leq 0.1h$)**

In the surface layer, the TKE and EDR are given by (Arya, 2000)

$$e = 0.36w_*^2 + 0.85u_*^2\left(1 - 3\frac{z}{L}\right)^{2/3},\tag{8}$$

$$\epsilon = \frac{u_*^3}{kz}\left(1 + 0.5\left|\frac{z}{L}\right|^{2/3}\right)^{3/2}.\tag{9}$$

## (2) Mixed Layer

In the mixed layer, the TKE is given by (Arya, 2000)

$$e = \left(0.36 + 0.9\left(\frac{z}{h}\right)^{\frac{2}{3}}\left(1 - 0.8\frac{z}{h}\right)^2\right)w_*^2,\tag{10}$$

or, for most practical purposes,

$$e = 0.54\,w_*^2.\tag{11}$$

The EDR decreases slowly with height at a linear rate (Sorbjan, 1989), i.e.,

$$\epsilon = \frac{w_*^3}{h}\left(0.8 - 0.3\frac{z}{h}\right),\tag{12}$$

where the convective velocity scale $w_*$ is defined as

$$w_* = \left(\frac{g}{T_0}(\overline{w'\theta_v'})_s h\right)^{1/3}.\tag{13}$$

Here $g$ is the gravitational acceleration, $T_0$ is the reference temperature, and $(\overline{w'\theta_v'})_s$ is the mean surface heat flux.

### 2.2.2 Moderately Unstable Regime ($0.02 < |z/L| \leq 0.5$)

In this regime, the mechanical production of TKE is comparable with buoyancy production of TKE, i.e., turbulence generation from vertical wind shear is comparable to that generated from surface heating. The TKE in this regime is more or less uniform over the boundary layer or may decrease slightly with height, and the boundary layer structure may be more uncertain.

### 2.2.3 Weakly Unstable (Near-Neutral) Regime ($|z/L| \leq 0.02$ or $|h/L| \leq 1.5$)

This regime often occurs during the transition period of early morning and late afternoon or during overcast days with strong winds. The lapse rate for temperature tends to be near-neutral. In this regime, mechanical (shear) production dominates the TKE budget.

5

# 3 Software Description

In order to generate vertical profiles of TKE and EDR for operational applications, software is written which utilizes the algorithms in the previous section with observations measured at 5 and 40 m above the ground. With the determination of the characteristic similarity scales (such as $L$, $u_*$, $w_*$, and $h$), the computation of the TKE and EDR profiles is straightforward. The characteristic similarity scales can be estimated from the winds and virtual potential temperatures measured at two levels near the ground.

Since the atmospheric similarity relationships are based on the mean quantities of the observed wind, temperature, and turbulence, the required time averaging interval for EDR and TKE profiles should be at least 30 minutes (Stull, 1988). Hence, with the exception of TKE, all measured variables are 30-minute averaged. For the measured TKE, a 30-minute median value is used, since sporadic measurements of exceptionally large TKE can cause an unrealistic TKE average.

The vertical profiles generated from similarity theory are additionally required to match the measured values at $z = 5$ and $40\,m$ as closely as possible. Often the profiles generated from similarity expressions do not exactly match the observed values at $z = 5$ and $40\,m$ simultaneously. Therefore, the TKE and EDR profiles between $z = 5$ and $40\,m$ are assumed to be linear and independent of the similarity relationships. In addition, upper and lower bounds for the values of TKE and EDR at $z = 5\,m$ are specified to prevent unrealistically large or small values compared with those at $z = 40\,m$. Above $40\,m$, the similarity profiles are used, but are adjusted to match the observed TKE and EDR at $z = 40\,m$.

## 3.1 Determination of Surface Layer Similarity Scales

According to algorithms in the previous section, software requires to first determine surface layer similarity scales $L$ and $u_*$.

The Obukhov length is defined as

$$L = -\frac{u_*^3}{k(g/T_0)(\overline{w'\theta_v'})_s},$$ (14)

in which friction velocity and the surface heat flux can be estimated from measurements of the mean differences or gradients of velocity and temperature between any two heights $z_1$ and $z_2$ within the surface layer, but well above the tops of roughness elements.

Letting $\Delta \bar{u} = \bar{u}_2 - \bar{u}_1$ and $\Delta \bar{\theta}_v = \bar{\theta}_{v2} - \bar{\theta}_{v1}$ be the difference in mean velocities and virtual potential temperatures across the height interval $\Delta z = z_2 - z_1$, one can determine the gradient Richardson number $(Ri)$ at the geometric height $z_m = (z_1 z_2)^{1/2}$ by

$$Ri(z_m) = \frac{g}{T_0} z_m \left( ln \frac{z_2}{z_1} \right) \frac{\Delta \bar{\theta}_v}{(\Delta \bar{u})^2}. \tag{15}$$

The corresponding value of the Monin-Obukhov stability parameter $\zeta_m = z_m/L$ can be determined from the relations given by (Arya, 1988)

$$\zeta_m = Ri(z_m), \quad \text{for } Ri < 0, \tag{16}$$

$$\zeta_m = \frac{Ri(z_m)}{1 - 5Ri(z_m)}, \quad \text{for } 0 \leq Ri < 0.2. \tag{17}$$

Then, the basic universal similarity functions $\phi_m$ and $\phi_h$ are directly related to $\zeta_m$, i.e.,

$$\phi_h = \phi_m{}^2 = (1 - 15\zeta_m)^{-1/2}, \quad \text{for } \zeta_m < 0 \tag{18}$$

$$\phi_h = \phi_m = (1 + 5\zeta_m), \quad \text{for } \zeta_m \geq 0 \tag{19}$$

The similarity relations of $Eqs.$(17) and (19) are not valid for $Ri \geq 0.2$ and $\zeta_m > 1$.

Finally, the friction velocity and the surface heat flux can be obtained from the following relations

$$u_* = \frac{k \Delta \bar{u}}{\phi_m(\zeta_m) ln(z_2/z_1)}, \tag{20}$$

$$(\overline{w'\theta_v'})_s = - \left[ \frac{k^2 \Delta \bar{u} \Delta \bar{\theta}_v}{\phi_m(\zeta_m) \phi_h(\zeta_m) \left( ln \frac{z_2}{z_1} \right)^2} \right]. \tag{21}$$

The parameters $Ri(z_m)$ and $z_m/L$ are used to determine the stability criteria discussed in the previous section, while the friction velocity $u_*$ is used to estimate the ABL height $h$ in the neutral and stable boundary layer.

7

## 3.2 TKE and EDR Profiles in Neutral and Stable Boundary Layer $(z_m/L \geq 0)$

The boundary layer height can be estimated as the minimum of those given by the following diagnostic relations (Arya, 1995):

$$h = 0.3 \frac{u_*}{f}, \tag{22}$$

$$h = 0.4 \left( \frac{u_* L}{f} \right)^{1/2}, \tag{23}$$

where $f$ is the Coriolis parameter. Note that $Eq.(22)$ is valid only for a stationary neutral boundary layer, but it gives an upper bound for $h$ in slightly stable or near-neutral conditions when $L$ becomes too large and $Eq.(23)$ overestimates $h$.

Then, $Eqs.(4)$ and (5) are applied to obtain TKE and EDR profiles above $z = 40\,m$ height. The friction velocity in $Eqs.(4)$ and (5) is adjusted so that the profiles are continuous at $z = 40\,m$, and might be slightly different from that given by $Eq.(20)$.

## 3.3 TKE and EDR Profiles in Unstable Boundary Layer $(z_m/L < 0)$

### 3.3.1 Strongly Unstable (Convective) Regime $(|z_m/L| > 0.5)$

In this regime, the ABL height is usually estimated from the height of the inversion base, which can be determined from the vertical temperature sounding. However, it is difficult to obtain the temperature inversion base from the existing sounding data from the Dallas/Ft. Worth (DFW) and Memphis field experiments. This is because the soundings often do not extend above a height of $1\,km$, whereas the ABL height in this regime can easily reach a height of $2 - 3\,km$. Alternatively, we estimate the boundary layer height from $Eqs.(11)$ and (12), using the measured TKE and EDR at $z = 40\,m$, i.e.,

$$h = \frac{0.4 + \sqrt{0.16 + 0.3\, z_{40}\, \epsilon_{40}/(e_{40}/0.54)^{1.5}}}{\epsilon_{40}/(e_{40}/0.54)^{1.5}}, \tag{24}$$

where subscript 40 represents $z = 40\,m$. Although the height of $z = 40\,m$ is within the surface layer $(z \leq 0.1h)$ in most of cases of this regime, the observations indicate that the

mixed layer similarity may also be used for the entire boundary layer except for the layer very close to the surface.

Then, $Eqs.(10)$ and $(12)$ are applied to obtain TKE and EDR profiles above $z = 40\,m$ height, respectively. The convective velocity scale in $Eq.(10)$ is adjusted for the TKE profile to be continuous at $z = 40\,m$, and will be slightly different from that estimated from $Eq.(11)$.

### 3.3.2 Moderately Unstable Regime ($0.02 < |z_m/L| \leq 0.5$)

This regime also includes the cases of $e_5 > e_{40}$ but $|z_m/L| > 0.5$, since TKE (i.e., $e$) usually increases with height near the surface in the convective regime. The profiles are obtained in the same way as in the convective regime except that $Eq.(11)$ is used for TKE profile rather than $Eq.(10)$.

### 3.3.3 Weakly Unstable (Near-Neutral) Regime ($|z_m/L| \leq 0.02$ or $|h/L| \leq 1.5$)

In this regime, the formulations for the neutral boundary layer are applied for the profiles.

# 4 Comparisons with Observed Data

The friction velocity and TKE and EDR at $z = 5\,m$ and $40\,m$ estimated from the similarity relations in the previous sections have been compared to measurement data from the Dallas/Ft. Worth (DFW) Airport Field Experiment (Dasey et al., 1998) during the period of September 15 - October 3, 1997. The height of $z = 5\,m$ is essentially assumed to be within the surface layer. The measured $u_*$ and EDR are 30-minute averaged, while the measured TKE is a median value over 30-minutes. The frequency for each stability regime is shown in Table 1, indicating that most of data belong to stable and moderately unstable regimes. In the following, the comparisons are performed in two stability groups, that is, neutral and stable regime including the weakly unstable regime and unstable regime including moderately unstable and convective regimes.

## 4.1 Friction Velocity ($u_*$)

Figure 1 shows that the estimated $u_*$ from mean velocity measurements with $Eq.$ (20) agrees well with the measured $u_*$ from the momentum flux at $z = 5\,m$, but the data scatter becomes larger for weaker $u_*$. In particular, for very small values of $u_*$, which are often obtained during very stable conditions, the estimated $u_*$ tends to be significantly smaller than the measured $u_*$. This is because the Monin-Obukhov similarity theory on which $u_*$ estimates are based, is not applicable under very stable conditions (Nappo and Johansson, 1999).

## 4.2 TKE at $z = 5\,m$ and $40\,m$

As formulated in sections 2 and 3, the estimated TKE at $z = 5\,m$ in neutral and stable conditions is given as a function of only $u_*$, while in unstable conditions, it is given as a function of $u_*$, $w_*$, $L$ and $z$. As shown in Fig. 2, the estimated TKE appears to agree with the measured, although data scatter becomes larger for smaller values. This is especially true in neutral and stable conditions. For very small values of TKE, most of the estimated

TKE values are significantly lower than the measured TKE. The agreement between the estimated and measured TKE is much better for the unstable conditions.

At $z = 40\,m$, only a comparison for the neutral and stable conditions is conducted. In unstable conditions, the $w_*$ and $h$ are calculated from the measured EDR and TKE at $z = 40\,m$ and thus, the estimated TKE and EDR at $z = 40\,m$ will match their measured values at $z = 40\,m$, exactly. Figure 3 shows that similar to TKE at $z = 5\,m$, the estimated TKE in neutral and stable conditions agrees reasonably well with the measured TKE, but data scatter at $z = 40\,m$ is larger than that at $z = 5\,m$, especially for smaller TKE values.

## 4.3    EDR at $z = 5\,m$ and $40\,m$

Using the estimated values of $u_*$ and $L$, EDR at $z = 5\,m$ is calculated from *Eqs.* (2) and (9). Its 'measured' values were obtained from the power spectrum of the observed wind data using the theoretical Kolmogorov relations of the spectra in the inertial subrange.

Figure 4 shows that at $z = 5\,m$, the estimated EDR appears to increase linearly with increasing measured EDR, but is considerably overestimated in both stability regimes. Data scatter is somewhat larger compared to that of TKE. Similar to that of TKE, however, the data scatter increases with decreasing values of EDR and is larger in neutral and stable conditions than in unstable conditions. As explained in section 4.2, the comparison for EDR at $z = 40\,m$ is conducted only for the neutral and stable conditions. Figure 5 shows that agreement and data scatter between estimated and measured EDR at $z = 40\,m$ are similar to those at $z = 5\,m$, but with smaller overestimation.

## 4.4    Adjustments in TKE and EDR Profiles

As shown in the above comparison plots, the ABL similarity theory appears to represent the measured $u_*$ and TKE at $z = 5\,m$ and $z = 40\,m$ reasonably well, but with increasing data scatter for decreasing values of $u_*$ and TKE. On the other hand, the estimated EDR considerably overestimates the measured EDR, although estimated and measured values appear to

11

be strongly correlated with a linear relationship between the two. As described in section 3, therefore, we require that the generated profiles for TKE and EDR match the measured values at $z = 5$ and $40\,m$ while maintaining the profile shape from the similarity theory above $z = 40\,m$. Otherwise, the estimated profiles for TKE and EDR may significantly deviate from those 'measured', especially for small values of TKE and EDR.

# 5  Procedure of Running Software

The software is coded in FORTRAN and is designed for operational use. The code is composed of one main program and two subroutines. As input the main program reads data files containing TKE and EDR at $z = 5\,m$ and $z = 40\,m$, as well as mean winds and virtual potential temperatures at two levels near the surface. The subroutine "EDRTKE_STABLE" computes TKE and EDR profiles under neutral and stable conditions. The other subroutine "EDRTKE_UNSTABLE" computes TKE and EDR profiles under unstable conditions. On output, vertical profiles of TKE and EDR are generated from the main program.

In executing the code, one needs to enter the following:

- latitude (degree) of the airport, which is used to calculate the Coriolis parameter $f$.

- one-minute averaged tower data file for wind and virtual potential temperature at two levels near the surface.

- measured 30-minute averaged EDR data file at $z = 5\,m$.

- measured 30-minute averaged EDR data file at $z = 40\,m$.

- measured 5-minute averaged TKE data file at $z = 5\,m$.

- measured 5-minute averaged TKE data file at $z = 40\,m$.

Once the input data files have been successfully entered, the code then generates an output file, which contains not only the vertical profiles of TKE and EDR, but also the output of similarity scales such as $h$, $L$, $u_*$, and $w_*$. Figures 6 and 7 show a diurnal variation of TKE and EDR profiles generated by the software for a typical sunny day.

# 6  Summary and Discussion

Based on the existing similarity theories in the atmospheric surface layer and boundary layer under different stability conditions, the expressions and parameterizations for the vertical profiles of TKE and EDR have been suggested. Compared with observation, theoretically estimated TKE at 5 and 40 m heights above ground appears to agree reasonably well with those observed at the same heights except for the very small values of TKE. However, theoretically estimated EDR at 5 and 40 m heights considerably overestimates the observed EDR with large data scatter, although estimated and measured values appear to be strongly correlated with a linear relationship between the two.

From the ABL similarity relationships and their comparisons with the observations, software has been developed to generate realistic vertical profiles of TKE and EDR. The input parameters for the software are the measured TKE and EDR at the heights of $z = 5$ and 40 m above the ground, and the measured winds and virtual potential temperatures at two levels near the ground from which characteristic similarity scales, such as $L$ and $u_*$, can be estimated. In the software, to minimize the difference between the similarity relations and observations it has been required that calculated values match the observed values at the heights of 5 and 40 m while maintaining the profile shape from the similarity theory above 40 m. Although the software yields very plausible vertical profiles and their diurnal variations, statistics for the difference between the values estimated from the software and the measured values of TKE and EDR at the heights other than 5 and 40 m has to be obtained for further improvement of the software.

# 7 Acknowledgments

# 8 References

Arya, S. P., 1988: Introduction to Micrometeorology. Academic Press, 307 pp.

Arya, S. P., 1995: Atmospheric Boundary Layer and Its Parameterizations. *Wind Climate in Cities*, Cermak, J. E., Davenport, A. G., Plate, E. J., and Viegas, D. X., Eds., Kluwer Academic Publishing, 41-46.

Arya, S. P., 2000: Atmospheric Boundary Layers and Turbulence. *Mesoscale Atmospheric Dispersion*, Boybeyi, Z., ed., WIT Press, Computational Mechanics Publications. (in press)

Caughey, S. J., Wyngaard, J. C., and Kaimal, J. C., 1979: Turbulence in the Evolving Stable Boundary Layer. *J. Atmos. Sci.*, Vol. 36, 1041-1052.

Dasey, T. J., Cole, R. E., Heinrichs, R. M., Matthews, M. P., and Perras, G. H., 1998: Aircraft Vortex Spacing System (AVOSS) Initial 1997 System Deployment at Dallas/Ft. Worth (DFW) Airport. *Project Report NASA/L-3*, 68 pp.

Deardorff, J. W., 1972: Numerical Investigation of Neutral and Unstable Planetary Boundary Layers. *J. Atmos. Sci.*, Vol. 29, 91-115.

Hinton, D. A., 1995: Aircraft Vortex Spacing System (AVOSS) Conceptual Design. *NASA TM-110184*, 27 pp.

Hinton, D. A., Charnock, J. K., Bagwell, D. R., and Grigsby, D., 1999: NASA Aircraft Vortex Spacing System Development Status. *37th Aerospace Sciences Meeting & Exhibit*, Reno, NV, AIAA-99-0753, 17 pp.

Hogstrom, U., 1996: Review of Some Characteristics of the Atmospheric Surface Layer. *Boundary-Layer Meteorol.*, Vol. 78, 215-246.

Monin, A. S. and Obukhov, A. M., 1954: Basic Laws of Turbulent Mixing in the Atmosphere Near the Ground. *Tr. Akad. Nauk SSSR Geoph. Inst.*, No. 24 (151), 1963-1987.

Nappo, C. J. and Johansson, P. -E., 1999: Summary of the LOVANGER International Workshop on Turbulence and Diffusion in the Stable Planetary Boundary Layer. *Boundary-Layer Meteorol.*, Vol. 90, 345-374.

Perry, R. B., Hinton, D. A., and Stuever, R. A., 1997: NASA Wake Vortex Research for Aircraft Spacing. *35th Aerospace Sciences Meeting & Exhibit*, Reno, NV, AIAA-97-0057, 9 pp.

Rao, K. S. and Nappo, C. J., 1998: Turbulence and Dispersion in the Stable Atmospheric Boundary Layer. *Dynamics of the Atmospheric Flows: Atmospheric Transport and Diffusion Processes*, Singh, M. P. and Raman, S., eds., Computational Mechanics Publications, 39-91.

Robins, R. E., Delisi, D. P., and Greene, G. C., 1998: Development and Validation of a Wake Vortex Prediction Algorithm. *36th Aerospace Sciences Meeting & Exhibit*, Reno, NV, AIAA-98-0665, 10 pp.

Sarpkaya, T., Robins, R. E., and Delisi, D. P., 2000: Wake-Vortex Eddy-Dissipation Model Predictions Compared with Observations. *38th Aerospace Sciences Meeting & Exhibit*, Reno, NV, AIAA-2000-0625, 10 pp.

Sorbjan, Z., 1989: Structure of the Atmospheric Boundary Layer. Prentice Hall, 317 pp.

Stull, R. B., 1988: An Introduction to Boundary Layer Meteorology. Kluwer Academic Publishers, 666 pp.

| Stability | Frequency (%) |
|---|---|
| Stable | 54 |
| Weakly Unstable | 5 |
| Moderately Unstable | 37 |
| Strongly Unstable | 4 |

Table 1: Stability frequency (%) in the Dallas/Ft. Worth (DFW) Airport Field Experiment during the period of September 15 - October 3, 1997, where data from two rainy days and one day for which data are partly missing have been omitted from the total data set.
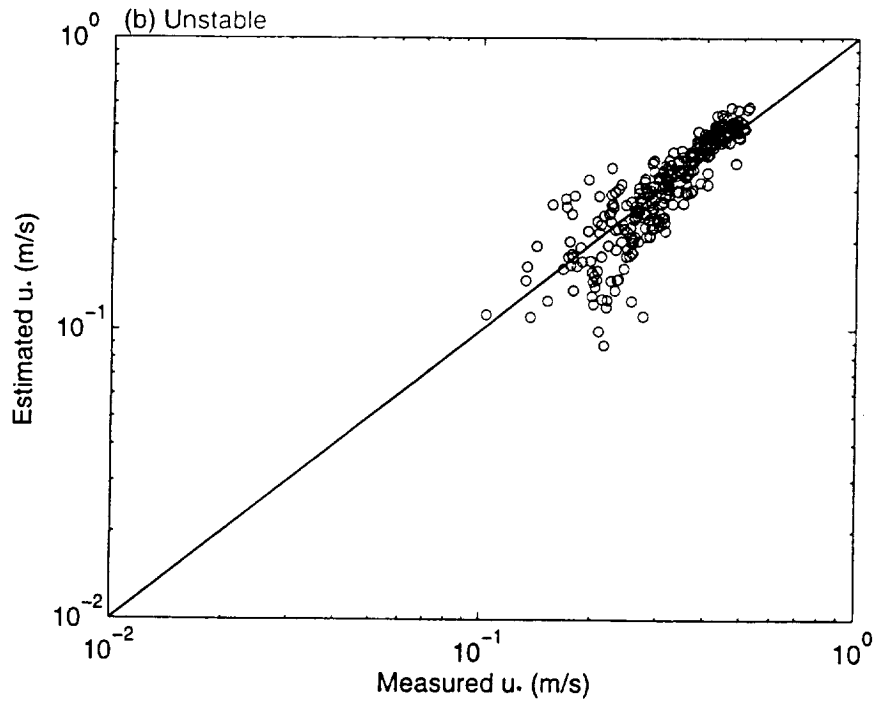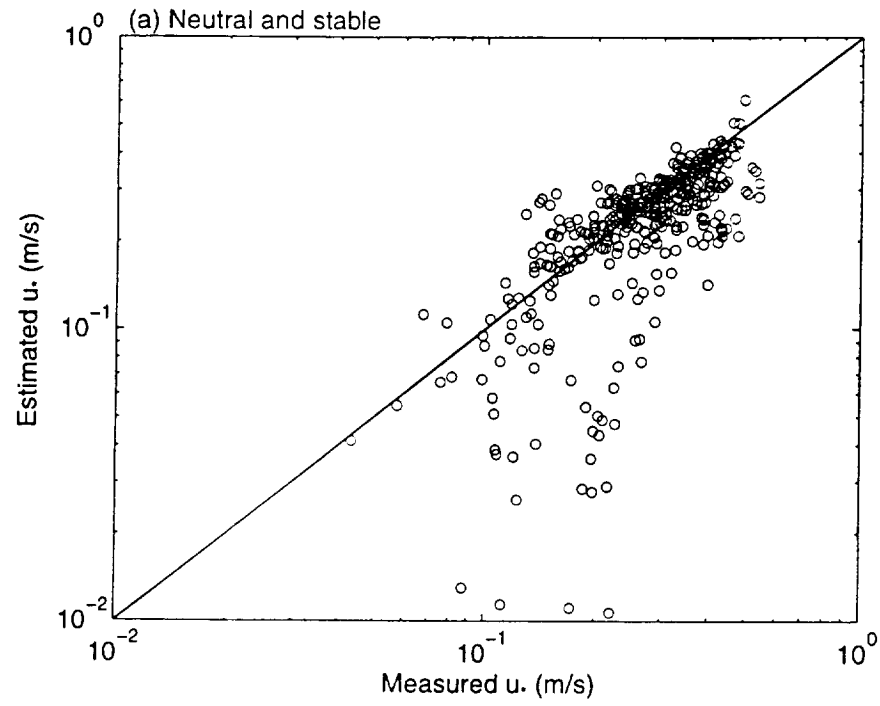
Figure 1: Comparison plots between measured and estimated $u_*$, where the solid lines represent lines of estimated $u_* = $ measured $u_*$.
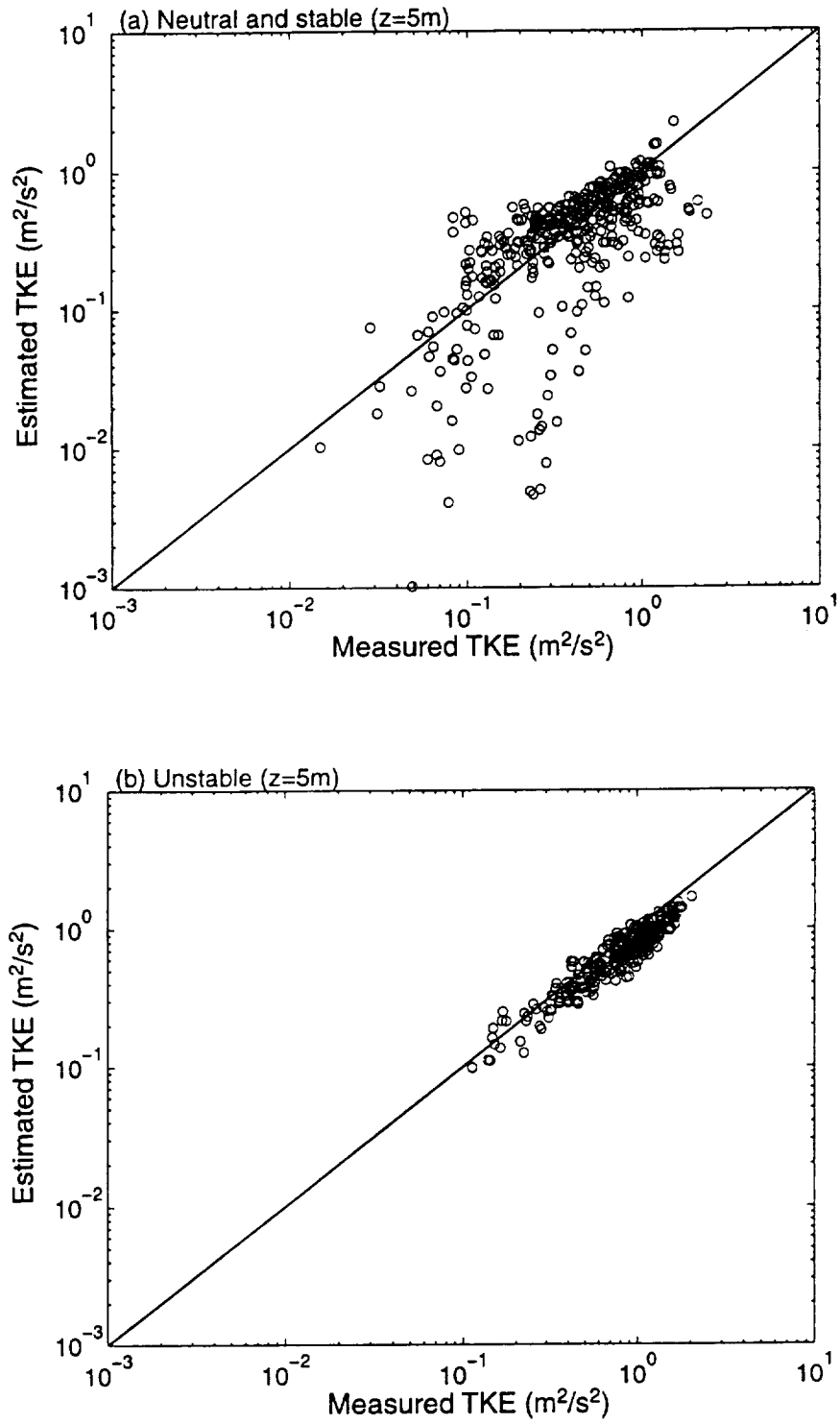
Figure 2: Same as Fig. 1 but for TKE at $z = 5\,m$.
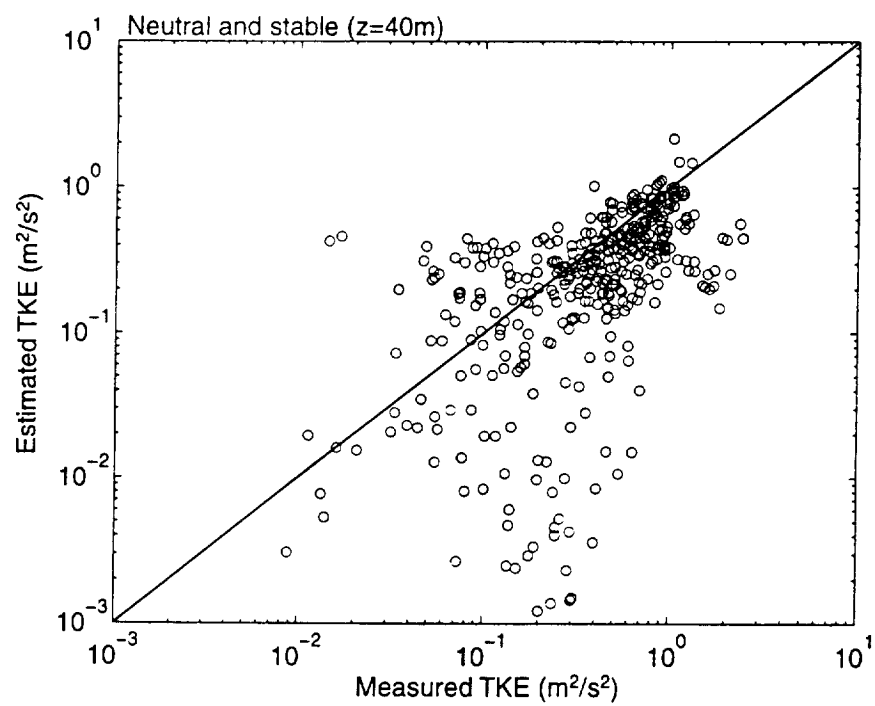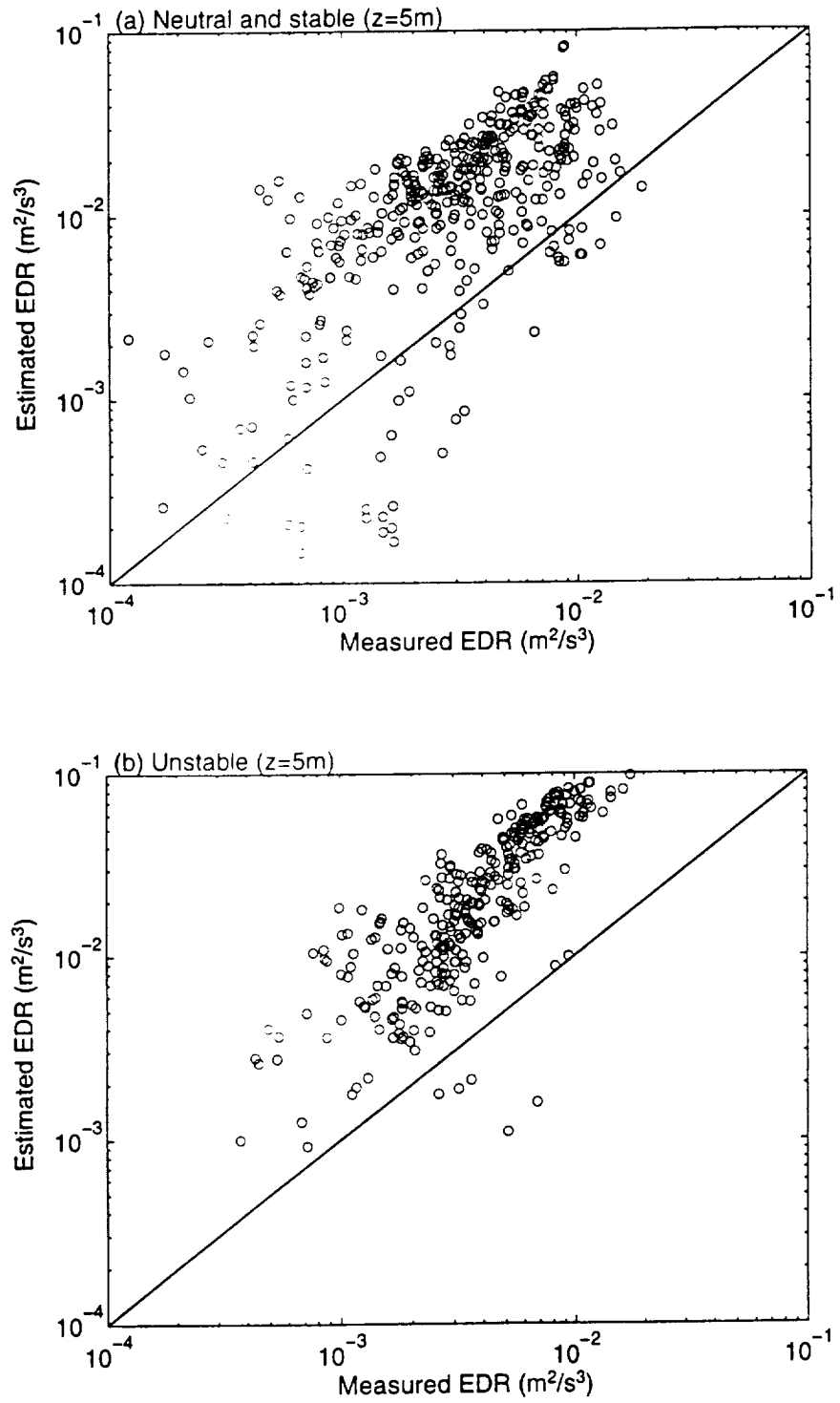
Figure 3: Same as Fig. 1 but for TKE at $z = 40\,m$.
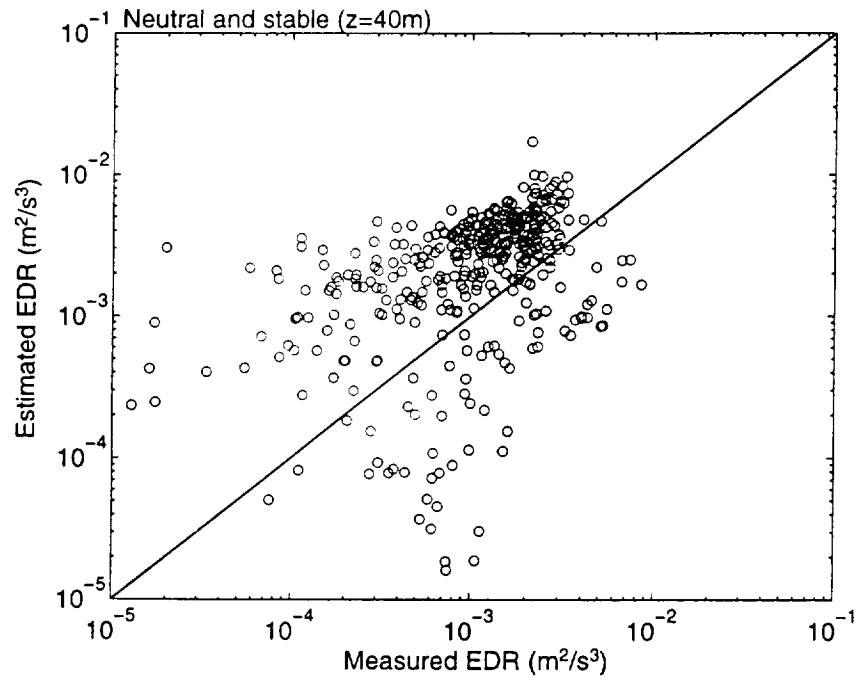
Figure 4: Same as Fig. 1 but for EDR at $z = 5\,m$.
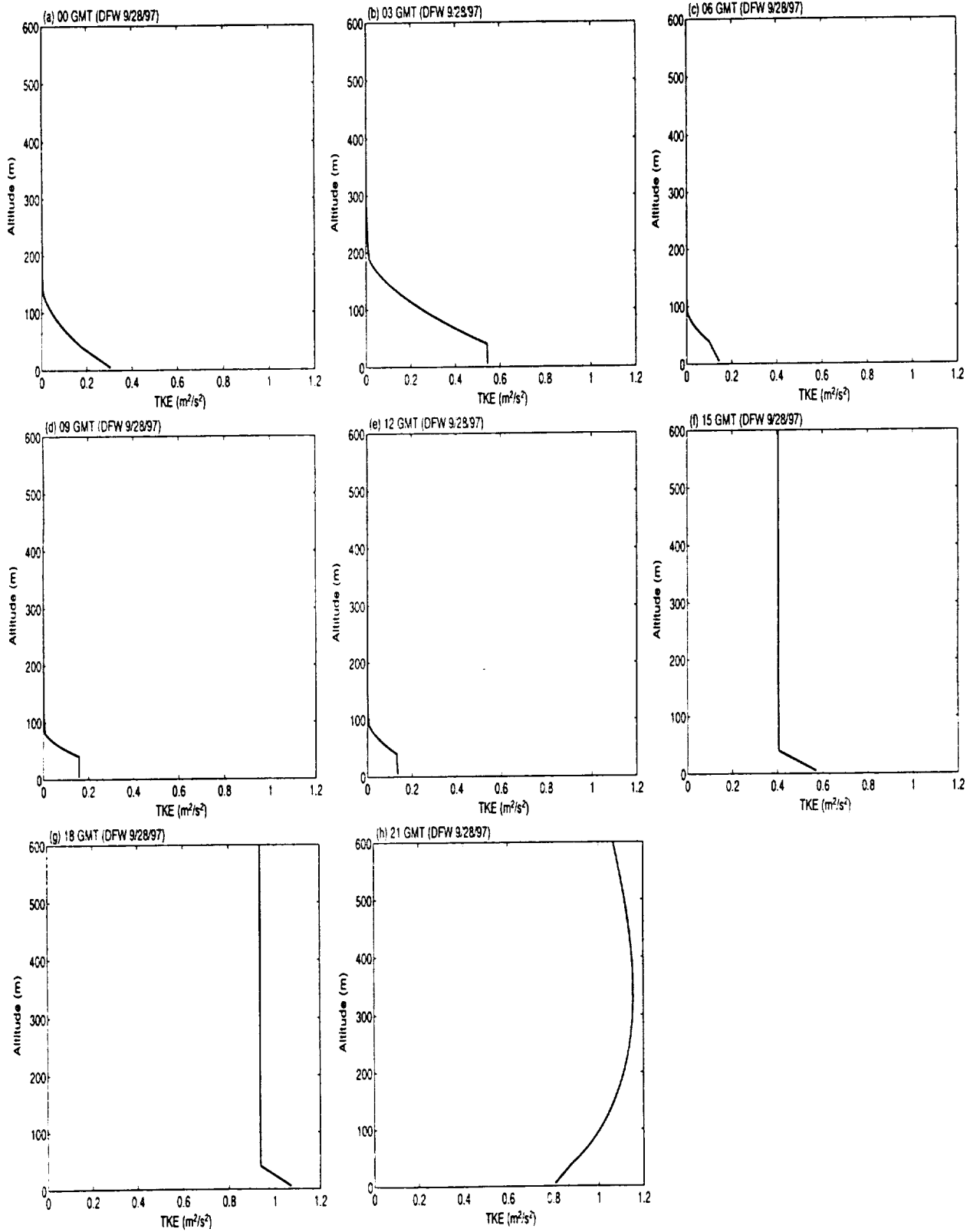
Figure 5: Same as Fig. 1 but for EDR at $z = 40\,m$.

Figure 6: Diurnal variation of TKE profiles obtained from the ABL similarity theory and the observed values of TKE and EDR at $z = 5\,m$ and $40\,m$.
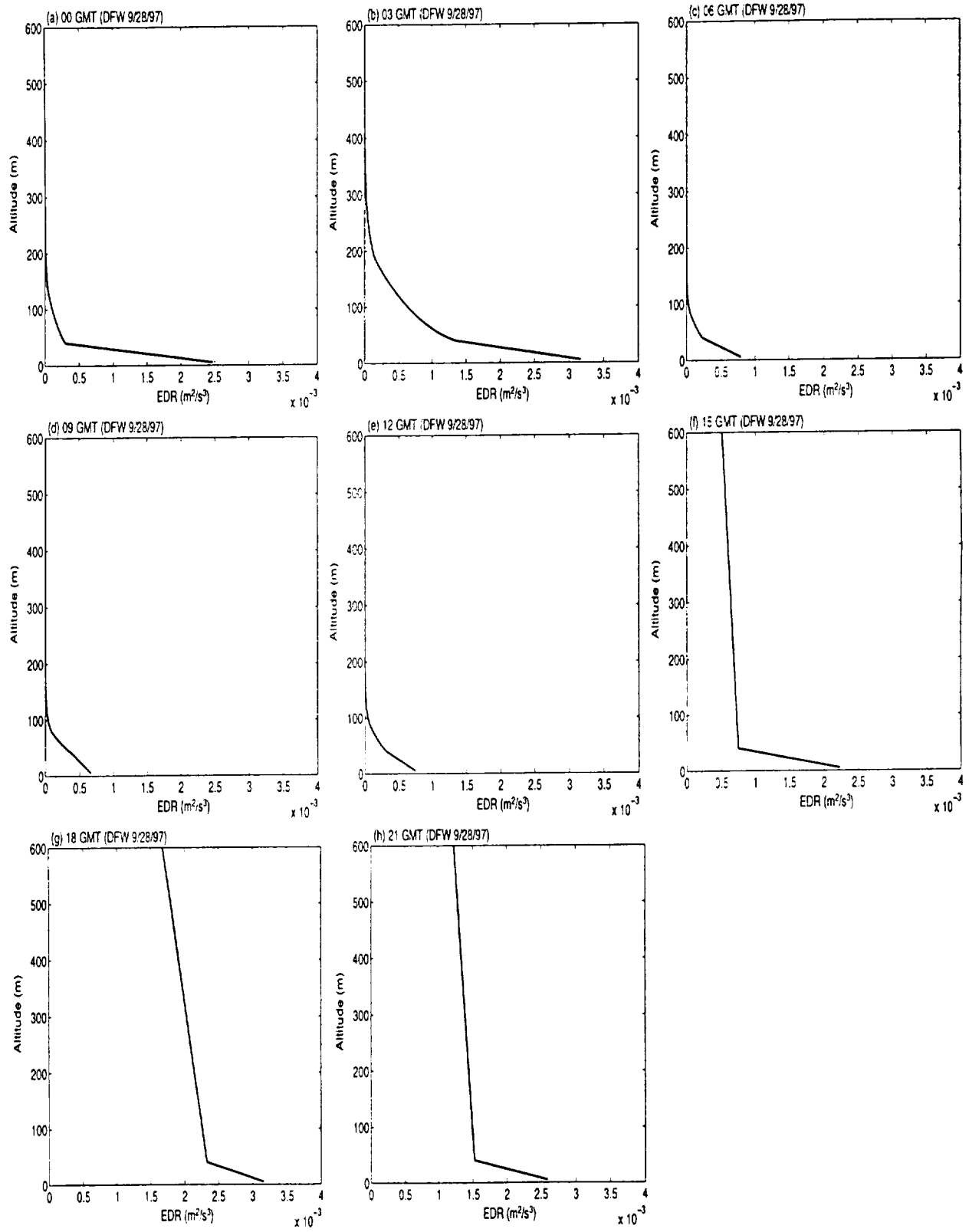
24

Figure 7: Same as Fig. 8 but for EDR profiles.